

School of Civil and Mechanical Engineering

**Development of Ambient Cured High-Strength Fiber Reinforced
Geopolymer Composites**

Musaad Zaheer Nazir Khan

**This thesis is presented for the Degree of
Doctor of Philosophy
of
Curtin University**

November 2018

Declaration

To the best of my knowledge and belief, this thesis contains no material previously published by any other person except where due acknowledgment has been made.

This thesis contains no material which has been accepted for the award of any other degree or diploma in any university.

Signature:  (Musaad Zaheer Nazir Khan)

Date: 02/11/2018

Copyright

I warrant that I have obtained, where necessary, permission from the copyright owners to use any third-party copyright material reproduced in the thesis (e.g., questionnaires, artwork, unpublished letters), or to use any of my own published work (e.g., journal articles) in which the copyright is held by another party (e.g., publisher, co-authors).

Signature:  (Musaad Zaheer Nazir Khan)

Date: 02/11/2018

Dedication

I would like to dedicate my thesis to my parents for their tremendous love, constant prayers, and continuous support!

To my beloved wife, son, and daughter!

To my (late) grandmother, who laid the stepping stone for my educational career, carrying me every day on her lap when I was a child and walking nearly 5 km to the nearest school in the village!

To my thesis advisors (Professor Hong Hao and Professor Yifei Hao)!

To all those people who face hardships in their lives, but always stay strong, have a firm belief in Allah SWT and transform every challenge into a strength!

ABSTRACT

Ordinary Portland Cement (OPC) is a primary ingredient in concrete. However, significant concerns over the required amount of energy, the gradual depletion of natural resources, and carbon dioxide (CO₂) emissions during the production of OPC have led the civil engineering community to find alternatives. The idea of sustainable development has further recognized the urge of using new environment-friendly materials in construction applications. In this regard, the use of pozzolanic wastes including fly ash and slag as partial OPC replacement is well established in the concrete industry due to their latent hydraulic properties. On the other hand, recent studies have shown that these by-products can be directly activated with the alkaline solutions and could potentially replace OPC from the concrete in entirety. Geopolymer materials offer several advantages such as reduced greenhouse gas emissions and recycling of the industrial by-products.

Several previous studies have reported the development of fly ash based geopolymer formulations, yet a vast majority requires heat curing to gain appropriate strength. This is considered to be a significant limitation for the commercial uptake of geopolymer technology as the energy-intensive curing method is not feasible for the in-situ applications. Besides, brittleness, low tensile strength, and poor ductility are the main drawbacks of geopolymer materials. The inclusion of short fibers has been of significant interest to improve their intrinsically brittle nature. However, in addition to the differences in choice of fiber reinforcement, most of the previous studies on geopolymer composites are limited to static material tests only. It is widely accepted that apart from the quasi-static actions, all concrete structures during their designed lifespan may face natural and manmade dynamic hazards, such as unwanted vehicle impacts or accidental explosions, etc. For better design and analysis of structures subjected to these dynamic actions, understanding the material properties at high strain rates is essential. Unfortunately, the existing literature lacks information on the dynamic material properties of geopolymers, and no research data are available on the dynamic material properties of high-performance geopolymer composites suitable for ambient curing. Furthermore, there is also a general lack of understanding about the behaviour of geopolymer materials under multiaxial stress conditions which is of crucial importance for structural protection against highly dynamic loads.

Based on the state-of-the-art of the development of geopolymer material and the need of understanding material properties under impact and multi-axial stress states, the primary aim of this research is to develop high-strength and ductile geopolymer composites that can be cured in ambient condition, followed by characterization of the material properties under quasi-static, dynamic, and multiaxial stress conditions. An overview of the literature and research significance are described in Chapter 1. This thesis is a collection of a series of experimental works and predominantly utilizes low-calcium fly ash as the primary binder which is activated by a multi-compound mixture of sodium hydroxide and sodium silicate precursor. A novel spiral-shaped steel fiber is combined with hooked-end steel fibers and high-strength polyethylene (HSPE) fibers at different fiber volume fractions and combinations to reinforce the brittle matrix. Moreover, this thesis also provides valuable insight into the dynamic tensile, dynamic compressive, and triaxial compressive behaviour of unreinforced and fiber reinforced geopolymer composite (FRGC). A broad range of testing methods, samples sizes, and equipment are used. The obtained results are also compared with the

existing standards (Australian Standard, Comite Euro-International du Beton) and literature on high-performance cement-based composites to assess the extent of the reliability of code predictions for these new materials.

Chapter 2 discusses the synthesis of high-strength geopolymer matrix by combining low-calcium fly ash with different additives including slag, ultrafine fly ash (UFFA), and calcium hydroxide ($\text{Ca}(\text{OH})_2$) at varying mass ratios and binder combinations. It is found that high-strength geopolymer composite with a compressive strength of more than 100 MPa at 28 days can be produced by blending an appropriate quantity of slag with fly ash. Moreover, the microstructural and mineralogical studies including the thermogravimetric analysis (TGA), Mercury Intrusion Porosimetry (MIP), Scanning electron microscopy (SEM), and X-ray diffraction (XRD) are found in good agreement with the measured compressive strength properties for different geopolymer matrices.

Chapter 3 presents the effects of curing conditions and fine aggregates content on the compressive strength properties of blended high-strength geopolymer mortar mixtures. It is observed that the water curing method causes abridged dissolution of fly ash particles which is not suitable for the curing purposes adopted in many studies in the literature. The use of air curing environment results in fewer microcracks at the aggregate-gel interfaces and additional geopolymerization which improves the compressive strength.

Chapter 4 reports the development of high-performance FRGC using a new spiral-shaped steel fiber in a series of fiber volume fractions and combinations with hooked-end and HSPE fibers. The test results indicate a threefold increase in the flexure-tensile strength of unreinforced geopolymer specimens with the inclusion of fibers. All FRGCs showed multiple-cracking failure modes and deflection-hardening response. Moreover, the energy absorption capability of geopolymer composites is significantly improved by hybridizing HSPE fibers with the steel fiber reinforcement. The individual fiber pull-out tests showed a strong bond between the spiral-steel fiber and geopolymer matrix. The existing Australian Standards may not be applied to estimate the modulus of elasticity of geopolymer materials.

Chapter 5 deliberates upon the influence of strain rate on the dynamic splitting-tensile properties of unreinforced and two types (i.e., steel and hybrid steel-polyethylene) of FRGC using a modified 100-mm Split Hopkinson Pressure Bar (SHPB). The quasi-static test results indicate a substantial increase in the peak-load carrying capacity and post-cracking behaviour of geopolymer composites using the proposed hybrid steel-polyethylene fiber reinforcement. At strain rates higher than 3 sec^{-1} , the fabricated geopolymer composites display strong strain rate dependency and the DIF_{ft} (dynamic increase factor) versus strain rate relationships increase approximately linearly with the strain rate. Comparison between the test results, data from other researchers and CEB recommendations identify the inadequacy of code recommendations to estimate the tension DIF_{ft} of geopolymers composites. Consequently, empirical formulae are proposed based on test data for direct use in structural analysis and material modeling.

Chapter 6 evaluates the dynamic compressive material properties of unreinforced and hybrid steel-polyethylene FRGC materials. Similar to the dynamic splitting tension tests, the synthesized materials show a prominent increase in compressive strength with an increase in the strain rate and the sensitivity threshold exists at 30 sec^{-1} and 66 sec^{-1} , respectively. The strain energy density analysis shows obvious binomial constitutive relationships between the

energy absorption capacity of the tested materials and the average strain rates. However, due to a slight overestimation of dynamic compressive strength by CEB model code, empirical relationships are proposed to signify the rate dependence of developed geopolymer composites which increases in a linear logarithmic manner with the strain rate.

Chapter 7 presents experimental results on the influence of lateral confinement on geopolymer materials. Fifteen different levels of confining pressures are used to comprehensively investigate the triaxial stress-strain characteristics of unreinforced geopolymer and hybrid steel-polyethylene FRGC. The results confirm the confinement sensitivity of geopolymer materials as both peak axial stress and axial strain increase with the confining pressure, similar to OPC concrete. However, compared with existing literature, some variances do exist regarding the compressive meridian strength boundaries. The triaxial failure curve of high-strength geopolymer tends to reach a plateau at higher confinement levels, while for fiber reinforced geopolymer material, it is more linear. Based on the results, constitutive models are proposed using the Power-law and Willam-Warnke failure criterion to predict the peak axial strength of plain and FRGC materials upon confinement.

In summary, the findings of this study have multiple outlooks in terms of reassuring the engineering community of using geopolymer materials in construction applications requiring high-energy absorbing materials. Moreover, the test data also provide significant input for developing the corresponding material model, which allows simulating the behaviour of high-strength geopolymer materials in mathematical form.

ACKNOWLEDGMENTS

“In the name of Allah, the most gracious, the most merciful”

This whole Ph.D. study has been an incredible learning experience for me and is filled with both exciting and challenging moments. I firmly believe that the completion of this thesis would not have been possible without the special blessings from Allah SWT and the help of many individuals that I received along the way.

First and foremost, I would like to express my sincere gratitude for my thesis supervisor Professor Hong Hao, who has been a constant source of motivation and encouragement. For me, it is complicated to describe in words the level of care and personal support; I received from him. All I can write, he has an attitude of a genius and easily qualifies as the most exceptional human being that I have ever met in my life. I feel fortunate to be one of his Ph.D. students. I now realize after three years that with what ease he has sowed the seed for the quest of knowledge in me. I consider it invaluable and a real asset for a researcher, which will help me considerably both in my professional career and personal life. I would also like to express my highest appreciation to my thesis co-supervisor, Professor Yifei Hao for his relentless efforts, patience, and guidance towards the successful completion of this study. A special thanks to Associate Professor Faiz Shaikh for introducing me to the geopolymer technology and extending valuable suggestions. I am incredibly grateful to my supervisors for their time that they allocated for reviewing the draft manuscripts before their submission to the valued journals. My sincere thanks also go to the anonymous reviewers for their positive comments and suggestions to improve the quality of the publications that form a part of this thesis.

Secondly, I would like to thank Curtin University, Australia and National University of Sciences and Technology (NUST), Pakistan for providing me with the necessary financial support for the Ph.D. study. Without these scholarship awards from both of these academic institutions, it would have been impossible for me to undertake a Higher Degree by Research in Australia. I am highly obliged and will ever remain grateful to both of these universities for financial support. I am also thankful to the Australian Research Council for supporting this research project through ARC grant DP160104557.

Thirdly, a heartfelt thanks must go to the Head of Civil Engineering department at Curtin University, Dr. Andrew Whyte for providing me with the opportunities to present my research at the refereed national and international conferences. Honest gratitude is also due for all the administrative support staff at School of Civil and Mechanical Engineering, especially for Mrs. Sucey Leong, Ms. Cheryl Cheng, Mr. Frankie Sia, and Ms. Ying Hong Lin for assisting me with the administrative tasks. I would also like to extend a heartfelt thanks to all the lab technicians in Civil Engineering Laboratory at Curtin University including Mr. Mick Elliss,

Mr. Luke English, Mr. Craig Gwyther, Mr. Ashely Hughes, Mr. Rob Cutter, Dr. Arnie Bredin, and Dr. Ray Mahidasht for their help in many ways. Special recognition is also extended to the Laboratory staff at Central South University, China for their assistance during the triaxial tests. Likewise, I acknowledge the use of equipment, scientific and technical assistance of the Curtin University Electron Microscopy Facility, which has been partially funded by the University, State, and Commonwealth Governments and thank Mrs. Ellaine Miller and Ms. Veronica Avery for their help in microstructural studies.

Furthermore, I am grateful to all the students, research associates, and staff members in Professor Hao's research group at Curtin University for their constructive feedbacks during regular Friday group meetings. I would especially thank Dr. Kinzang Thinley for being a wonderful friend with whom I used to gossip, engage in deep conversations, and discuss a majority of personal affairs during the early part of my Ph.D. study.

In the end, no acknowledgment will ever be complete without conveying my honest gratefulness to my family. I would like to pay special gratitude to my mother, father, and siblings for their constant encouragement, love, and continued prayers. A particular deep sense of acknowledgment remains outstanding for my (late) grandmother, who herself being uneducated knew the importance of education. Unfortunately, she passed away while I was in Australia. My most profound appreciation is for my soul mate and beloved wife, Dr. Anum Musaad for her trust, selfless support in difficult times, and continuous encouragement throughout this journey. Without her sacrifices, I would have never been able to complete my studies. I also wish to express my sincere love for my kids, Arham Musaad and Rahmeen Musaad and make an apology for the limited time I spent with them. Last but not least, many thanks are also due to my parents-in-law for their understanding during the difficult times and prayers which I consider priceless.

LIST OF PUBLISHED WORKS AND WORK PREPARED FOR PUBLICATION

The list of published papers and work prepared for publication, with the full bibliographic citations in the order they appear in the thesis, are listed below.

Chapter 2

Khan, M. Z. N., Shaikh, F. U. A., Hao, Y., & Hao, H. (2016). Synthesis of high strength ambient cured geopolymer composite by using low calcium fly ash. *Construction and Building Materials*, 125, 809-820. DOI: <http://dx.doi.org/10.1016/j.conbuildmat.2016.08.097>.

Chapter 3

Khan, M. Z. N., Shaikh, F. U. A., Hao, Y., & Hao, H. (2017). Effects of curing conditions and sand-to-binder ratios on compressive strength development of fly ash geopolymer. *Journal of Materials in Civil Engineering*, 30(2), 04017267. DOI: <https://ascelibrary.org/doi/10.1061/%28ASCE%29MT.1943-5533.0002119>.

Chapter 4

Khan, M. Z. N., Hao, Y., Hao, H., & Shaikh, F. U. A. (2018a). Mechanical properties of ambient cured high strength hybrid steel and synthetic fibers reinforced geopolymer composites. *Cement and Concrete Composites*, 85(Supplement C), 133-152. DOI: <https://doi.org/10.1016/j.cemconcomp.2017.10.011>.

Chapter 5

Khan, M. Z. N., Hao, Y., Hao, H., & Shaikh, F. U. A. (2018). Mechanical properties and behaviour of high-strength plain and hybrid-fiber reinforced geopolymer composites under dynamic splitting tension. *Cement and Concrete Composites*, (under review).

Chapter 6

Khan, M. Z. N., Hao, Y., Hao, H., & Shaikh, F. U. A. (2018b). Experimental evaluation of quasi-static and dynamic compressive properties of ambient-cured high-strength plain and fiber reinforced geopolymer composites. *Construction and Building Materials*, 166, 482-499. DOI: <https://doi.org/10.1016/j.conbuildmat.2018.01.166>.

Chapter 7

Khan, M. Z. N., Hao, Y., Hao, H., Shaikh, F. U. A., & Liu, K. (2018c). Mechanical properties of ambient cured high-strength plain and hybrid fiber reinforced geopolymer composites from triaxial compressive tests. *Construction and Building Materials*, 185, 338-353. DOI: <https://doi.org/10.1016/j.conbuildmat.2018.07.092>.

LIST OF RELEVANT ADDITIONAL PUBLICATIONS

The list of additional publications relevant to the thesis, with the full bibliographic citations, is given below.

1. **Khan, M. Z. N.**, Shaikh, F. U. A., Hao, Y., & Hao, H. (2016). *Workability and compressive strength properties of high strength geopolymer mortars*. Proceedings of the 24th Australasian Conference on the Mechanics of Structures and Materials (ACMSM 24), Perth, Australia.
2. **Khan, M. Z. N.**, Hao, Y., Hao, H., & Shaikh, F. U. A. (2017a). *Flexural responses of hybrid hook-end, spiral steel and synthetic fiber reinforced geopolymer composites*. Proceedings of the 28th Biennial National Conference on Advances in Concrete Materials and Structures (Concrete 2017), Adelaide, Australia.
3. **Khan, M. Z. N.**, Hao, Y., Hao, H., & Shaikh, F. U. A. (2017b). *Impact response of plain and fiber reinforced ambient-cured high-strength geopolymer composites*. Proceedings of the 6th International Conference on Design and Analysis of Protective Structures (DAPS 2017), Melbourne, Australia.
4. Cui, Y., Hao, H., Li, J., Chen, W., & **Khan, M. Z. N.** (2018). *Mechanical properties of new short fiber reinforced geopolymer composite for skin of structural insulated Panels*. Proceedings of the 13th International Conference on Steel, Space and Composite Structures SS 18), Perth, Australia.

STATEMENT OF CONTRIBUTION OF OTHERS

This research project was initiated by Prof. Hong Hao in collaboration with Assoc. Prof. Faiz Shaikh. As a primary supervisor, Prof. Hong Hao helped significantly in defining the overall scope and objectives of the study. The research works presented in this thesis were primarily carried out by the first author (Musaad Zaheer Nazir Khan) including the literature reviews, the design of experimental studies, preparation of specimens, performing the laboratory experiments, interpretation and evaluation of test results, and writing the manuscripts. The contributions from others are mentioned below, while the signed contribution forms for co-authors are attached in Appendix - II.

Chapter 2 - 3

The experimental studies were formulated by the candidate (Musaad Zaheer Nazir Khan) under the supervision of Prof. Hong Hao and Prof. Yifei Hao. Associate Professor Faiz Shaikh suggested the methodologies for microstructural investigations and assisted in conducting the mercury intrusion porosity tests at Asian Institute of Technology, Thailand. Prof. Hong Hao provided unwavering financial support through ARC project DP160104557 for carrying out the microstructural and mineralogical studies in Curtin University and Asian Institute of Technology, Thailand. Based on the experimental findings, the manuscripts were written by the first author (Musaad Zaheer Nazir Khan) which were later scrutinized and edited by all co-authors before their submission to the respective journals.

Chapter 4 - 6

Musaad Zaheer Nazir Khan prepared the research plans for the experimental studies in thorough discussions with Prof. Hong Hao and Prof. Yifei Hao. Prof. Yifei Hao and Assoc. Prof. Faiz Shaikh also provided additional support in purchasing the spiral steel and synthetic fibers from China and Japan, respectively. The candidate performed the quasi-static and dynamic material tests at Curtin University, Australia with constant intellectual inputs from Prof. Hong Hao and Prof. Yifei Hao. Prof. Hong Hao provided considerable financial support via ARC project DP160104557 which was also supplemented through the opening project of State Key Laboratory of Explosion Science and Technology (Beijing Institute of Technology) under grant no. KFJJ17-07M. Based on the results and their exposition, the manuscripts were written by the candidate (Musaad Zaheer Nazir Khan) which were thoroughly revised and edited by Prof. Hong Hao, Prof. Yifei Hao, and proof-read by Assoc. Prof. Faiz Shaikh.

Chapter 7

The candidate (Musaad Zaheer Nazir Khan) designed the experimental study with Prof. Yifei Hao and Prof. Hong Hao. The test samples were prepared in Curtin University, Australia and tested using the triaxial test facility at Central South University, China. Assoc. Prof Faiz provided the support in purchasing the waste materials required for the preparation of test samples. Kewei Liu extended the logistical and technical assistance to conduct the triaxial compressive tests at Central South University. Since the inception of the work, Prof. Hong Hao and Prof. Yifei Hao were readily available for the intellectual discussions till its successful completion. The first author (Musaad Zaheer Nazir Khan) wrote the manuscript which was later finalized by Prof. Hong Hao and Prof. Yifei Hao.

TABLE OF CONTENTS

ABSTRACT	v
ACKNOWLEDGMENTS	viii
LIST OF PUBLISHED WORKS AND WORK PREPARED FOR PUBLICATION.....	x
LIST OF RELEVANT ADDITIONAL PUBLICATIONS	xi
STATEMENT OF CONTRIBUTION OF OTHERS	xii
TABLE OF CONTENTS	xiv
LIST OF FIGURES	xix
LIST OF TABLES	xxii
NOTATION	xxiii
ABBREVIATIONS.....	xxvii
CHAPTER 1 INTRODUCTION & LITERATURE REVIEW	1
1.1 Research Background	1
1.2 Problem Statement and Research Significance.....	4
1.2.1 Ambient Curing of Geopolymer Materials	4
1.2.2 Fiber-Reinforcement of Geopolymer Materials.....	6
1.2.3 Performance of Geopolymer Composite/Concrete Materials under Dynamic Loads and Multi-Hazard Environment	7
1.3 Research Objectives.....	9
1.4 Original Contribution of Thesis	10
1.4.1 Thesis Outline and Structure.....	11
1.5 References.....	13
CHAPTER 2 SYNTHESIS OF HIGH STRENGTH AMBIENT CURED GEOPOLYMER COMPOSITE BY USING LOW-CALCIUM FLY ASH.....	17
2.1 Abstract.....	17
2.2 Introduction.....	17
2.3 Experimental Details and Testing Methods	20
2.3.1 Materials	20
2.3.2 Mixture proportions, mixing, and curing of samples	21
2.4 Methods.....	23
2.4.1 Workability and Compressive Strength Test	23
2.4.2 Differential Thermal Analysis (DTA) / Thermogravimetric Analysis (TGA) & Pore Size Measurement.....	23
2.4.3 X-ray diffraction (XRD) analysis	23
2.4.4 Scanning electron microscopy (SEM) and Energy dispersive X-ray (EDX) analysis	24
2.5 Results and Discussions	24
2.5.1 Workability	24

2.5.2	Compressive Strength	25
2.5.3	Pore Size Measurement.....	29
2.5.4	X-ray Diffraction (XRD) Analysis.....	32
2.5.5	Differential Thermal Analysis (DTA) and Thermogravimetric Analysis (TGA)	35
2.5.6	Scanning electron Microscopy (SEM) and Energy dispersive X-ray Spectroscopy (EDS) Analysis.....	37
2.6	Conclusions.....	40
2.7	References.....	41

**CHAPTER 3 EFFECTS OF CURING CONDITIONS & SAND-TO-BINDER RATIOS
ON COMPRESSIVE STRENGTH DEVELOPMENT OF FLY ASH GEOPOLYMER.
..... 45**

3.1	Abstract.....	45
3.2	Introduction.....	45
3.3	Experimental Procedures	48
3.3.1	Materials	48
3.3.2	Mix designs.....	49
3.3.3	Mixing, sample preparation and curing conditions.....	50
3.4	Test Methods.....	51
3.4.1	Workability and compressive strength test	51
3.4.2	Porosity Measurement.....	51
3.5	Results and Discussion.....	52
3.5.1	Workability	52
3.5.2	Compressive strength.....	53
3.5.2.1	Effect of curing conditions on strength development	53
3.5.2.2	Effect of additives and sand-binder ratios on strength development	55
3.5.3	Porosity Measurement.....	58
3.5.4	Scanning electron Microscopy (SEM) and Energy dispersive X-ray Spectroscopy (EDS) Analysis.....	61
3.6	Conclusions.....	66
3.7	References.....	67

**CHAPTER 4 MECHANICAL PROPERTIES OF AMBIENT CURED HIGH
STRENGTH HYBRID STEEL AND SYNTHETIC FIBERS REINFORCED
GEOPOLYMER COMPOSITES..... 71**

4.1	Abstract.....	71
4.2	Introduction.....	71
4.3	Experimental Section	75
4.3.1	Materials and Methods.....	75
4.3.2	Preparation of Geopolymer Composites	78
4.4	Test Methods.....	80
4.4.1	Workability	80
4.4.2	Compressive Strength	81
4.4.3	Modulus of Elasticity & Poisson's Ratio	81
4.4.4	Flexural Strength Properties.....	81
4.4.5	Fiber Pull-out Testing	82
4.4.6	Fiber Distribution in Geopolymer Composites	82

4.5	Results and Discussion.....	83
4.5.1	Flow Measurement.....	83
4.5.2	Compressive Strength.....	85
4.5.3	Modulus of Elasticity and Poisson’s Ratio.....	87
4.5.4	Flexural Tensile Behaviour of Geopolymer Composites.....	91
	4.5.4.1 General discussion regarding the test parameters.....	91
	4.5.4.2 Load bearing capacity vs. mid-span deflection.....	93
	4.5.4.3 Fracture toughness (energy absorption capacity) and equivalent bending stress.....	97
	4.5.4.4 Cracking behaviour of geopolymer composites.....	100
4.5.5	Pull-out behaviour of spiral steel fibers.....	101
4.5.6	Fiber distribution in geopolymer composites.....	104
4.6	Conclusions.....	107
4.7	References.....	108

CHAPTER 5 MECHANICAL PROPERTIES AND BEHAVIOUR OF HIGH-STRENGTH PLAIN AND HYBRID-FIBER REINFORCED GEOPOLYMER COMPOSITES UNDER DYNAMIC SPLITTING TENSION 113

5.1	Abstract.....	113
5.2	Introduction.....	113
5.3	Materials and Experimental methods.....	116
5.3.1	Description of materials.....	116
	5.3.1.1 Fly ash and slag.....	116
	5.3.1.2 Alkaline solution, fine aggregates, and water.....	116
	5.3.1.3 Fibers.....	117
5.3.2	Mix proportion and fiber combinations.....	117
5.3.3	Sample preparation.....	118
5.4	Test Methods and Equipment details.....	119
5.4.1	Quasi-static compressive strength and modulus of elasticity tests.....	119
5.4.2	Quasi-static split-tensile tests.....	120
5.4.3	Dynamic splitting-tensile tests and SHPB equipment.....	121
5.4.4	Digital image correlation (DIC) technique, set-up, and analysis.....	122
5.5	Results and Discussions.....	123
5.5.1	Quasi-static compression test results (modulus of elasticity, compressive strength) and density.....	123
5.5.2	Quasi-static splitting tensile results.....	124
5.5.3	Dynamic splitting-tensile SHPB test results.....	127
	5.5.3.1 Processing of the SHPB test data.....	127
	5.5.3.2 Typical voltage data output, stress-balance check in SHPB tests.....	128
	5.5.3.3 Effect of strain rate on DIF_{ft} and tensile strength characteristics of plain and FRGC mixtures.....	129
	5.5.3.4 Comparison of fracture development processes of plain and FRGC samples.....	133
	5.5.3.5 Comparison of crack-opening displacement (COD) of plain and FRGC samples.....	138
	5.5.3.6 Comparison of post-test failure patterns of plain geopolymer and FRGC samples.....	140
5.6	Conclusions.....	142
5.7	References.....	143

CHAPTER 6 EXPERIMENTAL EVALUATION OF QUASI-STATIC AND DYNAMIC COMPRESSIVE PROPERTIES OF AMBIENT-CURED HIGH-STRENGTH PLAIN AND FIBER REINFORCED GEOPOLYMER COMPOSITES ...
..... **147**

6.1	Abstract	147
6.2	Introduction.....	147
6.3	Experimental Section	152
6.3.1	Material classification	152
6.3.2	Mix proportions, Workability, Sample preparation and Curing	154
6.3.2.1	Mix Proportions	154
6.3.2.2	Synthesis, workability, and curing of plain & fiber geopolymer composite samples.....	154
6.3.3	Test Methods.....	156
6.3.3.1	Density & Quasi-static compressive strength tests	157
6.3.3.2	Dynamic impact compression test set-up and equipment details.....	157
6.4	Results and Discussions	160
6.4.1	Density & Quasi-static compressive strength test results	160
6.4.2	Dynamic SHPB test results	163
6.4.2.1	Typical stress-wave output signal in SHPB tests	163
6.4.2.2	Data processing, test validity assumptions and stress equilibrium check	163
6.4.2.3	Comparison of dynamic stress-strain curves.....	164
6.4.2.4	Comparison of rate effects on strength characteristics.....	166
6.4.2.5	Comparison of Impact Toughness	170
6.4.2.6	Comparison of failure processes	172
6.4.2.7	Comparison of post-test failure patterns	174
6.5	Conclusions.....	177
6.6	References.....	178

CHAPTER 7 MECHANICAL PROPERTIES OF AMBIENT CURED HIGH-STRENGTH PLAIN AND HYBRID FIBER REINFORCED GEOPOLYMER COMPOSITES FROM TRIAXIAL COMPRESSIVE TESTS
..... **182**

7.1	Abstract.....	182
7.2	Introduction.....	183
7.3	Experimental Approach	186
7.3.1	Mixture proportions	186
7.3.2	Material composition and fiber properties	187
7.3.3	Mixing process, casting, curing, and sample design	190
7.3.4	Test Procedures - Uniaxial and Triaxial compression test setup	192
7.3.4.1	Loading schemes.....	192
7.4	Results and Discussions	195
7.4.1	Effect of confining pressure on stress-strain response of HSG.....	195
7.4.2	Effect of confining pressure on stress-strain response of FRGC	198
7.4.3	Effect of confining pressure on triaxial strength of HSG and FRGC	203
7.4.3.1	Power-law failure criterion	204
7.4.3.2	Willam-Warnke failure criterion.....	207
7.4.4	Damage mechanism of HSG and FRGC samples in uniaxial and triaxial compression	209
7.5	Conclusions.....	212
7.6	References.....	213

CHAPTER 8 CONCLUSIONS AND RECOMMENDATIONS.....	217
8.1 Main Findings	217
8.2 Recommendations and Outlook for future studies.....	221

LIST OF FIGURES

Figure 1-1 Predicted annual global cement production (Hasanbeigi et al., 2012).	1
Figure 1-2 Advantages of using geopolymer binder in construction materials.	3
Figure 1-3 Research Outline and Thesis structure.	12
Figure 2-1 Effect of additives on the workability of geopolymer composites.	24
Figure 2-2 Effect of additives on the compressive strength development of fly ash geopolymer (a) $\text{Ca}(\text{OH})_2$ (b) UFFA and $\text{Ca}(\text{OH})_2$ (c) slag (d) UFFA and slag.	26
Figure 2-3 Effect of additives on cumulative intrusion curves of geopolymer composites (a) $\text{Ca}(\text{OH})_2$, UFFA, and slag (b) UFFA and slag.	30
Figure 2-4 Effect of additives on pore size distribution of geopolymer composites (a) $\text{Ca}(\text{OH})_2$, UFFA, and slag (b) UFFA and slag.	31
Figure 2-5 XRD 2θ ($^\circ$) Cu, $K\alpha$ patterns of low calcium fly ash, slag, and UFFA.	33
Figure 2-6 XRDs of G10, G11, and G12 mixes.	34
Figure 2-7 XRDs of G11, G13, and G17 mixes.	34
Figure 2-8 XRDs of G4, G7, and G17 mixes.	34
Figure 2-9 TGA profiles of geopolymer composites (a) For hybrid fly ash, slag, UFFA & $\text{Ca}(\text{OH})_2$ (b) fly ash & slag blend.	35
Figure 2-10 DTG curves of geopolymer composites (a) For hybrid fly ash, slag, UFFA & $\text{Ca}(\text{OH})_2$ (b) fly ash & slag blend.	37
Figure 2-11 SEM/EDX spectra of geopolymer composites (a) G1 (FA100) (b) G11 (FA60S40).	38
Figure 2-12 SEM/EDX spectra of geopolymer composites (a) G7 (FA60UFFA35Ca5) (b) G4 (FA95Ca5).	39
Figure 3-1 Workability of geopolymer mixtures with different additives and sand-binder ratios.	52
Figure 3-2 Compressive strength of geopolymer mortars in different curing conditions (a) sand-binder = 2.00 (b) sand-binder = 2.75.	54
Figure 3-3 Compressive strength of geopolymer with different additives and sand-binder ratios (a) sand-binder = 1.60 (b) sand-binder = 2.00 (c) sand-binder = 2.75.	57
Figure 3-4 Cumulative intrusion curves for geopolymer samples cured in (a) ambient air (b) ambient water, and (c) heat curing conditions.	60
Figure 3-5 SEM images of M5 (FA50S50) geopolymer samples cured in (a) ambient air (b) ambient water.	62
Figure 3-6 SEM images of M4 (FA60S40) geopolymer samples cured in (a) ambient air (b) ambient water.	63
Figure 3-7 Higher magnification SEM images of M4 (FA60S40) geopolymer gels (sand-binder = 2.0) (a) air cured (b) water cured.	64
Figure 3-8 SEM/EDS spectra of M2 (FA60UFFA10S30) water cured geopolymer samples.	65
Figure 3-9 SEM/EDS spectra of M3 (FA70S30) water cured geopolymer samples.	65
Figure 4-1 Particle size distribution of (a) low-calcium FA (b) slag.	77
Figure 4-2 Schematic of spiral steel fiber.	77
Figure 4-3 Schematic arrangement of casting molds for spiral fiber pull-out tests.	80
Figure 4-4 (a) Schematic diagram and (b) a close-up for the actual setup for fiber pull-out test specimens.	83
Figure 4-5 Effect of different fiber combinations on flowability of the geopolymer composites.	84
Figure 4-6 Comparison of (a) compressive strength and (b) failure modes of plain and fiber reinforced geopolymer composites (FRGCs).	86

Figure 4-7 Comparison of Modulus of elasticity (E) and Poisson's ratio (μ) of plain and FRGCs.	88
Figure 4-8 Modulus of elasticity of investigated mixes compared with the existing test results and models.	90
Figure 4-9 (a) Typical load-deflection response curves of FRCC (Kim et al., 2008) and (b) Explanation of parameters for first peak load, peak load, and other characteristic response values in ASTM C1609 (ASTM, 2012).	92
Figure 4-10 Load-deflection plots of plain geopolymer matrix and FRGCs.	94
Figure 4-11 Comparison of peak deflection at MOR and quantitative increase in MOR of geopolymer matrix with the addition of fibers.	96
Figure 4-12 Effect of different fiber combinations on (a) toughness and (b) equivalent bending stress until designated points in geopolymer composites.	99
Figure 4-13 Cracking behaviour of geopolymer composites.	101
Figure 4-14 Comparison of force end-slip curves (a-c) for three different embedment lengths and (d) absorbed energy during the pull-out tests.	103
Figure 4-15 Comparison of fiber distribution along two cross-sections in (a) G-2 (b) G-4 (c) G-6 (d) G-7 (e) G-8.	106
Figure 5-1 Flow chart for the preparation of plain geopolymer and FRGC.	118
Figure 5-2 Samples for (a) quasi-static compression (b) quasi-static and dynamic splitting-tensile tests.	119
Figure 5-3 Testing set-up for quasi-static compression and strain-gauge installation.	120
Figure 5-4 Testing set-up for quasi-static splitting tensile and extensometer installation. ...	121
Figure 5-5 Schematic illustration of Split-Hopkinson pressure bar (SHPB) device.	121
Figure 5-6 Comparison of quasi-static splitting tensile strengths vs. LDC of plain geopolymer and FRGCs.	125
Figure 5-7 Failed samples (a) plain geopolymer (b) SFRGC-1 in quasi-static splitting tensile tests (c) HFRGC.	126
Figure 5-8 Typical waveform from SHPB dynamic splitting tensile tests.	128
Figure 5-9 Typical dynamic stress equilibrium check.	129
Figure 5-10 Comparison of DIF_{ft} of plain geopolymer with modified CEB recommendations and results from previous studies.	130
Figure 5-11 DIF_{ft} versus strain rate relationships of (a) plain geopolymer (b) SFRGC-1 (c) SFRGC-2 and (d) HFRGC.	131
Figure 5-12 Failure modes and high-speed camera image comparison of plain geopolymer and SFRGC-1 samples under loading rates of (a) 140 GPa/sec (b) 230 GPa/sec.	135
Figure 5-13 Failure modes and high-speed camera image comparison of SFRGC-2 and HFRGC samples under loading rates of (a) 140 GPa/sec (b) 230 GPa/sec.	136
Figure 5-14 Comparison of tensile stress time histories of plain geopolymer and FRGC samples under loading rates of (a) 140 GPa/sec (b) 230 GPa/sec.	137
Figure 5-15 Comparison of COD time histories of plain geopolymer and FRGC samples under stress rate of 230 GPa/sec.	138
Figure 5-16 Comparison of COD time histories of SFRGC-2 and HFRGC samples over extended time duration.	139
Figure 5-17 Comparison of post-test failure patterns of plain geopolymer and FRGC specimens in dynamic splitting tension.	141
Figure 6-1 DIF_{fc} results for geopolymer concrete mixtures from past investigations (Luo et al., 2013; Feng et al., 2015; Gao et al., 2015).	150
Figure 6-2 Picture of (a) Spiral steel (b) Hooked-end steel (c) HSPE fibers.	153
Figure 6-3 PVC formwork (a) before and (b) after the pour.	155
Figure 6-4 Prepared samples for (a) quasi-static and (b) dynamic compression tests on plain and FRGC samples.	156

Figure 6-5 Quasi-static test set-up in 160-ton universal testing machine.	157
Figure 6-6 (a) Schematic and (b) actual picture of the SHPB equipment.	158
Figure 6-7 Compressive wave initiated strains and interfaces between pressure bars-sample.	159
Figure 6-8 Rubber pulse shaper placed on the incident bar.	160
Figure 6-9 Comparison of quasi-static stress-strain relation of (a) plain geopolymer matrix (b) FRGC.	162
Figure 6-10 Failure modes of (a) plain geopolymer matrix (b) FRGC under quasi-static loading.	162
Figure 6-11 Typical stress wave histories in SHPB tests.	163
Figure 6-12 Typical dynamic stress equilibrium relationship between stress and time.	164
Figure 6-13 Comparison of dynamic stress-strain curves of (a) plain geopolymer matrix (b) FRGC.	165
Figure 6-14 Relationship between the compressive DIF and strain rate of (a) plain and (b) FRGC.	167
Figure 6-15 Comparison of DIF and average strain rate from current research and previous studies.	169
Figure 6-16 Comparison of energy absorption capability of plain and FRGC at different strain rates.	171
Figure 6-17 Fracture images and failure process of plain geopolymer matrix at different time instants.	172
Figure 6-18 Fracture images and failure process of FRGC at different time instants.	173
Figure 6-19 Damage pattern of plain geopolymer matrix samples in a range of strain rates.	175
Figure 6-20 Damage pattern of FRGC samples in a range of strain rates.	176
Figure 7-1 (a) XRD 2 θ ($^{\circ}$) Cu, K- α patterns and (b) particle size distributions of fly ash and slag.	188
Figure 7-2 Physical appearances of (a) Hooked-end steel (b) Spiral steel (c) HSPE fibers.	189
Figure 7-3 (a) Cast slab and prepared samples (b) HSG and (c) FRGC for uniaxial and triaxial tests.	191
Figure 7-4 (a) Triaxial test setup (b) Axis direction and (c) Load path for triaxial tests.	193
Figure 7-5 Uniaxial and triaxial stress-strain behaviour of HSG under various confining pressures.	196
Figure 7-6 Uniaxial and triaxial stress-strain behaviour of FRGC under various confining pressures.	199
Figure 7-7 Comparison of increase in ductility of HSG and FRGC at different confining pressures.	200
Figure 7-8 Triaxial strength of HSG and comparison with previous experimental studies on HSCs.	205
Figure 7-9 Triaxial strength of FRGC and comparison with previous experimental studies of FRCCs.	206
Figure 7-10 Comparison of compressive meridian of HSG and HSCs from previous studies.	208
Figure 7-11 Comparison of compressive meridian of FRGC and FRCCs from previous studies.	209
Figure 7-12 Failure modes of (a) HSG and (b) FRGC in uniaxial and triaxial compressive loading conditions.	211

LIST OF TABLES

Table 2-1 Chemical compositions of fly ash, UFFA, and slag as determined by XRF (%) ..	21
Table 2-2 Weight proportions and oxide molar ratios of geopolymer composites	22
Table 3-1 Chemical composition of solid precursors and alkali activators	49
Table 3-2 Mixture proportions of geopolymer mortar samples	50
Table 3-3 Total pore volume and porosity values measured for air and water cured geopolymer samples.....	60
Table 4-1 Chemical compositions of FA and slag	76
Table 4-2 Properties of steel and synthetic fibers	78
Table 4-3 Mix constituents and details of different fiber combinations used in geopolymer matrix	79
Table 4-4 Summary of mechanical properties of geopolymer composites.....	95
Table 4-5 Average characteristic response values for flexural tensile behaviour of geopolymer composites	100
Table 5-1 Mixture proportions of plain and fiber reinforced geopolymer composites	117
Table 5-2 Quasi-static compressive strengths and material properties of plain geopolymer and FRGC	124
Table 5-3 Quasi-static splitting tensile strength of plain geopolymer and FRGC	124
Table 5-4 Parameters values for DIF_{fi} formulae of geopolymer composites	132
Table 6-1 Constituents of low-calcium FA and slag.....	153
Table 6-2 Properties of spiral steel, hooked-end steel and HSPE fibers.....	153
Table 6-3 Mix Proportions of geopolymer matrix and fiber reinforced composites.....	154
Table 7-1 Mix proportions of HSG and FRGC.....	186
Table 7-2 Chemical composition of low-calcium fly ash, slag and alkali-activators	189
Table 7-3 Physical and mechanical properties of fibers	190
Table 7-4 Experimental program for uniaxial and triaxial compression tests	195
Table 7-5 Uniaxial and Triaxial compression test results of HSG samples.....	201
Table 7-6 Uniaxial and Triaxial compression test results of FRGC samples	202

NOTATION

a = Material constant

A = Cross-sectional area of SHPB elastic bars, mm²

A_s = Cross-sectional area of sample in dynamic compression, mm²

b = Material constant

b = Width of the prism sample, mm

b_o = Willam-Warnke model coefficient

b_1 = Willam-Warnke model coefficient

b_2 = Willam-Warnke model coefficient

c_o = Elastic wave velocity, m/sec

d_o = Pore width, μm

d = Depth of prism samples, mm

D = Base diameter in flow table tests, mm

D_o = Original base diameter in flow table tests, mm

D^\wedge = Diameter of sample tested in quasi-static indirect tensile tests, mm

E = Modulus of Elasticity, GPa

E_B = Elastic modulus of Split Hopkinson Pressure Bar, mm

f = Flexural strength, MPa

f'_c = Compressive strength, MPa

f'_{co} = Reference concrete compressive strength, MPa

f_{cm} = Mean compressive strength, MPa

$f_{c, \text{imp}, k}$ = Impact compressive strength, MPa

f_{td} = Dynamic tensile strength, MPa

f_P = Peak flexural strength, MPa

f_{td} = Dynamic tensile strength at $\dot{\epsilon}$, MPa

f_{ts} = Quasi-static tensile strength at $\dot{\epsilon}_s$, MPa

$f \frac{L}{600}$ = Residual strength at net deflection of $L/600$, MPa

$f_{\frac{L}{150}}$ = Residual strength at net deflections of L/150, MPa

$f_{\frac{L}{50}}$ = Residual strength at net deflections of L/50, MPa

H_{so} = Height of sample tested in dynamic indirect tension, mm

I_1 = First invariant of stress tensor

l = Span length of prism samples, mm

L_o = Length of sample in dynamic compression, mm

L = Length of cylindrical sample, mm

L/B = Liquid to binder ratio

p = Net Pressure across the mercury meniscus at the time of the cumulative intrusion measurement, MPa

P = Flexure load, N

P_o = Maximum compressive failure load, kN

P_1 = First-peak load, kN

P_p = Peak load, kN

R_{so} = Radius of sample tested in dynamic indirect tension, mm

R_B = Radius of Split Hopkinson Pressure Bar, mm

S_2 = Stress corresponding to 40% of ultimate load

S_1 = Stress corresponding to a longitudinal strain, ϵ_a , of 50 millionths, MPa

t = Time lag between the start and peak of transmitted stress wave in dynamic indirect tensile tests, sec

$T_{\frac{D}{150}}$ = Area under the load deflection curve 0 to L/150, N.m.

w/s = water to solids ratio

W = Energy absorption capability (Strain Energy Density), KJ/m³

x = Material parameter in dynamic tensile constitutive relationship

y = Material parameter in dynamic tensile constitutive relationship

x_1 = Material parameter in dynamic tensile constitutive relationship

y_1 = Material parameter in dynamic tensile constitutive relationship

σ = Quasi-static indirect tensile strength, MPa
 σ_1 = Stress in 1st principal direction in triaxial compression (Willam-Warnke model), MPa
 σ_2 = Stress in 2nd principal direction in triaxial compression (Willam-Warnke model), MPa
 σ_3 = Stress in 3rd principal direction in triaxial compression (Willam-Warnke model), MPa
 σ_m = Average normal mean stress in triaxial test, MPa
 τ_m = Average mean shear stress in triaxial test, MPa
 σ_f = Mean compressive strength of composite with fibers, MPa
 σ_{mo} = Mean compressive strength of plain geopolymer in uniaxial compression, MPa
 $\dot{\sigma}$ = Stress rate in indirect SHPB tensile tests, GPa/sec
 σ_l = Peak axial stress, MPa
 σ_3 = Confining pressures, MPa
 σ_1/f'_c = Failure strength ratio
 σ_3/f'_c = Confinement ratio
 $\Delta\sigma$ = Deviatoric stress ($\Delta\sigma = \sigma_1 - \sigma_3$), MPa
 ε_2 = Longitudinal strain produced by stress S_2
 ε_{t2} = Transverse strain at midheight of the specimen produced by stress S_2
 ε_{t1} = Transverse strain at midheight of the specimen produced by stress S_1
 $\dot{\varepsilon}_s = 1 \times 10^{-6}$ (quasi-static strain rate in tensile tests), sec^{-1}
 $\dot{\varepsilon}_d$ = Dynamic strain rate in tensile tests, sec^{-1}
 $\varepsilon_i(t)$ = Incident strain
 $\varepsilon_r(t)$ = Reflected strain
 $\varepsilon_t(t)$ = Transmitted strain
 $\dot{\varepsilon}$ = Strain rate in SHPB dynamic compression and indirect tensile tests, sec^{-1}
 $\dot{\varepsilon}_{co} = 30 \times 10^{-6} \text{sec}^{-1}$ (quasi-static strain rate in compression tests), sec^{-1}
 $\dot{\varepsilon}_c$ = Dynamic strain rate in compression tests, sec^{-1}
 $\varepsilon(t)$ = Strain in sample in dynamic compression
 ε_{cu} = Critical axial strain of plain geopolymer in uniaxial compression
 ε_l = Confined peak axial strain

ε_3 = Confined peak lateral strain

$\varepsilon_1/\varepsilon_{cu}$ = Ductility Increase ratio

γ = Surface tension, mN/m

θ = Contact angle between mercury and Pore wall, (°)

μ = Poisson's ratio

ρ = Density, kg/m³

δ_1 = Net deflection at first-peak load, mm

δ_p = Net deflection at peak load, mm

ABBREVIATIONS

AACMs	Alkali-Activated Cementitious Materials
AAS	Alkali Activated Slag
AS	Australian Standards
ASTM	American Society for Testing and Materials
CEB	Comite Euro-International du Beton
COD	Crack-opening displacement
CO ₂	Carbon dioxide
CSH	Calcium Silicate Hydrate
DIC	Digital Image Correlation
DIF _{ft}	Dynamic Increase Factor (Tension)
DIF _{fc}	Dynamic Increase Factor (Compression)
DTA	Differential Thermal Analysis
EDS/EDX	Energy-Dispersive X-ray Spectroscopy
FRCCs	Fiber Reinforced Cement Composites
FRGCs	Fiber Reinforced Geopolymer Composites
GGBFS	Ground-Granulated Blast Furnace Slag
HPFRCC	High-Performance Fiber Reinforced Cementitious Composites
HFRGC	Hybrid Fiber Reinforced Geopolymer Composite
HPFRC	High-Performance Fiber Reinforced Concrete
HM	Hydration Modulus
HSC	High Strength Concrete
HSPE	High Strength Polyethylene
HVFA	High Volume Fly Ash
IPCC	Intergovernmental Panel on Climate Change
LOI	Loss on Ignition
LOP	Limit of Proportionality
LVDTs	Linear Variable Differential Transducers

MIP	Mercury Intrusion Porosimetry
MOR	Modulus of Rupture
NaOH	Sodium hydroxide
Na ₂ SiO ₃	Sodium silicate
N-A-S-H	Sodium aluminosilicate hydrate
NSC	Normal Strength Concrete
OPC	Ordinary Portland cement
PP	Polypropylene
PVA	Polyvinyl alcohol
RH	Relative Humidity
ROI	Region of interest
SCM	Supplementary Cementitious Materials
SHPB	Split-Hopkinson Pressure Bar
SFRGC	Steel Fiber Reinforced Geopolymer Composite
SSD	Saturated Surface Dry
TGA	Thermogravimetric analysis
UFC	Unified Facilities Criteria
UFFA	Ultrafine Fly Ash
UHPCC	Ultra-high Performance Fiber Reinforced Cement Composites
UHSFRC	Ultra-high Strength Fiber Reinforced Concrete
XRD	X-ray Diffraction
XRF	X-ray Fluorescence

CHAPTER 1 INTRODUCTION & LITERATURE REVIEW

1.1 Research Background

Concrete is the most extensively used material around the world. About 90% of all construction works carried out today are concrete based, where ordinary Portland cement (OPC) is the fundamental ingredient in the composite besides water and aggregates. However, industrialization, competition, and a high demand for OPC particularly in the developing countries have pushed the cement manufacturing techniques to become more harmful to the environment.

The cement industry contributes to around 5-7% of the global anthropogenic greenhouse gas emissions (Benhelal et al., 2013). Carbon dioxide (CO₂) is generated not only during the sintering of raw materials to form clinker but also from fuels used for grinding and power generation for the equipment functioning. Moreover, there has been a continuous growth in the demand for OPC. As such, the global yearly production of OPC was around 10 million tons in 1900 (Aïtcin, 1998). While in a survey undertaken by Hasanbeigi et al. (2012), it was found that OPC production will increase up to 4.38 Gt in 2050 (an upper estimate) as depicted in Figure 1-1.

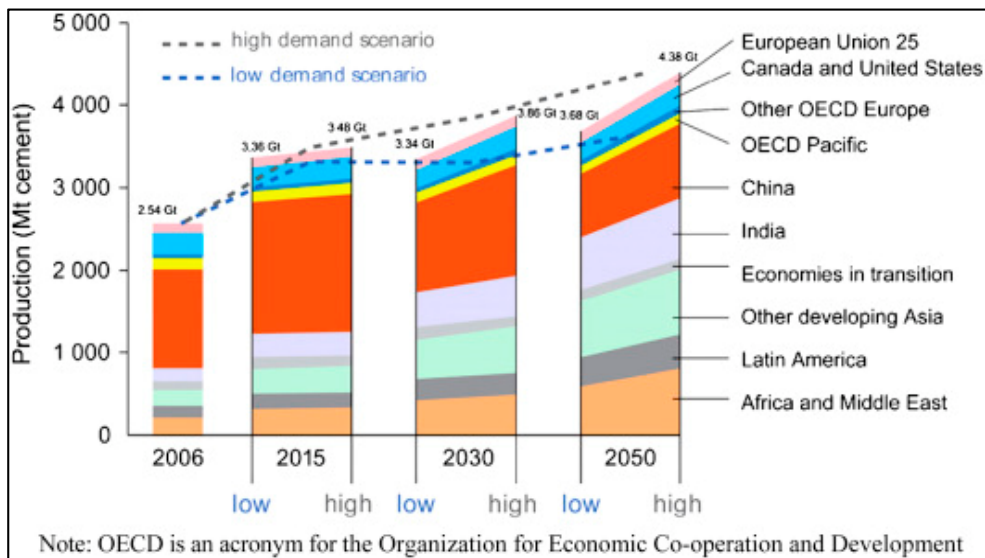


Figure 1-1 Predicted annual global cement production (Hasanbeigi et al., 2012).

A considerable increase in the production of OPC is likely to be associated with massive growth in the greenhouse gas emissions in the future. This is expected to further deteriorate the sustainability issues of the conventional cement-based construction materials. Many countries working under the umbrella of the intergovernmental panel on climate change (IPCC) have agreed to reduce the CO₂ emissions especially from the cement manufacture and

necessitated its lower consumption in concrete to move towards more sustainable development policies.

Alternatively, coal-burning power stations worldwide and exclusively in Australia have been producing large quantities of fly ash as a by-product to meet the increasing power demands. Indeed, coal burning process also releases an excessive amount of toxic gases into the atmosphere; however, the energy balance ratio, i.e., the percentage of energy produced to energy input for the coal-combustion process is very high. Furthermore, many countries including Australia have vast reserves of coal, and energy making based on the coal-burning process is a well-adopted technique. Therefore energy generation based on the coal-burning method is expected to continue in the foreseeable future, which produces a significant amount of fly ash. As such, the annual production of fly ash in China is estimated to be around 600 million tonnes (Ma et al., 2017), while in India 200 million tons of fly ash is generated every year (Chatterjee, 2014) with effective utilization of the waste product ranges between 67% and 50%, respectively. Similarly, in Australia, 12.30 million tonnes of low-calcium fly ash is produced annually by coal-fired power plants and approximately 400 million tons of the waste product is expectedly stored in the ponds and other landfill sites (Ash Dev. Association of Australia, 2018). Therefore, it is essential to use this industrial waste product more effectively which otherwise ends up in landfills or is sporadically flushed out into the open oceans, hence causing severe threats to the aquatic life.

The exploitation of by-products from other industries is a well-recognized approach to improve the early- and late-age mechanical properties of OPC concrete. This not only reduces the environmental impact associated with the excessive use of OPC but also allows for the conservation of virgin resources and recycling of the waste products. Many studies have focused on partial replacements of OPC in the concrete with supplementary cementitious materials (SCM), e.g., including ground granulated blast furnace slag (slag) and fly ash, etc. It has been found (Lothenbach et al., 2011) that the addition of pozzolans improves the early-age properties of concrete such as retardation in the setting time, reduced heat of hydration in the case of massive dam structures, increased late-age hardened material properties and improved resistance to the carbonation or sulfate attack. This has been further investigated by using high volumes of fly ash (HVFA) to improve the durability characteristics of OPC concrete. In the past, HVFA concretes replacing as much as 60% of OPC have been produced successfully (Shaikh & Supit, 2014). However, OPC can only be replaced up to a specified maximum amount with fly ash or slag in the concrete.

Separately, in 1972, a three-dimensional silicon-oxo-aluminates gel structure (mainly comprising of SiO_4 and AlO_4 anions linked alternatively with oxygen atoms and Na^+ , K^+ , and

Ca⁺⁺ cations to balance the negative charge) was discovered by Davidovits (1991) that could be formed by activating silico-aluminous materials. The material was defined as “Geopolymer” since it had a similar chemical structure as that of naturally occurring zeolites. Although the original formulation used metakaolin, another more critical development (Wastiels et al., 1994) was the recognition of using other industrial by-products such as fly ash for the synthesis of geopolymers. Unlike OPC, these inorganic materials are more environmentally friendly, and their manufacture emits about 80% less CO₂ than OPC (Duxson et al., 2007). With the assistance of mild heat curing, geopolymer products embodying 70% less energy have been synthesized exhibiting similar behaviour to that OPC (Tempest et al., 2009).

Generally, the main drivers for exploring geopolymer materials have not only been the environmental concerns but also the economic benefits. The cost of making one ton of OPC is non-comparable to that of fly ash since the production of fly ash does not require any additional processing as mandatory for OPC. An estimate shows that after allowing for the cost of activators, geopolymer construction materials could be approximately 10 to 30% more cost-effective than OPC concrete (McLellan et al., 2011). Besides, as per the “Green Star” certification concept introduced by Green Building Council of Australia (GBCA, 2018); 1 point is available towards the material rating for every 30% replacement of OPC in the construction material in comparison to the reference case. Since geopolymer materials do not contain any OPC, they will be expectedly ranked much higher on the greenness scale. Figure 1-2 illustrates some of the immediate and long-term benefits of using geopolymer technology.

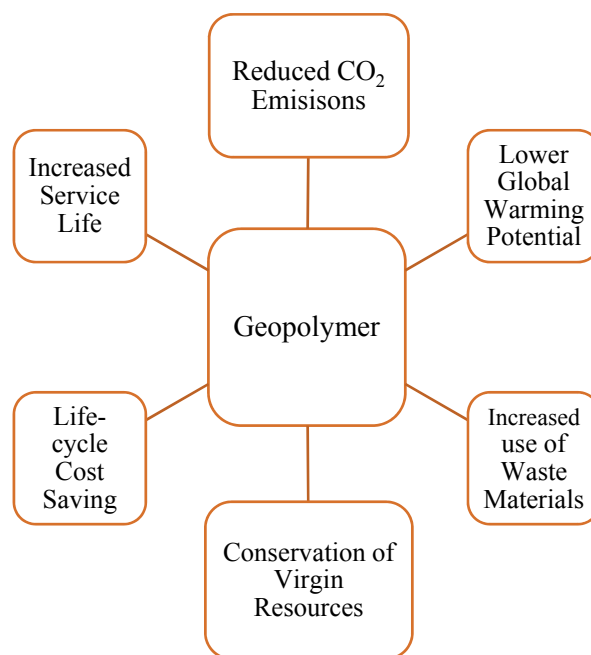


Figure 1-2 Advantages of using geopolymer binder in construction materials.

1.2 Problem Statement and Research Significance

For practical use of geopolymer materials in construction applications, many researchers, to list a few, including Hardjito et al. (2004), Bakharev (2005), Duxson et al. (2005), Wallah (2006), Ng et al. (2013), Sanjayan et al. (2015), etc. have investigated the material properties and performance of structural components made of geopolymer concrete. It has been observed that heat-cured geopolymer materials possess excellent durability properties (Fernandez-Jimenez et al., 2007). In some cases, with the correct mix design, the structural behaviour of reinforced geopolymer columns and beams outperformed the OPC based counterparts alongside the additional advantages of lower carbon footprint (Sumajouw et al., 2007). However, despite showing comparable performance to that of OPC, the use of geopolymer based construction materials in actual projects has been limited. There are many factors which are independently discussed below to establish the gaps in the literature and to highlight the significance of this research. At present, considerable information on various aspects is not available or has been inadequately investigated that these new materials can encounter during their service life as a part of the built infrastructure, especially in the multi-hazard environment.

1.2.1 Ambient Curing of Geopolymer Materials

A vast majority of previous studies on geopolymer materials correspond to a specific waste product with variable material composition and mixture parameters. The quasi-static uniaxial compressive strength properties of geopolymer concrete made from wastepaper sludge were investigated by Anuar et al. (2011). A combination of NaOH and Na₂SiO₃ solutions at different concentrations was used to activate the material in ambient conditions. The test results showed that the increased alkalinity of NaOH is beneficial for achieving better strength properties at the age of 3, 7, 14, 21, and 28 days. However, due to the presence of higher calcium content in the waste paper sludge in comparison to fly ash, the fabricated geopolymer mixtures set considerably faster. Instead, Pangdaeng et al., (2014) used high-calcium fly ash in combination with OPC (0%, 5%, 10%, and 15%) to investigate the material characteristics of geopolymer materials. It was observed that the use of OPC in high-calcium fly ash geopolymer mixtures improved the strength and microstructural characteristics of geopolymers due to the development of calcium silicate hydrate (C-S-H) binding gel. Besides, the use of elevated temperature resulted in high-early age strength.

Since in Australia and some other parts of the world, low-calcium fly ash is the commonly available source material and is much cheaper than metakaolin, most studies have investigated the microstructural, mechanical, and durability properties and in some cases performance of

the structural components made out of the heat-cured geopolymer mortars and concretes (Shaikh, 2013b). As of today, different investigators report the effects of various parameters including the concentrations of the alkaline solution (Görhan and Kürklü, 2014), activator combinations (Mustafa et al., 2012), the influence of curing temperatures, and heat curing durations (Atiş et al., 2015) on the compressive strength development of fly ash geopolymers. For example, a combination of NaOH and calcium hydroxide ($\text{Ca}(\text{OH})_2$) was used to activate the low-calcium fly ash based mortars from Southern Brazil (De Vargas et al., 2014). The activated materials were cured at 80°C for the first 24 hours followed by their storage at $24 \pm 1^\circ\text{C}$ and relative humidity of 50% until the test day. The mortar materials achieved compressive strengths in the range of 30 MPa at 7 days followed by a drop in these measurements to 22 MPa and 16 MPa at the age of 28 days and 91 days, respectively. In another research, the influence of different curing temperatures between 65°C and 85°C was evaluated on geopolymer mortars activated with different concentrations (3M, 6M, and 9M) of NaOH solution (Görhan and Kürklü, 2014). The results indicated that the increase of curing temperature facilitates the strength property in general, while 6M alkaline solution produced the optimum results. In a recent work, Atiş et al. (2015) studied the effects of curing temperatures range (45°C to 115°C increasing at the 10°C interval) and duration (24h, 48h, and 72h) on the compressive and flexural strength properties of fly ash geopolymer mortars. It was observed that geopolymer mortar materials with very high (120 MPa) compressive strength could be achieved by curing the geopolymer mixtures at a temperature of 115°C. However, the energy-intensive heat curing process is not suitable for the in-situ applications and also accounts for approximately 12.5% of the total CO_2 emissions for the synthesized geopolymer products (Turner and Collins, 2013).

Previous research shows that (Hardjito et al., 2004; Mustafa et al., 2012) low-calcium fly ash reacts very slowly at the ambient temperature and may result in geopolymer products with inferior mechanical properties and of poor quality. This has been a fundamental challenge for their broad use in the in-situ applications. Besides, the lack of specifications for the production of geopolymer materials and their non-recognition in the existing concrete standards is an additional impediment. Most of the current guidelines are primarily written with the viewpoint of using OPC, and they follow prescriptive compositional limits for the inclusion of by-products in concrete instead of performance-based criteria for the construction materials (Hooton, 2015).

Nonetheless, some recent studies (Nath and Sarker, 2014; Nematollahi et al., 2015) have found that the inclusion of calcium-bearing compounds in a small portion to low-calcium fly ash can allow curing the geopolymer mixtures in ambient conditions. In this regard, Nematollahi et al. (2015) combined low-calcium fly ash with $\text{Ca}(\text{OH})_2$ and slag in different mass ratios

(89%:11%, 75%:25%), and in ternary blends (75%:14%:11%) to prepare the ambient geopolymer formulations. A medium grade strength of around 37 MPa was achieved at the 28 days. In another study (Nath and Sarker, 2014) the inclusion of slag up to 30% by mass of fly ash has been reported with positive results as the strength of geopolymer mixtures increased with an increase of slag content and the curing age. Added to this, the fly ash containing higher amounts of glass contents and finer particles have also been observed to undergo a greater extent of geopolymerisation reaction which can further improve the compressive strength properties of geopolymers (Ivan Diaz-Loya et al., 2011).

From the above reviews, it is evident that the fabrication of geopolymers with consistent material properties by using different waste products is a challenging problem. However, a combination of source materials having different reactivity and degree of amorphicity could be a possible way forward to obtain the desired properties for geopolymer products. To-date, not enough research evidence is available concerning the formulation of high-strength geopolymer materials from low-calcium fly ash at the ambient temperature. Besides, the influence of other factors such as the choice of ambient curing environment on the strength development pattern of geopolymers is not well described in the open literature.

1.2.2 Fiber-Reinforcement of Geopolymer Materials

In addition to the above, one of the significant drawbacks of geopolymer materials is their low tensile strength in comparison to their ability to resist the compressive stresses, similar to OPC concrete. Moreover, it is well-established that High strength concrete (HSC) mixtures are much more brittle in comparison to normal strength concrete (NSC). However, no one material can satisfy the diverse end-user requirements which often leads to the combination of various constituents to form a composite, necessary for the industrial applications (Hull and Clyne, 1996). In the last 50 years, substantial progress has been made in regards to the availability of different types of fiber reinforcement techniques to improve the inferior tensile strength of cement-based construction materials. Early research efforts by Romualdi and Batson (1963) demonstrate that the tensile strength of cementitious materials can be significantly improved by incorporating closely spaced thin steel wires. The inclusion of fibers not only increases the tensile strength but also transforms the post-cracking behaviour of concrete-like materials. The technology has advanced to the stage that a wide range of fiber types in variable geometries are commercially available and being used in the construction industry.

Numerous high-performance fiber reinforced cementitious composites (HPFRCC) have been proposed which exhibit improved ductility in tension and flexure (Naaman and Reinhardt, 1995); yet, their ultimate tensile strength is low (Li, 2003). Others report the development of

ultra-high fiber reinforced cement composites with compressive strength as high as 180 MPa and tensile strength/strain capacity of 20 MPa and 1%, respectively (Kwon et al., 2014). Even though extraordinary mechanical properties have been achieved for these composites, they suffer from poor sustainability as no coarse or fine aggregates are included in the matrix design, and the composites contain a relatively high volume of cement. Recently, some researchers have tried to overcome the limitation by using fly ash instead of OPC (Shaikh, 2013a; Nematollahi et al., 2014). The measured mechanical properties of these newly engineered geopolymer composites such as compressive strength and flexural tensile strength were found comparable to those of cement-based counterparts. However, due to the inclusion of fly ash, heat curing method was used to complete the geopolymer reaction which impedes the possibility of using the proposed composites in in-situ applications.

In another research, steel fiber reinforced geopolymer composites with 28-days compressive strength of 120-175 MPa were developed under ambient curing environment (Ambily et al., 2014). The matrices in these composites primarily contained slag, silica fume, and a highly alkaline activator. In spite of achieving very high compressive strength, no significant improvement in flexure strength and ductility was observed by increasing the steel fiber volume fraction from 1% to 3%. Similarly, Gao et al. (2017) studied the possibility of using two types of straight hybrid-steel fiber reinforcement (Fiber 1; length = 13mm, diameter = 0.2mm and Fiber 2; length = 6 mm and diameter = 0.6 mm) in alkali-activated slag-fly ash composites. The combined use of long and short steel fibers presented a synergistic effect in inhibiting the cracks during compression and increased the compressive strength of high-performance composites by 16%. In flexure tests, the incorporation of long fibers for a fiber volume fraction higher than 0.25% significantly improved the flexural strength and changed the composite failure mode from brittle to plastic. But the use of short fibers did not influence the failure patterns and marginally increased the flexure strength. The current state of research on the development of high-performance fiber reinforced geopolymer composites is still in its infancy. For the use of geopolymer materials in the construction of structures that may require high-strength and improved energy absorption capabilities, significant further studies are required by exploring new types of fibers and their combinations in ambient cured geopolymer matrices.

1.2.3 Performance of Geopolymer Composite/Concrete Materials under Dynamic Loads and Multi-Hazard Environment

Another important aspect which has not received much attention is that previous studies on geopolymer mortar, composites/concrete materials have primarily investigated the quasi-static material properties from uniaxial compression, tensile, and flexural tests only. It is pertinent

to mention that all types of civil engineering structures can face dynamic loadings during their lifespan in addition to the static load actions, e.g., marine structures are under the constant effect of ocean waves, bridges and high rise buildings come across wind loadings, dams suffer from hydrodynamic pressure and all structures can encounter earthquakes, blasts, and impact. Due to their unpredictability and difference in the load magnitude, dynamic loads are essential in controlling the structural design process, and vulnerability assessment of any construction material becomes indispensable under these situations. Unfortunately, limited studies have considered investigating the dynamic properties of geopolymer binder based construction materials. In particular, no study has been reported on the dynamic material properties of high-strength fiber reinforced geopolymer composites that are appropriate for ambient curing.

Nevertheless, some examples include the work of Li and Xu (2009), who utilized Ø100-mm Split Hopkinson Pressure Bar (SHPB) to determine the dynamic compressive strength, energy absorption capacity, and deformation of basalt fibers reinforced geopolymer concrete (BFRGC) specimens. A combination of slag and fly ash (75% and 25%) concrete was reinforced by basalt fibers (length= 18mm, diameter = 15µm) and activated with NaOH and Na₂SiO₃ solutions. The test results showed that the inclusion of basalt fibers improved the ductility and energy absorption capacity of geopolymer concrete specimens. However, no apparent increase in the dynamic compressive strength of the material was observed at higher strain rates.

In another study, Luo et al. (2013) reported the dynamic compressive and dynamic splitting-tensile (Luo, 2013) properties of slag-fly ash based geopolymer concrete specimens which were activated with a multi-compound mixture of NaOH and sodium carbonate (Na₂CO₃) solutions. Although no information was provided for the geopolymer formulations, the fabricated material exhibited a strong strain rate dependency both in dynamic compression and splitting-tension tests within the rates of 30-100 sec⁻¹ and 1-10 sec⁻¹, respectively. Both the tensile and compressive DIFs (Dynamic Increase Factor, defined as a ratio between the quasi-static material strength and dynamic strength at higher strain rates) showed a linear increase with the logarithm of the average strain rate. Recently, Feng et al. (2014) and Feng et al. (2015) used different activator combinations to study the dynamic material characteristics of heat cured geopolymer concrete and mortar mixtures. It was observed that at lower strain rates, the concrete mixtures with low compressive strength exhibited a higher increase in the splitting tensile tests due to the viscous effect. While at higher strain rates, crack-inertia was mainly responsible for the improvement in DIF. The preliminary research on dynamic properties of geopolymer materials indicates that the dynamic compressive and tensile strength increase with higher strain rates vary for different geopolymer mixture designs.

Furthermore, there are many practical design situations where construction materials are continuously under multiaxial states of stress. Besides, materials undergo high levels of confinement in the events of impact and blast which necessitate not only investigating their triaxial compressive behaviour for reliable structural designs, but also the information is useful for the calibration of the existing concrete constitutive models. However, a general lack of knowledge exists about the behaviour of geopolymer materials under multiaxial stress conditions. Only two studies in the literature (Lyu et al., 2013; Haider et al., 2014) have investigated the triaxial compressive behaviour of geopolymer pastes under low to medium levels of confining pressures, ranging from 0 MPa to 35 MPa. In one of the investigations, the test samples were prepared using the heat curing method (Haider et al., 2014). While metakaolin (Lyu et al., 2013) was used in the other study whose cost is high in comparison to fly ash and prohibits its use on a large scale and is not sustainable. No research data are available on the mechanical characteristics of geopolymer mortar, concrete or fiber reinforced geopolymer composites that are commonly used in the construction applications under a high range of confining pressures. It is essential to quantitatively predict the material response under such highly dynamic loads and establish their failure strength under combined states of stress.

In summary, geopolymer materials offer many advantages over OPC mainly because of low CO₂ emissions, recycling of the industrial wastes, and reduced greenhouse gas emissions. Despite the increasing popularity, there are no standards or specified guidelines available for their production yet. For their broad use in the construction industry, it is essential to develop geopolymer materials which are suitable for the ambient curing environment. So far, limited research has been devoted to study the influence of higher strain rates and confining pressures on their material characteristics which is equally important for the safe and economical designs of geopolymer structures. Therefore, in this research, an emphasis is placed on the development of high-performance geopolymer composites using ordinary by-product source materials. In addition, thorough investigations are carried out on the quasi-static, dynamic material, and multiaxial stress-strain characteristics of these promising new materials. The findings gained from this research improve our understanding of various fundamental aspects of the material properties and pave the way to large-scale applications.

1.3 Research Objectives

The primary objective of this thesis is to develop high-strength and ductile geopolymer composites at the ambient temperature. Other objectives include the characterization of the mechanical properties of synthesized composites under wide-ranging quasi-static and multi-hazard loading conditions. The specific aims derived from the aforementioned objectives are:

1. To optimize and produce high-strength geopolymer matrix based on low-calcium fly ash and to establish the influence of various additive combinations on the compressive strength, microstructural characteristics, and porosity of geopolymers.
2. To study the effects of ambient curing conditions and fine aggregates content on the strength, morphology, and pore structure of the resulting blended high-strength geopolymer formulations.
3. To investigate the viability of developing high-performance fiber reinforced geopolymer composites using novel combinations of spiral-shaped steel fibers with hooked-end steel and high-strength polyethylene fibers.
4. To quantify the influence of strain rate on the material behaviour of unreinforced and fiber reinforced geopolymer composite (FRGC) materials under dynamic splitting tension and dynamic compression.
5. To determine the energy absorption capability of the unreinforced and FRGC materials under quasi-static and dynamic actions.
6. To propose empirical constitutive relationships for the dynamic increase factors under compression and tension for geopolymer materials and compare with the existing test data from other researchers and the latest CEB recommendations for OPC concrete.
7. To determine the influence of high levels of confinement on the triaxial stress-strain characteristics and to establish the strength parameters for geopolymer materials in general, and proposed FRGC materials.

1.4 Original Contribution of Thesis

Geopolymers are sustainable materials produced from the industrial by-products (fly ash, slag) and have a significant potential to be used in the construction industry. The following are the main contributions/originalities of this research:

1. Development of high-performance geopolymer composites using simple and cost-effective methods in the ambient environment.
2. Introducing a novel spiral-shaped steel fiber in combination with hooked-end steel and high-strength polyethylene fibers for geopolymer matrix reinforcement.
3. Study on the dynamic tensile and dynamic compressive material behaviour of unreinforced and high-performance geopolymer composites under widespread high strain rates.

4. Accentuating the non-suitability of existing CEB guidelines to predict the increase in tensile and compressive strength of geopolymer materials at higher loading rates, and their shortfall for the design of geopolymer structures.
5. Investigating in detail the triaxial compressive stress-strain behaviour of neat geopolymer and FRGC materials under high levels of confinement.
6. Proposed empirical formulae based on the dynamic material and triaxial compressive tests on neat geopolymer and FRGC materials for their further use in numerical analyses.

1.4.1 Thesis Outline and Structure

This thesis consists of eight chapters and is presented by combining author's journal publications as per the regulations of Curtin University. The main body comprises of six chapters, i.e., Chapter 2 to Chapter 7. A brief research outline is illustrated in Figure 1-3, and it can be seen that the overall research progress was well defined. After this introductory chapter that broadly provides an overview; each chapter starts with a detailed literature review related to the individual research component, followed by the description of materials/methodology section, presentation of the results and their exposition, and ends with the concluding remarks.

In particular, Chapter 2 and Chapter 3 cover the fabrication of high-strength geopolymer mortar matrix and detailed microstructural studies related to the influence of curing conditions and sand-binder ratios on compressive strength properties of geopolymers, respectively. Chapter 4 proposes using a new type of spiral-shaped steel fibers with hooked-end steel fiber and high-strength polyethylene fibers to develop high-performance fiber reinforced geopolymer composites (FRGC). The influence of fiber addition on different mechanical properties of the geopolymer composites is investigated alongside the individual fiber pull-out tests and fiber distribution analyses.

Chapter 5 studies the dynamic tensile material properties of high-strength geopolymer and FRGCs under a wide range of high strain-rates, while Chapter 6 quantifies the dynamic compressive material behaviour of high-strength geopolymer matrix and FRGC containing the most effective hybrid steel-polyethylene fiber reinforcement established from Chapters 4 and 5. Chapter 7 presents the influence of a wide-ranging low to high levels of confining pressures on the triaxial compressive stress-strain characteristics of high strength geopolymer and FRGC materials.

Chapter 8 summarizes the main contributions of this research along with recommendations for future studies.

Note: Chapter 2 – 7 are author’s journal publications which have been reproduced in this thesis. Due to the selected format, some details in the text may appear more than once across different chapters and readers may like to read them separately. Publication 4 is currently under review. The relevant copyright agreements between the author and the respective journals are attached in Appendix - I.

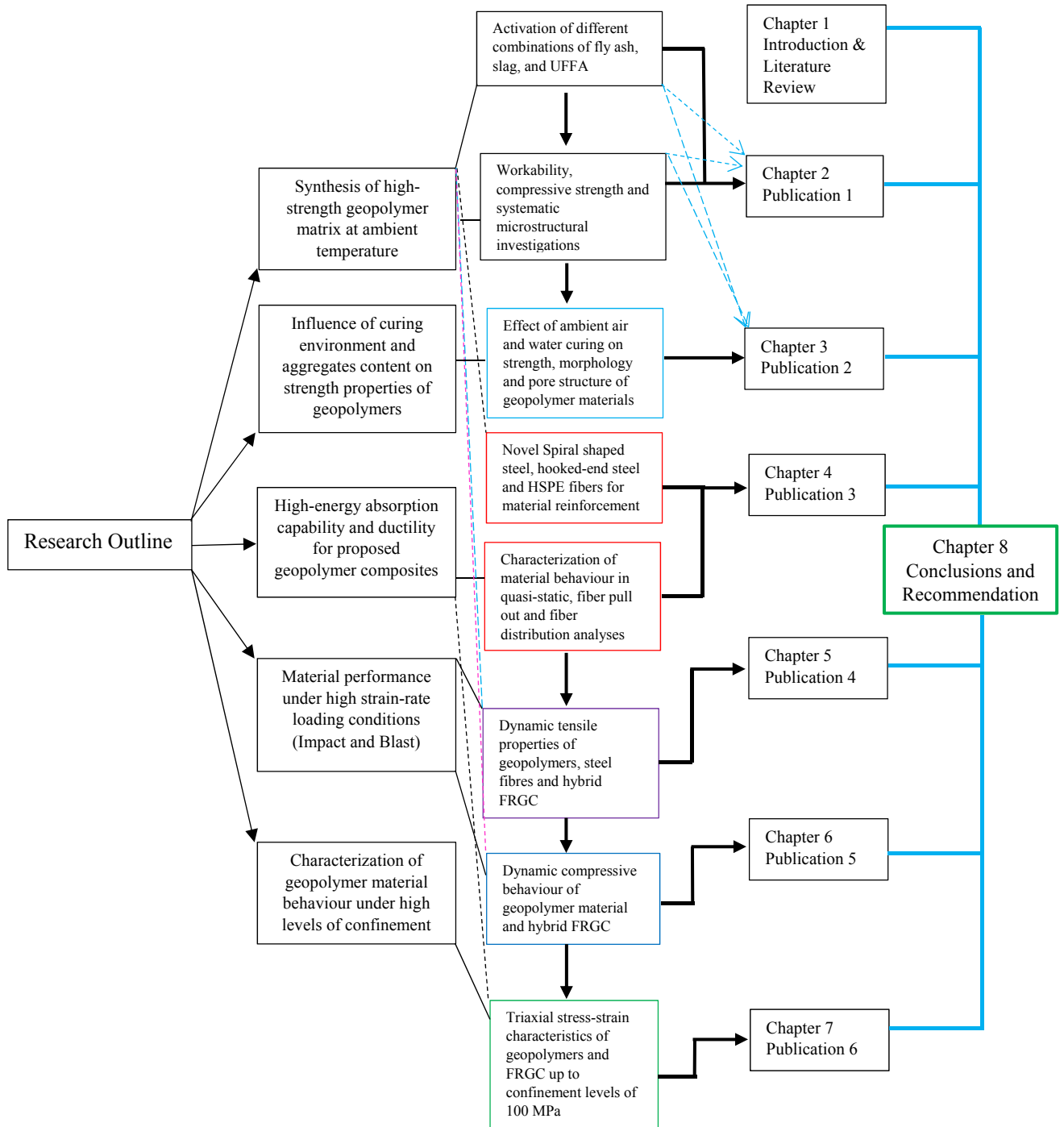


Figure 1-3 Research Outline and Thesis structure.

1.5 References

<http://www.adaa.asn.au/resource-utilisation/ccp-utilisation> <accessed on 04/09/2018>.

https://www.gbca.org.au/uploads/149/35477/MAT_Concrete%20Sourcing%20and%20Usedraft_D1_distributed.pdf <accessed on 04/09/2018>.

Aïtcin, P.C. (1998). High Performance concrete. E. & F.N. Spon, London, xxxii, 591pp.

Ambily, P. S., Ravisankar, K., Umarani, C., Dattatreya, J. K., & Iyer, N. R. (2014). Development of ultra-high-performance geopolymer concrete. *Magazine of Concrete Research*, 66, 82-89.

Anuar, K., Ridzuan, A., & Ismail, S. (2011). Strength characteristics of geopolymer concrete containing recycled concrete aggregate. *International Journal of Civil & Environmental Engineering*, 11(1), 59-62.

Atiř, C. D., Görür, E. B., Karahan, O., Bilim, C., İlkentapar, S., & Luga, E. (2015). Very high strength (120 MPa) class F fly ash geopolymer mortar activated at different NaOH amount, heat curing temperature and heat curing duration. *Construction and Building Materials*, 96, 673-678.

Bakharev, T. (2005). Geopolymeric materials prepared using Class F fly ash and elevated temperature curing. *Cement and Concrete Research*, 35(6), 1224-1232.

Benhelal, E., Zahedi, G., Shamsaei, E., & Bahadori, A. (2013). Global strategies and potentials to curb CO₂ emissions in cement industry. *Journal of Cleaner Production*, 51, 142-161.

Chatterjee, A. (2014). Technological initiatives and status of fly ash in India. In P. K. Sarker (Ed.), *Fly Ash: Sources, Applications and Potential Environmental Impacts* (1st ed., pp. 315-359). New York, USA: Nova Science Publishers

Davidovits, J. (1991). Geopolymers: inorganic polymeric new materials. *Journal of Thermal Analysis and Calorimetry*, 37(8), 1633-1656.

De Vargas, A. S., Dal Molin, D. C., Masuero, Â. B., Vilela, A. C., Castro-Gomes, J., & de Gutierrez, R. M. (2014). Strength development of alkali-activated fly ash produced with combined NaOH and Ca(OH)₂ activators. *Cement and Concrete Composites*, 53, 341-349.

Douglas Hooton, R. (2015). Current developments and future needs in standards for cementitious materials. *Cement and Concrete Research*, 78, 165-177.

Duxson, P., Fernández-Jiménez, A., Provis, J. L., Lukey, G. C., Palomo, A., & van Deventer, J. S. J. (2007). Geopolymer technology: the current state of the art. *Journal of Materials Science*, 42(9), 2917-2933.

Feng, K. N., Ruan, D., Pan, Z., Collins, F., Bai, Y., Wang, C. M., & Duan, W. H. (2014). Effect of strain rate on splitting tensile strength of geopolymer concrete. *Magazine of Concrete Research*, 66, 825-835.

Feng, K. N., Ruan, D., Pan, Z., Collins, F., Bai, Y., Wang, C. M., & Duan, W. H. (2015). Mechanical behavior of geopolymer concrete subjected to high strain rate compressive loadings. *Materials and Structures*, 48(3), 671-681.

Fernandez-Jimenez, A., Garcia-Lodeiro, I., & Palomo, A. (2007). Durability of alkali-activated fly ash cementitious materials. *Journal of Materials Science*, 42(9), 3055-3065.

- Gao, X., Yu, Q. L., Yu, R., & Brouwers, H. J. H. (2017). Evaluation of hybrid steel fiber reinforcement in high performance geopolymer composites. *Materials and Structures*, 50(2), 165.
- Görhan, G., & Kürklü, G. (2014). The influence of the NaOH solution on the properties of the fly ash-based geopolymer mortar cured at different temperatures. *Composites Part B: Engineering*, 58, 371-377.
- Haider, G. M., Sanjayan, J. G., & Ranjith, P. G. (2014). Complete triaxial stress–strain curves for geopolymer. *Construction and Building Materials*, 69(0), 196-202.
- Hardjito, D., Wallah, S. E., Sumajouw, D. M., & Rangan, B. V. (2004). On the development of fly ash-based geopolymer concrete. *ACI Materials Journal-American Concrete Institute*, 101(6), 467-472.
- Hasanbeigi, A., Price, L., & Lin, E. (2012). Emerging energy-efficiency and CO₂ emission-reduction technologies for cement and concrete production: A technical review. *Renewable and Sustainable Energy Reviews*, 16(8), 6220-6238.
- Hull, D., & Clyne, T. W. (1996). *An introduction to composite materials*: Cambridge university press.
- Ivan Diaz-Loya, E., Allouche, E. N., & Vaidya, S. (2011). Mechanical Properties of Fly-Ash-Based Geopolymer Concrete. *ACI Materials Journal*, 108(3).
- Kwon, S., Nishiwaki, T., Kikuta, T., & Mihashi, H. (2014). Development of Ultra-High-Performance Hybrid Fiber-Reinforced Cement-Based Composites. *ACI Materials Journal*, 111(3).
- Li, V. C. (2003). On engineered cementitious composites (ECC). *Journal of Advanced Concrete Technology*, 1(3), 215-230.
- Li, W., & Xu, J. (2009). Impact characterization of basalt fiber reinforced geopolymeric concrete using a 100-mm-diameter split Hopkinson pressure bar. *Materials Science and Engineering: A*, 513–514(0), 145-153.
- Lothenbach, B., Scrivener, K., & Hooton, R. D. (2011). Supplementary cementitious materials. *Cement and Concrete Research*, 41(12), 1244-1256.
- Luo, X., Xu, J.-y., Bai, E.-l., & Li, W. (2013). Research on the dynamic compressive test of highly fluidized geopolymer concrete. *Construction and Building Materials*, 48, 166-172.
- Lyu, S.-J., Hsiao, Y.-H., Wang, T.-T., Cheng, T.-W., & Ueng, T.-H. (2013). Microstructure of geopolymer accounting for associated mechanical characteristics under various stress states. *Cement and Concrete Research*, 54(0), 199-207.
- Ma, S., Xu, M., Qiqige, X.-H. W., & Zhou, X. (2017). Challenges and Developments in the Utilization of Fly Ash in China. *Int. J. Environ. Sci. Dev.*, 8(11), 781-785.
- McLellan, B. C., Williams, R. P., Lay, J., van Riessen, A., & Corder, G. D. (2011). Costs and carbon emissions for geopolymer pastes in comparison to ordinary portland cement. *Journal of Cleaner Production*, 19(9), 1080-1090.

- Mustafa Al Bakri, A., Kamarudin, H., Bnhussain, M., Rafiza, A., & Zarina, Y. (2012). Effect of Na₂SiO₃/NaOH Ratios and NaOH Molarities on Compressive Strength of Fly-Ash-Based Geopolymer. *ACI Materials Journal*, 109(5).
- Naaman, A., & Reinhardt, H. (1995). Characterization of high performance fiber reinforced cement composites-HPFRCC. *Paper presented at the High performance fiber reinforced cement composites*.
- Nath, P., & Sarker, P. K. (2014). Effect of GGBFS on setting, workability and early strength properties of fly ash geopolymer concrete cured in ambient condition. *Construction and Building Materials*, 66(0), 163-171.
- Nematollahi, B., Sanjayan, J., & Shaikh, F. U. A. (2014). Comparative deflection hardening behavior of short fiber reinforced geopolymer composites. *Construction and Building Materials*, 70, 54-64.
- Nematollahi, B., Sanjayan, J., & Shaikh, F. U. A. (2015). Synthesis of heat and ambient cured one-part geopolymer mixes with different grades of sodium silicate. *Ceramics International*, 41(4), 5696-5704.
- Ng, T. S., Amin, A., & Foster, S. J. (2013). The behaviour of steel-fibre-reinforced geopolymer concrete beams in shear. *Magazine of Concrete Research*, 65(5), 308-318.
- Oluokun, F. A., Burdette, E. G., & Deatherage, H. J. (1991). Splitting tensile strength and compressive strength relationship at early ages. *ACI Mater. J.*, 88, 115.
- Pangdaeng, S., Phoo-ngernkham, T., Sata, V., & Chindaprasirt, P. (2014). Influence of curing conditions on properties of high calcium fly ash geopolymer containing Portland cement as additive. *Materials & Design*, 53(0), 269-274.
- Romualdi, J.P., and Batson, G.B. (1963). Behaviour of reinforced concrete beams with closely spaced reinforcement. *Journal of the American Concrete Institute, Proceedings*, Vol. 60, No. 6, June, pp: 775-789.
- Sanjayan, J. G., Nazari, A., & Pouraliakbar, H. (2015). FEA modelling of fracture toughness of steel fibre-reinforced geopolymer composites. *Materials & Design*, 76, 215-222.
- Shaikh, F. U. A. (2013a). Deflection hardening behaviour of short fibre reinforced fly ash based geopolymer composites. *Materials & Design*, 50, 674-682.
- Shaikh, F. U. A. (2013b). Review of mechanical properties of short fibre reinforced geopolymer composites. *Construction and Building Materials*, 43(0), 37-49.
- Shaikh, F. U. A., & Supit, S. W. M. (2014). Mechanical and durability properties of high volume fly ash (HVFA) concrete containing calcium carbonate (CaCO₃) nanoparticles. *Construction and Building Materials*, 70(0), 309-321.
- Sumajouw, D. M. J., Hardjito, D., Wallah, S. E., & Rangan, B. V. (2007). Fly ash-based geopolymer concrete: study of slender reinforced columns. *Journal of Materials Science*, 42(9), 3124-3130.
- Tempest, B., Sanusi, O., Gergely, J., Ogunro, V., & Weggel, D. (2009). Compressive strength and embodied energy optimization of fly ash based geopolymer concrete. *Paper presented at the world of coal ash (WOCA) conference*.

Turner, L. K., & Collins, F. G. (2013). Carbon dioxide equivalent (CO₂-e) emissions: A comparison between geopolymer and OPC cement concrete. *Construction and Building Materials*, 43, 125-130.

Wallah, S. E. A. R. (2006). *Low-Calcium fly ash-based geopolymer concrete: Long-term properties*. Curtin University of Technology.

Wastiels, J., Wu, X., Faignet, S., & Patfoort, G. (1994). Mineral polymer based on fly ash. *Journal of Resource Management Technology*, 22(3), 135-141.

Xin Luo, J.-Y. X. (2013). Dynamic splitting-tensile testing of highly fluidised geopolymer concrete. *Magazine of Concrete Research*, 65(14), 7.

CHAPTER 2 SYNTHESIS OF HIGH STRENGTH AMBIENT CURED GEOPOLYMER COMPOSITE BY USING LOW- CALCIUM FLY ASH

2.1 Abstract

Geopolymer is an environment-friendly binder, which has gained significant interest amongst the research community in last few decades. Previous studies show that low calcium fly ash geopolymer exhibits similar or comparatively better mechanical properties upon heat curing. This paper evaluates the viability of developing high-strength geopolymer composite by using low calcium fly ash as a principal binder and its partial replacement with slag, hydrated lime, and ultra-fine fly ash in the mortar mixtures. The solid precursors were activated with a multi-compound mixture of 12M sodium hydroxide and D-grade sodium silicate at an alkaline liquid/binder ratio of 0.60 at ambient temperature. The effect of binder composition on the workability and compressive strength gain from 3 to 28 days is discussed. Mineralogical and microstructural properties were also observed to identify the different reaction phases, thermal decomposition, morphology, and cumulative porosity of the resulting geopolymer formulations. The results indicated that the compressive strength of geopolymer binder is primarily dependent upon the nature of source materials for a selected alkali-activating solution. Ambient cured geopolymer composites with very high compressive strength, i.e., more than 100 MPa were obtained with adequate workability by including an optimum amount of slag in low calcium fly ash geopolymer. The results also reflected a dense microstructure and reduced porosity for fly ash-slag geopolymer composites. However, the addition of UFFA and hydrated lime at higher proportions was diminutively effective in the selected alkaline activator to binder or water to solids ratios.

2.2 Introduction

Ordinary Portland cement (OPC) production contributes about 5-7% of global carbon dioxide (CO₂) emissions, which is a highly energy intensive process (Benhelal et al., 2013). The CO₂ is released during the calcination of limestone, fuel used for grinding, and transportation, etc. (Sakulich, 2011). Considering the monetary expenditures, environmental consequence associated with OPC and increased demand for cement production, efforts have been made to partially replace cement and introduce pozzolans (fly ash, GGBFS (slag)) in concrete production (Shaikh and Supit, 2014). Synchronously, studies have also been focused on complete replacement of OPC with a green cementitious binder such as “Geopolymer” to improve the sustainability performance of built infrastructure. Davidovits (1988) defined the

term “Geopolymer” for cement-less binders which are very similar to zeolites and synthesized as a result of several distinct reactions between an alkaline solution and aluminosilicate source material. These materials are either from a geological origin (kaolinite, clays, metakaolin, etc.) or an industrial by-product (such as low calcium fly ash, high calcium fly ash, silica fume, slag, rice-husk ash, etc.). However, the source material needs to be rich in silicon (Si) and aluminum (Al) (Davidovits, 1994; Shi et al., 2006).

Low calcium fly ash is considered an important source of geopolymer in Australia due to its widespread availability (Nath and Sarker, 2014; Gourley, 2003). It has been reported (Chindaprasirt et al., 2007; Fernández-Jiménez et al., 2005; Wallah and Rangan, 2006) that heat cured fly ash geopolymer achieves compressive strength of the same order as that of OPC binder in normal concrete with excellent durability (Fernandez-Jimenez et al., 2007). It can resist aggressive acid attacks, alkali-aggregate reaction (García-Lodeiro et al., 2007) and is more durable at elevated temperatures and under fire (Fernández-Jiménez et al., 2006). Geopolymer also provides a better bond with reinforcement and exhibit corrosion resistance (Bastidas et al., 2008). However, one major constraint associated with its use on a commercial scale is its low strength development at ambient temperature (Wallah and Rangan, 2006).

Different additives have been incorporated in fly ash geopolymer to accelerate its strength development at room temperature (Rashad, 2014). It is generally believed that the existence of calcium in raw ingredients has a positive effect on geopolymer material due to the formation of an additional calcium silicate hydrate (CSH) gel and its coexistence with the geopolymer products (N-A-S-H) (Alomayri et al., 2014; Pangdaeng et al., 2014). On the other hand, an excessive presence of calcium hydroxide (beyond 10%) was reported with reduced compressive strength after 14 days of curing (Pacheco-Torgal et al., 2008). In another study, (Temuujin et al., 2009) addition of calcium oxide (CaO) and calcium hydroxide (Ca(OH)₂), at a rate of 2 to 3% and 1.3 to 3.9% by weight of fly ash was stated beneficial in the ambient environment, however, similar inclusion showed detrimental properties in the samples cured at 70°C.

A number of researchers (Shi and Day, 1999; Puertas et al., 2000; Shen et al., 2011; Deb et al., 2014; Phoo-ngernkham et al., 2015) indicated that the addition of slag is more advantageous in fly ash geopolymer due to its easy activation in an alkaline medium. It is a glassy phase material and contains a high content of free CaO ions, both SiO₂ and Al₂O₃ in an amorphous state, whereas a much larger crystalline phase exists in fly ash which requires heat curing to accelerate the reaction (Puertas et al., 2000). Upon alkali activation, an exothermal reaction between the activator and the additional CaO present in slag releases heat, which promotes the geopolymerization process (Phoo-ngernkham et al., 2015). However, despite the

source material modification, geopolymer binder is very sensitive to the type/nature or composition of the alkali activators (Chi, 2015). Usually, sodium hydroxide (NaOH) based geopolymer is considered more sustainable as compared to water glass (Na_2SiO_3) (Turner and Collins, 2013). It was concluded that the solubility of fly ash depends on the molarity of NaOH solution, where an optimum concentration is required for the leaching of Al^{3+} and Si^{4+} ions and subsequent reaction at elevated temperature (Rattanasak and Chindaprasirt, 2009). However, a 10M NaOH based activator showed lower dissolution in an equal part fly ash-slag and slag alone precursor at ambient temperature, with the compressive strength as low as 18.3 MPa and 27.1 MPa at 28 days respectively (Phoo-ngernkham et al., 2015). On the contrary, a 50/50 blend of fly ash and slag paste was activated with a similar alkali solution, where it developed a compressive strength of 50 MPa at the same age (Puertas et al., 2000).

Van Jaarsveld et al. (2002) demonstrated that when different source materials are used to produce geopolymer, additional silica (Si) is required for the polymerization reaction. The alkali hydroxides are necessary for the dissolution process, while the alkali silicates act as a binder. The most commonly used alkali activators are a combination of NaOH and Na_2SiO_3 solutions, where a critical factor that influences the mechanical properties of geopolymer is the $\text{Na}_2\text{SiO}_3/\text{NaOH}$ ratio (Mustafa Al Bakri et al., 2012). Rattanasak and Chindaprasirt (2009) reported a heat cured, high calcium fly ash geopolymer exhibiting compressive strength as high as 70 MPa corresponding to a $\text{Na}_2\text{SiO}_3/\text{NaOH}$ of 1.0 with 10M NaOH solution, whereas Wallah and Rangan, (2006) established an optimum $\text{Na}_2\text{SiO}_3/\text{NaOH}$ ratio of 2.5 for low calcium fly ash geopolymer, realizing a compressive strength of 56.8 MPa. The ratio of 0.40 yielded the most inferior compressive strength, i.e., 17.3 MPa at 28 days, even with the catalytic heat action. In another study (Nematollahi et al., 2015) three different grades of Na_2SiO_3 powders and a combination of Na_2SiO_3 and NaOH powder were used to activate a combination of fly ash, slag or hydrated lime at ambient temperature, where a low to medium compressive strength geopolymer material (around 40 MPa) was realized at 28 days. Furthermore, other inherent factors such as fly ash fineness, the degree of vitrification, and particle size distribution were also found to influence the mechanical properties of geopolymers (Chindaprasirt et al., 2011).

As reviewed, partial replacement of fly ash with hydrated lime/blast furnace slag has been tested with some positive results and is very promising. However, the activator modulus ratio, liquid to binder ratio, Na_2O percentage dosage, nature of the source material and the activators types vary widely in the literature. The existing geopolymer formulations exhibit medium to low compressive strengths at ambient temperature with reduced workability (Puertas et al., 2000; Shen et al., 2011; Deb et al., 2014; Nath and Sarker, 2014; Nematollahi et al., 2015). Many current high-strength geopolymer compositions require heat curing for compressive

strength gain (Rattanasak and Chindaprasirt, 2009; Atiş et al., 2015) and are mostly accomplished with pastes (van Riessen and Chen-Tan, 2013; Phoo-ngernkham et al., 2015).

Therefore, further research is required on the compressive strength development of low calcium fly ash geopolymer, as heat curing not only impedes the possibility of large-scale cast in-situ application of this binder but also add to the cost and extra energy associated with it. This study is focused on producing a high strength geopolymer composite, which can be cured at ambient temperature by exploiting full binding properties of low calcium class (F) fly ash and blending it with different additives (i.e., slag, ultrafine fly ash (UFFA), and $\text{Ca}(\text{OH})_2$). The methods used to assess the performance of composites include the workability and compressive strength test and the microstructural characteristics via mercury intrusion porosimetry (MIP), thermogravimetric analysis (TGA), X-ray diffraction (XRD) analysis, and scanning electron microscopy (SEM).

2.3 Experimental Details and Testing Methods

2.3.1 Materials

The commercially available fly ash was obtained from Gladstone power plant in Queensland Australia. It was classified as class F according to ASTM C618 (ASTM, 2012a), ($\text{SiO}_2 + \text{Al}_2\text{O}_3 + \text{Fe}_2\text{O}_3 = 89.15\% > 70\%$ and $\text{CaO} < 10\%$). Slag was supplied by Builders choice, and ultrafine fly ash (UFFA) was provided by Flyash Australia. The basicity coefficient of the slag was 1 ($K_b = (\text{CaO} + \text{MgO}) / (\text{SiO}_2 + \text{Al}_2\text{O}_3)$), with a hydration modulus exceeding 1.4 ($\text{HM} = (\text{CaO} + \text{MgO} + \text{Al}_2\text{O}_3) / \text{SiO}_2$). The laboratory grade $\text{Ca}(\text{OH})_2$ was obtained from Rowe Scientific Pty Ltd, Australia. The median particle sizes of fly ash, slag and UFFA were 9.7, 11.5 and 3.4 μm respectively. 12M sodium hydroxide solution was prepared at least one day prior the casting schedule by mixing 97-98% pure NaOH pellets with tap water. Commercially available D-grade Na_2SiO_3 solution with a specific gravity of 1.53 and modulus ratio (M_s) ($\text{SiO}_2/\text{Na}_2\text{O}$) of 2.0 ($\text{SiO}_2 = 29.4\%$, $\text{Na}_2\text{O} = 14.7\%$, water = 55.9%) was obtained from PQ Australia Ltd. Locally available natural sand with a maximum nominal size of 1.18mm, fineness modulus of 2.77 and a specific gravity of 2.65 was prepared in saturated surface dry (SSD) condition as per ASTM C128 (ASTM, 2015). The chemical compositions of the raw ingredients are shown in Table 2-1.

Table 2-1 Chemical compositions of fly ash, UFFA, and slag as determined by XRF (%)

Oxide (wt. %)	Fly ash	UFFA	Slag
SiO ₂	51.11	73.40	32.45
Al ₂ O ₃	25.56	17.70	13.56
Fe ₂ O ₃	12.48	4.40	0.85
CaO	4.30	0.90	41.22
MgO	1.45	0.60	5.10
MnO	0.15	< 0.10	0.25
K ₂ O	0.70	1.03	0.35
Na ₂ O	0.77	0.11	0.27
P ₂ O ₅	0.885	0.20	0.03
TiO ₂	1.32	0.70	0.49
SO ₃	0.24	0.20	3.20
Others	0.46	0.06	1.12
LOI*	0.57	0.60	1.11

*Loss on Ignition

2.3.2 Mixture proportions, mixing, and curing of samples

A parametric study was carried out by successively exchanging different weight proportions of fly ash with Ca(OH)₂ (2%, 5%, 8%, and 10%), slag (20% to 50%) and UFFA (50%). The ternary blending of raw materials, i.e. (fly ash, UFFA, and Ca(OH)₂), (fly ash, slag, and Ca(OH)₂) and (fly ash, UFFA, and slag) was also considered to study the response of synthesized geopolymer mixtures. To focus on the binder composition and its effect on the compressive strength gain, a single alkaline activator having 12M NaOH and Na₂SiO₃ solutions with a Na₂SiO₃ / NaOH ratio of 2.5, was chosen based on a previous investigation on heat cured geopolymer (Wallah and Rangan, 2006). Initial trial experiments also suggested that constant high molarity of NaOH solution and higher modulus ratio is essential for appropriate strength gain. The activator to binder, sand to binder and water to solid ratios were kept constant at 0.60, 1.60, and 0.28, respectively for all mixes. As a key consideration, slightly higher water to binder ratio was selected to ensure the fluidity/self-consolidating workability of mixtures. No extra water was added to the mixtures. The percentage weight proportion and the critical oxide molar ratios of mixtures are given in Table 2-2.

Table 2-2 Weight proportions and oxide molar ratios of geopolymer composites

Mix ID	Specimen Designation	Geopolymer Binder Proportions (wt. %)				Oxide Molar Ratios			
		Fly Ash	UFFA	Slag	Ca(OH) ₂	Na ₂ O /SiO ₂	Na ₂ O /Al ₂ O ₃	Si/Al	H ₂ O/Na ₂ O
G1	FA100	100	-	-	-	0.18	0.78	2.12	10.32
G2	FA50UFFA50	50	50	-	-	0.15	0.90	2.94	10.60
G3	FA98Ca2	98	-	-	2	0.18	0.79	2.12	10.33
G4	FA95Ca5	95	-	-	5	0.19	0.82	2.14	10.35
G5	FA92Ca8	92	-	-	8	0.19	0.85	2.15	10.37
G6	FA90Ca10	90	-	-	10	0.20	0.86	2.16	10.38
G7	FA60UFFA35Ca5	60	35	-	5	0.17	0.91	2.72	10.55
G8	FA60UFFA38Ca2	60	38	-	2	0.16	0.88	2.74	10.55
G9	FA80S20	80	-	20	-	0.19	0.86	2.20	10.40
G10	FA70S30	70	-	30	-	0.20	0.90	2.25	10.45
G11	FA60S40	60	-	40	-	0.21	0.95	2.30	10.49
G12	FA50S50	50	-	50	-	0.21	1.00	2.36	10.53
G13	FA60UFFA10S30	60	10	30	-	0.19	0.93	2.42	10.50
G14	FA60UFFA20S20	60	20	20	-	0.18	0.91	2.53	10.52
G15	FA60UFFA25S15	60	25	15	-	0.17	0.90	2.59	10.52
G16	FA60UFFA30S10	60	30	10	-	0.17	0.89	2.64	10.53
G17	FA60S35Ca5	60	-	35	5	0.21	0.98	2.31	10.50

The mixing was performed in a 10-liters Hobart mixer. In the initial 30 mins, the required quantities of sodium silicate and sodium hydroxide solutions were combined. The solid ingredients including fly ash, slag, hydrated lime or UFFA were dry mixed with fine aggregates for 3 mins at a slow speed (140 ± 5 r/m). Following which, the activating solution was included slowly over a 45 sec period. Later, the mixer was stopped, and all the constituents were hand mixed to ensure the homogeneity of mixtures and no dry residuals were left in the mixer. This was followed by another 3 mins of mixing at a medium speed (285 ± 10 r/m). Subsequently, acrylic plastic molds ($50 \times 50 \times 50$ mm³ cubes) were used to cast the specimens in two layers with adequate vibration to remove the entrapped air bubbles. The specimens were stored at room temperature for 24 hours in a controlled environment. After which, they were demolded, wrapped (to prevent any moisture loss) and moved into an ambient curing room until the test day. G1 and G2 specimens were very weak and did not allow demolding after 24 hours, the specimens were discarded and an elevated curing regime (85°C for the first 24 hours) was selected to compare the compressive strength development of fly ash and UFFA based composites.

2.4 Methods

2.4.1 Workability and Compressive Strength Test

The effect of additives on the workability of mixtures was measured in terms of flow diameter as per ASTM C1437 (ASTM, 2013b). The flow tests were conducted immediately, after mixing each batch and all the mixtures were tested twice. The compressive strength tests were conducted at the ages of 3, 7, 14, and 28 days according to ASTM C109 (ASTM, 2013a) at a loading rate of 20MPa/min. The reported compressive strengths are an average of three samples.

2.4.2 Differential Thermal Analysis (DTA) / Thermogravimetric Analysis (TGA) & Pore Size Measurement

Simultaneous TGA and DTA measurements were made by heating a 50 mg of finely ground powder for selected samples between ambient temperature and 1000°C, at a rate of 5°C/min under airflow, whereas mercury intrusion porosimetry (MIP) was used to measure the cumulative porosity of geopolymer samples. The pore diameter and intruded mercury volume was recorded at each pressure point for a pressure ranged between 0.0083 and 207 MPa. The pressures values were converted into an equivalent pore width using the Washburn expression (Shaikh and Supit, 2014), as expressed in Equation (2.1):

$$d_0 = -2\gamma\cos\theta / p \quad (2.1)$$

where d_0 is the pore width (μm), γ is the surface tension (mN/m), θ is the contact angle between mercury and the pore wall ($^\circ$), and p is the net pressure across the mercury meniscus at the time of the cumulative intrusion measurement (MPa).

2.4.3 X-ray diffraction (XRD) analysis

Randomly oriented powder samples (about 1 g in weight) were prepared for XRD analysis by grinding dried portions of the tested samples. The XRD patterns were obtained by a Bruker – AXS D8 Advance Diffractometer with the Cu-K α source at room temperature. The diffractograms were scanned for 2θ values between 10° and 80° at a step size of 0.02° . The peaks positions were established with the DIFFRAC.EVA program.

2.4.4 Scanning electron microscopy (SEM) and Energy dispersive X-ray (EDX) analysis

The specimens with dimensions of 10 mm × 10 mm × 5 mm were prepared from a representative cube sample (50 × 50 × 50 mm³) at the age of 28 days. The sectioned portions were first air dried, followed by platinum coating for microstructural imaging. SEM analyses were performed using a Zeiss EVO 40XVP microscope equipped with an energy dispersive X-ray analyzer.

2.5 Results and Discussions

2.5.1 Workability

The effect of additives on the workability of geopolymer mixtures is shown in Figure 2-1. Generally, the flow values decreased for all batches with the inclusion of slag, UFFA and Ca(OH)₂ in the control G1 mixture. It can be seen that all composites had a minimum flow diameter of 120 mm. However, the flow loss increased dramatically with an increase in the hydrated lime content in G3 to G6, G7, and G8 geopolymer mixes. The flow values reduced from 160 to 130 mm. Similarly, the workability of mixes containing UFFA (G2) or slag (G9 – G12) was also reduced proportionately to the replacement level of these additives in the G1 matrix. The lowest workability was measured for G17 composition, containing both the hydrated lime and slag. While fluctuations in the flow diameters were measured for composites prepared from the ternary blending of fly ash, slag, and UFFA (G13 – G16).

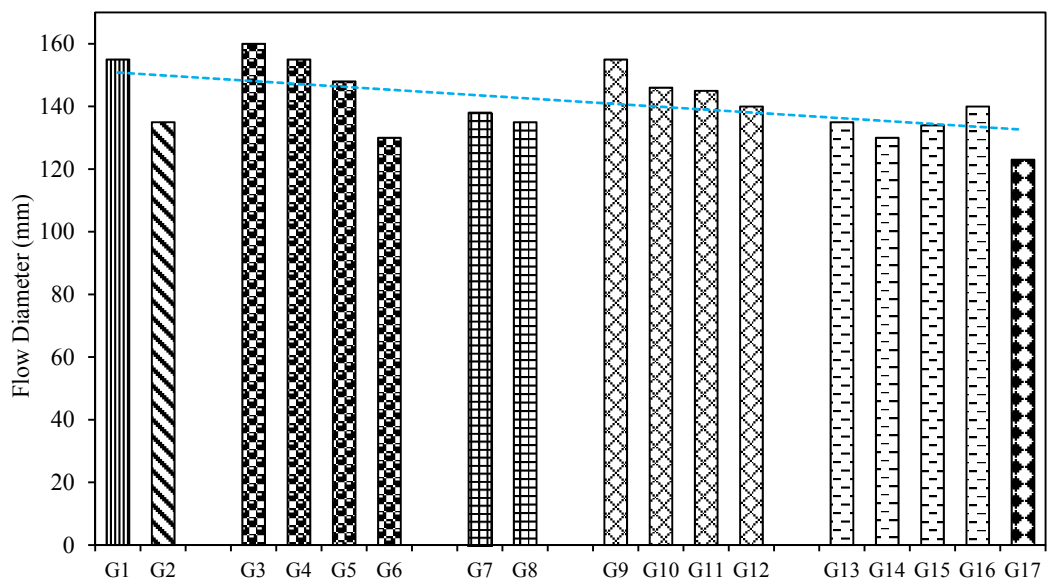
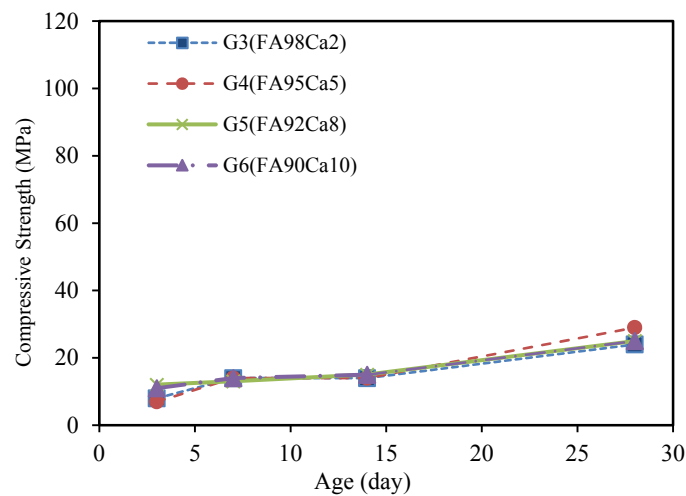


Figure 2-1 Effect of additives on the workability of geopolymer composites.

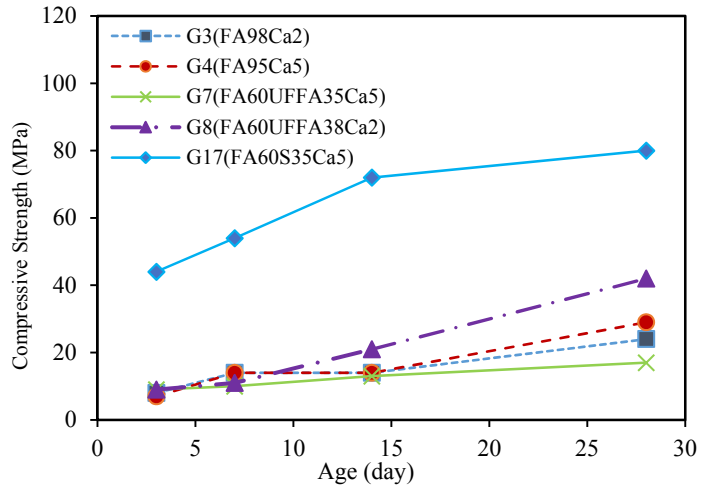
The lower workability of mixes containing $\text{Ca}(\text{OH})_2$ or slag is attributed to the increase in calcium content and its rapid reaction with the alkaline activator. A significant acceleration in the setting and hardening process was observed with hydrated lime, where additional calcium served as nuclei for the precipitation of dissolved species from fly ash and affected the coagulation rate (Lee and van Deventer, 2002). It should be noted that addition of higher quantity of hydrated lime can generate casting difficulties. In contrast, geopolymer matrices containing slag up to 40% were workable for more than 90 minutes and is comparable to the initial set time of Portland cement. The reduced workability of mixes containing UFFA is related to the increased reactivity of the binder, the smaller particle size and higher surface area. A similar observation was reported in the past, where an increased reactive proportion of the source material produced unworkable mixes (van Riessen and Chen-Tan, 2013).

2.5.2 Compressive Strength

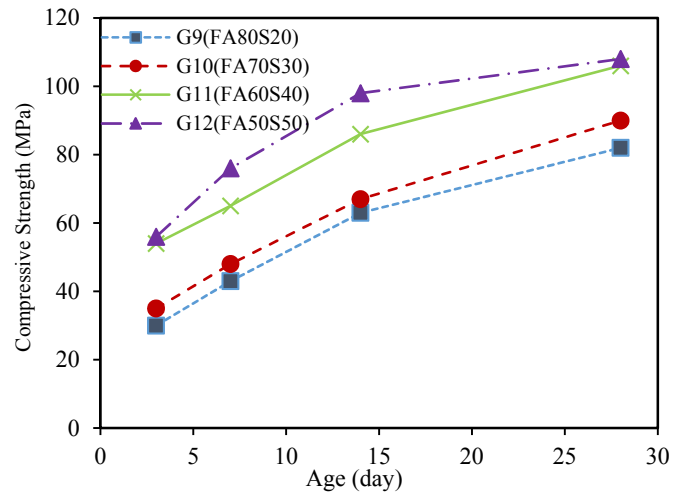
The compressive strength results of geopolymer composites are shown in Figure 2-2. Since all binder compositions were activated with an identical alkaline activator at ambient temperature, it is clear that any change in the strength development is directly related to the nature of binder material and presence of amorphous oxides of silicon, aluminum, and calcium elements in the initial solid precursor. It can be seen that the compressive strength increased with age for all geopolymer mixes except for the G1 and G2 matrices. Heat cured mixtures (G1, G2) exhibited compressive strengths of 103 MPa and 104 MPa at 3 days respectively, with a little increase of 4% in the G2 samples containing UFFA at 28 days, i.e., from 104 MPa to 108 MPa. The slight increase in compressive strength is associated to the improved reactivity of the binder material and higher Si/Al ratio (see Table 2-2), which assisted the Al^{3+} and Si^{4+} ions dissolution and the subsequent polymerization reaction to continue outside the heat curing period, thus exhibiting slightly better mechanical properties.



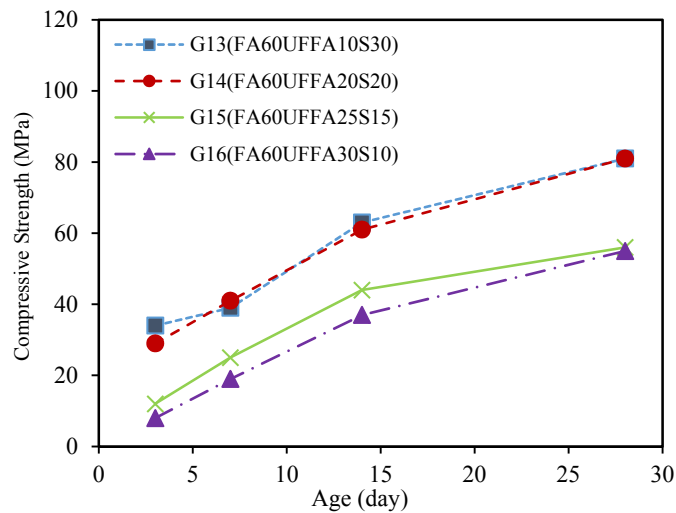
(a)



(b)



(c)



(d)

Figure 2-2 Effect of additives on the compressive strength development of fly ash geopolymer (a) $\text{Ca}(\text{OH})_2$ (b) UFFA and $\text{Ca}(\text{OH})_2$ (c) slag (d) UFFA and slag.

Figure 2-2(a) depicts the influence of hydrated lime content on the compressive strength of low calcium fly ash geopolymer. It can be seen that the strength development of G3, G4, G5 and G6 mixes was very similar up to 28 days despite an increase in the replacement level of $\text{Ca}(\text{OH})_2$ from 2% to 10%. The maximum compressive strength achieved was about 30 MPa at 28 days. This low strength development is partly connected to the higher porosities of these mixtures, presented in section 2.5.3, where higher pore volumes were found in the G4 mix as compared to the slag based composites. Otherwise, the strength development of geopolymer binder is mainly dependent upon the degree of polymerization which in turn relies on the extent of dissolved silicate and aluminate monomers from the source material in an alkaline medium and their further nucleation, i.e., formation of zeolite precursors (geopolymer gel). In this case, the low strength development was not only linked to the lower dissolution of fly ash at ambient temperature but also to the presence of $\text{Ca}(\text{OH})_2$, which reduced the alkalinity of the reaction medium and interfered with the coagulation process, either by reacting with the dissolved species or providing extra nucleation sites for the dissolved monomers (Yip et al., 2008). Visual inspection of the specimens also showed efflorescence due to an excess presence of the alkaline solution. Similar findings were reported by Temmujin et al. (2009) in the previous investigation.

For the mixes containing UFFA or slag as partial replacement of low calcium fly ash in G3 and G4 series, the mortar samples with slag gave the highest compressive strength. Figure 2-2(b) presents a comparison of these binder compositions. It can be seen that the inclusion of UFFA at a rate of 38% in G8 mix improved the compressive strength of G3 samples, while an opposite trend was observed for G4 specimens, where the compressive strength was reduced at 28 days. There was an increase of 75% and a decline of 70% in the compressive strength of G3 and G4 samples with the inclusion of 38% and 35% UFFA, respectively. The lowest compressive strength was observed for the G7 mix (around 20 MPa) containing 5% free lime, 35% UFFA and 60% low calcium fly ash. A possible reason for the observed mechanical behavior is related to the surplus presence of UFFA combined with the restraining effect of calcium-bearing additive, which has led to the instability of these binder compositions. Moreover, this can also be associated to the local alteration of Si/Al ratio, due to the presence of UFFA in the solid precursor and providing regions of less-than-optimal microstructure which act as flaws in the matrix, thus producing minimal geopolymer products and resultantly reduced compressive strength. However, the addition of slag in fly ash-hydrated lime binder composition (G4) showed a significant increase in the early age strength of G17 mixture, with a 3-day value as high as 44 MPa and 80 MPa at 28 days. These values are much higher as compared to the UFFA and hydrated lime based composites.

The effect of slag addition on the compressive strength of low calcium fly ash geopolymer is presented in Figure 2-2(c). The compressive strengths increased with increasing slag content for all the series. It can be seen that fly ash-slag blend was the most effective binder composition and exhibited very high compressive strengths at ambient temperature as compared to the other source material combinations, shown in Figure 2-2(a), 2(b) or 2(d). For example, the G12 mix (FA50S50) showed the highest compressive strength of 108 MPa, followed by G11 mix (FA60S40) exhibiting 106 MPa at 28 days. It is evident that the incorporation of slag as an additional source of calcium, silica, and alumina has strongly affected the formation of binding gels.

For these mixtures, the high compressive strengths were achieved due to a modified binder acquiring the reaction products both from the alkali activation of fly ash (N-A-S-H) and slag (C-(A)-S-H), thus improving the mechanical properties of geopolymers. Ismail et al. (2014) reported that the alkali activation of fly-slag blends indicate a co-formation of C-(A)-S-H and N-A-S-H gels and the rate of formation of these gel phases depend on the fly ash/slag content in the solid precursor. The reaction involves the disassociation of Ca in the alkaline medium and participation of Si and Al ions in the polymerization reaction together with the leachates of fly ash to form a secondary gel, i.e., calcium alumina-silicate hydrate (C-A-S-H) in conjunction with N-A-S-H. Besides this, the compressive strength of geopolymer is considerably dependent upon the Si/Al mole ratio of binder (Phoo-ngernkham et al., 2015). Previous researchers (Chi and Huang, 2013; Nath and Sarker, 2014) reported an increased compressive strength, similar to this study (see Table 2-2) with an increasing Si/Al mole ratio for fly-ash slag based geopolymer mixtures.

Figure 2-2(d) shows the effect of UFFA inclusion on the mechanical properties of fly ash-slag geopolymer. It can be seen that mixtures G13 to G16, displayed slightly better compressive strength development (i.e., medium to high) at 28 days. The highest compressive strength (80 MPa) was exhibited by G13 mix containing 60% fly ash, 10% UFFA, and 30% slag. Identical compressive strength results were observed for the G14 series having 60% fly ash and both slag/UFFA at 20% each. However, any further increase in the UFFA content (i.e., 25% and 30%) or Si/Al ratio in the solid precursor resulted in reduced mechanical behavior and higher porosity both for G15 and G16 mixtures. Usually, in ceramics, mechanical strength decreases with higher porosity (Subaer, 2004). Duxson et al. (2005) also reported reduced dissolution of the solid precursor beyond a maximum threshold of Si/Al ratio in metakaolin geopolymer and observed higher porosities.

Furthermore, it is admitted that the fly ash is composed of glassy beads and its outer layer is very dense and stable, therefore if an activity has to take place, the firm silica-alumina glassy

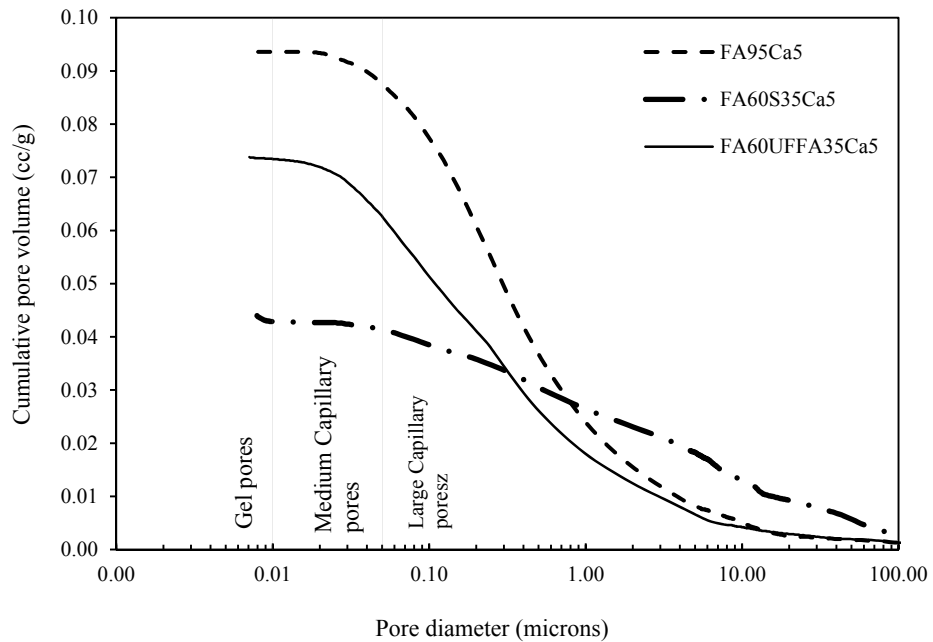
chain on the surface must be disintegrated (Fan et al., 1999). Upon alkali activation, the NaOH solution attacks the surface of fly ash and forms small spherical units of N-A-S-H gel, which gradually merge to form a larger mass. In addition, the median particle size of UFFA is much smaller as compared to the unprocessed, low calcium fly ash. Due to the limited availability of some fly ash particles for the alkali attack during the first stage of the reaction, the gel produced in the initial phases either restricts them from participating in the reaction or react very slowly (Fernández-Jiménez et al., 2005). This can translate into the lower dissolution of fly ash particles further at higher Si/Al ratios and act as defect sites, which eventually lead to higher porosity and simultaneously reduced mechanical strength. The SEM micrographs and EDX spectra presented in the later section (section 2.5.6) for G4 (FA95Ca5) and G7 (FA90UFFA35Ca5) mixtures, also show a wide distribution of unreacted fly ash or UFFA particles embedded within the geopolymer gel matrix and indicate very little activation of the source material.

2.5.3 Pore Size Measurement

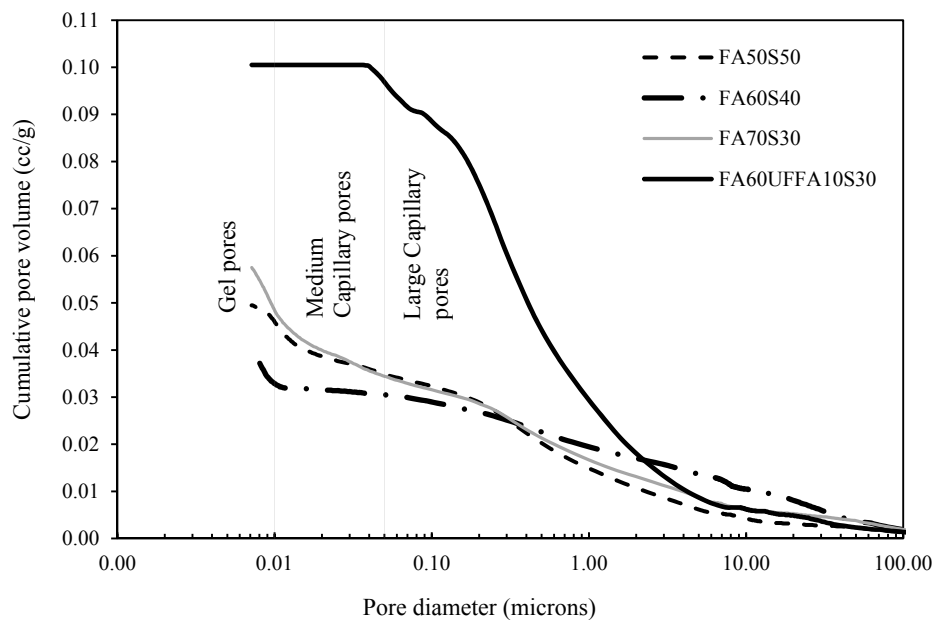
To investigate into the reasoning for compressive strength variation in different geopolymer mixtures, mercury intrusion porosimetry (MIP) was used to evaluate the total porosity and pore size distribution of selected geopolymer samples which exhibited the lowest or highest compressive strength at 28 days. The MIP results show the distribution of cumulative pore volume within pore size of 0.01 to 100 μm , where the pores can be classified as large capillary pores (10 to 0.05 μm), medium capillary pores (0.05 to 0.01 μm) or gel pores ($< 0.01 \mu\text{m}$) (Zhang and Islam, 2012; Shaikh and Supit, 2015). The curves presented in Figure 2-3, evidence the existence of the three modes and it can be seen that the binder compositions containing hydrated lime or ultrafine fly ash were more porous as compared to the corresponding slag based combinations in fly ash geopolymer. The total porosity of G4, G7, and G13 mixtures was about 0.094 cc/g, 0.074 cc/g, and 0.10 cc/g, respectively as compared to the G11 mix (FA60S40) showing the lowest value of 0.041 cc/g. It can also be seen that the total porosity of G4 mix was reduced by 21% by including UFFA in G7 composite. However, there was a slight difference between the cumulative porosity of slag based formulations, i.e., the highest measurement of 0.057 cc/g was made for G10 mix (FA70S30).

Furthermore, it can also be observed that the large capillary and medium capillary pores have reduced significantly by including slag in fly ash geopolymer (see Figure 2-3(b)). This identifies a more compact microstructure with minimal presence of large size pores between 0.1 and 100 μm and confirms that the addition of slag was more beneficial in terms of reducing the average pore size diameter. On the other hand, the existence of higher capillary and medium capillary pores in G4, G7, and G13 mixtures indicate the lower dissolution of fly ash

particles and presence of partially dissolved hollow spheres, which usually form open pores and are easily identifiable through MIP. It should be noted that slag is more reactive in an alkaline medium whereas fly ash needs to react to a much large extent before it can significantly influence the total pore volume.



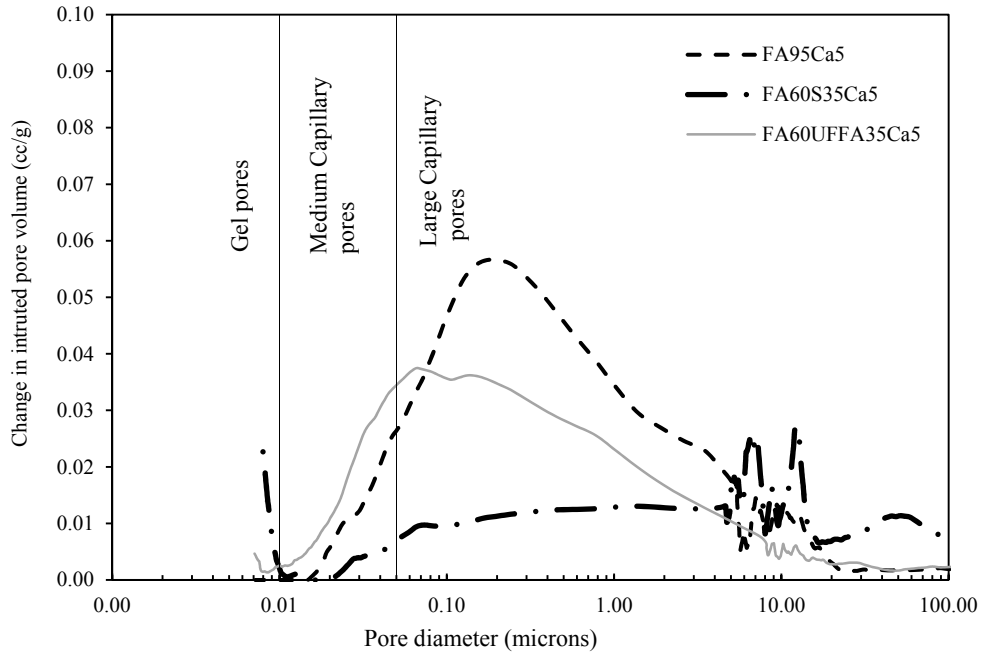
(a)



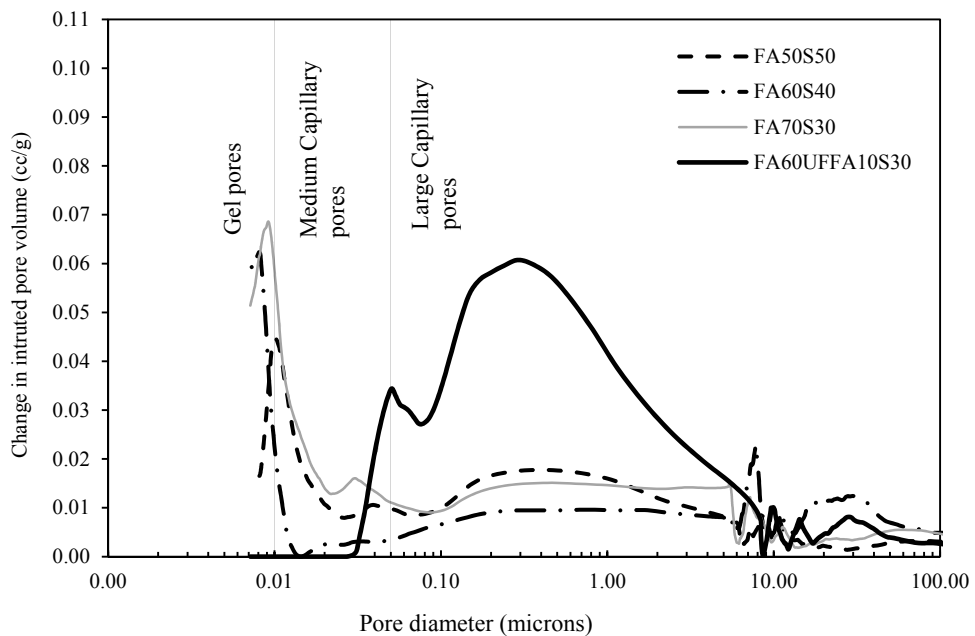
(b)

Figure 2-3 Effect of additives on cumulative intrusion curves of geopolymer composites (a) Ca(OH)_2 , UFFA, and slag (b) UFFA and slag.

Figure 2-4 shows the pore size distribution of geopolymer composites, obtained by differentiating the cumulative intrusion curves presented in Figure 2-3. The area under the curve represents the pore concentration, and the peak point of the log differential curve corresponds to the critical pore diameter.



(a)



(b)

Figure 2-4 Effect of additives on pore size distribution of geopolymer composites (a) $\text{Ca}(\text{OH})_2$, UFFA, and slag (b) UFFA and slag.

As can be seen in Figure 2-4, the curve peaks have shifted towards the smaller sizes, i.e., gel pores with the inclusion of slag as compared to the fly ash-hydrated lime or UFFA-hydrated lime based binder combinations. In addition, the porosity of the mortar mixtures containing slag is concentrated around 0.01 μm , except for the G13 mix, which is around 0.5 μm as shown in Figure 2-4(b). It can further be seen that the pore concentration of G4 (FA95Ca5) and G13 (FA60UFFA10S30) mixtures at higher pore diameters could explain the exhibited reduced mechanical behavior by these compositions. Whereas, the pore concentration of fly ash-slag blends at a smaller diameter and improved porosity specifies a refined pore structure, which has contributed to the strength enhancement. The selected binder compositions were also examined using the XRD and TGA analysis techniques

2.5.4 X-ray Diffraction (XRD) Analysis

The XRDs of raw geopolymer constituents are presented in Figure 2-5, where a broad hump between 18-28° for fly ash and UFFA and around 25-35° for slag show that the sourced materials were mainly amorphous. Some crystalline phases of Quartz (SiO_2), Mullite ($\text{Al}_6\text{Si}_2\text{O}_{13}$) and Maghemite (Fe_2O_3) in fly ash, Gypsum ($\text{CaSO}_4 \cdot 2\text{H}_2\text{O}$) in slag and both Quartz (SiO_2) and Aluminum silicon oxide (Al_2SiO_5) in UFFA were also present. Powder samples of the selected binder compositions were analyzed using XRD to evaluate the changes in crystalline peaks as well as the amorphous humps formation in those composites.

Figure 2-6 presents a comparison for the XRD patterns of G10 (FA70S30), G11 (FA60S40) and G12 (FA50S50) mixes, where the effect of increasing slag content in the geopolymerization of fly ash binder can be seen. By comparing the XRD patterns of powder fly ash and slag in Figure 2-5 with those of fly ash-slag geopolymers in Figure 2-6, it can be observed that some of the dominant peaks in slag and fly ash have disappeared, meaning they have dissolved in the polymerization reaction and formed amorphous geopolymer gels.

For example, in all three XRD patterns of fly ash-slag geopolymer, no trace of the crystalline peak at 2 theta angle 11.6° of slag is present. Furthermore, the intensity of the crystalline peak at 2 theta angle of 16.4° is found to be much less in the case of geopolymer. The same is true for other crystalline peaks at 2 theta angles of 29.2°, 30.1°, 33.2°, 40.8°, etc. in the case of fly ash and slag, whose intensities are much lower than their original intensities in respective raw materials. These are the clear indication of geopolymerization and also by relating the intensity peaks at 2 theta angles of 29.2°, 30.1°, 33.2° and 40.8° among the three different geopolymers it can be seen that the intensity peaks at those 2 theta angles for mixes G11 and G12 are slightly lower than those for G10 mix. In addition, the XRD pattern of the G11 mix also shows an additional crystalline peak of CSH at the indicated location. This could explain the slightly

higher 28 days compressive strengths of G11 and G12 mixes than the G10 mix observed in this study. The amorphous hump between 2 theta angle 25° and 31° in mixes G11 and G12 is also slightly higher than that of G10 fly ash-slag combination, which also supports the formation of more geopolymer gels in the former mixes than the later and is in line with the previous research (Phoo-ngernkham et al., 2015).

The XRD patterns of G11, G13, and G17 mixes are also shown in Figure 2-7. By comparing the three XRD patterns no significant differences in terms of crystalline peaks of Mullite [Al₆Si₂O₁₃], Sodalite [Na₈(Al₆Si₆O₂)Cl₂] or Chabazite [Ca₂(Al₂Si₄O₁₂)₂.12H₂O] can be observed. This is in agreement with the 28 days compressive strength of respective mixes, where their strength values are in the range of 80-100MPa. On the other hand in Figure 2-8, significant changes in the intensity peaks of high strength geopolymer mixture (G17) can be easily noticed corresponding to the G4 and G7 binder compositions. By comparing the XRD patterns of G4 (28 days compressive strength about 30 MPa) and G7 mixes (28 days compressive strength about 20 MPa) with those of G17 mix (28 days compressive strength about 80 MPa). It can be seen that the intensity peaks associated with Mullite are significantly smaller than those in the former mixes, and also an amorphous hump between 2 theta angle 25° and 31° is indicative of geopolymer gel formation in the later mix. Similar geopolymer amorphous hump between 2 theta angle of 25° and 32° in the case of fly ash-slag geopolymer is also reported by Lee et al. (2016).

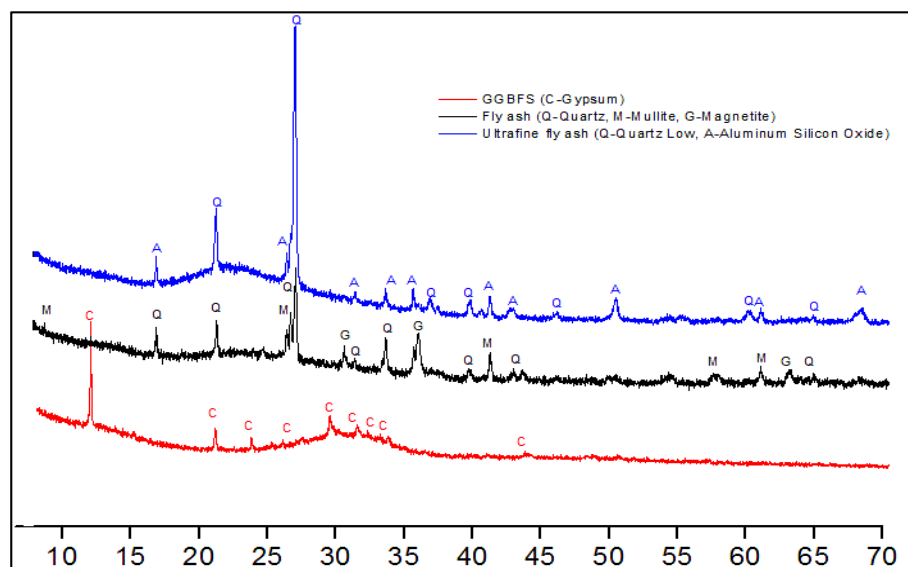


Figure 2-5 XRD 2θ (°) Cu, Kα patterns of low calcium fly ash, slag, and UFFA.

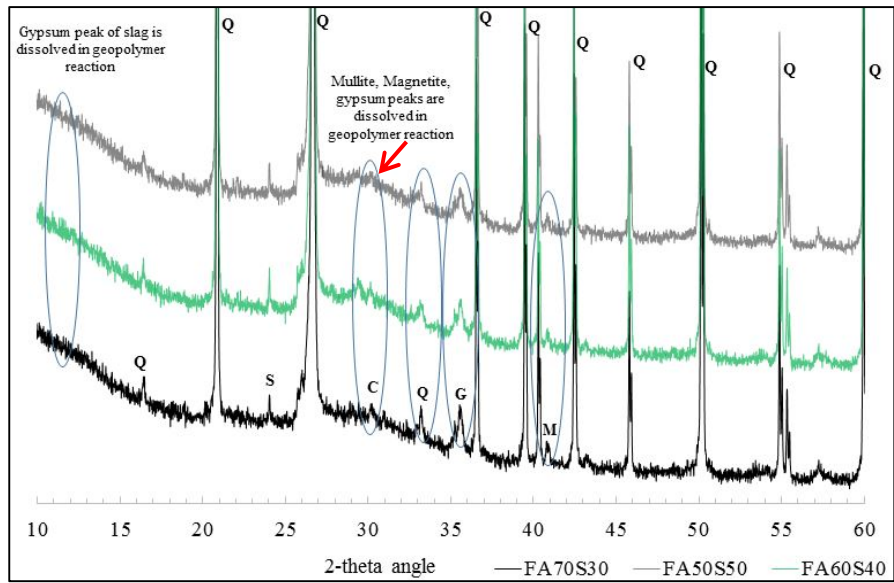


Figure 2-6 XRDs of G10, G11, and G12 mixes.

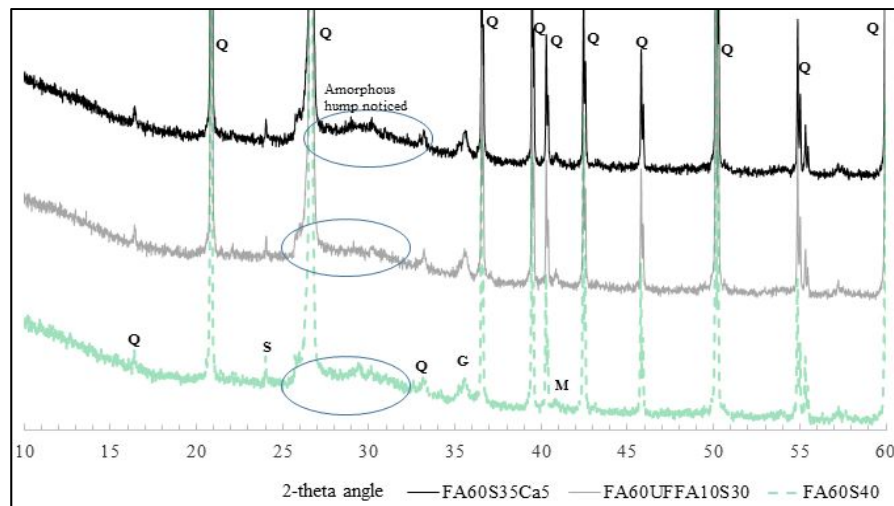


Figure 2-7 XRDs of G11, G13, and G17 mixes.

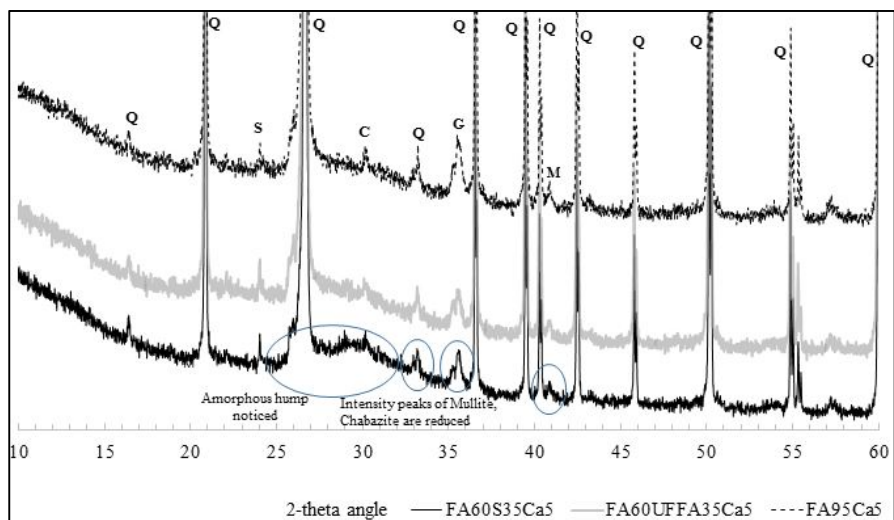
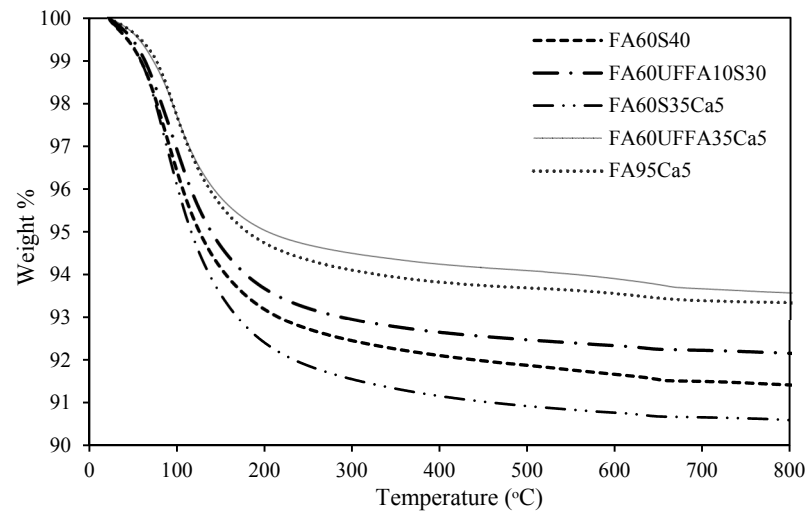


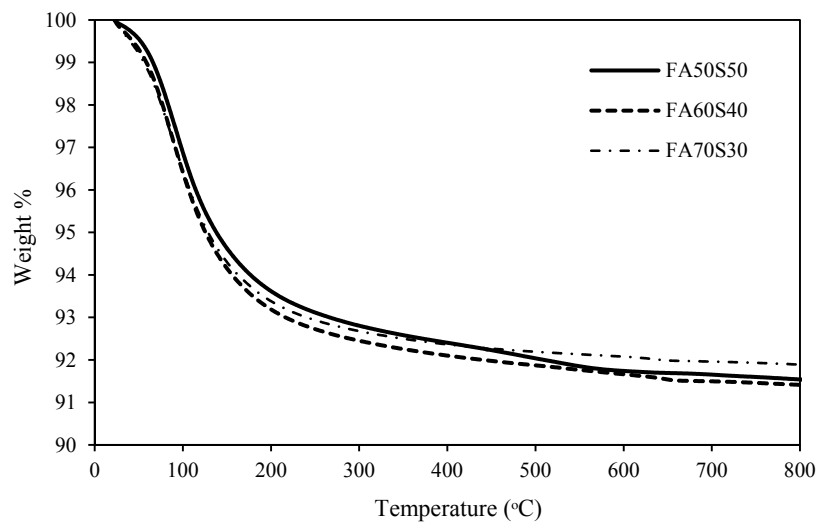
Figure 2-8 XRDs of G4, G7, and G17 mixes.

2.5.5 Differential Thermal Analysis (DTA) and Thermogravimetric Analysis (TGA)

Figure 2-9 shows the thermogravimetric analysis results of selected samples, with a total mass loss of 6.5 to 9% approximately. It can be seen that all binder compositions showed an initial rapid decline in the weight percentage around 110°C, this is mainly due to the evaporation of free water present in the matrix (Kong and Sanjayan, 2010). It can also be observed (see Figure 2-9(a)) that the evaporable water content bound within the reaction products is primarily dependent upon the nature of source material, where the highest weight loss was measured for slag based mixtures.



(a)

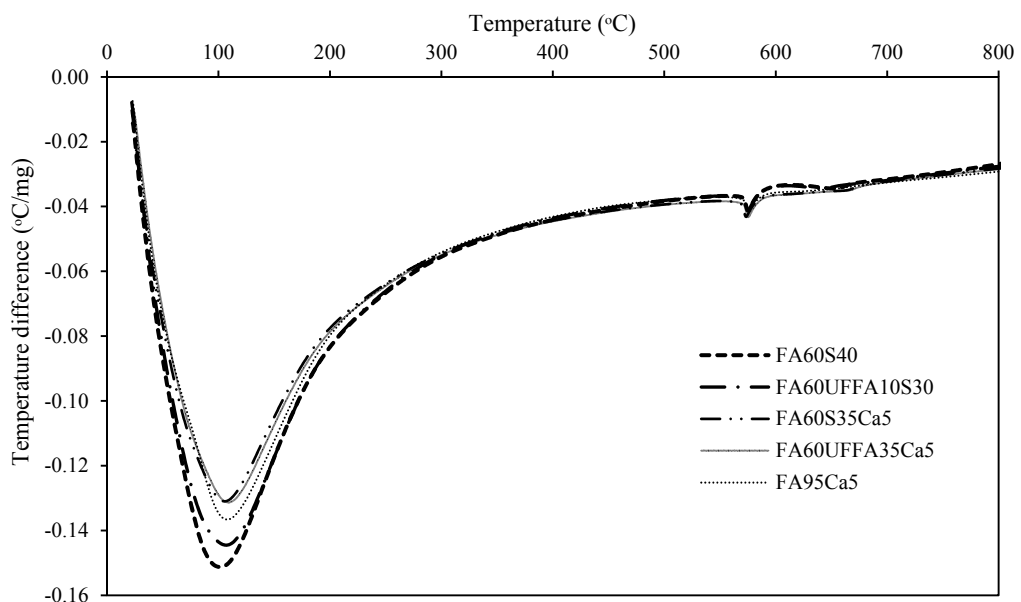


(b)

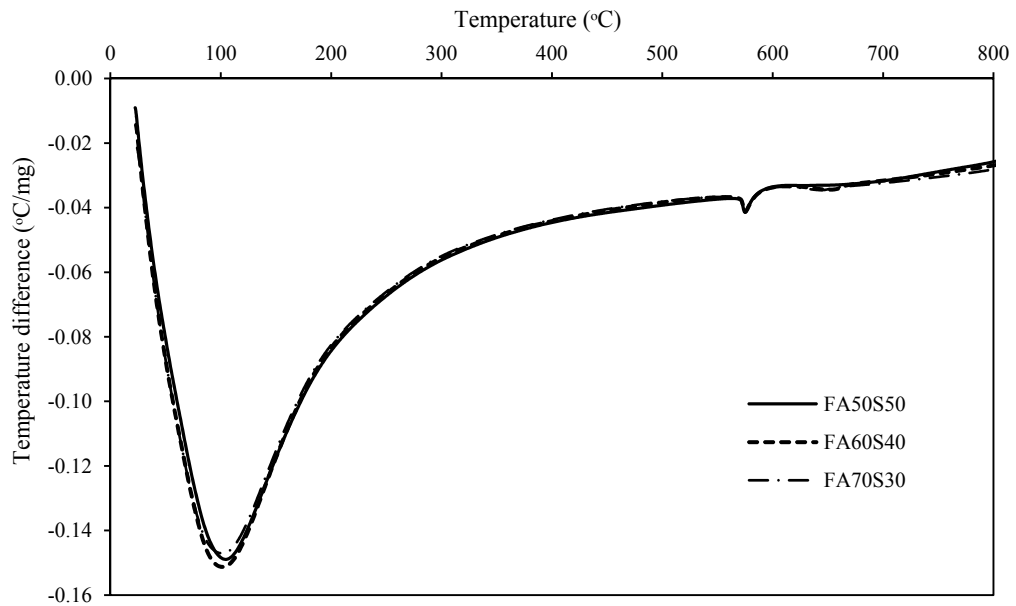
Figure 2-9 TGA profiles of geopolymer composites (a) For hybrid fly ash, slag, UFFA & Ca(OH)₂ (b) fly ash & slag blend.

Furthermore, it can also be seen that after a quick mass loss in the initial stages, all samples displayed a gradual weight loss from 200°C to 800°C, following which all the profiles became linear. This steady weight loss after 200°C is attributed to the slow decomposition of binding gels which are mainly amorphous, as no abrupt mass loss peaks have been detected in the TGA profiles. Previous research by Gao et al. (2015) also concluded that for a constant activator modulus, the percentage weight loss in fly ash-slag geopolymer is primarily influenced by the fly ash/slag content in the solid precursor, where higher mass losses were reported with increasing slag content in the fly ash geopolymer.

Differential thermograms (DTG) of the composites are shown in Figure 2-10, where two very distinct heat absorption peaks and a weak mass loss effect just after 600°C is visible for the slag based formulations. The maximum weight loss peaks are found between 100°C and 300°C. As can be seen in the graphs, the first peak is located around 110°C, which is related to the removal of physically bound water present within the pores of binding gels, which are either zeolite (N-A-S-H) type gels or C-(A)-S-H gels (Bernal et al., 2011). However, as seen in Figure 2-9, the intensity of these peaks vary depending upon the nature of source materials. The lowest peak is observed for the G11 mix, containing 60% fly ash and 40% slag, which intrinsically depends upon the extent of water loss from the dehydration of binding gels (Alarcon-Ruiz et al., 2005). This is followed by the gradual decomposition of the hydrated gels starting from 200°C, and the evaporation of chemically bound water in the gel structure.



(a)



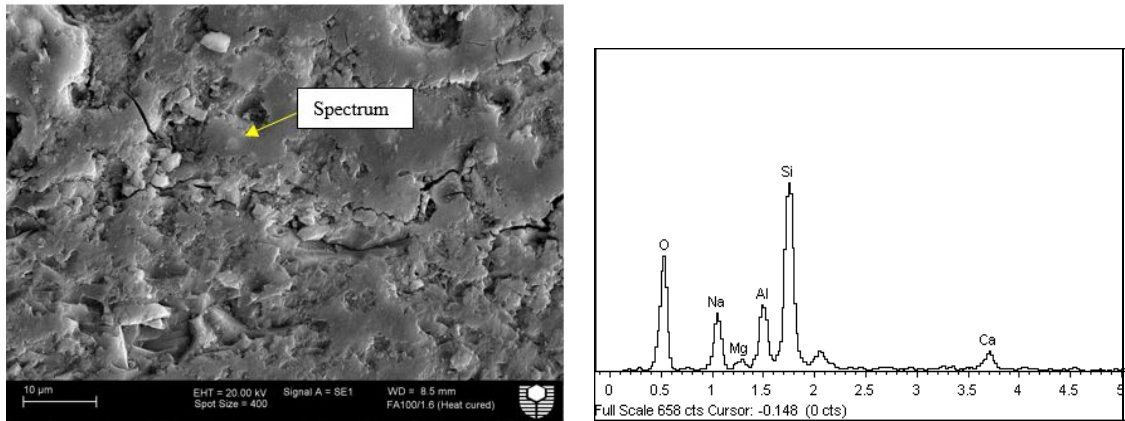
(b)

Figure 2-10 DTG curves of geopolymer composites (a) For hybrid fly ash, slag, UFFA & $\text{Ca}(\text{OH})_2$ (b) fly ash & slag blend.

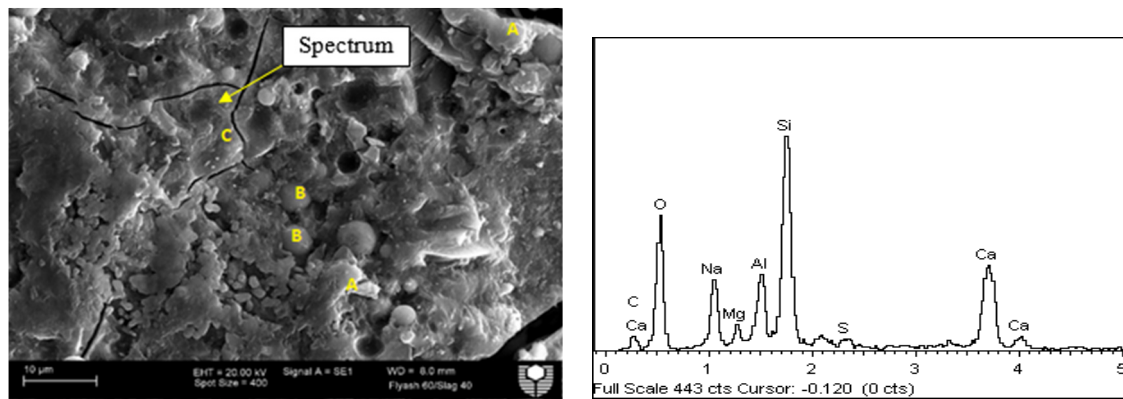
A second peak is observed just below 600°C , which can be attributed to the decomposition of carbonate minerals such as calcite, as it usually disintegrates between 505°C and 600°C (Frost et al., 2008). Beyond 600°C the presence of weak mass loss peaks in slag based binders, at higher decomposition temperatures is the indication of the presence of other structural forms of carbonates, such as poorly crystalline or amorphous in G9 to G12 mixtures and is consistent with the previous research (Ismail et al., 2012).

2.5.6 Scanning electron Microscopy (SEM) and Energy dispersive X-ray Spectroscopy (EDS) Analysis

The SEM images and EDX spectrums of geopolymer mixes G1 (FA100), G11 (FA60S40), G7 (FA60UFFA35Ca5) and G4 (FA95Ca5) are shown in Figures 2-11 and 2-12. It is obvious that the incorporation of different additives in geopolymer composites has significantly influenced the formation of binding gels and ultimately the hardened microstructure. For example, Figure 2-11(a) and 2-11(b) present a microstructural comparison of heat cured fly ash G1 (FA100) and ambient cured fly ash-slag, G11 (FA60S40) matrices. As can be seen in Figure 2-11(a) that the majority of fly ash particles have dissolved in the alkaline activator with little or zero traces of unreacted or partially reacted fly ash particles. However, a small number of unreacted or partially reacted fly ash particles (see Figure 2-11(b)) can be found in the ambient cured fly ash-slag hybrid binder composition.



(a)



(b)

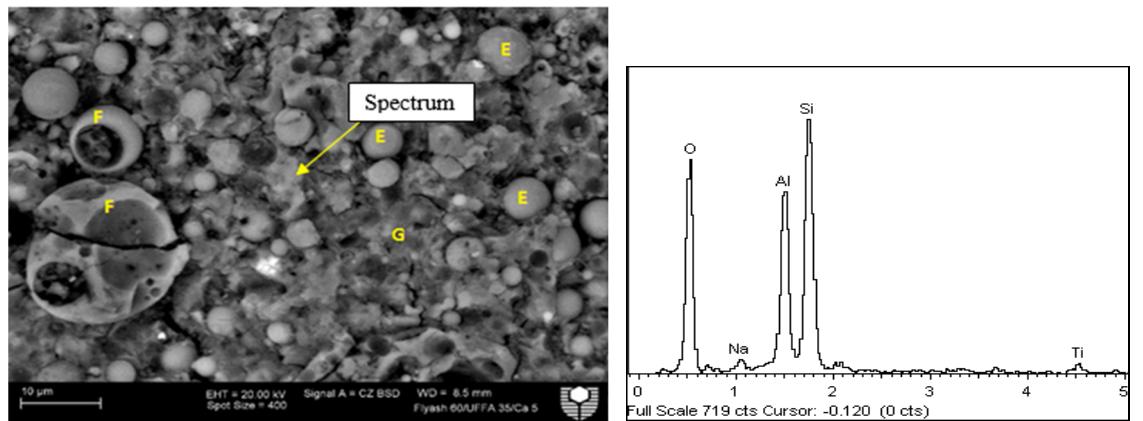
Figure 2-11 SEM/EDX spectra of geopolymer composites (a) G1 (FA100) (b) G11 (FA60S40).

Furthermore, it can also be seen in the EDX spectra that the geopolymer gel produced, from the dissolution of silicate and aluminate ions in low calcium fly ash has an insignificant presence of the calcium elements in reaction products and is mainly sodium aluminosilicate hydrate gel (N-A-S-H). The EDX diagram in Figure 2-11(b) shows a relatively higher count both for the sodium and calcium elements together with the silicon, aluminum, and oxygen elements in the reaction products. This can only be attributed to the inclusion of slag and disassociation of Ca, Si, and Al ions in the alkaline medium and their further participation in the polymerization reaction together with the leachates of fly ash (silica and alumina ions) to form a secondary gel, i.e., calcium aluminosilicate hydrate (C-A-S-H) in conjunction with N-A-S-H (zeolite) gel, which has resulted in a more compact and dense microstructure.

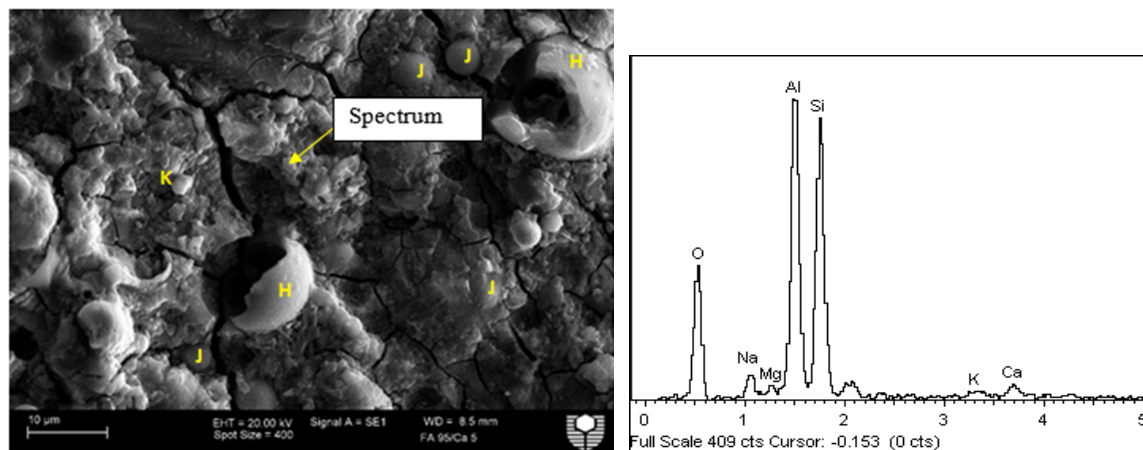
As mentioned earlier, a few unreacted or partially reacted fly ash particles designated with symbol “B” at some places can also be seen in the SEM micrograph of the G11 mix. However, they are firmly held within the gel and are well connected with the reaction products.

Furthermore, a “dreierketten” type structure marked with symbol “A” is also visible which has been previously associated to a poorly crystalline calcium silicate hydrate gel, arising from the alkali activation of fly ash-slag blends (Chi and Huang, 2013).

On the other hand, significant differences in the microstructure were observed for geopolymer composites containing either free lime (G4) or both hydrated lime and UFFA (G7) as an additive in low calcium fly ash binder. As shown in Figure 2-12, the SEM micrographs for both compositions, present a rather loose microstructure and a large amount of unreacted or partially activated fly ash particles. It can be seen that (see Figure 2-12(a)), the presence of ultrafine fly ash has significantly increased the elemental counts of silicon, aluminum, and oxygen in the EDX spectra. However, very few traces of sodium elements can also be noticed in the reaction products, which implies the very little dissolution of the fly ash/UFFA particles in the alkaline medium and their contribution towards the formation of binding gel (N-A-S-H) at ambient temperature.



(a)



(b)

Figure 2-12 SEM/EDX spectra of geopolymer composites (a) G7 (FA60UFFA35Ca5) (b) G4 (FA95Ca5).

Furthermore, it is also evident that the presence of calcium hydroxide in the starting ingredient has interfered with the polymerization reaction and resulted in the reduced formation of three-dimensional aluminosilicate geopolymer network (see Figure 2-12(b)). The places marked with symbol “E” in Figure 2-12(a) and ‘J” in 2-12(b) show completely unreacted fly ash particles whereas “F” and “H” are partially reacted hollow fly ash spheres. It seems that the concurrent presence of hydrated lime and an increased reactive proportion of the fly ash in the G7 mix has led to the formation of partially hydrated gels with large voids. Based on the observation, it is suggested that the replacement of UFFA in low calcium fly ash be made at lower proportions, with minimal inclusion of hydrated lime in the solid precursor.

2.6 Conclusions

The feasibility of synthesizing high strength geopolymer composite at ambient temperature was investigated with various combinations of solid precursors by including UFFA, slag, and hydrated lime at higher proportions in the low calcium fly ash. The compressive strength development from 3 to 28 days and microstructural characteristics were studied. The key conclusions drawn from this study are the following:

- 1) The compressive strength of the binders synthesized from low calcium fly ash and slag increased with an increasing slag content. Equal parts fly ash-slag geopolymer material exhibited the highest compressive strength of around 108 MPa at 28 days, followed by a compressive strength of 106 MPa in a 60% fly ash and 40% slag blend.
- 2) The binary blending of fly ash with free lime did not show any significant improvement in the compressive strength at ambient temperature. Incomplete dissolution of fly ash particles and surplus presence of alkaline solution led to the efflorescence of specimens in these matrices.
- 3) Addition of calcium hydroxide at higher proportions (up to 10%) in low calcium fly ash geopolymer was also not effective and gave low strengths due to the reduced formation of three-dimensional aluminosilicate geopolymeric network.
- 4) Partial replacement of fly ash with ultrafine fly ash or slag showed about 44% and 275% improvement in the 28 days compressive strength of the above geopolymer containing fly ash and free lime only.
- 5) The addition of ultrafine fly ash as partial replacement of slag adversely affected the compressive strength in fly ash-slag geopolymer, whose compressive strength was 30% lower than the dual blended fly ash-slag geopolymer.
- 6) Early age strength was significantly accelerated by including a small amount of CaO in fly ash-slag geopolymer. However, this inclusion does not affect the 28 days compressive strength of the resulting formulation.

- 7) The XRD analysis, SEM, and EDX spectra results for fly ash-slag geopolymers agree well with the observed mechanical behavior. An additional crystalline CSH/C-A-S-H gel was formed in conjunction with the amorphous aluminosilicate N-A-S-H gel, which modified the microstructure/pore size of these composites and thus the associated compressive strength.
- 8) The effective porosity of the composites was reduced with the addition of slag and ultrafine fly ash. However, the little formation of N-A-S-H gel in UFFA based composites presented reduced mechanical properties.

2.7 References

ASTM. (2012a). Standard specification for coal fly ash and raw or calcined natural pozzolan for use in concrete. *ASTM C618-12a*, Philadelphia.

ASTM. (2013a). Standard test method for compressive strength of hydraulic cement mortars, (using 50-mm cube specimens). *ASTM C109-13*, Philadelphia.

ASTM. (2013b). Standard test method for flow of hydraulic cement mortar. *ASTM C1437-13*, Philadelphia.

ASTM. (2015). Standard test method for relative density (Specific Gravity) and absorption of fine aggregate. *ASTM C128-15*, Philadelphia.

Alarcon-Ruiz, L., Platret, G., Massieu, E. & Ehlacher, A. (2005). The use of thermal analysis in assessing the effect of temperature on a cement paste. *Cement and Concrete Research*, 35, 609-613.

Alomayri, T., Shaikh, F. U. A. & Low, I. M. (2014). Mechanical and thermal properties of ambient cured cotton fabric-reinforced fly ash-based geopolymer composites. *Ceramics International*, 40, 14019-14028.

Atiř, C. D., Görür, E. B., Karahan, O., Bilim, C., İlkentapar, S. & Luga, E. (2015). Very high strength (120 MPa) class F fly ash geopolymer mortar activated at different NaOH amount, heat curing temperature and heat curing duration. *Construction and Building Materials*, 96, 673-678.

Bastidas, D. M., Fernández-Jiménez, A., Palomo, A. & González, J. A. (2008). A study on the passive state stability of steel embedded in activated fly ash mortars. *Corrosion Science*, 50, 1058-1065.

Benhelal, E., Zahedi, G., Shamsaei, E. & Bahadori, A. (2013). Global strategies and potentials to curb CO₂ emissions in cement industry. *Journal of Cleaner Production*, 51, 142-161.

Bernal, S. A., Rodríguez, E. D., Mejía De Gutiérrez, R., Gordillo, M. & Provis, J. L. (2011). Mechanical and thermal characterisation of geopolymers based on silicate-activated metakaolin/slag blends. *Journal of Materials Science*, 46, 5477-5486.

Chi, M. (2015). Effects of modulus ratio and dosage of alkali-activated solution on the properties and micro-structural characteristics of alkali-activated fly ash mortars. *Construction and Building Materials*, 99, 128-136.

- Chi, M. & Huang, R. (2013). Binding mechanism and properties of alkali-activated fly ash/slag mortars. *Construction and Building Materials*, 40, 291-298.
- Chindaprasirt, P., Chareerat, T., Hatanaka, S. & Cao, T. (2011). High-Strength geopolymer using fine high-calcium fly ash. *Journal of Materials in Civil Engineering*, 23, 264-270.
- Chindaprasirt, P., Chareerat, T. & Sirivivatnanon, V. (2007). Workability and strength of coarse high calcium fly ash geopolymer. *Cement and concrete composites*, 29, 224-229.
- Davidovits, J. (1988). Soft mineralogy and geopolymers. *Proceedings of 1st International Conference on Geopolymers, vol. 1*.
- Davidovits, J. (1994). High-alkali cements for 21st century concretes. *Special Publication*, 144, 383-398.
- Deb, P. S., Nath, P. & Sarker, P. K. (2014). The effects of ground granulated blast-furnace slag blending with fly ash and activator content on the workability and strength properties of geopolymer concrete cured at ambient temperature. *Materials & Design*, 62, 32-39.
- Duxson, P., Provis, J. L., Lukey, G. C., Mallicoat, S. W., Kriven, W. M. & Van Deventer, J. S. J. (2005). Understanding the relationship between geopolymer composition, microstructure and mechanical properties. *Colloids and Surfaces A: Physicochemical and Engineering Aspects*, 269, 47-58.
- Fan, Y., Yin, S., Wen, Z. & Zhong, J. (1999). Activation of fly ash and its effects on cement properties I. *Cement and Concrete Research*, 29, 467-472.
- Fernandez-Jimenez, A., García-Lodeiro, I. & Palomo, A. (2007). Durability of alkali-activated fly ash cementitious materials. *Journal of Materials Science*, 42, 3055-3065.
- Fernández-Jiménez, A., Palomo, A. & Criado, M. (2005). Microstructure development of alkali-activated fly ash cement: a descriptive model. *Cement and Concrete Research*, 35, 1204-1209.
- Fernandez-Jimenez, A. M., Palomo, A. & Lopez-Hombrados, C. (2006). Engineering properties of alkali-activated fly ash concrete. *ACI Materials Journal*, 103, 106.
- Frost, R. L., Hales, M. C. & Martens, W. N. (2008). Thermogravimetric analysis of selected group (II) carbonate minerals — Implication for the geosequestration of greenhouse gases. *Journal of Thermal Analysis and Calorimetry*, 95, 999-1005.
- Gao, X., Yu, Q. L. & Brouwers, H. J. H. (2015). Reaction kinetics, gel character and strength of ambient temperature cured alkali activated slag–fly ash blends. *Construction and Building Materials*, 80, 105-115.
- García-Lodeiro, I., Palomo, A. & Fernández-Jiménez, A. (2007). Alkali–aggregate reaction in activated fly ash systems. *Cement and Concrete Research*, 37, 175-183.
- Gourley, J. (2003). Geopolymers; opportunities for environmentally friendly construction materials. *Materials 2003 Conference: Adaptive Materials for a Modern Society, Sydney, Institute of Materials Engineering Australia*.
- Ismail, I., Bernal, S. A., Provis, J. L., Hamdan, S. & Deventer, J. S. J. (2012). Microstructural changes in alkali activated fly ash/slag geopolymers with sulfate exposure. *Materials and Structures*, 46, 361-373.

- Ismail, I., Bernal, S. A., Provis, J. L., San Nicolas, R., Hamdan, S. & Van Deventer, J. S. J. (2014). Modification of phase evolution in alkali-activated blast furnace slag by the incorporation of fly ash. *Cement and Concrete Composites*, 45, 125-135.
- Kong, D. L. Y. & Sanjayan, J. G. (2010). Effect of elevated temperatures on geopolymer paste, mortar and concrete. *Cement and Concrete Research*, 40, 334-339.
- Lee, N., An, G., Koh, K. & Ryu, G. (2016). Improved reactivity of fly ash-slag geopolymer by the addition of silica fume. *Advances in Materials Science and Engineering*, 2016.
- Lee, W. K. W. & Van Deventer, J. S. J. (2002). The effects of inorganic salt contamination on the strength and durability of geopolymers. *Colloids and Surfaces A: Physicochemical and Engineering Aspects*, 211, 115-126.
- Mustafa Al Bakri, A., Kamarudin, H., Bnhussain, M., Rafiza, A. & Zarina, Y. (2012). Effect of Na₂SiO₃/NaOH Ratios and NaOH molarities on compressive strength of fly-ash-based geopolymer. *ACI Materials Journal*, 109.
- Nath, P. & Sarker, P. K. (2014). Effect of GGBFS on setting, workability and early strength properties of fly ash geopolymer concrete cured in ambient condition. *Construction and Building Materials*, 66, 163-171.
- Nematollahi, B., Sanjayan, J. & Shaikh, F. U. A. (2015). Synthesis of heat and ambient cured one-part geopolymer mixes with different grades of sodium silicate. *Ceramics International*, 41, 5696-5704.
- Pacheco-Torgal, F., Castro-Gomes, J. & Jalali, S. (2008). Investigations on mix design of tungsten mine waste geopolymeric binder. *Construction and Building Materials*, 22, 1939-1949.
- Pangdaeng, S., Phoo-Ngernkham, T., Sata, V. & Chindapasirt, P. (2014). Influence of curing conditions on properties of high calcium fly ash geopolymer containing Portland cement as additive. *Materials & Design*, 53, 269-274.
- Phoo-Ngernkham, T., Maegawa, A., Mishima, N., Hatanaka, S. & Chindapasirt, P. (2015). Effects of sodium hydroxide and sodium silicate solutions on compressive and shear bond strengths of FA-GBFS geopolymer. *Construction and Building Materials*, 91, 1-8.
- Puertas, F., Martínez-Ramírez, S., Alonso, S. & Vázquez, T. (2000). Alkali-activated fly ash/slag cements: Strength behaviour and hydration products. *Cement and Concrete Research*, 30, 1625-1632.
- Rashad, A. M. (2014). A comprehensive overview about the influence of different admixtures and additives on the properties of alkali-activated fly ash. *Materials & Design*, 53, 1005-1025.
- Rattanasak, U. & Chindapasirt, P. (2009). Influence of NaOH solution on the synthesis of fly ash geopolymer. *Minerals Engineering*, 22, 1073-1078.
- Sakulich, A. R. (2011). Reinforced geopolymer composites for enhanced material greenness and durability. *Sustainable Cities and Society*, 1, 195-210.
- Shaikh, F. U. A. & Supit, S. W. M. (2014). Mechanical and durability properties of high volume fly ash (HVFA) concrete containing calcium carbonate (CaCO₃) nanoparticles. *Construction and Building Materials*, 70, 309-321.

- Shaikh, F. U. A. & Supit, S. W. M. (2015). Compressive strength and durability properties of high volume fly ash (HVFA) concretes containing ultrafine fly ash (UFFA). *Construction and Building Materials*, 82, 192-205.
- Shen, W., Wang, Y., Zhang, T., Zhou, M., Li, J. & Cui, X. (2011). Magnesia modification of alkali-activated slag fly ash cement. *Journal of Wuhan University of Technology-Mater. Sci. Ed.*, 26, 121-125.
- Shi, C. & Day, R. L. (1999). Early strength development and hydration of alkali-activated blast furnace slag/fly ash blends. *Advances in Cement Research*, 11, 189-196.
- Shi, C., Roy, D. & Krivenko, P. (2006). *Alkali-activated cements and concretes*, CRC press.
- Subaer (2004). Influence of aggregate on the microstructure of geopolymer, *PhD Thesis*, Curtin University of Technology.
- Temuujin, J., Van Riessen, A. & Williams, R. (2009). Influence of calcium compounds on the mechanical properties of fly ash geopolymer pastes. *Journal of Hazardous Materials*, 167, 82-88.
- Turner, L. K., & Collins, F. G. (2013). Carbon dioxide equivalent (CO₂-e) emissions: A comparison between geopolymer and OPC cement concrete. *Construction and Building Materials*, 43, 125-130.
- Van Jaarsveld, J. G. S., Van Deventer, J. S. J. & Lukey, G. C. (2002). The effect of composition and temperature on the properties of fly ash- and kaolinite-based geopolymers. *Chemical Engineering Journal*, 89, 63-73.
- van Riessen, A. & Chen-Tan, N. (2013). Beneficiation of Collie fly ash for synthesis of geopolymer Part 2 – Geopolymers. *Fuel*, 111, 829-835.
- Wallah, S. E. A. R. (2006). Low-Calcium fly ash-based geopolymer concrete: Long-term properties. Curtin University of Technology.
- Yip, C. K., Lukey, G. C., Provis, J. L. & Van Deventer, J. S. J. (2008.) Effect of calcium silicate sources on geopolymerisation. *Cement and Concrete Research*, 38, 554-564.
- Zhang, M.-H. & Islam, J. (2012). Use of nano-silica to reduce setting time and increase early strength of concretes with high volumes of fly ash or slag. *Construction and Building Materials*, 29, 573-580

CHAPTER 3 EFFECTS OF CURING CONDITIONS & SAND- TO-BINDER RATIOS ON COMPRESSIVE STRENGTH DEVELOPMENT OF FLY ASH GEOPOLYMER

3.1 Abstract

This study presents the effects of curing conditions on a high strength geopolymer material synthesized by activating different combinations of low calcium fly ash (FA), ultrafine fly ash (UFFA), and slag with a multi-compound mixture of D-grade sodium silicate and 12M sodium hydroxide solution. The effect of ambient air and water curing on the strength properties, cumulative porosity, and microstructure of geopolymer mortar samples was evaluated at room temperature. Subsequently, the effects of two different sand-binder ratios, the amount of FA replacement with UFFA and slag on the short-term mechanical properties and workability of geopolymer mixtures is also discussed. The results showed that the geopolymer specimens cured in water medium possessed a higher total porosity in relation to the air cured samples. Air curing resulted in additional polymerization, and fewer micro-cracks were observed within the scanning electron microscope photographs, which led to high compressive strength. Moreover, the use of UFFA was found to significantly improve the strength of FA-slag blended geopolymers; where reduced porosity and denser microstructure in FA geopolymers was observed with the inclusion of UFFA and slag at higher proportions.

3.2 Introduction

In Australia, approximately 12.1 million tons of Fly Ash (FA, typically class F) is produced annually by coal-fired power plants; where cement or concrete only uses a small portion of this pozzolanic waste and the rest is sent to landfill (Ash Dev. Association of Australia, 2015). A recent upsurge in carbon taxes and the awareness to improve environmental impact has driven the focus of construction industry towards the increased use of by-products and reduced consumption of ordinary Portland cement (OPC) as a building material (Shaikh and Supit, 2014). Resultantly, recent decades have seen the emergence of a green synthetic binder from the family of alkali-activated cement, commonly known as “geopolymer” (Davidovits, 1988). The term refers to an inorganic polymer, produced by combining silico-aluminous materials with a highly alkaline activator (Davidovits, 1994). The most commonly used source materials are either by-products such as FA, ground granulated blast furnace slag (slag) and rice-husk ash or naturally occurring minerals, e.g., clay or metakaolin, etc.; where the activators can be a combination of sodium silicate (Na_2SiO_3) and sodium hydroxide (NaOH) solutions in

different mass ratios (Olivia and Nikraz, 2012; Sarker et al., 2013; Phoo-ngernkham et al., 2015).

A plethora of research has been carried out on FA geopolymer which was either heat or steam cured (Mustafa et al., 2012; van Riessen and Chen-Tan, 2013; Atis et al., 2015). Though, the real difficulty in actual construction practice for low calcium FA is related to its low strength development at ambient temperature (Wallah and Rangan, 2006) and the requirement of higher activation energy/temperature between 40 and 85°C (Bakharev, 2006). Recently, a number of researchers have reported avoiding the heat treatment by introducing a reactive solid precursor such as slag or OPC in the low calcium FA (Pangdaeng et al., 2014; Rashad, 2014; Phoo-ngernkham et al., 2016); where the inclusion of slag has been identified as more beneficial, since it is also a waste product and contains a high content of free lime together with a rich glassy phase, i.e., both SiO₂ and Al₂O₃ are present in an amorphous form (Puertas et al., 2000). However, it is well established that the nature of binding gels in alkali-activated systems is extremely sensitive to the composition of starting materials, i.e., a fundamental difference exists in terms of the reaction products obtained from the alkali-activation of FA or slag. It is believed that in FA activated systems, the mechanical strength develops from an amorphous three-dimensional sodium aluminosilicate hydrate (N-A-S-H) gel network, where water present in the reaction medium is expelled out during the hardening process (Fernandez et al., 2005). The excluded water exists as free or bound within the final reaction products and has no role to play in the polymerization reaction (Lizcano et al., 2012).

On the other hand, the major binding phases formed on the alkali-activation of slag are crystalline calcium silicate hydrate (CSH) and/or calcium aluminum silicate hydrate (C-(A)-S-H) type gels (Puertas et al., 2011). Unlike N-A-S-H, these hydration products share the same level of sensitivity to the lack of curing, as observed in OPC (Collins and Sanjayan, 2001). Consequently, many researchers have proposed to use either fully immersed water curing condition or nearly saturated humidity levels for alkali-activated slag binders (Kutti and Malinowski, 1982; Talling, 1989; Luo et al., 2012; Qureshi and Ghosh, 2014; Jang et al., 2014).

Previous investigations on FA-slag/OPC blends concluded that their combined activation is an exothermal process at room temperature. The extra calcium incorporated in geopolymer system reacts with the alkaline activator and yields a secondary gel (CSH, C-(A)-S-H) in conjunction with the geopolymer products (N-A-S-H, N-(C)-A-S-H); while these two distinct binding gels do not develop separately, instead they interact, undergoing a constant structural or compositional change during the process (Ismail et al., 2014). However, apart from ongoing research to find the exact combination between FA-slag precursors that can be used as an

alternative to OPC, a significant gap in the literature is associated with the choice of curing conditions for such hybrid binder combinations. Some of the recent investigations on these modified source materials used complete air moisture and temperature controlled environment to synthesize the geopolymer material, considering their polymeric nature (Deb et al., 2014; Nath and Sarker, 2015). While others used a standard water curing regime (Pangdaeng et al., 2014, Nematollahi et al., 2015; Wardhono et al., 2015a) for the continued hydration of C-S-H and/or C-(A)-S-H gels for strength gain.

A review of the ambient curing conditions and reported results for such modified binders in the previous studies highlighted several inconsistencies, which are discussed here. For example, Nematollahi et al. (2015) activated hybrid FA-slag and FA-calcium hydroxide ($\text{Ca}(\text{OH})_2$) binder compositions in different weight percentages with three different grades of Na_2SiO_3 powders and a combination of Na_2SiO_3 and NaOH powder. The samples were cured in water at $23^\circ\text{C} \pm 3^\circ\text{C}$, where low to medium compressive strength (around 40 MPa) was realized at 28 days. No results were presented for the microstructure or porosity of the matrix synthesized by one part geopolymer mixes. Likewise (Wardhono et al., 2015a), six different combinations between slag and FA precursors (1:0, 0.9:0.1, 0.8:0.2, 0.7:0.3, 0.6:0.4, 0.5:0.5) were activated with a Na_2O dosage of 15% and activator modulus of ($M_s = 1.25$). These samples were also stored in a water tank, where an equal parts slag-FA blend achieved the highest compressive strength (around 63 MPa) at 28 days. The binder composition containing 100% slag exhibited reduced mechanical behaviour (40 MPa) at the same age. The loss of strength was interpreted as a result of increased micro-cracking within specimens over the curing time period. However, this observation contradicts to the conclusions made by others (Collins and Sanjayan, 2001; Bernal et al., 2012) for alkali-activated slag binders that showed reduced porosity and better compressive strength results in the water curing medium. Many researchers (Deb et al., 2014; Nath and Sarker, 2015; Phoo-ngernkham et al., 2015) used air curing for hybrid FA-slag binder combinations, where the effect of slag addition in FA geopolymer was appreciated. However, apart from the variation in mix designs, the difference in curing environment and its possible influence on the extent of polymerization was never deliberated appropriately.

Similar opposing selection of curing medium was noticed for hybrid FA-OPC binder combinations, where, Pangdaeng et al. (2014) included OPC at a rate of 0%, 5%, 10% and 15% in high calcium FA geopolymer. $\text{Na}_2\text{SiO}_3/\text{NaOH}$ at a mass ratio of 0.67 and alkaline liquid/binder ratio of 0.40 was employed to activate the source materials. A concomitant increase in the compressive strength was measured with an increase in the replacement level of OPC. However, the mortar samples stored in water bath exhibited higher compressive strength and reduced porosities in relation to the air cured specimens at 23°C . On the other

hand, Pradip et al. (2015) activated low calcium FA geopolymer mortar and concrete samples containing OPC at a rate of 0%, 5%, 6%, 8%, 10% and 12%.with three different mass ratios between $\text{Na}_2\text{SiO}_3/\text{NaOH}$., i.e., 1.5, 2.0, and 2.5. There was a noticeable increase in the compressive strength of both mortar and the concrete samples with higher inclusion levels of OPC. However, the samples were left in the air to cure after demolding at a controlled room temperature of 23°C and 65% relative humidity (RH) until the test day.

It is evident from the review that previous research efforts were focused on facilitating one of the two-hybrid binding gels, i.e., either CSH or N-A-S-H that may have co-existed upon the combined activation of FA and slag/OPC. However, the selection of curing medium for a hybrid binding gel is a crucial factor that seems to have been adopted randomly, while aiming at optimizing other mix parameters. A wide scatter in the reported results make it extremely difficult to conclude whether the selected curing environment for a proposed ambient binder combination was the most effective for FA activation or otherwise. Moreover, there is scarcely any investigation in the literature that quantifies the change in porosity or morphology of the ambient cured geopolymer material encompassing low calcium FA as a principal binder, in relation to its curing medium. Therefore, in this research, the effect of curing conditions was investigated on a high strength geopolymer material containing low calcium FA, ultra-fine fly ash (UFFA), and slag in varying proportions and two different sand-binder ratios, activated with a multi-compound mixture of Na_2SiO_3 and NaOH solutions. The performance of synthesized geopolymer materials was evaluated by observing the relative characteristics of mechanical strength at different ages, microstructural development and the changes in porosity at 28 days of ambient air and water curing at room temperature. These parameters were also compared with a standard heat cured geopolymer containing FA as a sole binder.

3.3 Experimental Procedures

3.3.1 Materials

The aluminosilicate materials used in this investigation were FA, slag, and UFFA. FA with a median particle size of 9.7 μm was obtained from Gladstone power station in Queensland Australia. It had a calcium oxide (CaO) content of 4.30% (< 10%), thus classified as class F according to ASTM C618 (ASTM, 2012a). A construction grade slag was obtained from BGC cement Australia, whose basicity coefficient was 1 ($K_b = (\text{CaO} + \text{MgO}) / (\text{SiO}_2 + \text{Al}_2\text{O}_3)$), with a hydration modulus exceeding 1.4 ($\text{HM} = (\text{CaO} + \text{MgO} + \text{Al}_2\text{O}_3) / \text{SiO}_2$). The UFFA was provided by Flyash Australia, where the median particle sizes of slag and UFFA were 11.5 and 3.4 μm respectively. The alkaline solution was made by blending a 12M NaOH solution and a commercial D-grade Na_2SiO_3 (specific gravity of 1.53 and modulus ratio

($M_s=SiO_2/Na_2O$) of 2.0) sourced from PQ Australia Ltd. Local silica sand with a fineness modulus of 2.77, specific gravity of 2.65 and a maximum nominal size of 1.18 mm was used in saturated surface dry (SSD) condition as per ASTM C128 (ASTM, 2015). The chemical compositions of the solid precursors and alkali activators are given in Table 3-1.

Table 3-1 Chemical composition of solid precursors and alkali activators

Component (%)	FA	UFFA	Slag	Na ₂ SiO ₃ solution	NaOH solution
SiO ₂	51.11	73.40	32.45	29.40	-
Al ₂ O ₃	25.56	17.70	13.56	-	-
Fe ₂ O ₃	12.48	4.40	0.85	-	-
CaO	4.30	0.90	41.22	-	-
MgO	1.45	0.60	5.10	-	-
MnO	0.15	< 0.10	0.25	-	-
K ₂ O	0.70	1.03	0.35	-	-
Na ₂ O	0.77	0.11	0.27	14.70	28.05
P ₂ O ₅	0.88	0.20	0.03	-	-
TiO ₂	1.32	0.70	0.49	-	-
SO ₃	0.24	0.20	3.20	-	-
H ₂ O	-	-	-	55.90	71.95
Others	0.46	0.06	1.12	-	-
Loss on Ignition	0.57	0.57	1.11	-	-

3.3.2 Mix designs

The mix designs of geopolymers were developed from previous work (Khan et al., 2016) and are shown in Table 3-2. As such, these binder compositions were found the most effective regarding strength and microstructure development at ambient temperature. The mixtures are designated based on the proportions of their constituents, such as FA100 or FA60UFFA10S30, etc., where a typical binder formation named as FA60UFFA10S30 had 60% of FA, 10% of UFFA and 30% of slag by mass respectively. A small proportion of UFFA was included in two matrices to increase the reactive component of the FA binding material. A multi compound mixture of 12M NaOH and Na₂SiO₃ solutions, with a mass ratio of 2.50 between Na₂SiO₃/NaOH was used to activate the hybrid FA, slag, and UFFA binder compositions.

The alkaline liquid to binder (L/B) and water to solid (w/s) ratios were kept constant at 0.60 and 0.28 for all mixes. Furthermore, two different sand-binder ratios at 2.00 and 2.75 were employed, where a duplicate set of 12 samples were cast for each series except for the M1 and M6 mixtures. In order to improve the workability of mixes having a sand-binder ratio as 2.75, polycarboxylate ether based superplasticizer was added 1% by mass to the binder. No extra water was included in any mixture. The critical oxide molar ratios, e.g., Na₂O/SiO₂, H₂O/Na₂O and Si/Al ratio are also calculated and presented in Table 3-2.

Table 3-2 Mixture proportions of geopolymer mortar samples

Mix ID	Sample Designation	FA:UFFA:slag Proportion (wt. %)			Sand-Binder ratio	Oxide Molar Ratios			
		FA	UFFA	Slag		Na ₂ O/SiO ₂	Na ₂ O/Al ₂ O ₃	Si/Al	H ₂ O/Na ₂ O
M1	FA100	100	0	0		0.17	0.70	2.11	11.41
M2	FA60UFFA10S30	60	10	30		0.17	0.83	2.42	11.64
M3	FA70S30	70	0	30	2.00	0.18	0.81	2.25	11.57
M4	FA60S40	60	0	40		0.18	0.85	2.30	11.62
M5	FA50S50	50	0	50		0.19	0.90	2.36	11.68
M6	FA100	100	0	0		0.18	0.75	2.11	10.70
M7	FA60UFFA10S30	60	10	30		0.18	0.89	2.42	10.90
M8	FA70S30	70	0	30	2.75	0.19	0.87	2.25	10.84
M9	FA60S40	60	0	40		0.20	0.91	2.30	10.89
M10	FA50S50	50	0	50		0.20	0.96	2.36	10.93

3.3.3 Mixing, sample preparation and curing conditions

A 10-liters Hobart mixer was used for mixing the dry ingredients including FA, slag, UFFA and sand with the alkaline activator. The total mixing procedure was completed in around 8 mins; however, the required quantities of Na₂SiO₃ and NaOH solutions were combined at least 30 mins ahead of the mixing sequence. At first, the solid precursors were dry-mixed initially with fine aggregates for 3 mins at a slow speed (140 ± 5 r/m). This was followed by the gradual and slow addition of alkaline solution over a 60 secs period. Later the mixing was continued for another 3 to 4 mins at a medium speed (285 ± 10 r/m).

Subsequently, after measuring the flow, the mixtures were poured into acrylic plastic molds (50 × 50 × 50 mm³ cubes) in two layers and vibrated to remove the entrapped air bubbles. The cast samples were stored at room temperature (20°C ± 3°C) and in a controlled environment (RH, 65% ± 10%) for the next 24 hours. After taking out from molds, one set of 12 samples from each series was wrapped (to prevent any moisture loss) and moved into an ambient curing room until the test day. The second set was submerged in the water bath at controlled room temperature (20°C ± 3°C). The samples from M1 and M6 batches were subjected to heat curing (85°C) for the first 24 hours. Following which, they were removed from the oven and allowed to cool at room temperature. The demolded samples were then tagged and stored in an ambient curing room along with the other specimens until the test day.

3.4 Test Methods

3.4.1 Workability and compressive strength test

The workability of fresh geopolymer mixes was measured as flow diameter in accordance with ASTM C1437 (ASTM, 2013b). Each combination was tested twice, immediately after mixing all the constituents, while the spread diameter was measured across the four perpendicular edges of the flow table and the reported values are an average of these readings. The compressive strength tests were made at the ages of 3, 7, 14, and 28 days as per ASTM C109 (ASTM, 2013a) at a loading rate of 0.33 MPa/sec. The stated strength results are an average of three samples.

3.4.2 Porosity Measurement

The pore size distribution was evaluated utilizing mercury intrusion porosimetry (MIP) in geopolymer samples stored in different curing regimes. The intruded mercury volume and pore diameter were logged at each pressure point, for a pressure ranged between 0.0083 and 207 MPa. The pressure values were converted into an equivalent pore width using the Washburn expression (Khan et al., 2016), as expressed in Equation (3.1):

$$d_0 = -2\gamma\cos\theta / p \quad (3.1)$$

where d_0 is the pore width (μm), γ is the surface tension (mN/m), θ is the contact angle between mercury and the pore wall ($^\circ$), and p is the net pressure across the mercury meniscus at the time of the cumulative intrusion measurement (MPa).

3.4.3 Scanning electron microscopy (SEM) and Energy dispersive X-ray spectroscopy (EDS) analysis

A scanning electron microscope (Zeiss EVO 40XVP) equipped with an energy-dispersive X-ray analyzer was used to study the microstructure of geopolymer samples. The samples with a dimension of $10\text{ mm} \times 10\text{ mm} \times 5\text{ mm}$ were sectioned from a representative cube ($50 \times 50 \times 50\text{ mm}^3$) at the age of 28 days, which were later air dried and platinum coated before being used for microstructural imaging.

3.5 Results and Discussion

3.5.1 Workability

The workability results of geopolymer mortars containing different additives (slag and UFFA) and sand-binder ratios are shown in Figure 3-1. As can be seen, the flow values decreased for all mixtures with the inclusion of additives in M1 and M6, FA binders. The highest flow diameter (140 mm) was measured for M1 series, whereas the lowest workability was observed for the M7 mixture containing 60% FA, 30% slag and 10% UFFA. It can be seen that the rate of flow loss for all binder compositions, having a sand-binder ratio of 2.75 was approximately 50 to 100% higher in relation to the mixes with lower fine aggregates content. Furthermore, it can be observed that the reduction in the workability of mortar mixtures containing slag was proportionate to the replacement level of the reactive precursor in M1 series, such that the workability of M3, M4, and M5 mixes were around 22% lower than FA geopolymer.

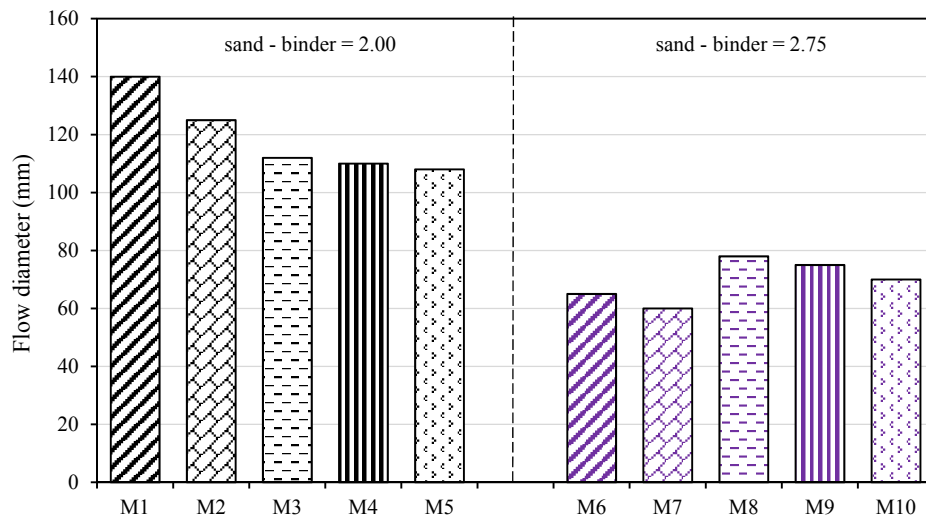


Figure 3-1 Workability of geopolymer mixtures with different additives and sand-binder ratios.

The reduced workability of FA-slag geopolymer was primarily related to the rapid reaction of the increased calcium content and chemical activator since slag contained a relatively high percentage of CaO (41.22%). It is believed that the excess calcium presented in geopolymer system provided additional nucleation sites for precipitation of dissolved FA monomers and affected the solidification rate (Lee and van Deventer, 2002). While the lower workability of mixes containing UFFA can be associated with the higher surface area, smaller particle size, and increased reactivity of the binder composition. Similar observations were reported earlier, where an increased reactive proportion of FA produced unworkable mixes (van Riessen and Chen-Tan, 2013). By comparing the results for different binder compositions and sand-binder

ratios, it can be concluded that for a selected constant water to solids (w/s) or liquid to binder (L/B) ratio, the nature of solid precursors and amount of fine aggregates significantly influenced the flow values. The combined presence of UFFA and slag in M7 series led to the higher stiffness and viscosity in that particular mixture, thus lower workability.

3.5.2 Compressive strength

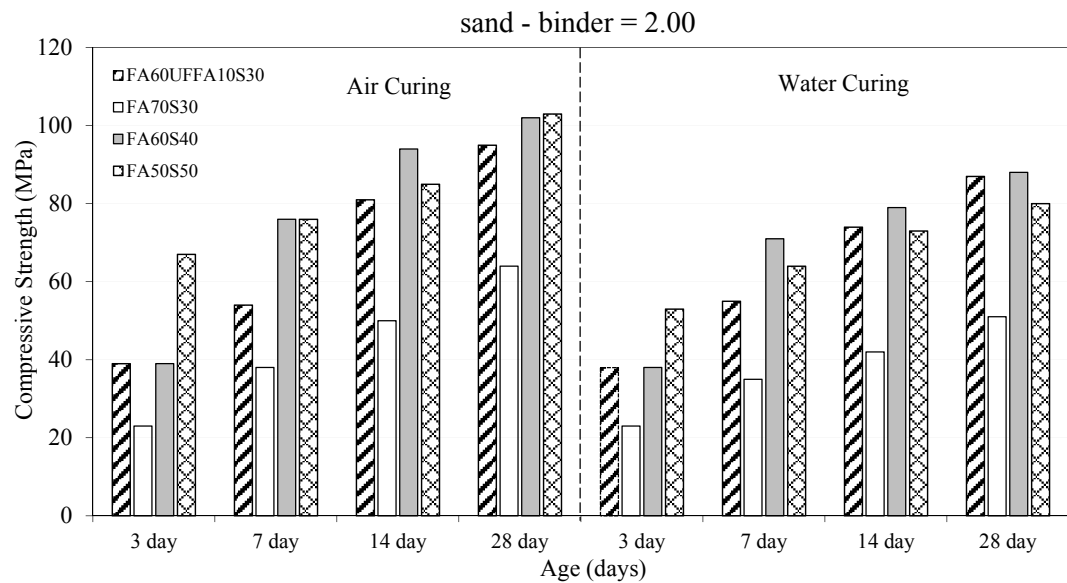
3.5.2.1 Effect of curing conditions on strength development

The effect of curing conditions on the strength development of FA geopolymers containing different additives is shown in Figure 3-2. As can be seen, the compressive strength increased with ages for all binder compositions except for the heat cured FA only geopolymer samples (M1 and M6). These mixtures exhibited 97 and 54 MPa, respectively compressive strength at the age of 3 days with zero increase at 28 days. It has been observed previously that the strength of geopolymers is little affected by age after the completion of an initial heat curing period (Khan et al., 2016). It can be further established from the results that apart from two mix designs (i.e., M5 and M9), for a given hybrid binder combination and sand-binder ratio, early age strengths of all mixtures were nearly similar irrespective of their curing medium, i.e., ambient air or water. However, the compressive strength of water cured specimens decreased at later ages, i.e., at 7, 14, and 28 days.

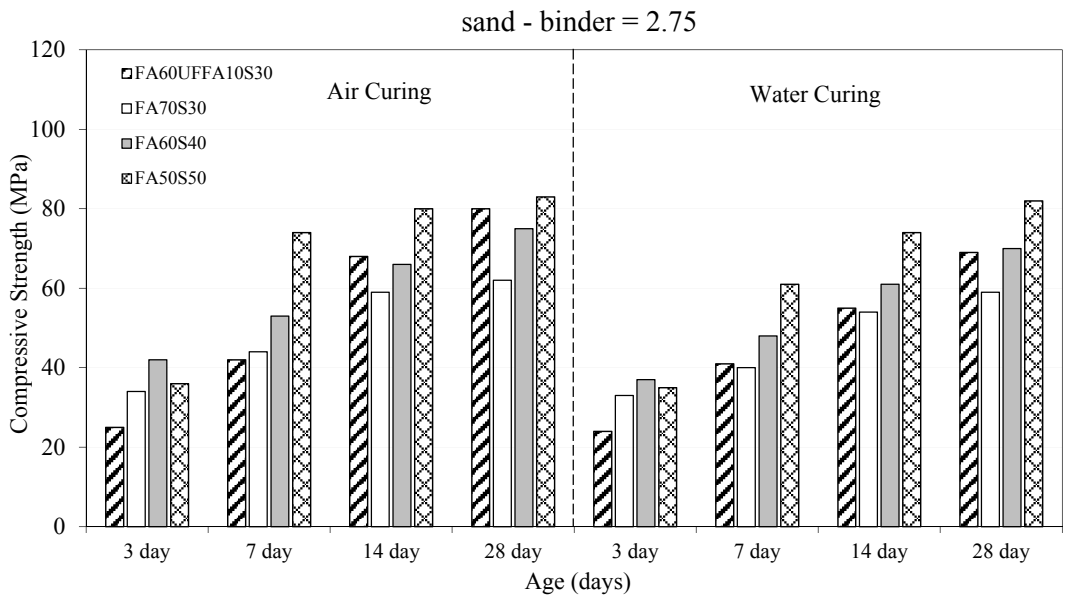
By comparing the strength graphs, it can be seen that the 3-day strength of M5 and M9 mixes in the water curing medium was 21% and 12% lower than air cured counterparts. Moreover, a progressive increase in strength reduction with age may also be noticed in other matrices, such that the geopolymer samples from M3, M4, and M5 binder compositions exhibited 8%, 7%, and 16% reduced strength development in water curing medium in comparison to the samples cured in air at 7 days, whereas the said difference increased to 20%, 14%, and 23% respectively at 28 days. A similar trend was observed for other source material blends containing UFFA as a partial replacement of FA, i.e., M2 and M7, which displayed 9% and 14% reduced strength development in the water curing medium corresponding to the air cured matrices.

On the other hand, the mortar mixtures having a sand-binder ratio of 2.75 showed an improved mechanical behaviour at 28 days of water curing in relation to their 7 days compressive strength. It can be seen that the 7-day strength of M8, M9, and M10 water cured specimens was 9%, 8%, and 18% lower than air cured counterparts, though the stated variance reduced to 5%, 7%, and 2% respectively, at the end of 28-day curing period. It is exciting to note that M10 mixture containing 50% FA and 50% slag was the least sensitive binder composition to the curing effect. The mortar mixtures with a similar FA-slag content and a sand-binder ratio

of 2.0 (M5) exhibited 23% reduced strength development at 28 days in the water curing regime. It can be concluded that despite the variation in compressive strength amongst different source materials, the rate of strength development in these modified binders was consistently lower in the presence of water in comparison to air curing, where the effect of curing conditions looked more evident in samples enclosing a sand-binder ratio of 2.00.



(a)



(b)

Figure 3-2 Compressive strength of geopolymer mortars in different curing conditions (a) sand-binder = 2.00 (b) sand-binder = 2.75.

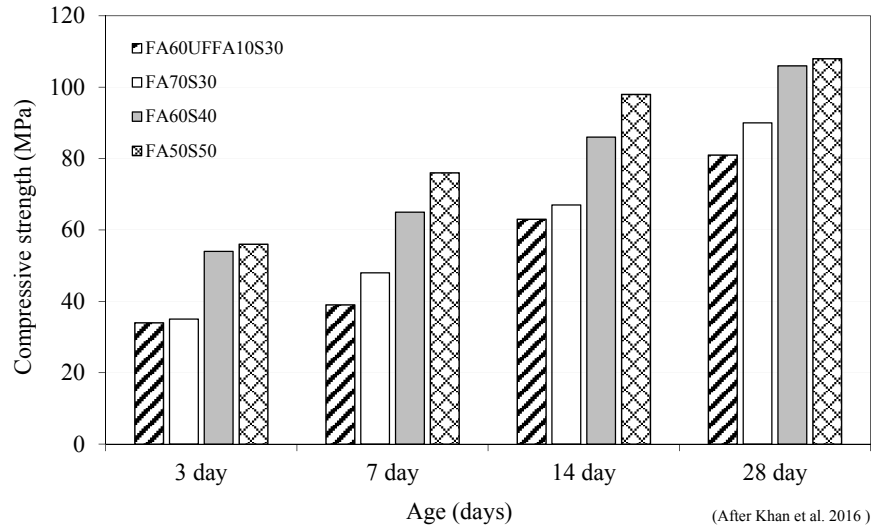
It is well-known that the reaction kinetics and rate of crystallization in geopolymer precursors depend on the availability of reactive silica and alumina in the starting material. However, the reduced mechanical behaviour of samples cured in water medium can be associated with the possible leaching of metal cations from the alkaline solution over the curing period (Giasuddin et al., 2013). It can be seen that in both the curing situations, the quantity of available silica and alumina from the source materials remained same for the reaction purposes; however, a progressive activator lixiviation and the leaching of alkali ions (N^+) has prevented the continuous dissolution of FA monomers in the water medium. It is believed that the loss of strength is contributed by the growth of defect sites in the form of pores or non-activated material existing in the water cured samples, i.e., additional voids were present within the mortar samples that weaken the interfacial transitional zone (ITZ) between the aggregates and the cementitious gel, which reduced the mechanical strength. The porosity measurements shown in the later section (section 3.5.3) evidence that the mortar samples stored in an air wrapped environment were less porous as compared to the water cured matrices. Moreover, as presented in SEM images, a relatively large number of unreacted FA particles and pores can be seen embedded within the water cured geopolymer specimens.

Similar findings were reported by other researchers, where Giasuddin et al. (2013) identified reduced compressive strength in water cured geopolymer pastes corresponding to the samples cured in saline water. A significant leaching of the alkaline solution was noticed during the first few hours of sample storage in ordinary water. It was demonstrated that the pH of water curing medium increased about 4.5 units as compared to 4.05 units in saline water from the initial value. Ren et al. (2012) also measured a 14% reduced compressive strength (47.6 MPa) in water cured slag-FA concrete (70-30 blend) compared to the air cured samples (54.1 MPa). However, the loss of mechanical strength was specified as a result of lower Van der Waals forces between the gel particles and possible micro-cracks coalescence due to the existence of absorbed water in water cured samples.

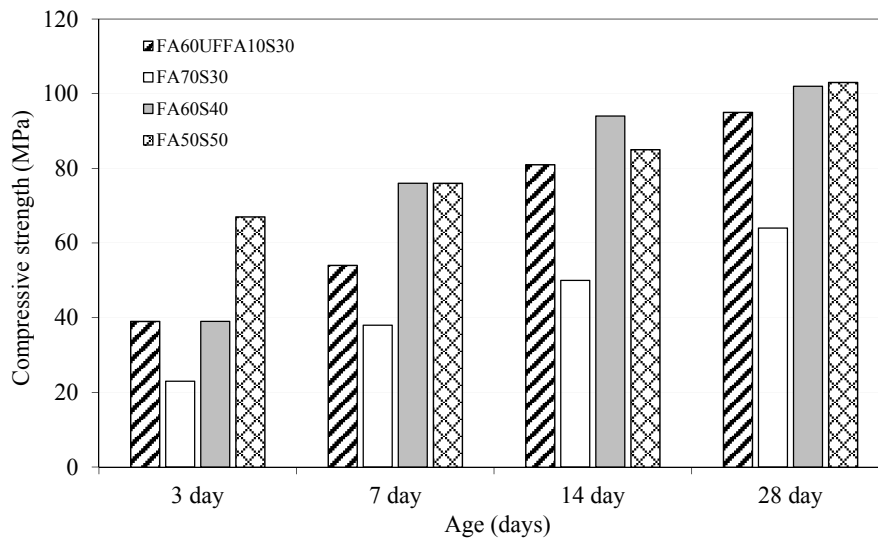
3.5.2.2 Effect of additives and sand-binder ratios on strength development

In addition to the reported behaviour of geopolymer specimens cured in air and water medium, the test results presented in the earlier section also indicate that for a selected curing environment (i.e., either ambient air or water), the strength development pattern in a customized hybrid binder could inevitably be influenced by the nature of source materials, quantity of alkaline solution or fine aggregates in a particular mixture. Therefore, Figure 3-3 shows a comparison between the compressive strength of geopolymer mortars for two different sand-binder ratios, stored in an air wrapped environment. These results are also linked to the previous investigation (Khan et al., 2016) (see Figure 3-3(a)), where a constant

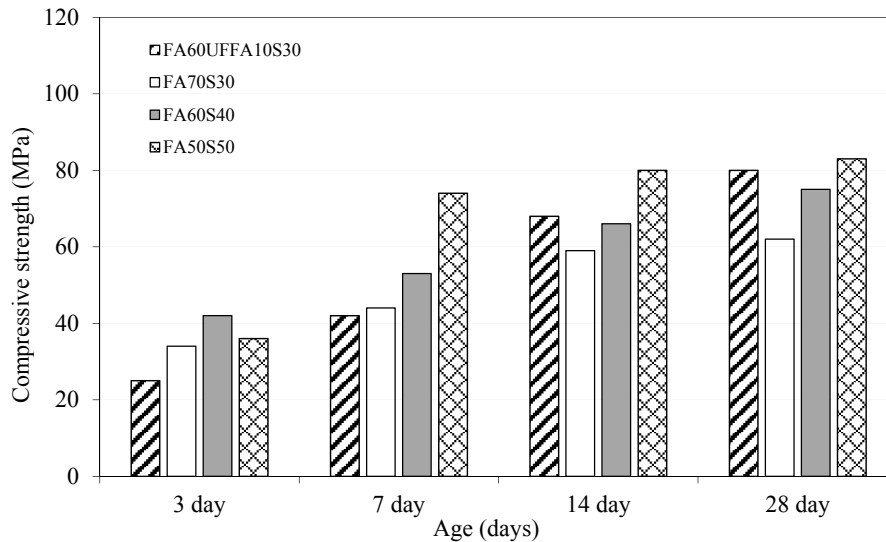
sand-binder ratio of 1.60 was used. It should be noted that although the discussion is made for air cured matrices, a similar evaluation can be recognized for water cured specimens.



(a)



(b)



(c)

Figure 3-3 Compressive strength of geopolymer with different additives and sand-binder ratios (a) sand-binder = 1.60 (b) sand-binder = 2.00 (c) sand-binder = 2.75.

It can be seen that the highest compressive strength (around 103 MPa) was measured for the M5 mixture containing an equal parts FA-slag combination and a sand-binder ratio of 2.0. The other ternary and binary blended binder compositions, i.e., M2, M3, and M4, which had a similar fine aggregates content exhibited 95, 64 and 102 MPa, respectively compressive strength at 28 days. A significant reduction in the compressive strength was observed at a higher sand-binder ratio (i.e., 2.75), where the M7, M8, M9 and M10 geopolymer mixes displayed 80, 62, 75 and 83 MPa, respectively compressive strength at the age of 28 days. It is apparent that the compressive strength decreased proportionately with an increase in the sand-binder ratio for a given hybrid binder combination. Despite maintaining a constant high $\text{Na}_2\text{O}/\text{SiO}_2$, $\text{Na}_2\text{O}/\text{Al}_2\text{O}_3$ and unchanged Si/Al ratios in M6 to M10 mixes (see Table 3-2), the loss of mechanical strength is reasonably related to the insufficient presence of the binder material and alkaline solution, which has led to the reduced formation of binding gels and poor bonding between the increased fine aggregates in these matrices.

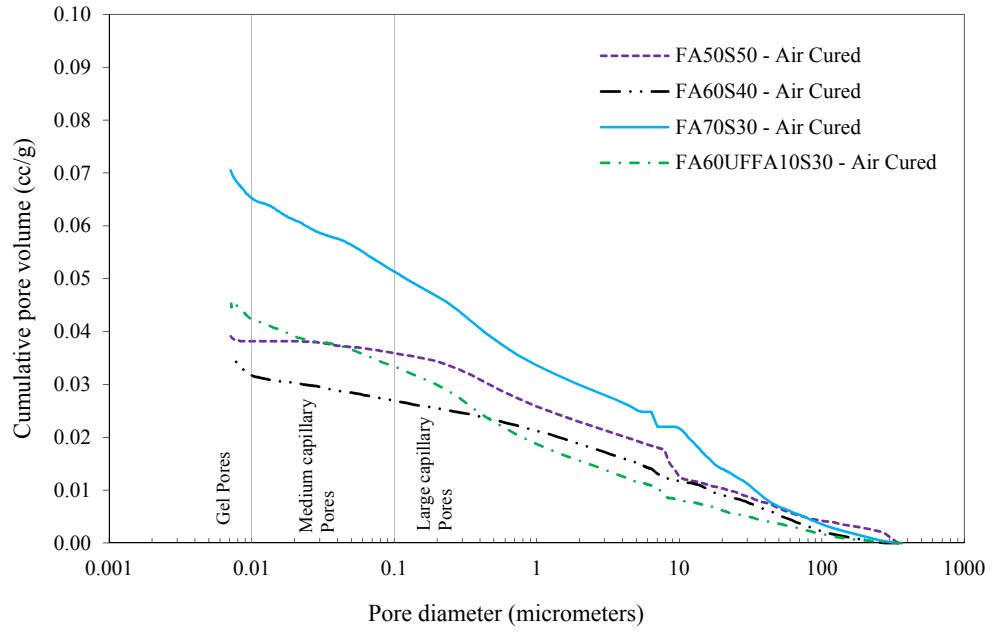
On the contrary, it can also be appreciated that for a constant sand-binder ratio, the strength development in different compositions was directly influenced by the presence of amorphous oxides of silicon, aluminum, and calcium in the initial solid precursor. For example, by relating the strength development pattern of mixes containing UFFA in Figure 3-3(b) and Figure 3-3(c), it can be concluded that the improved reactivity of FA has modified the strength properties of M2 and M7 (FA60UFFA10S30) mixtures, such that the 28 days compressive strength of M2 (FA60UFFA10S30, see Figure 3-3(b)) hybrid binder was 48 % higher than

M3, while the strength development of M7 series (see Figure 3-3(c)) was 29% higher than the corresponding M8 mortar samples.

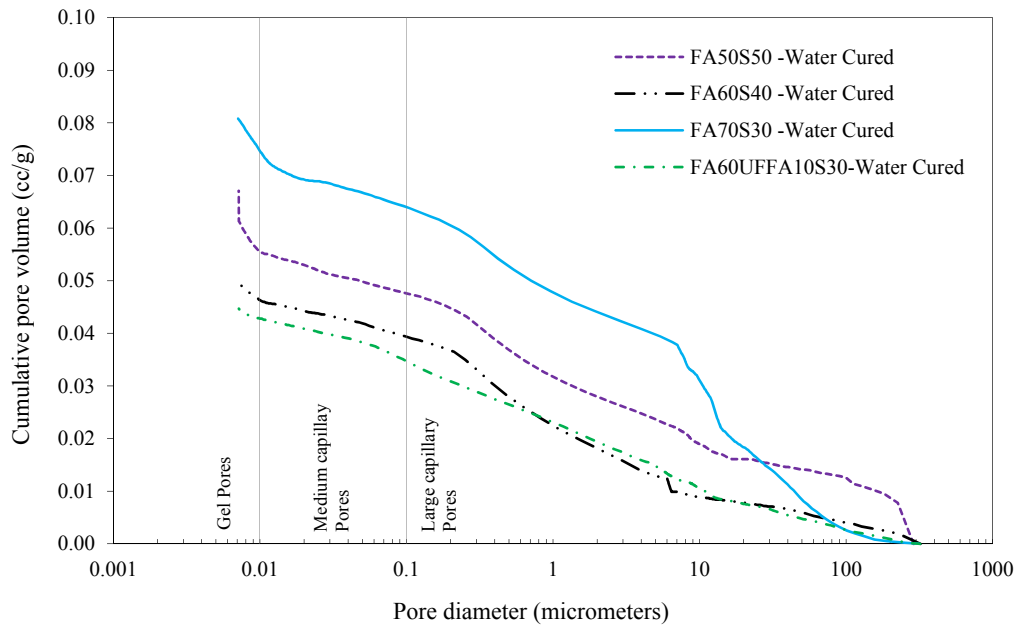
For FA mixtures containing slag, the compressive strength increased with increasing slag contents and ages in all the series. The increase in strength was higher for mortars having a sand-binder ratio of 2.00 as compared to 2.75. It is implicit that the inclusion of slag as an additional source of silica, alumina, and calcium in the geopolymer system has strongly affected the formation of binding gels. The increasing compressive strength in these matrices indicates additional reaction of the calcium elements and creation of a hybrid binder, acquiring the reaction products both from the alkali activation of slag (C-S-H, C-(A)-S-H) and FA (N-A-S-H, N-(C)-A-S-H) (Ismail et al. 2014). While, the increased compressive strength in M2 and M7 mixtures in relation to M3 and M8 series can be attributed to the higher dissolution rate of UFFA particles, which had a much smaller median particle size as compared to the unprocessed, low calcium FA. Similar findings were reported in the literature (Kumar et al., 2007; Temuujin et al., 2009), where increased reactivity of the binder improved the properties of geopolymer binder. The effect has also been observed in high-calcium FA geopolymer (Chindapasirt et al., 2011).

3.5.3 Porosity Measurement

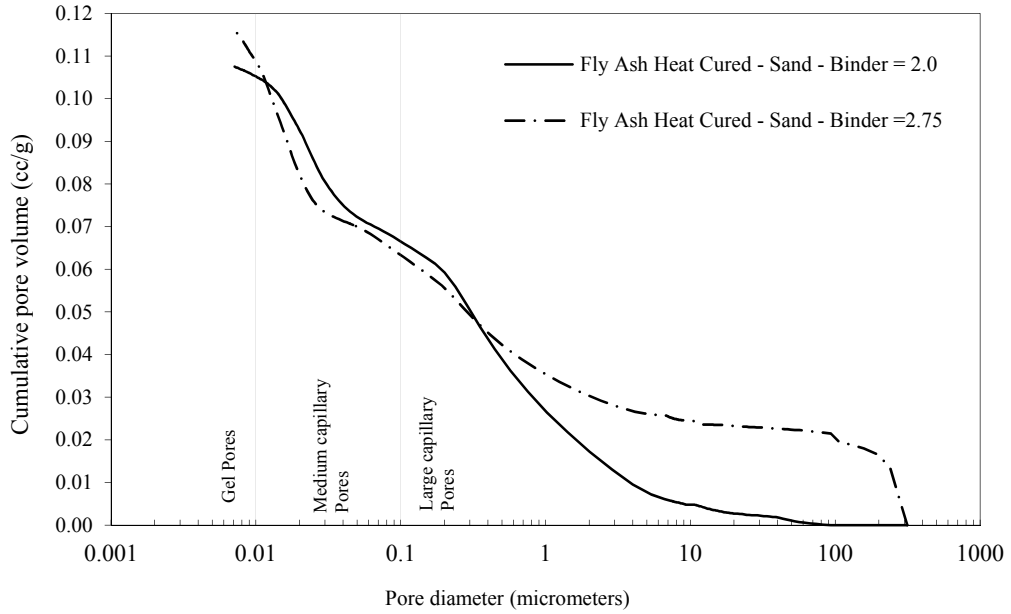
To investigate further into the reasoning for compressive strength variation in different geopolymer materials, small broken pieces (10mm×10mm×5mm approx.) from the center of 28 days compression tested specimens (stored in ambient air, water or heat cured) were analyzed through mercury intrusion porosimetry (MIP) to evaluate the total porosity and pore size distribution in mortar samples. The MIP results show the distribution of cumulative pore volume and pore diameter in the range of 0.01 to 100 μm , whereas the pores can be classified as large capillary pores (10 to 0.05 μm), medium capillary pores (0.05 to 0.01 μm) or gel pores (< 0.01 μm) (Zhang and Islam, 2012). The curves presented in Figure 3-4 evidence the existence of three modes and it can be seen that the heat cured FA binder compositions (see Figure 3-4(c)) were more porous, had coarser pore size distribution as compared to the ambient cured hybrid FA-slag or FA-UFFA-slag geopolymer materials. The total porosity in M1 and M6 mixtures was found to be 22% and 24% respectively with a cumulative pore volume of around 0.11 cc/g (sand-binder = 2.0) and 0.12 cc/g (sand-binder = 2.75), in comparison to the mortar mixtures having a sand-binder ratio of 1.60 (Khan et al., 2016), which had a cumulative porosity of 18.0%. This was no surprise as slag is more reactive in an alkaline medium, whereas FA needs to react to a much large extent before it can significantly influence the total pore volume.



(a)



(b)



(c)

Figure 3-4 Cumulative intrusion curves for geopolymer samples cured in (a) ambient air (b) ambient water, and (c) heat curing conditions.

Table 3-3 Total pore volume and porosity values measured for air and water cured geopolymer samples

Mixture ID	Sample Designation	Type of curing condition	Sand-Binder ratio	Porosity (%)	Total pore volume (cc/gm)
After Khan et al. 2016	FA100	Heat	1.60	18.09	0.0883
M1			2.00	22.25	0.1075
M6			2.75	24.03	0.1161
M2	FA60UFFA10S30	Air	2.00	9.62	0.0447
		Water		9.08	0.0447
M3	FA70S30	Air		14.82	0.0705
		Water		17.30	0.0808
M4	FA60S40	Air		7.93	0.0359
		Water		10.54	0.0496
M5	FA50S50	Air		8.17	0.0391
		Water		14.52	0.0671

Moreover, Figure 3-4(a) and Figure 3-4(b) show a porosity comparison between the air and water cured geopolymer samples for different binder combinations containing a sand-binder ratio of 2.00. It can be seen (see Table 3-3) that water cured geopolymer samples possessed

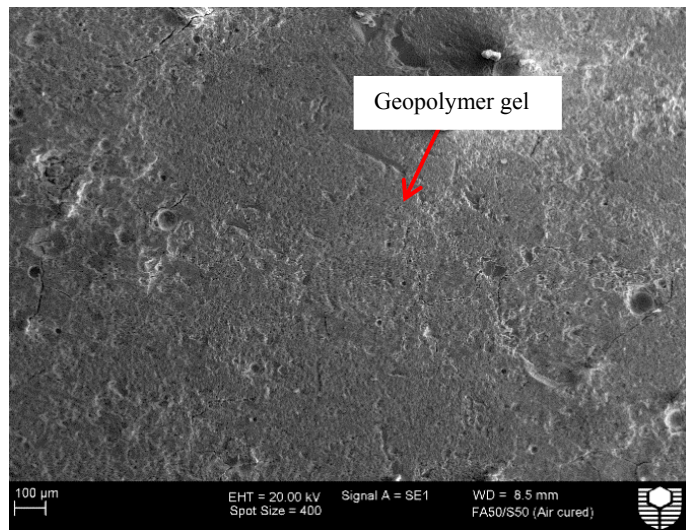
higher porosity in comparison to the air cured counterparts, such that the total porosity in M3, M4, and M5 binder compositions increased to 17.30%, 10.54%, and 14.52%, respectively in water from 14.82%, 7.93%, and 8.17% for the other group cured in ambient air environment. The higher porosity measurements of water cured samples indicate the presence of large permeable voids or micro-cracks within these samples, where the increased porosity is in good agreement with the decrease of compressive strength for all the series. It is well established for ceramics that mechanical strength decreases with higher porosity (Subaer, 2004). In addition, by observing the cumulative intrusion curves for geopolymer mixtures containing UFFA, it can be recognized that only a marginal difference in terms of pore size distributions and porosity for air and water cured samples existed; yet a slight reduction in the 28 days compressive strength was also seen for samples cured in water medium from this mix design.

It can be further established from the results that for particular mix design, apart from the difference in porosity values seen under the influence of curing conditions, the results show increasing pore refinement in FA only geopolymers with the inclusion of additives such as UFFA or slag. The observation is valid for both air and water cured geopolymer samples. By comparing the data for heat cured FA geopolymers with those of hybrid binders cured in ambient air, it can be seen that the total porosity of FA geopolymers was reduced to 14.82% with the addition of 30% slag in M1 mixture. Similarly, the porosity of M3 slag blended geopolymer was further reduced to 9.62% with the inclusion 10% UFFA in M2 series, in fact, the total porosity of M3 matrix was approximately 54% higher than the corresponding M2 mortar samples. It should be noted the decrease in porosity for M2 samples is consistent with its strength findings, where the inclusion of UFFA is believed to have resulted in the formation of additional aluminosilicate gel that eventually reduced the total pore volume and pore size by filling up the larger pores. This reduced pore pattern for UFFA based geopolymer samples has also been stated in another investigation (Deb and Sarker, 2016). The lowest porosity measurements were observed for M4 (FA60S40) and M5 (FA50S50) mixtures, i.e., around 7.93% and 8.17% respectively. It can be concluded (see Figure 3-4) that the inclusion of slag at higher proportions was significantly effective in reducing the medium and large sized capillary pores in FA geopolymers, which generated a more compact microstructure and hence improved the strength properties.

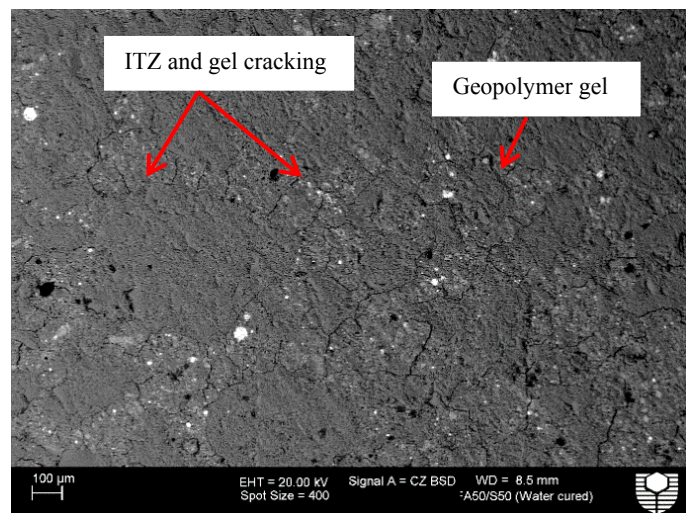
3.5.4 Scanning electron Microscopy (SEM) and Energy dispersive X-ray Spectroscopy (EDS) Analysis

The SEM images of M4 (FA60S40) and M5 (FA50S50) hardened geopolymer samples cured in the ambient air and water medium are shown in Figures 3-5 and 3-6, while Figure 3-7 presents magnified images of the gel structure for M4 mixture. As can be seen in Figures 3-5

(a) and 3-6 (a) that the interfaces between the aggregates and the binding gels were relatively smooth and mostly crack free, whereas a significant number of micro-cracks were noticed not only at the aggregates-gel interfaces but also within the binding gels for water cured samples. It is believed that the increased micro-cracking in water cured samples was mainly related to the formation of unstable gel phases during the drying mechanism of slag activated precursors, which can reduce the particle to particle bond and introduce many breaks throughout the gel structure (Collins and Sanjayan, 2001). These micro-cracks were believed to progress further and became continuous in the presence of water after the initial air curing period. The argument is consistent with the results reported by Wardhono et al. (2015b).

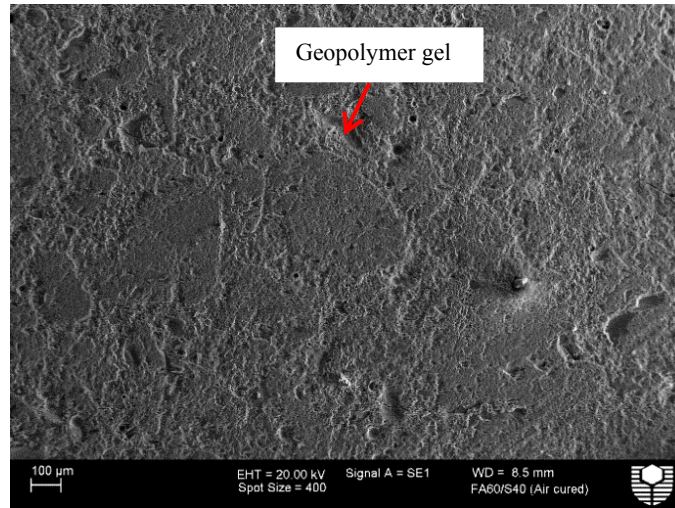


(a)

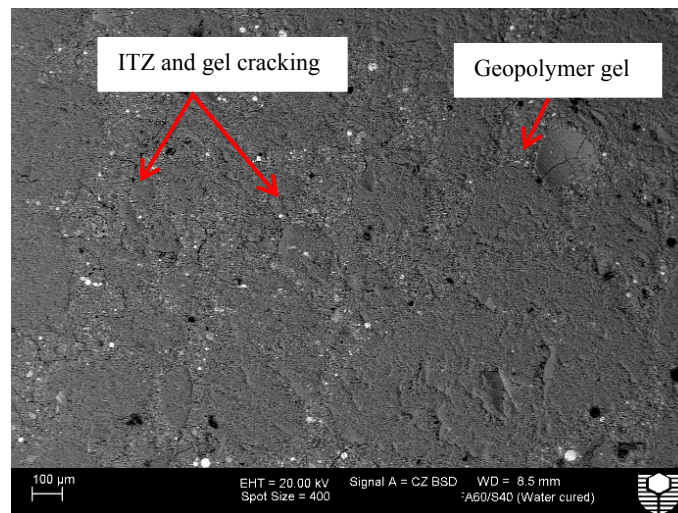


(b)

Figure 3-5 SEM images of M5 (FA50S50) geopolymer samples cured in (a) ambient air (b) ambient water.



(a)

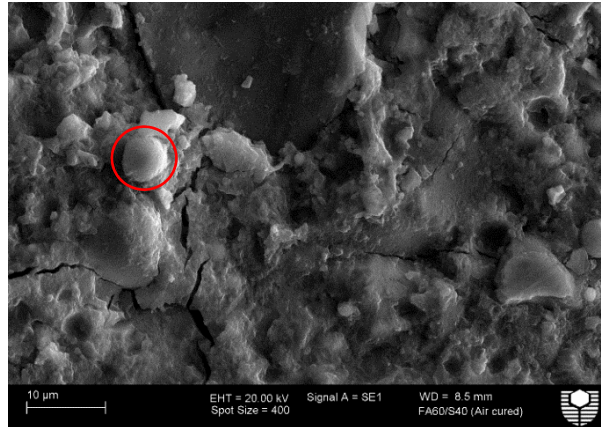


(b)

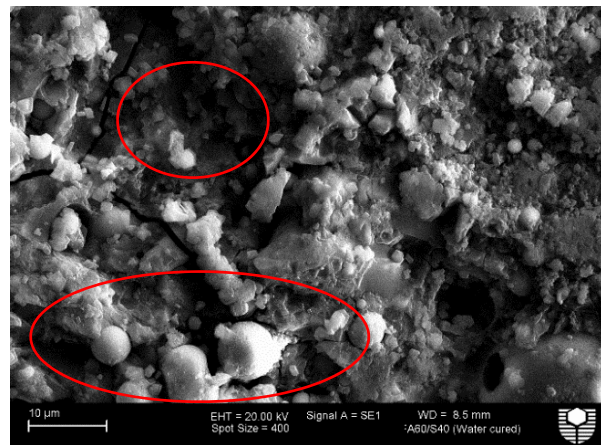
Figure 3-6 SEM images of M4 (FA60S40) geopolymer samples cured in (a) ambient air (b) ambient water.

Moreover, by observing the magnified images of geopolymers gels for the M4 mixture, it can be seen that the combined activation of FA and slag in air medium showed a reasonably homogeneous formation of gel matrix with very few unreacted or partially reacted FA particles. In contrast, the SEM image of water cured samples presented a somewhat loose microstructure, where a large number of unreacted FA particles and pores can be seen embedded in the gel structure. It is admitted that the outer layer of FA particles is very dense and stable, therefore for the formation of N-A-S-H products, the firm silica-alumina glassy chain present on the surface of FA glassy beads must be disintegrated. However, the existence of a relatively large number of spherically shaped particles in the micrograph indicates reduced activation of the FA in water media. The observed microstructure for water cured samples

provides a qualitative representation of the extent of geopolymer reaction that has occurred in the water medium and establishes the understanding for the reduced strength properties.



(a)



(b)

Figure 3-7 Higher magnification SEM images of M4 (FA60S40) geopolymer gels (sand-binder = 2.0) (a) air cured (b) water cured.

On the other hand, Figures 3-8 and 3-9 show a microstructural comparison between the water cured M2 (FA60UFFA10S30) and M3 (FA70S30) hybrid binder compositions. It can be seen that (see Figure 3-8) most of the FA or UFFA particles in M2 mixture appeared to have dissolved in the alkaline medium and the microstructure itself has a compact appearance. The denser microstructure specifies the formation of increased reaction products, which is apparently in good agreement with the porosity and strength results. A similar FA-slag content, in the absence of UFFA, presented a slightly porous and heterogeneous microstructure as shown in Figure 3-9, identical to the water cured image shown earlier for the M4 mix (FA60S40). It appears that the presence of UFFA in the mix design played a

distinctive role in the formation of additional aluminosilicate gels, such that the compressive strength of M2 binder composition was 71% higher as compared to M3 mixture in the water curing medium and was only 9% lower to its air cured counterpart.

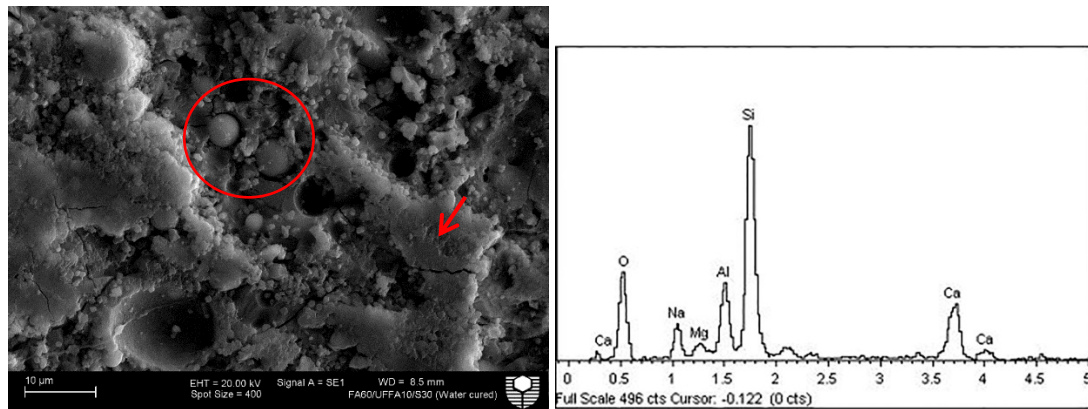


Figure 3-8 SEM/EDS spectra of M2 (FA60UFFA10S30) water cured geopolymer samples

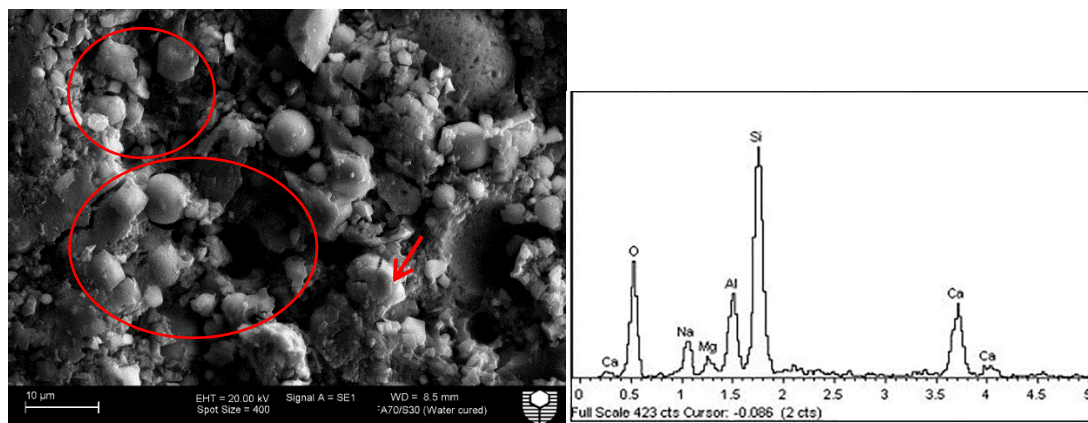


Figure 3-9 SEM/EDS spectra of M3 (FA70S30) water cured geopolymer samples.

Moreover, by comparing the EDX spectrums at the indicated location for both binary (M3) and ternary (M2) blended binder compositions, it can be seen that the reaction products contain a significant number of calcium elements together with the silicon, aluminum, and oxygen elements; which evidence the co-formation of calcium silicate hydrate or calcium aluminum silicate hydrate gel (C-S-H/C-A-S-H) in conjunction with the geopolymers products, i.e., sodium aluminum-silicate hydrate gel (zeolite gel, N-A-S-H). However, the use of water curing medium appeared little useful for dissolution of FA at ambient temperature.

Based on the strength development pattern for different mix designs recognized in this study, the co-activation of FA with slag in air and water curing medium suggests two possible

reaction mechanisms. From Figure 3-2(a) it can be concluded that perhaps the polymerization reaction of FA and the hydration reaction of slag occurred simultaneously, meaning by slag reaction with the alkaline activator promoted the FA activation at ambient temperature. For water cured specimens, reduced availability of the alkali ions (N^+) made the geopolymer system extremely sensitive to the choice of curing environment and is consistent with the observed morphology. On the other hand, Figure 3-2(b) highlights an outside possibility of these two reactions happening independently of each other, i.e., at first slag reacted with the chemical activator to form a matrix around the FA-UFFA particles, which were gradually activated and filled up the larger sized pores to improve the compressive strength. This argument is though little supported can still be observed by relating the strength development mechanisms of M2, M3, M7, and M8 mixtures.

3.6 Conclusions

The effects of curing conditions and sand-binder ratios were investigated on a high strength geopolymer material having different combinations of low calcium FA, slag, and UFFA. The compressive strength development from 3 to 28 days, pore size distribution and microstructural characteristics were studied in ambient air and water curing medium. The main conclusions drawn from this study are:

- 1) The heat cured FA only geopolymer exhibited high early age strength, with zero increase in the 28 days compressive strength measurement.
- 2) The hybrid FA-slag blends cured in ambient air environment realized higher compressive strength than the water cured counterparts. The highest compressive strength was measured for an equal-parts FA-slag geopolymer material exhibiting 103 MPa at 28 days of ambient air curing in comparison to 80 MPa observed for a similar mix design in water media.
- 3) The samples cured in water medium showed higher porosity or change in micro-crack density as compared to their equivalents cured in an air wrapped environment, such that the total porosity of M3, M4, and M5 cured in water media were 17%, 33%, and 78% higher than air cured specimens.
- 4) Moreover, the effective porosity of mortar samples was observed to reduce in both the curing environments, with the addition of slag and UFFA in the FA only geopolymer.
- 5) For a given hybrid-binder combination, a proportionate decrease in the strength properties was observed with the inclusion of higher fine aggregates content, such that the mix designs enclosing a sand-binder ratio of 2.00 displayed more sensitivity to the curing effect.

- 6) The 28-day compressive strength of FA-slag blended geopolymers was significantly modified by improving the reactivity of FA binding material, such that the compressive strength of FA70S30 blend was 48% and 71% higher in the air and water curing medium respectively, with the presence of 10% UFFA in the mix design.
- 7) The SEM and EDX spectra results for air and water cured FA-slag geopolymers agree well with the observed mechanical behaviour. An additional crystalline CSH and/or C-A-S-H gel was formed in conjunction with the amorphous aluminosilicate N-A-S-H gel, which improved the compressive strength of geopolymers with age.

3.7 References

- Ash Development Association of Australia. (2016). Annual Membership Survey Results, January – December 2015.
http://www.adaa.asn.au/uploads/default/files/adaa_mship_report_20162.pdf (Oct 20, 2016).
- ASTM. (2012a). Standard specification for coal fly ash and raw or calcined natural pozzolan for use in concrete. *ASTM C618-12a*, Philadelphia.
- ASTM. (2013a). Standard test method for compressive strength of hydraulic cement mortars, (using 50-mm cube specimens). *ASTM C109-13*, Philadelphia.
- ASTM. (2013b). Standard test method for flow of hydraulic cement mortar. *ASTM C1437-13*, Philadelphia.
- ASTM. (2015). Standard test method for relative density (Specific Gravity) and absorption of fine aggregate. *ASTM C128-15*, Philadelphia.
- Atiş, C. D., Görür, E. B., Karahan, O., Bilim, C., İlkentapar, S., & Luga, E. (2015). Very high strength (120 MPa) class F fly ash geopolymer mortar activated at different NaOH amount, heat curing temperature and heat curing duration. *Construction and Building Materials*, *96*, 673-678.
- Bakharev, T. (2006). Thermal behaviour of geopolymers prepared using class F fly ash and elevated temperature curing. *Cement and Concrete Research*, *36*(6), 1134-1147.
- Bernal, S. A., Rodríguez, E. D., Mejía de Gutiérrez, R., & Provis, J. L. (2012). Performance of alkali-activated slag mortars exposed to acids. *Journal of Sustainable Cement-Based Materials*, *1*(3), 138-151.
- Chindapasirt, P., Chareerat, T., Hatanaka, S., & Cao, T. (2011). High-Strength Geopolymer Using Fine High-Calcium Fly Ash. *Journal of Materials in Civil Engineering*, *23*(3), 264-270.
- Collins, F., & Sanjayan, J. G. (2001). Microcracking and strength development of alkali activated slag concrete. *Cement and Concrete Composites*, *23*(4-5), 345-352.
- Davidovits, J. (1988). *Soft mineralogy and geopolymers. Paper presented at the Proceedings 1st International Conference on Geopolymers*, Volume. 1.
- Davidovits, J. (1994). High-alkali cements for 21st century concretes. *Special Publication*, *144*, 383-398.

- Deb, P. S., Nath, P., & Sarker, P. K. (2014). The effects of ground granulated blast-furnace slag blending with fly ash and activator content on the workability and strength properties of geopolymer concrete cured at ambient temperature. *Materials & Design*, 62, 32-39.
- Deb, P. S., & Sarker, P. K. (2016). Effects of Ultrafine Fly Ash on Setting, Strength, and Porosity of Geopolymers Cured at Room Temperature. *Journal of Materials in Civil Engineering*, 06016021.
- Fernández-Jiménez, A., Palomo, A., & Criado, M. (2005). Microstructure development of alkali-activated fly ash cement: a descriptive model. *Cement and Concrete Research*, 35(6), 1204-1209.
- Giasuddin, H. M., Sanjayan, J. G., & Ranjith, P. G. (2013). Strength of geopolymer cured in saline water in ambient conditions. *Fuel*, 107, 34-39.
- Ismail, I., Bernal, S. A., Provis, J. L., San Nicolas, R., Hamdan, S., & van Deventer, J. S. J. (2014). Modification of phase evolution in alkali-activated blast furnace slag by the incorporation of fly ash. *Cement and Concrete Composites*, 45, 125-135.
- Khan, M. Z. N., Shaikh, F. U. A., Hao, Y., & Hao, H. (2016). Synthesis of high strength ambient cured geopolymer composite by using low calcium fly ash. *Construction and Building Materials*, 125, 809-820.
- Kumar, S., Kumar, R., Alex, T. C., Bandopadhyay, A., & Mehrotra, S. P. (2007). Influence of reactivity of fly ash on geopolymerisation. *Advances in Applied Ceramics*, 106(3), 120-127.
- Kutti, T., & Malinowski, R. (1982). Influence of the Curing Conditions on the Flexural Strength of Alkali Activated Blastfurnace Slag Mortar. *Nordic Concrete Research*(1).
- Lee, W. K. W., & van Deventer, J. S. J. (2002). The effects of inorganic salt contamination on the strength and durability of geopolymers. *Colloids and Surfaces A: Physicochemical and Engineering Aspects*, 211(2-3), 115-126.
- Lizcano, M., Gonzalez, A., Basu, S., Lozano, K., & Radovic, M. (2012). Effects of Water Content and Chemical Composition on Structural Properties of Alkaline Activated Metakaolin-Based Geopolymers. *Journal of the American Ceramic Society*, 95(7), 2169-2177.
- Luo, X., Xu, J., Bai, E., & Li, W. (2012). Systematic study on the basic characteristics of alkali-activated slag-fly ash cementitious material system. *Construction and Building Materials*, 29, 482-486.
- Mustafa Al Bakri, A., Kamarudin, H., Bnhussain, M., Rafiza, A., & Zarina, Y. (2012). Effect of $\text{Na}_2\text{SiO}_3/\text{NaOH}$ Ratios and NaOH Molarities on Compressive Strength of Fly-Ash-Based Geopolymer. *ACI Materials Journal*, 109(5).
- Nath, P., & Sarker, P. K. (2015). Use of OPC to improve setting and early strength properties of low calcium fly ash geopolymer concrete cured at room temperature. *Cement and Concrete Composites*, 55(0), 205-214.
- Nematollahi, B., Sanjayan, J., & Shaikh, F. U. A. (2015). Synthesis of heat and ambient cured one-part geopolymer mixes with different grades of sodium silicate. *Ceramics International*, 41(4), 5696-5704.

- Olivia, M., & Nikraz, H. (2012). Properties of fly ash geopolymer concrete designed by Taguchi method. *Materials & Design*, 36, 191-198.
- Pangdaeng, S., Phoo-ngernkham, T., Sata, V., & Chindapasirt, P. (2014). Influence of curing conditions on properties of high calcium fly ash geopolymer containing Portland cement as additive. *Materials & Design*, 53(0), 269-274.
- Phoo-ngernkham, T., Maegawa, A., Mishima, N., Hatanaka, S., & Chindapasirt, P. (2015). Effects of sodium hydroxide and sodium silicate solutions on compressive and shear bond strengths of FA–GBFS geopolymer. *Construction and Building Materials*, 91, 1-8.
- Phoo-ngernkham, T., Sata, V., Hanjitsuwan, S., Ridtirud, C., Hatanaka, S., & Chindapasirt, P. (2016). Compressive strength, Bending and Fracture Characteristics of High Calcium Fly Ash Geopolymer Mortar Containing Portland Cement Cured at Ambient Temperature. *Arabian Journal for Science and Engineering*, 41(4), 1263-1271.
- Puertas, F., Martínez-Ramírez, S., Alonso, S., & Vázquez, T. (2000). Alkali-activated fly ash/slag cements: Strength behaviour and hydration products. *Cement and Concrete Research*, 30(10), 1625-1632.
- Puertas, F., Palacios, M., Manzano, H., Dolado, J. S., Rico, A., & Rodríguez, J. (2011). A model for the C-A-S-H gel formed in alkali-activated slag cements. *Journal of the European Ceramic Society*, 31(12), 2043-2056.
- Qureshi, M. N., & Ghosh, S. (2014). Effect of Silicate Content on the Properties of Alkali-Activated Blast Furnace Slag Paste. *Arabian Journal for Science and Engineering*, 39(8), 5905-5916.
- Rashad, A. M. (2014). A comprehensive overview about the influence of different admixtures and additives on the properties of alkali-activated fly ash. *Materials & Design*, 53(0), 1005-1025.
- Ren, W., Xu, J., Liu, J., & Su, H. (2015). Dynamic mechanical properties of geopolymer concrete after water immersion. *Ceramics International*, 41(9, Part B), 11852-11860.
- Sarker, P. K., Haque, R., & Ramgolam, K. V. (2013). Fracture behaviour of heat cured fly ash based geopolymer concrete. *Materials & Design*, 44, 580-586.
- Shaikh, F. U. A., & Supit, S. W. M. (2014). Mechanical and durability properties of high volume fly ash (HVFA) concrete containing calcium carbonate (CaCO₃) nanoparticles. *Construction and Building Materials*, 70(0), 309-321.
- Subaer. (2004). *Influence of aggregate on the microstructure of geopolymer*. Curtin University of Technology.
- Talling B. (1989). Effect of curing conditions on alkali-activated slags. *Proceedings of the Third International Conference on Fly Ash, Silica Fume, Slag, and Natural Pozzolans in Concrete*, Trondheim, Norway. ACI SP-114, (2); p.1485-500.
- Temuujin, J., van Riessen, A., & Williams, R. (2009). Influence of calcium compounds on the mechanical properties of fly ash geopolymer pastes. *Journal of Hazardous Materials*, 167(1–3), 82-88.
- van Riessen, A., & Chen-Tan, N. (2013). Beneficiation of Collie fly ash for synthesis of geopolymer Part 2 – Geopolymers. *Fuel*, 111, 829-835.

Wallah, S., & Rangan, B. V. (2006). Low-calcium fly ash-based geopolymer concrete: Long-term properties.

Wardhono, A., Law, D. W., & Molyneaux, T. C. (2015a). Long term performance of alkali activated slag concrete. *Journal of Advanced Concrete Technology*, 13(3), 187-192.

Wardhono, A., Law, D. W., & Strano, A. (2015b). The Strength of Alkali-activated Slag/fly Ash Mortar Blends at Ambient Temperature. *Procedia Engineering*, 125, 650-656.

Zhang, M.-H., & Islam, J. (2012). Use of nano-silica to reduce setting time and increase early strength of concretes with high volumes of fly ash or slag. *Construction and Building Materials*, 29(0), 573-580.

CHAPTER 4 MECHANICAL PROPERTIES OF AMBIENT CURED HIGH STRENGTH HYBRID STEEL AND SYNTHETIC FIBERS REINFORCED GEOPOLYMER COMPOSITES

4.1 Abstract

Ambient cured geopolymer offers significant promise to the construction world as a possible alternative to ordinary Portland cement (OPC). However, as a member of the ceramic family, geopolymers exhibit extremely brittle behaviour. The inclusion of short discrete fibers is an effective way to enhance their ductility. In this research, a series of fiber combinations and volume fractions between steel fibers with end-hooked or spiraled and synthetic fibers (made of high strength polyethylene (HSPE)) were incorporated in a high strength ambient cured geopolymer matrix. The performance of synthesized geopolymer composites was compared in terms of fresh and hardened state properties, such as workability, uniaxial compressive strength, modulus of elasticity, Poisson's ratio, flexural tensile strength, energy absorption capacity, and post-peak residual strength, etc. The interfacial bond between the spiral steel fiber and the geopolymer matrix as well as fiber distribution in the composites were assessed through individual fiber-pull out tests and physical examination of the cast samples, respectively. The test results show that the addition of fibers significantly improved the load carrying capacity of the composites under flexure load, i.e., increased from 3.89 MPa to 11.30 MPa together with an improved behaviour in compression. In general, all fiber reinforced composites displayed a stable deflection hardening response and multiple-cracking failure mode. Moreover, among composites with different fiber volume fractions, the composite having 1.60% steel+0.40% HSPE showed the highest ultimate flexure strength, correspondingly the highest energy absorption capacity. The individual fiber pull-out test curves ascertained a strong bonding between the geopolymer mortar and spiral-steel fiber.

4.2 Introduction

Concrete is the most widely used man-made construction material on earth. However, an increased emission of carbon dioxide (CO₂) into the atmosphere has become a serious issue, where cement manufacturing process is professed to generate 5-7% of the total CO₂ emissions and contribute massively to global warming (Huntzinger and Eatmon, 2009). To this end, different approaches have been considered to moderate its negative environmental impacts; such as, reduced consumption of energy in clinker production (Madlool et al., 2011), higher

volume inclusion of supplementary cementitious materials (SCMs) in the concrete (Shaikh and Supit, 2015) and discovering other binders as a possible alternative to ordinary Portland cement (OPC) (Singh et al., 2015). Based on their low manufacturing cost, improved durability against chemical attacks, high early-age strength, and increased environmental sustainability, aluminosilicate inorganic polymers (IPs) or more commonly “Geopolymers” (Shi et al., 2011) have gained significant popularity and displayed a high potential to be used in the construction industry (Davidovits, 1988; Davidovits, 1994). These IPs are formed through a series of distinct reactions between the aluminosilicate sources, mostly by-products source materials (e.g., fly ash, slag, rice husk ash, etc.) and unified mixtures of sodium silicate (Na_2SiO_3) and sodium hydroxide (NaOH) alkali activators (Hardjito et al., 2004; Sumajouw et al., 2007).

Regardless of these superior characteristics, geopolymer materials show very little resistance to cracking due to their extremely brittle, ceramics-like nature. It is believed that geopolymer cement exhibits much lower fracture energy and strain capacities in mode-I type failure as compared to the OPC, mainly due to an intrinsic difference in the microstructure of their hydrated gels and the crack propagation mechanism around the unreacted fly ash particles (Pan et al., 2011). However, among different ways to improve the brittleness of geopolymer material, such as, by using an emulsion of polymers (Xu and Van Deventer, 2000) or incorporating epoxy resins and polysiloxanes into the inorganic matrix as discussed by Roviello et al. (2015), an effective method to improve the flexural and tensile strength of brittle materials for their application in the construction industry is through short fiber inclusion (Bernal et al., 2010). The earliest attempt in this direction for geopolymers was made by Davidovits (1991), who synthesized different fiber reinforced molding tools and patterns for their use in the plastics processing industry. This was further extended by other researchers, utilizing different types of fibers, such as carbon and glass (Natali et al., 2011), polyvinyl alcohol (PVA) (Yunsheng et al., 2008; Natali et al., 2011; Chen et al., 2013; Nematollahi et al., 2014), polypropylene (PP) (Ranjbar et al., 2016), polyethylene (PE) (Ahmed and Ronnie, 2017), basalt fibers (Dylmar, 2005), organic fibers like cotton, flax, etc. (Alomayri et al., 2013; Assaedi et al., 2016) and steel fibers (Ng et al., 2013; Ambily et al., 2014; Ganesan et al., 2015; Ranjbar et al., 2016; Gao et al., 2017) in a diverse range of geopolymers containing different source materials and alkaline solutions (Shaikh, 2013).

Generally, fibers are utilized to increase the fracture toughness of a brittle matrix and assumed to have little influence on its compressive strength (Ganesan et al., 2015). Fiber debonding, pull-out, and sliding are the local mechanisms that ensure the bridging action of both micro and macro cracks within the matrix and increase the energy demand for further crack propagation. However, the extent of improvement in the mechanical deformation capability

in any composite depends primarily on the fiber properties, such as its geometry or stiffness, etc.; fibers with inert surfaces can result in interface debonding failure of the composites (Shaikh, 2013). Similarly, previous studies show that synthetic fibers (e.g., PVA, PE, PP) exhibit better post-crack strain-hardening behaviour in comparison to the steel fibers, yet they rarely have a high-enough stiffness to improve the first-crack control or the ultimate load (Chandransu and Naaman, 2003). Hence, steel fibers remain an important choice for the structural application of geopolymer binder, since they can be molded into any shape and size to enhance the frictional resistance between the fiber-matrix interfaces.

Geopolymer being a new binder, very few studies (Bernal et al., 2010; Ng et al., 2013; Shaikh, 2013; Ambily et al., 2014; Ganesan et al., 2015; Ranjbar et al., 2016; Gao et al., 2017) have reported on steel fiber reinforced geopolymer composites. A significant increase in the shear capacity of hot water cured geopolymer concrete beams was seen with the inclusion of 1.5% equal parts long hooked-end and straight steel fibers, designed without any transverse reinforcement (Ng et al., 2013). Nearly 10 to 45% increase in the flexure strength of ambient cured silica fume blended slag geopolymer was observed in different binder combinations with the inclusions of two differently sized 3% short steel fibers compared to the fiber-less matrix (Ambily et al., 2014). Despite using a high fiber volume fraction, the said composite showed poor ductility with about 1 mm of deflection capacity at the peak load. Other researchers used samples with non-standard sizes for the estimation of the modulus of rupture with relatively higher fiber volume fractions and an early age heat curing at elevated temperature (Shaikh, 2013; Ambily et al., 2014; Ranjbar et al., 2016). Some very high flexural strength and strain capacities of these composites were reported; however, it is really difficult to identify the real application for such composites. A previous investigation (Chandransu and Naaman, 2003) on OPC fiber reinforced composites with three different fiber types (i.e., Torex, PVA, and spectra) indicated a strong size effect for the smaller sized plate specimens (75 mm × 12.5 mm × 225 mm) in flexure testing. The larger or standard sized (100 mm × 100 mm × 400 mm) samples showed 80% lower flexural strength and 500% less deflection capacity at peak load compared with the smaller specimens. The widely used ASTM C1609 (2012) standard for the bending tests also appreciates this limitation in its section 5.4.

Nevertheless, as mentioned previously, the efficiency of fiber inclusion in any composite depends on the frictional resistance or bond-slip characteristics between the fiber and the matrix (Marchese and Marchese, 1993). For steel fibers reinforced composites, it has been observed that after the onset of a single crack on the tension face of a concrete element in flexure, a gradual fiber debonding or its pull-out mechanism from the matrix controls the failure process. Yet, the said feature is rarely available under impulsive loading due to the sudden debonding of fibers which prevent them from yielding or utilizing their full strength

capacity before the structural failure. Based on this premise, recently a spiral shaped-steel fiber (Xu et al., 2012) was introduced to improve the bond-slip characteristics between the fiber/matrix interfaces and enhance the composite properties beyond the quasi-static loading conditions. This fiber is capable of generating a better 3D anchorage bond due to its helical properties in comparison to the orthodox steel fibers (e.g., hooked-end, undulated, twisted or crimped), which can only provide frictional resistance along one or two directions in a 2D plane. A series of laboratory experiments have demonstrated the superiority of spiral-shaped steel fiber in resisting dynamic loads and displayed better impact resistance or high energy-absorption capacity at high strain rates than their counterparts in OPC concrete (Xu et al., 2012; Hao et al., 2016). In an experimental investigation conducted under quasi-static loading mode for structural beam elements reinforced with three different fiber combinations, i.e. 1.0% of spiral steel fibers, 1.0 % of hooked-end steel fibers and an equal part combination between these two fibers at 1.0%, it was observed that beam elements containing spiral steel fibers displayed much higher deformability in comparison to their counterpart reinforced with hooked-end steel fibers (Hao and Hao, 2017). A similar trend was reported in another study (Hao and Hao, 2016), where the presence of spiral steel fibers in the tested samples significantly increased the post-failure load carrying capacity in quasi-static split tensile tests in relation to the samples reinforced with hooked-end steel fibers, which demonstrated their effectiveness in quasi-static loading scenarios. However, to this date, the performance of spiral steel fibers in reinforcing the brittle geopolymer matrix and their efficacy in this medium is unknown.

Interestingly, a wide majority of the previous studies on geopolymer binders (Natali et al., 2011; Choi et al., 2016; Ranjbar et al., 2016) have only focused on mono-fiber reinforcement of the brittle matrix; on the other hand, hybridizing different types of fibers can offer many advantages. It is well understood that the synergistic effect created by a hybrid fiber system can surpass the performance of either fiber used alone in a particular composite. Therefore, Banthia and Gupta (2004) suggested creating a synergy between the fibers exhibiting higher strength and stiffness along with the fibers capable of providing toughness and ductility. Instead, the combination of fibers with different sizes, shapes or strengths was also reported to effectively control both the micro and macro cracks during different loading stages and improve the ductility of the composites. A relatively large number of fiber combinations between metallic and non-metallic types, such as, steel and polyethylene (PE), steel and PVA etc. have been studied in OPC based composites (Ahmed et al., 2007), where it was demonstrated that significant improvement in the ultimate strength and strain capacity was achievable by using a proper volume fraction of high and low modulus fibers. Conversely, owing to the reduced workability and highly viscous nature of the geopolymer cement, very

few studies, such as (Shaikh, 2013) tried combining short steel (1%) and PVA (1%) fibers in low calcium fly ash geopolymer and showed better post-crack strain capacity with a relatively higher first crack load. However, in (Shaikh, 2013), plate-shaped samples (20 mm × 75 mm × 300 mm) were used for the bending tests, which might significantly overestimate the structural performance of the composite due to size effect as discussed above.

Summarizing the review, most of the previously synthesized fiber reinforced geopolymer composites either were made through complicated fabrication process (Yunsheng et al., 2008), which contained high fiber volume fractions (Ambily et al., 2014; Ranjbar et al., 2016), had no fine aggregates (Nematollahi et al., 2016) or subjected to heat curing to gain sufficient strength development (Ng et al., 2013; Shaikh, 2013), thus limiting their real-time application in the construction industry and are cost prohibitive. The auxiliary limitations of different source material combination, fiber choices and the requirement of heat curing for low calcium fly ash make the task even more challenging for any new kind of fiber to be investigated with this binder. Therefore, in this research, an effort has been made to synthesize a more user-friendly high strength and ductile geopolymer composite using a new kind of spiral-shaped steel fiber in conjunction with conventional hooked-end steel and high strength polyethylene (HSPE) fibers. Furthermore, the used high strength geopolymer material is well suited for the ambient curing environment and was recently proposed (Khan et al., 2016). The maximum fiber dosage incorporated into different mixtures was up to 2% by volume. The performance of the geopolymer composites was evaluated in terms of their fresh state properties such as workability and hardened properties, i.e., uniaxial compressive strength, modulus of elasticity, Poisson's ratio, flexural tensile strength, toughness or energy absorption capacity, and post-crack residual strength. In order to assess the interfacial bond strength between the spiral steel fiber and geopolymer matrix, fiber pull-out tests were also conducted for three different embedment lengths. It should be noted that for the measurement of each mechanical property, a set of three samples was used. Besides this, the distributions of fibers in cast samples were examined via cross-sectional analysis.

4.3 Experimental Section

4.3.1 Materials and Methods

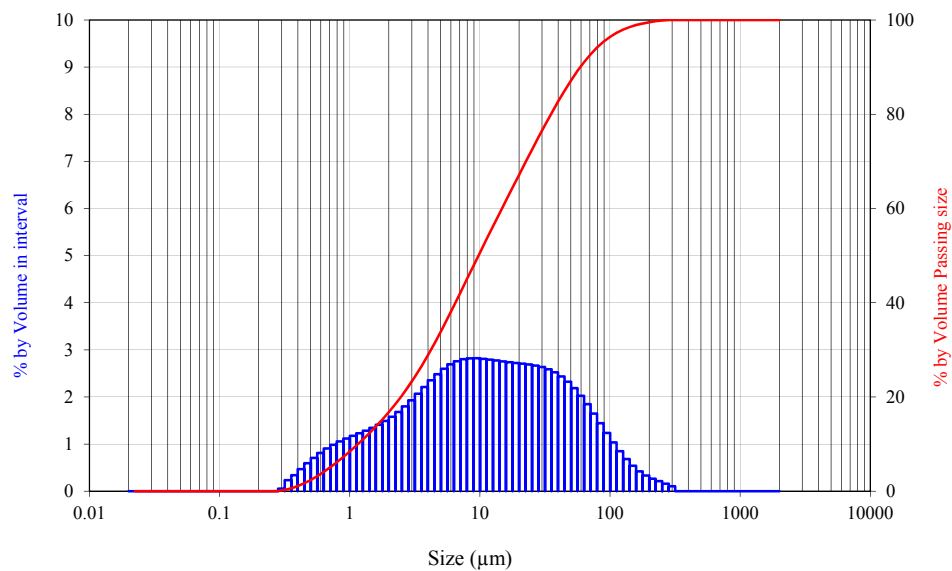
To prepare geopolymer matrix, low calcium fly ash (FA) was collected from the Gladstone Power Station in Queensland Australia to prepare the geopolymer matrix. It was classified as class F according to ASTM C618 (ASTM, 2012a), with a pozzolanic component ($\text{SiO}_2 + \text{Al}_2\text{O}_3 + \text{Fe}_2\text{O}_3$) of 89.14%. The commercially available construction grade slag was obtained from BGC cement Australia. Figure 4-1 presents the particle size distribution of the FA and

slag with median particle sizes of 9.7 and 11.5 μm , respectively. The chemical compositions of raw ingredients were determined by the X-ray fluorescence (XRF) analysis and are listed in Table 4-1. As shown, the basicity coefficient of the slag was 1.00 with hydration modulus exceeding 1.40.

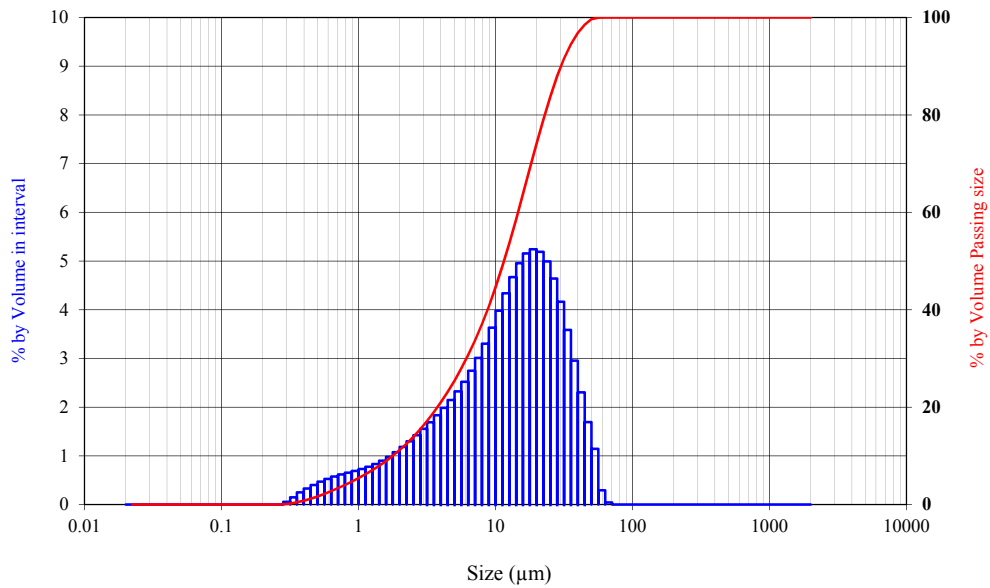
Table 4-1 Chemical compositions of FA and slag

Composition wt. (%)	FA	Slag
SiO ₂	51.1	32.5
Al ₂ O ₃	25.56	13.56
Fe ₂ O ₃	12.48	0.85
CaO	4.30	41.2
MgO	1.45	5.10
MnO	0.15	0.25
K ₂ O	0.70	0.35
Na ₂ O	0.77	0.27
P ₂ O ₅	0.885	0.03
TiO ₂	1.32	0.49
SO ₃	0.24	3.2
H ₂ O	-	-
Others	0.46	1.12
LOI*	0.57	1.11

*Loss on ignition



(a)



(b)

Figure 4-1 Particle size distribution of (a) low-calcium FA (b) slag.

The alkaline activator used in the investigation was a combination of D-grade sodium silicate (Na_2SiO_3) (specific gravity = 1.53, modulus ratio, $M_s = \text{SiO}_2/\text{Na}_2\text{O} = 2.0$; $\text{SiO}_2 = 29.4\%$, $\text{Na}_2\text{O} = 14.7\%$, $\text{H}_2\text{O} = 55.9\%$) and 12M sodium hydroxide (NaOH) solutions. Locally available silica sand having a specific gravity of 2.65, fineness modulus of 2.77 and maximum nominal size of 1.18 mm was prepared in saturated surface dry condition (SSD) according to ASTM C128 (ASTM, 2015b). The relevant properties of fibers are outlined in Table 4-2, while Figure 4-2 shows the schematic appearance and different geometrical characteristics of spiral steel fiber.

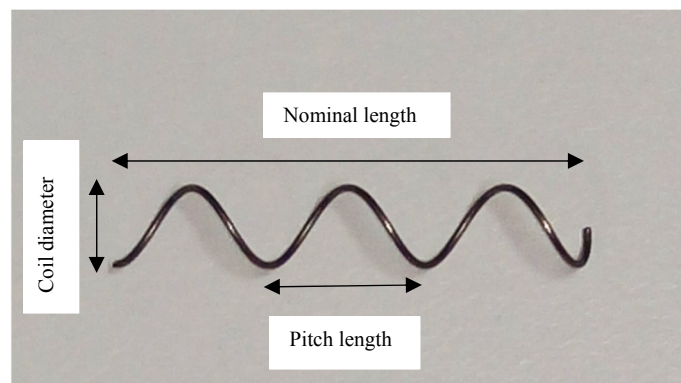


Figure 4-2 Schematic of spiral steel fiber.

Table 4-2 Properties of steel and synthetic fibers

Fiber Type	Wire diameter (mm)	Nominal length (mm)	Coil diameter (mm)	Pitch length (mm)	Tensile strength (MPa)	Modulus of Elasticity (GPa)	Density (gm/cm ³)
Spiral steel	0.55	25	6	10	1400	200	7.80
Hooked-end steel	0.30	25	-	-	2500	200	7.80
HSPE	0.012	12	-	-	3500	123	0.97

4.3.2 Preparation of Geopolymer Composites

The preparation of geopolymer composites was carried out in a 70L large size pan mixer. The alkaline solution used in the investigation was prepared by combining 12M NaOH and D-grade sodium silicate solutions at least half hour before the mixing sequence, where 97-98% pure NaOH beads were diluted in tap water at a minimum one day before casting. Table 4-3 provides the details of geopolymer mix constituent. Based on the chemical compositions of source materials given in Table 4-1 and assuming that the polymerization has occurred at 100%, the final composition of the neat geopolymer system can be expressed as $Al_2O_3 \cdot 4.20SiO_2 \cdot 1.0Na_2O \cdot 10.50H_2O$.

At first, all the dry ingredients, including sand, FA, slag were combined together and mixed for 3 minutes. The alkaline solution was then gradually added, and the mixture was allowed to homogenize for another 3-4 minutes. After that, the individual fiber combinations, as shown in Table 4-3, were added to the geopolymer mortar in small quantities with continued mixing being ensured during the entire process. In this regard, the spiral steel and hooked-end steel fibers were included through a constant sieve shaking process, while high strength polyethylene fibers were separated loosely before being included via hand in small portions. It should be noted that these fiber combinations were selected from a series of preliminary trials to ensure sufficient workability and uniformity in fresh mixes. As such an equal parts combination of the spiral and hooked-end steel fibers was found to produce the optimum result (Hao and Hao, 2017). Due care was taken primarily for the spiral steel fibers to avoid their agglomeration within the fresh mixtures.

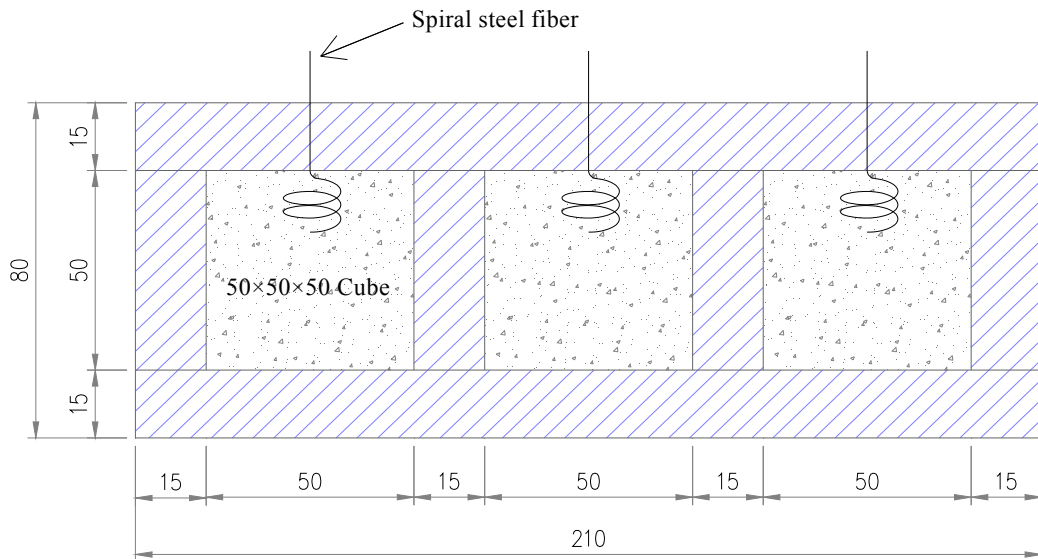
Table 4-3 Mix constituents and details of different fiber combinations used in geopolymer matrix

Composite No.	Constituent mix proportions (kg/m ³)					Fiber types (by volume %)			Total fiber volume fraction (%)
	FA	Slag	Sand	NaOH	Na ₂ SiO ₃	Spiral steel	Hooked end steel	HSPE	
G-1						-	-	-	-
G-2						0.50	0.50	-	1.00
G-3						0.75	0.75	-	1.50
G-4	412	276	1100	117.72	294.30	1.00	1.00	-	2.00
G-5						0.40	0.40	0.20	1.00
G-6						0.80	-	0.20	1.00
G-7						0.90	0.90	0.20	2.00
G-8						0.80	0.80	0.40	2.00

After measuring the workability, the mixtures were poured in three layers into 100 × 200 mm cylindrical and 100 × 100 × 400 mm flexural steel molds; adequate vibration for approximately 30 secs was provided to remove the entrapped air bubbles and prevent fiber protrusion from the finished surfaces. Subsequently, the cast molds were covered with cling wrapping sheet and were stored in an ambient environment for 24 hours at a temperature of 22 ± 2°C and relative humidity of 50 ± 5%. Later, the dismantled samples were also stored in the same environment, in an unwrapped condition until the testing day. It should be noted that the chosen atmosphere meets the criteria laid by the International Organization for Standardization for curing of materials well known to be sensitive to the variation in the temperature or relative humidity (Feng et al., 2014). Moreover, for wide application of the geopolymer binder, the used parameters are not far from the ambient conditions prevailing in many parts of the world, most time of the year.

For fiber pull-out tests, the plain geopolymer matrix was prepared in a 10L Hobart mixer. The mortar was poured into a 50 × 50 × 50 mm³ wooden molds similar to the ones utilized by ASTM C109 (ASTM, 2013a) as shown in Figure 4-3, such that the spiral steel fibers with desired embedment lengths were inserted axially through small holes present in the center of one of the side sheets. The arrangement allowed the fibers to be locked in place without any misalignment during the pour or vibration and enabled a smooth finish to the surface from where the fibers were pulled out during the individual fiber pull-out tests. It should be noted that in the present study, pull-out tests were only performed with spiral fibers. This is because no study has been reported on the pull-out performance of spiral-shaped fibers in geopolymer

matrix yet, while the pull-out tests on hooked-end fibers have been intensively investigated and the performances are well documented. Unfortunately, the pull-out tests on HSPE fibers could not be carried out because of the limitation of the testing equipment to grip the very thin fiber.



Note: All dimensions are in mm

Figure 4-3 Schematic arrangement of casting molds for spiral fiber pull-out tests.

4.4 Test Methods

4.4.1 Workability

The flow rates of composites were established using a bronze truncated cone, having a base diameter of 100 mm and shaking table with 25 drops as per ASTM C1437 (ASTM, 2013b). Each individual mix carrying different fiber combinations was tested twice; while the slump widths were measured across four perpendicular edges of the flow table. The flow rates (F) are expressed as a percentage of the average increase in base diameter (D) divided by the original base reading (D_o) through the following Equation (4.1);

$$\text{Flow rate } (F, \%) = (D - D_o) / D_o \times 100 \quad (4.1)$$

4.4.2 Compressive Strength

For uniaxial compressive strength, following the ASTM C39 (ASTM, 2015a) a set of three identical sulphur capped samples were tested under load control using an MCC8 testing machine with an equivalent loading rate of 15MPa/min.

4.4.3 Modulus of Elasticity & Poisson's Ratio

The Young's modulus (E) and the Poisson's ratio (μ) for composites were calculated as per the procedures outlined in ASTM C469 (ASTM, 2014), as the secant modulus for a stress range from 0 to 40% of the ultimate compressive strength. The longitudinal strains were measured over a gauge length of 100 mm, with the aid of two Linear variable differential transducers (LVDTs) attached on either side of the specimens, whereas a third LVDT was mounted onto a circular ring around the circumference at mid-height of the test samples to record the circumferential extension. Subsequently, the following expressions (Equations (4.2) and (4.3)) were used to calculate the modulus of elasticity (E) and Poisson's ratio (μ) for each test sample;

$$E = (S_2 - S_1) / (\varepsilon_2 - 0.000050) \quad (4.2)$$

$$\mu = (\varepsilon_{t2} - \varepsilon_{t1}) / (\varepsilon_2 - 0.000050) \quad (4.3)$$

where E = chord modulus of elasticity, MPa

S_2 = stress corresponding to 40% of ultimate load

S_1 = stress corresponding to a longitudinal strain, ε_1 , of 50 millionths, MPa

ε_2 = longitudinal strain produced by stress S_2

μ = Poisson's ratio

ε_{t2} = transverse strain at midheight of the specimen produced by stress S_2 , and

ε_{t1} = transverse strain at midheight of the specimen produced by stress S_1

4.4.4 Flexural Strength Properties

The flexural strength properties of different composites were measured using a displacement controlled INSTRON testing machine. Where three 100 mm × 100 mm × 400 mm prismatic samples were tested in the four-point bending in accordance with ASTM C1609 (ASTM, 2012), with a net displacement increase of 0.1mm/min for the first 2 mm deflection and was

later ramped up to 0.5mm/min to save the testing time. The load and mid-span deflection of all test samples were measured with the support of an in-built machine strain gauge and load cell sensor. These deflection measurements were also compared with the readings obtained from two mechanical LVDTs attached on either side in the middle of beam specimens. It should be noted that during the tests, the samples were rotated 90° from the casting positions to eliminate the effect of cast surface on test results.

4.4.5 Fiber Pull-out Testing

The fiber pull-out tests were carried out using Lloyds testing machine. The samples were placed in a rigid hollow steel tube with a circular opening on the top, which allowed the fiber to be clamped into the upper serrated grips of the machine without any slippage. While the bottom of the tube was connected to a long threaded screw bolt, held firmly by the lower jaws of the machine. Figures 4-4(a) and (b) provide a schematic and a close-up view of the actual test set-up for the fiber pull-out tests, respectively. These tests were also conducted under displacement control with a net displacement increase of 0.5 mm/min. Similar loading rate for individual fiber pull-out tests has been used in other investigations to characterize the fiber-matrix bond characteristics (Abbas and Khan, 2016). The pull-out load vs. end-slip measurements were accomplished with the assistance of a load cell attached externally to the machine jaws assembly and an in-built machine displacement sensor.

4.4.6 Fiber Distribution in Geopolymer Composites

The steel fiber distribution in geopolymer composites was examined by dissecting some of the cast flexural beam specimens into four equal pieces, using an angle grinder fitted with a diamond blade after 28 days of curing. The said investigation allowed a more detailed review onto the level of quality control exercised while mixing/pour in different mixtures and the distribution of discrete fibers in the hardened samples after setting.

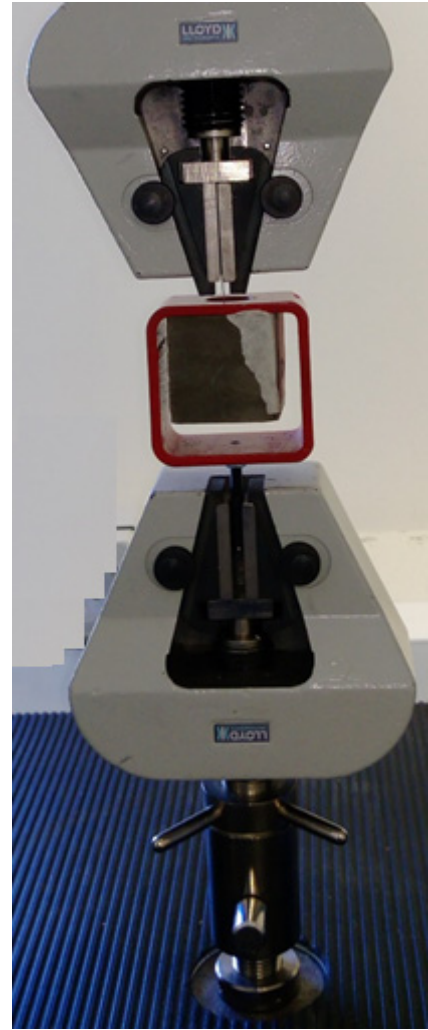
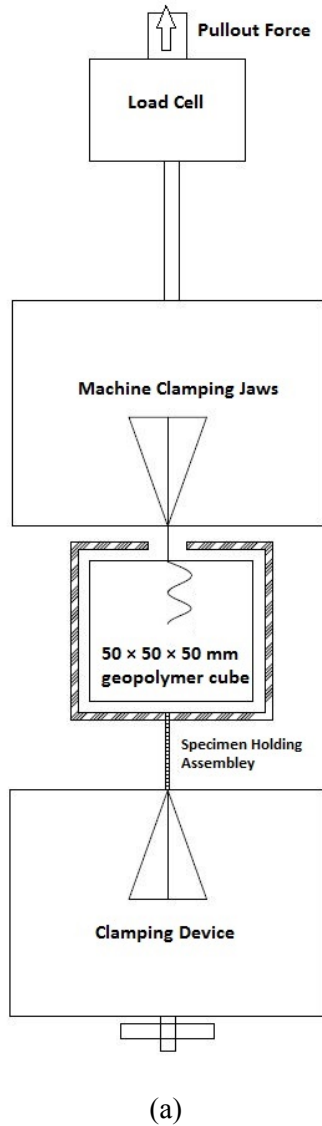


Figure 4-4 (a) Schematic diagram and (b) a close-up for the actual setup for fiber pull-out test specimens.

4.5 Results and Discussion

4.5.1 Flow Measurement

The effect of different fiber inclusions on the workability of fresh geopolymer composites is compared in Figure 4-5. As can be seen, the fresh state properties of geopolymer mortar change significantly with the addition of fibers. The highest flow diameter (145 mm) was measured for the G-1 series, which was self-consolidating in nature. It can be established that as the volume fraction of steel fibers increased, the flow diameter decreased respectively. Among different fiber combinations used to reinforce the brittle matrix, the percentage reduction in the workability for G-2 composites containing 1.0 % of steel fibers was minimum,

whereas, the workability values of G-3 and G-4 composites were 5% and 15% lower than the G-2 composites, respectively. Moreover, it should be noted that the addition of higher volume fraction of steel fibers, such as 1.5% and 2.0% in G-3 and G-4 series, respectively produced slightly harsh mixes in the fresh state under the static mode. Though, the stiffening effect of fibers on mortar was observed to disappear, upon dropping the flow table 25 times in 15 seconds during the workability test. It can be further deduced from the graph that the workability of geopolymer composites was negatively impacted by the inclusion of high-strength polyethylene fibers (HSPE). The flow rate dropped to 65% for the G-8 mixture, containing relatively higher fiber volume fractions of both HSPE and spiral steel fibers. Of note, despite the reported flow loss in different batches, all mixtures were placed, vibrated and compacted with ease into their respective molds.

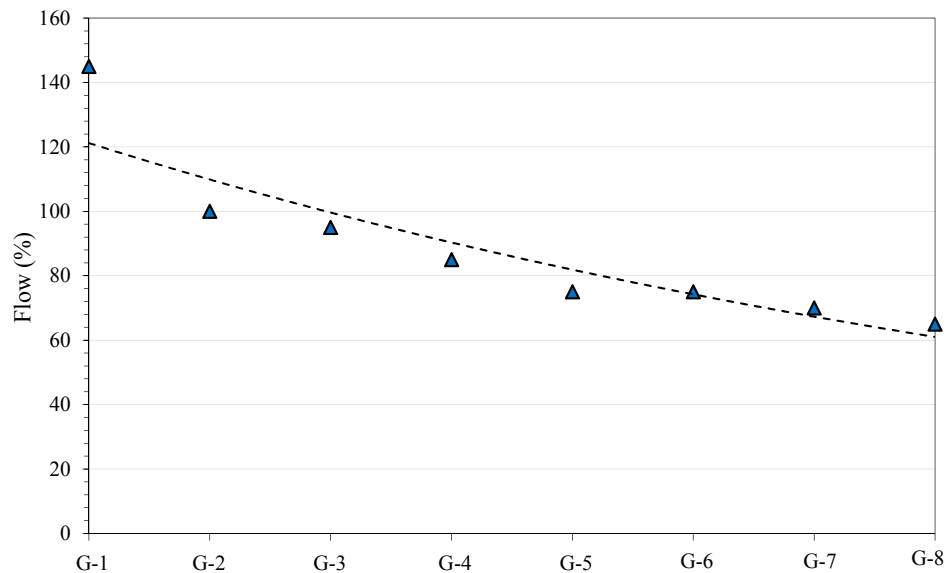


Figure 4-5 Effect of different fiber combinations on flowability of the geopolymer composites.

It is widely accepted that the loss of workability for steel fibers reinforced composites is primarily associated with the following reasons, i.e., (a) the elongated shape of steel fibers increases the cohesive forces among the fibers and the matrix due to higher surface area; (b) presence of surface deformation on steel fibers improves the anchorage between the fiber and matrix; (c) although steel fibers are hydrophilic in nature, due to their stiff nature they are believed to push apart the particles that are longer than the fiber length and tend to modify the internal granular skeleton structure to some extent (Gao et al. 2017). Considering that in the present investigation, both the hooked-end and spiral steel fibers were included in the inorganic polymeric phase, the loss of workability was primarily related to an increased surface area and the resulting increase in cohesive forces between the fiber and the matrix

which increased proportionately with the amount of hooked-end and spiral steel fibers present in the geopolymer mortar. Similar findings were observed by Gao et al. (2017), where a hybrid combination between short and long steel fibers was reported to significantly influence the fresh state properties of geopolymer composites. Moreover, the introduction of a more complex geometry to steel fibers in the form of spirals in combination with the viscous and sticky nature of geopolymer matrix is understood to have impacted further upon the workability of fresh steel fiber reinforced geopolymer composites by improving the anchorage between the fiber and the matrix.

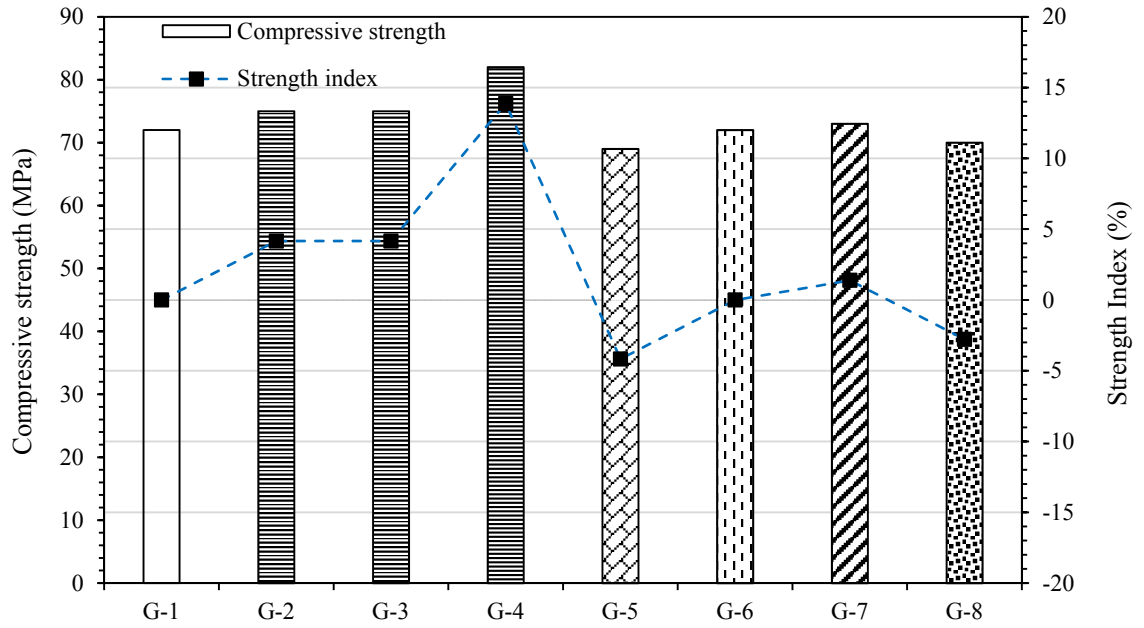
On the other hand, high strength polyethylene fibers are commonly regarded as hydrophobic in nature which necessitates that they are little influenced by the wet nature of geopolymer binder and are less susceptible to a fiber balling effect during the mixing process. However, since in the present investigation the polyethylene fibers were compounded with steel fibers, the reduced fluidity of mixes containing them is largely related to the low density of these fibers (approx. 0.97gm/cc). As for a small volume fraction, e.g., 0.20%, a much larger fiber quantity was included in the respective individual mix, which instigated a higher number of interactions between the fiber and the matrix, thus producing greater internal resistance against the flow. Similar observations were reported in a previous study, where a dramatic loss of workability was observed with low-density short polypropylene fibers (Ranjbar et al., 2016).

4.5.2 Compressive Strength

The compressive strength development of plain and fiber reinforced geopolymer composites are shown in Figure 4-6(a). As can be seen from the data, the geopolymer matrix (G-1) exhibited high compressive strength at 28 days of ambient curing. The high achieved compressive strength is largely related to the combined activation of the amorphous alumina-silicate species present in the FA and reactive calcium oxide (CaO) component in slag precursor with the alkaline activator. The underlying reaction mechanism has been discussed at length in the earlier study (Khan et al., 2016). However, the addition of different fiber types and volume fractions into the plain geopolymer mixture generated a marginal response variation in terms of the compressive strength development. Dealing with the same mix, the loss, and increase in strength of the composite samples with fibers is quantified on strength index via the following Equation (4.4):

$$\text{Strength index} = [(\sigma_f - \sigma_{mo}) / \sigma_{mo}] \times 100\% \quad (4.4)$$

where σ_f = Mean compressive strength of the composite samples with fibers and σ_{mo} = Mean compressive strength of plain G-1 geopolymer matrix.



(a)



(b)

Figure 4-6 Comparison of (a) compressive strength and (b) failure modes of plain and fiber reinforced geopolymer composites (FRGCs).

In general, there was an increase in the load carrying capacity of composite samples with the addition of steel fibers. A relative increase of 4% and a maximum improvement of 14% on strength index were realized in G-2, G-3, and G-4 mixtures with the addition of 1%, 1.5%, and 2% steel fibers respectively, whereas, the average 28-day compressive strength values of

G-1 and G-6 series were similar. Moreover, an insignificant loss of strength was also noticed in two other matrices, i.e., G-5 and G-8 containing HSPE fibers. This smallest of a decrease in the compressive strength of matrices containing polyethylene fibers is associated with their reduced workability and a probable growth of porosity in the tested samples. Similar findings were observed in an earlier investigation (Ahmed and Ronnie, 2017), where the addition of polyethylene fibers in geopolymer composites at five different volume fractions, i.e., between 0 and 2% resulted in the loss of compressive strength in fiber reinforced geopolymer composites in proportion to the number of synthetic fibers present within these mixtures. The gradual reduction in the compressive strength was related to the increased formation of pores and voids within these composites which increased with an increase in the fiber volume fraction. However, although in the current investigation the loss of strength is trivial due to the presence of polyethylene fibers in a fairly small quantity, yet, the said reduction can be accounted in the composite design procedure when the inclusion of fibers is intended to improve its other properties.

A comparison of the failure mode and the extent of damage observed in both unreinforced and reinforced samples after the completion of compression tests are presented in Figure 4-6(b). As can be seen, the geopolymer matrix exhibited an explosive failure at peak load, while the said response of samples transformed to a more ductile behaviour with the inclusion of steel fibers. It is believed that due to the transverse confinement effect of steel fibers and existence of an efficient bond between the fibers and the matrix, the crack propagation in geopolymer matrix was restrained under compression. This delayed the coalescence of micro-cracks to form macro-cracks during the pre-peak loading region, thus enabling the fiber reinforced composites to carry additional loads. As expected, all fiber reinforced composites retained their original shapes after the peak load. Similar findings were shared in another investigation (Ganesan et al., 2015), where a variable fiber dose (i.e., 0 to 1%) of long hooked-end steel fibers effectively increased the load carrying capacity of heat cured FA geopolymer concrete by 16%. Ambily et al. (2014) also reported a substantial increase of 41% in the compressive strength of slag based geopolymer concrete with the inclusion of two differently sized 3% short steel fibers in the fiber-less matrix, although the compression tests in their study were carried out on $70 \times 70 \times 70 \text{ mm}^3$ cubical samples.

4.5.3 Modulus of Elasticity and Poisson's Ratio

The ability to sustain induced stress for every unit strain within the elastic limit is defined as modulus of elasticity (E). Generally, a higher value of "E" for a given strength of concrete indicates its better quality. For investigated mixes, the experimentally determined mean

modulus of elasticity and Poisson's ratio using the relations listed in section 4.4.3 are shown in Figure 4-7.

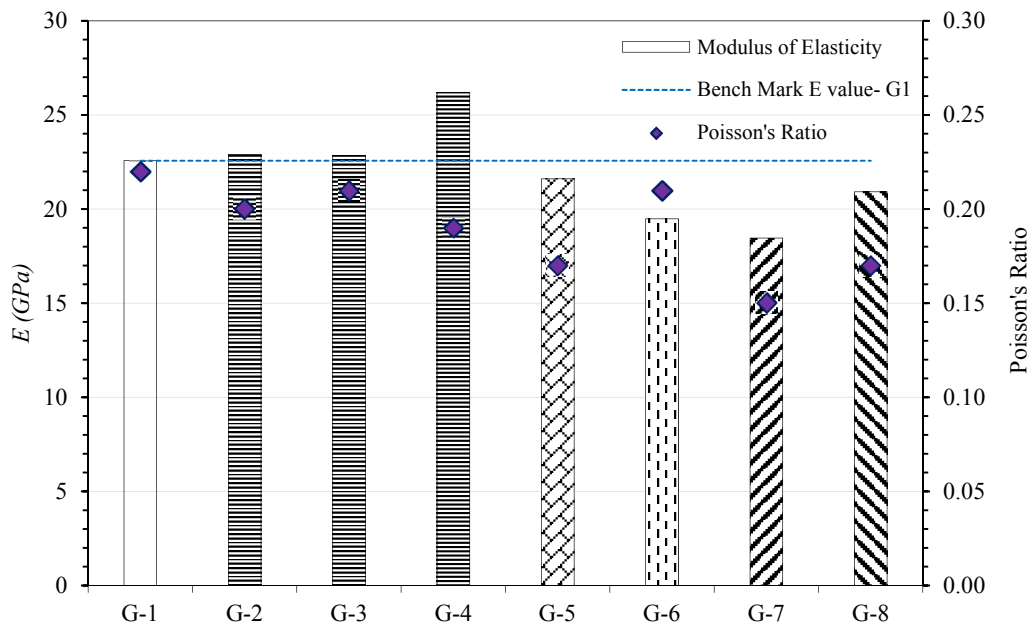


Figure 4-7 Comparison of Modulus of elasticity (E) and Poisson's ratio (μ) of plain and FRGCs.

As observed, the Young's modulus for geopolymer matrix (G-1) was around 22.57 GPa, while for fiber reinforced geopolymer composites, these values ranged between 18.46 to 26.18 GPa corresponding to variations between -18% and +16%. Overall, it can be seen that with the increase in the steel fiber volume fraction from 0 to 2%, the elastic behaviour of geopolymer composites was improved slightly. There was an increase of 16% for composites with 2% steel fiber volume fractions comparing with the unreinforced geopolymer matrix. On the other hand, the elastic modulus of composites containing a hybrid combination of steel and HSPE fibers decreased in comparison with the reference mixture. A slightly inconsistent response for modulus of elasticity was observed without any direct correlation to the amount or type of fiber combination used in G-5 to G-8 mixes.

In the same figure (Figure 4-7), the variation in the Poisson's ratio with respect to different fiber combinations used in the unreinforced matrix is presented. As seen, the Poisson's ratio for the G-1 mixture was the highest, i.e., 0.22, which was found to reduce (0.15 – 0.21) with an increase in the fiber volume fraction. Nonetheless, the reported value of Poisson's ratio for the investigated geopolymer matrix lies well within the prescribed range for high-strength concretes in the literature (i.e., 0.20-0.25) (Sofi et al., 2007). However, in the past, there has been a general lack of consensus regarding this parameter for geopolymers and its dependence

on the compressive strength (Pan et al., 2011). Some researchers found its value to be as low as 0.13 (Hardjito, 2005) for an optimized normal strength (44 MPa) geopolymer concrete (GC), while others (Sofi et al., 2007) reported a Poisson's ratio of 0.26 for a 50 MPa concrete.

Conversely, a value of 0.16 was also stated by Hardjito (2005) for their synthesized high strength (89 MPa) heat treated GC mixture. Clearly, it is obvious that in comparison to the OPC concrete and its well-refined Poisson's ratio limits, i.e., (0.12-0.20) and (0.20-0.25) for normal and high strength concretes, respectively (Sofi et al., 2007). The involvement of heat curing method for fly ash geopolymer and the variation in mix constituents/chemical compositions of the source materials in different studies have a significant influence on the said material parameter. Furthermore, the reduced Poisson's ratio of the samples with fibers is supposedly associated with the presence of spiral steel fibers in the mixtures, whose ability to provide a helical hoop reinforcement effect reduced the transverse expansion in the cylindrical composite samples under compression for a certain longitudinal strain, which appeared to have amplified in the presence of HSPE fibers.

Figure 4-8 provides a comparison between the current experimental data for modulus of elasticity with the previously reported values by other researchers for geopolymer concrete (Hardjito, 2005; Fernandez-Jimenez et al., 2006; Sofi et al., 2007; Ivan Diaz-Loya et al., 2011). Two regression models (Carraquillo et al., 1981; Ahmad and Shah, 1985) based on the studies on high strength OPC concrete (HSC) and the model proposed by AS3600 (AS, 2009) for the estimation of static chord modulus of elasticity within an error of $\pm 20\%$ are also plotted in the same graph. The three models are given in Equations (4.5a), (4.5b), (4.6), and (4.7).

$$E = (\rho)^{1.5} \times (0.043\sqrt{f_{cm}}); f_{cm} \leq 40 MPa \quad (4.5a)$$

$$E = (\rho)^{1.5} \times (0.024\sqrt{f_{cm}} + 0.12); f_{cm} \geq 40 MPa \quad (4.5b)$$

from AS 3600 (2009)

$$E = 3.38(\rho)^{2.5} \times (\sqrt{f'_c})^{0.65} \times 10^{-5} \quad (4.6)$$

from Ahmed and Shah (1985)

and

$$E = (3320\sqrt{f'_c} + 6900)(\rho / 2320)^{1.5} \quad (4.7)$$

from Carraquillo et al. (1981)

where in Equations (4.5), (4.6), and (4.7) f_{cm} and f'_c stand for mean compressive strength and the density (ρ), taken as 2400 kg/m^3

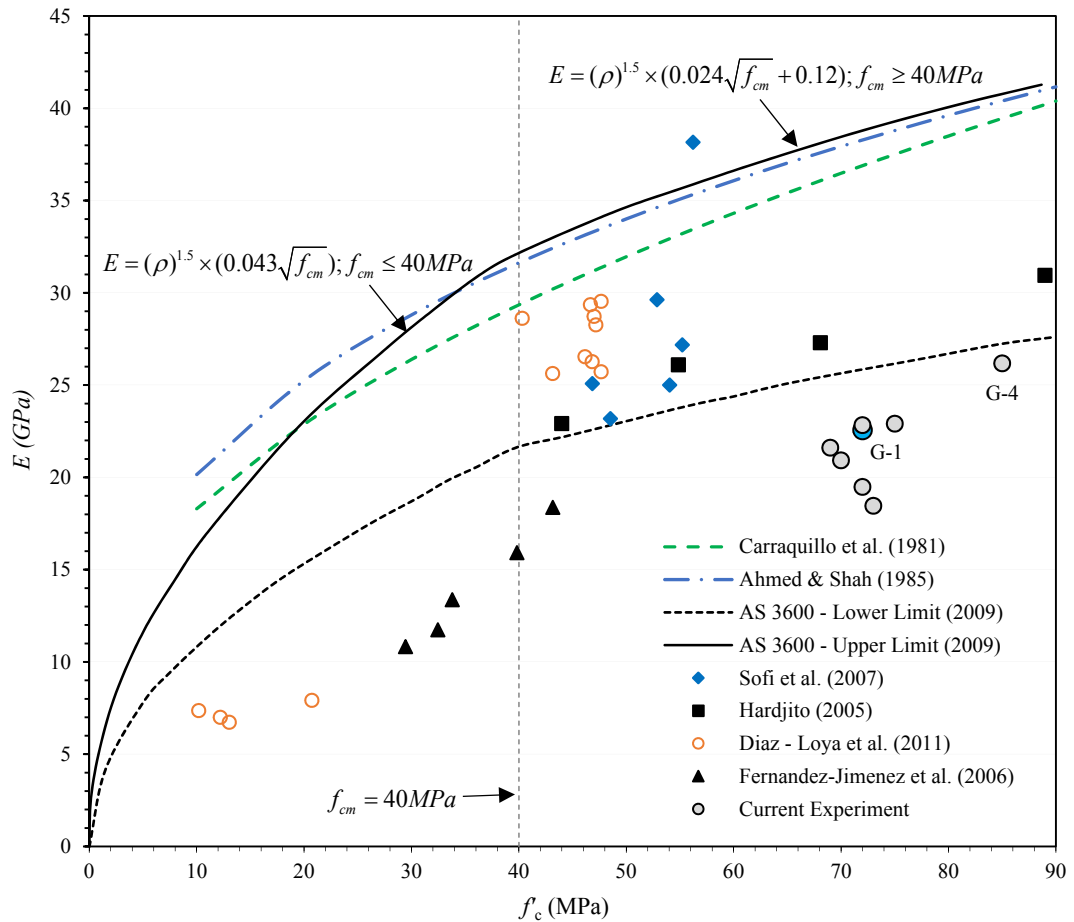


Figure 4-8 Modulus of elasticity of investigated mixes compared with the existing test results and models.

As can be seen, the two dotted lines in the graph represent the upper and lower bound limits for modulus of elasticity provided by AS 3600 model. The model proposed by Ahmed and Shah (1985) generates a closer fit to the upper limit of the interval for strengths greater than 40 MPa, while that of Carraquillo et al. (1981) falls well below the suggested recommendation by the Australian Standard (AS). Since the present investigation is carried out on geopolymer mortars instead of concrete, therefore the “*E*” values for all composites exist below the normal range. Moreover, it is obvious from the plot that the existing models for estimating the modulus of elasticity of HSCs in the literature are not suitable for the geopolymer concrete. It is also interesting to note that a majority of the data set on geopolymer concrete from previous studies and the current investigation is concentrated either just above or below the lower limit suggested by the AS for a wide range of concrete strengths.

It is well-known that concrete is a heterogeneous material and contains different phases, i.e., paste and coarse aggregates (Sofi et al., 2007). Therefore, its modulus of elasticity depends on that of its constituents. However, previous research by Pan et al. (2011) showed that the elastic modulus of geopolymer paste was approximately 27% lower than its cement based

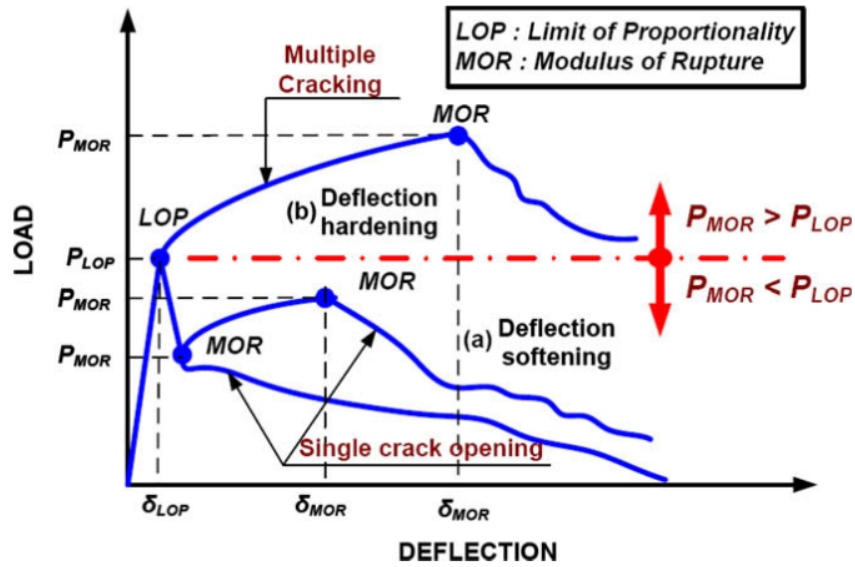
counterpart. Assuming this to be true and the lack of coarse aggregates in the present work, the measured value of geopolymer matrix (G-1) seem precise when compared with the results of Hardjito (2005) for a similar strength level, although the FA source used for the synthesis of geopolymer in that study was different from the current research. Moreover, the variability in the elastic modulus of composites carrying high strength polyethylene fibers in replacement of steel fibers is mainly due to their lower stiffness, (i.e., 123 GPa in the current study). Previous research on PVA fiber reinforced geopolymer composites by Nematollahi et al. (2016) also found the elastic modulus for their geopolymer composites to be around 7.6 GPa, only.

4.5.4 Flexural Tensile Behaviour of Geopolymer Composites

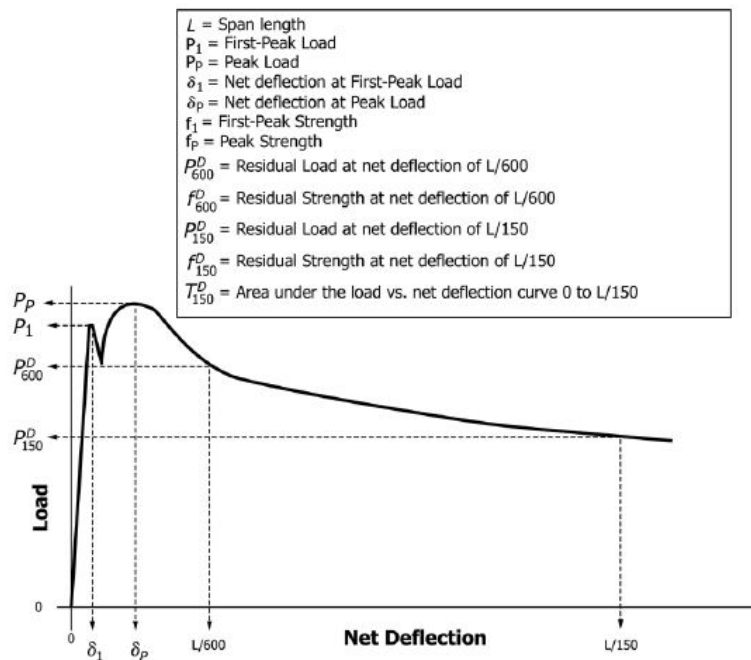
4.5.4.1 General discussion regarding the test parameters

The flexural behaviour of plain and fiber reinforced geopolymer composites are presented in this section. However, before discussing the results, it is necessary to present a short review of the two distinctive responses that can result from testing a simply supported beam in bending behaviour, i.e. (i) deflection-hardening or (ii) deflection-softening. In general, as illustrated in Figure 4-9(a) (Kim et al., 2008) and Figure 4-9(b) ASTM C1609 (ASTM, 2012), fiber reinforced composites that are able to higher loads after the first cracking are commonly known as deflection hardening composites compared to the others showing a deflection softening response. Usually, ASTM C1609 (ASTM, 2012) requires identifying certain thresholds on the load deflection curves for characterizing the flexural performance of fiber-reinforced concrete; such as, its first-peak load (P_1), defined as the first point on the load-deflection curve where the slope is zero and the associated net deflection of first-peak load (δ_1); also peak load (P_p) and the net deflection at peak load (δ_p).

Similarly, for estimating the residual strength capacity, the loads corresponding to a net deflection of $L/600$ and $L/150$ must be used. However, as observed by Kim et al. (2008), for composites exhibiting a stable deflection hardening behaviour, such as, in the current investigation (Figure 4-10), it is very difficult to locate the first cracking point in the initial portion of the load-deflection curve. Moreover, the recommended limit of net deflection ($T \frac{D}{150}$) for the computation of toughness in a strain hardening composite is often not suitable and hence requires to be adjusted. Based on their recommendation, the first cracking point on the load deflection curve can be established using a previous description of this point in ASTM C1018 (ASTM, 1997), where it was then known as the limit of proportionality (LOP) and defined as the point on the load-deflection graph from where onwards the bending curves show an obvious nonlinearity.



(a)



(b)

Figure 4-9 (a) Typical load-deflection response curves of FRCC (Kim et al., 2008) and (b) Explanation of parameters for first peak load, peak load, and other characteristic response values in ASTM C1609 (ASTM, 2012).

However, since in this work, the bending behaviour of the geopolymer matrix was also investigated alongside various other fiber combinations, the first-crack point (P_1) or the LOP

for all fiber reinforced composites is assumed to be equivalent to the first-peak load value (P_1) or the peak load value (P_p) exhibited by the plain geopolymer matrix (as shown in Figure 4-10). Likewise, the elastic deformation (δ_1) for all composites corresponds to the mid-span deflection demonstrated by the G-1 mixture. The assumption has been made purely for the simplicity of the analysis. It should be noted that this parameter as such has little influence on other characteristic values and is not used for the comparison among different test samples. Given that all composites had identical mix constituents, the variation in peak load carrying capacity, ultimate flexural tensile strength, toughness or energy absorption capacity, etc. for fiber reinforced composites can be attributed to the type of fiber combination and volume fractions used to reinforce the brittle matrix. As per ASTM C1609 (ASTM, 2012), the ultimate peak strength (f_p) (or more commonly modulus of rupture (MOR), i.e., the point after which the softening starts to occur) and residual strengths at the designated points ($f_{\frac{L}{600}}, f_{\frac{L}{150}}$) can be determined by inserting the relevant loads in the following Equation (4.8):

$$f = \frac{Pl}{bd^2} \quad (4.8)$$

where f = the strength (MPa), P = the load (N)

l = the span length (mm), b = width and d = depth of the samples, which are 300 mm and 100 mm each respectively.

4.5.4.2 Load bearing capacity vs. mid-span deflection

The flexural tensile behaviour of all prismatic samples at the age of 28 days is depicted by the load deflection curves in Figure 4-10. Each curve is averaged from three samples. As can be seen, the hardened geopolymer matrix showed a typical brittle failure and broke suddenly after reaching the peak load, where the samples cracked within the center third of the beam length (see Figure 4-13), with a maximum load carrying capacity of 12.98 kN and 0.65 mm mid-span deflection. The sudden splitting of the unreinforced geopolymer matrix samples in two halves was expected since in most brittle materials the tensile mode is the most active during bending in comparison to mode II or mode III types failures which are typically related to the shear-type failures, i.e., either in or out of the plane. Moreover, the inclusion of fibers in unreinforced geopolymer matrix provided an overall improvement in the peak strength and enabled the geopolymer composites to deform significantly without breaking during the bending tests, hence suggesting a more ductile fracture behaviour. It can be seen that despite the variance in peak strengths, all fiber reinforced geopolymer composites exhibited a stable deflection hardening response.

By comparing the load-deflection curves, it can be observed that increasing the steel fiber volume fraction i.e., from 1.0% to 2.0 %, generated a proportionate increase in the load carrying capacity of geopolymer matrix, whereas, the bending behaviours of G-2 and G-4 steel fiber reinforced composites were further improved, when a small volume fraction of steel fibers, i.e., 0.2% and 0.4% was replaced with HSPE fibers. It can be seen that the peak load carrying capacity of G-5 series in relation to G-2 and that of G-7 and G-8 matrices in comparison to G-4 fiber reinforced geopolymer composites was improved by 14%, 3%, and 18%, respectively. Moreover, of the series with different fiber combinations, the G-8 matrix containing a hybrid combination of 1.60% steel and 0.40% of HSPE fibers showed the maximum load carrying capacity, i.e., 37.50 kN. A summary of the flexural tensile strengths of different geopolymer composites along with other properties is shown in Table 4-4.

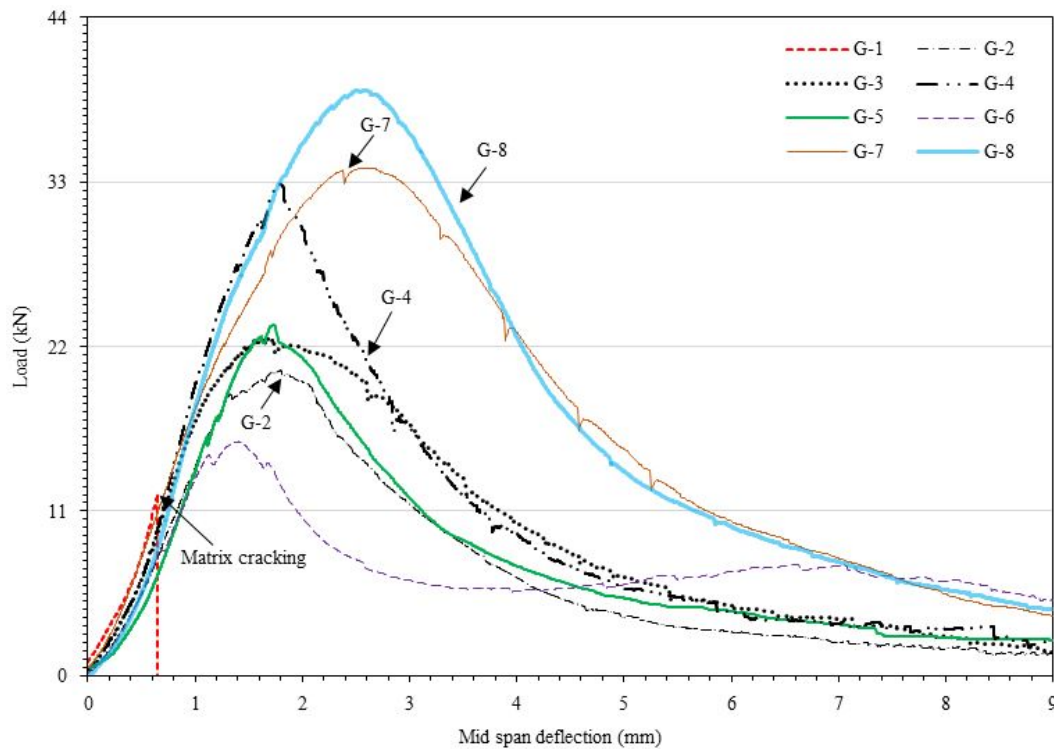


Figure 4-10 Load-deflection plots of plain geopolymer matrix and FRGCs.

Generally speaking, it is well-known that in a given mixture for the same volume fraction, steel fibers provide the highest load carrying capacity in comparison to synthetic fibers. However, the improved performance of composites containing a hybrid combination between steel and HSPE fibers is mainly related to the bridging effect adduced by the dispersion of fine HSPE fibers in the geopolymer matrix. Moreover, the cross-sectional analysis of cast samples, shown in section 4.5.6 suggest a minor fiber sinking in steel fibers reinforced geopolymer composites. The inclusion of fine HSPE fibers enabled a more uniform distribution of steel fibers and improved the peak bending force.

Figure 4-10 also indicates that the maximum load carrying capacities of hybrid steel and HSPE fiber composites occur at a much larger deflection compared with that of singly reinforced steel fiber geopolymer composites. This can be related to the higher elongation capacity of HSPE fibers (3.30%) in comparison to steel fibers (<1%) that has resulted in a higher deflection before the opening of a major crack. In addition, by observing the post-peak regions of the load-deflection curves, it can be further established that the rate of strength loss after the peak load for synthetic+steel fibers was also lower as compared to steel fiber reinforced composites. The mono steel fibers composites soften much more quickly in comparison to hybrid steel and synthetic fiber reinforced geopolymer composites. The addition of HSPE fibers significantly improved the energy absorption capacity.

Furthermore, although in general, the shapes of bending curves between different composites in Figure 4-10 appear similar; the current investigation also considered a possible reinforcement combination between the solo spiral-shaped steel and HSPE fibers in G-6 combination. As observed, in comparison to G-2 or G-5 composites, the load carrying capacity of these samples was 21% and 31% lower respectively. The loss of strength can be attributed to a lesser number of steel fibers present within the matrix and the replacement of high strength hooked-end steel fibers with a lower strength spiral steel fibers. But the major difference that differentiates this composite from others exists between the deflection capacity of 4 and 9 mm. The bending curve specifies a much higher post-peak residual strength capacity available in the said matrix and points to a much efficient bond of spiral steel fiber with the geopolymer matrix. The post-peak residual strength values for this matrix and the fiber pull out tests results for spiral steel fibers shown in the later sections confirm the said observation.

Table 4-4 Summary of mechanical properties of geopolymer composites

Composite No.	f'_c * (MPa)	Std. Dev.	COV (%)	f_p * (MPa)	Std. Dev.	COV (%)	E * (GPa)	Std. Dev.	COV (%)	μ
G-1	72.01	0.91	1.26	3.89	0.08	2.21	22.57	0.90	4.00	0.22
G-2	75.15	2.11	2.80	6.13	0.29	4.54	22.91	0.44	1.93	0.20
G-3	74.66 ^	0.28	0.37	6.72	0.36	5.43	22.83	1.18	5.15	0.21
G-4	82.05	1.30	1.58	9.56	0.28	2.93	26.18	0.14	0.53	0.19
G-5	68.88	3.10	4.50	6.95	0.19	2.74	21.61	0.56	2.59	0.17
G-6	72.10	2.40	3.33	4.86	0.24	4.93	19.48	0.64	3.27	0.21
G-7	72.87	1.40	1.93	9.83	0.11	1.12	18.46	0.29	1.57	0.15
G-8	70.66	1.17	1.66	11.30	0.35	3.18	20.92	0.99	4.75	0.17

*28 days average value of three test samples

^ 28 days average value of two samples

(f'_c : Compressive strength, f_p : Flexural strength, E : Modulus of elasticity, μ : Poisson's Ratio)

Figure 4-11 provides an overall comparison between the ultimate deflection capacities (δ_p) of the composites at MOR and the improvement in the MOR of geopolymer matrix, associated with different fiber combinations. As seen, the deflection of samples at maximum resistance had little dependence on the number of steel fibers present within the matrix. However, composites containing a higher quantity of steel fibers together with HSPE fibers exhibited superior ductility. For example, as presented, the peak deflection at the modulus of rupture (MOR) for G-4 composites with 2% steel fibers was around 1.79 mm, while that of G-8 composite containing 1.60% of steel fibers and 0.40% of HSPE was 2.51 mm. Similarly, it can be seen that the MOR of G-2, G-3, and G-4 composites was improved by 57%, 72% and 145% with the addition of 1%, 1.50% and 2% steel fibers, respectively in the geopolymer matrix. The highest ultimate flexural strength increase was seen for G-8 series, which was 189% more than the G-1 matrix.

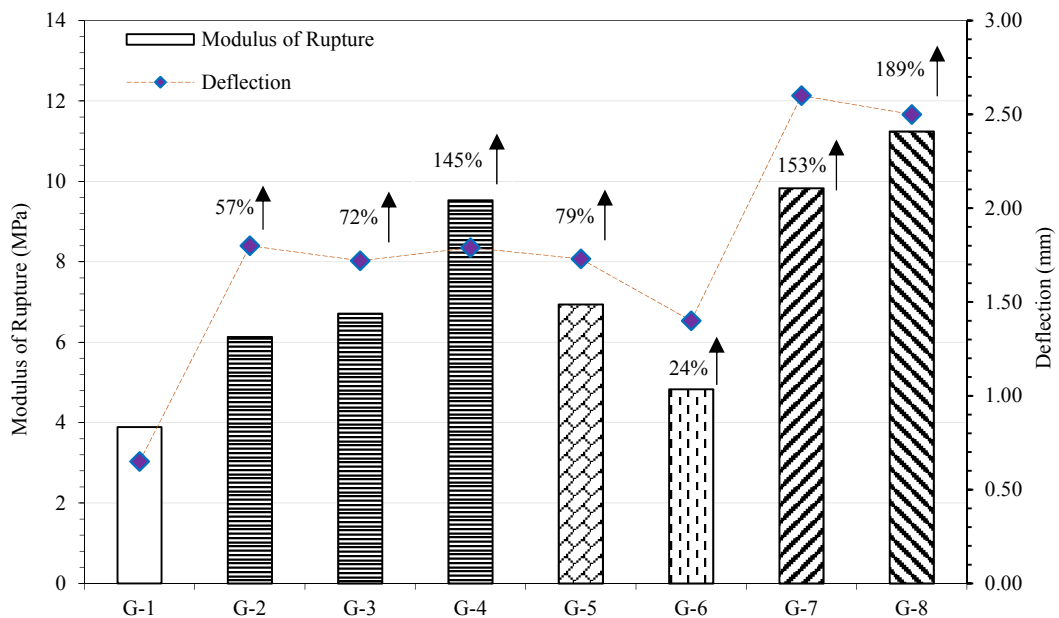


Figure 4-11 Comparison of peak deflection at MOR and quantitative increase in MOR of geopolymer matrix with the addition of fibers.

It is believed that the results presented in the current investigation for the flexural strength properties of geopolymer composites are significantly better than many existing studies in the literature, such as (Ambily et al., 2014; Ranjbar et al., 2016). In contrast to the current work that essentially contains a relatively higher volume fraction of low calcium FA, the composites in previous studies were prepared by using slag, silica fume, and highly basic alkali activators, which are more expensive and could be extremely corrosive in nature. The use of local silica sand and activation of the FA at ambient temperature, instead of special materials such as graded sands or quartz powder as in the case of (Ambily et al., 2014) or heat curing in (Ranjbar

et al., 2016) for strength gain, makes the proposed composites extraordinarily cost-effective and environment-friendly.

4.5.4.3 Fracture toughness (energy absorption capacity) and equivalent bending stress

Based on the results presented in the previous section, it can be concluded that apart from the fiber content, the appropriate fiber combinations and the presence of HSPE fibers in the matrix had a significant influence on the energy absorption capacity. Thus, comparing the said parameter will provide useful information for practical applications that require the use of high energy absorbing materials, such as structures susceptible to dynamic loads, i.e., impact or blast. Figure 4-12 provides a comparison of the amount of energy consumed for fracturing the matrix in all series, determined as the area under the load-deflection curve up to specific net deflections.

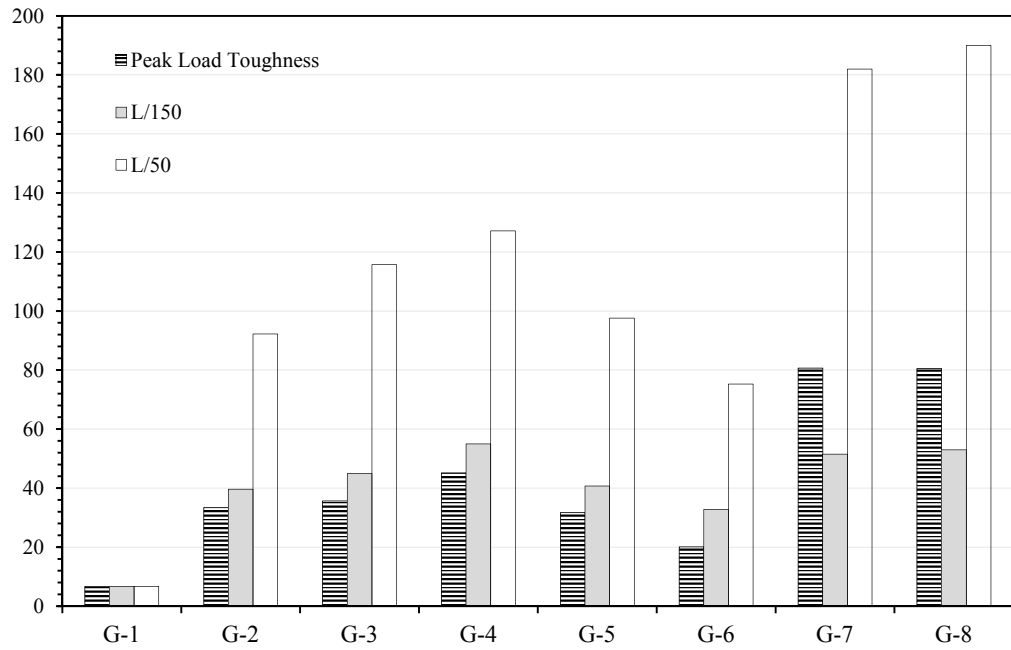
As mentioned in section 4.5.4.1, for the estimation of the toughness values ASTM C1609 (ASTM, 2012) requires the computation of area up to a net deflection limit of $1/150^{\text{th}}$ of the span. However, as shown in Figure 4-12(a), for different fiber reinforced geopolymer composites, the toughness values until peak load are nearly equivalent to the residual sample toughness established until the suggested limit ($L/150$). Moreover, for matrices exhibiting greater ductility, i.e., G-7 and G-8, it can be seen that the test samples did not even achieve their highest load carrying capacity and the suggested point exists on the ascending branch of the load-deflection curves. Therefore, in order to make a realistic comparison among different composites a third point on the load-deflection curve, i.e., $L/50$ is introduced.

A proportionate increase in the peak load toughness and the toughness values at deflection points $L/150$ and $L/50$ were observed by increasing the steel fiber volume fraction from 1 to 2%. It can be seen that the toughest response was provided by a hybrid combination of 1.60% steel and 0.40% of HSPE fibers, which was closely followed by a hybrid fiber combination of 1.80% steel and 0.20% HSPE fibers. The increase in the fracture toughness of G-8 series in relation to G-7 matrix is mainly related to a relatively large number of fine HSPE fibers that have prevented the tendency of cracks to localize along a certain path, hence enabling the composites to show more resistance in bending (Ranjbar et al., 2016). However, it should be noted that inclusion of HSPE fibers at higher volume fractions (e.g., 1% or 2%) may generate casting difficulties and increase the porosity in composite samples; hence their inclusion must be carefully controlled.

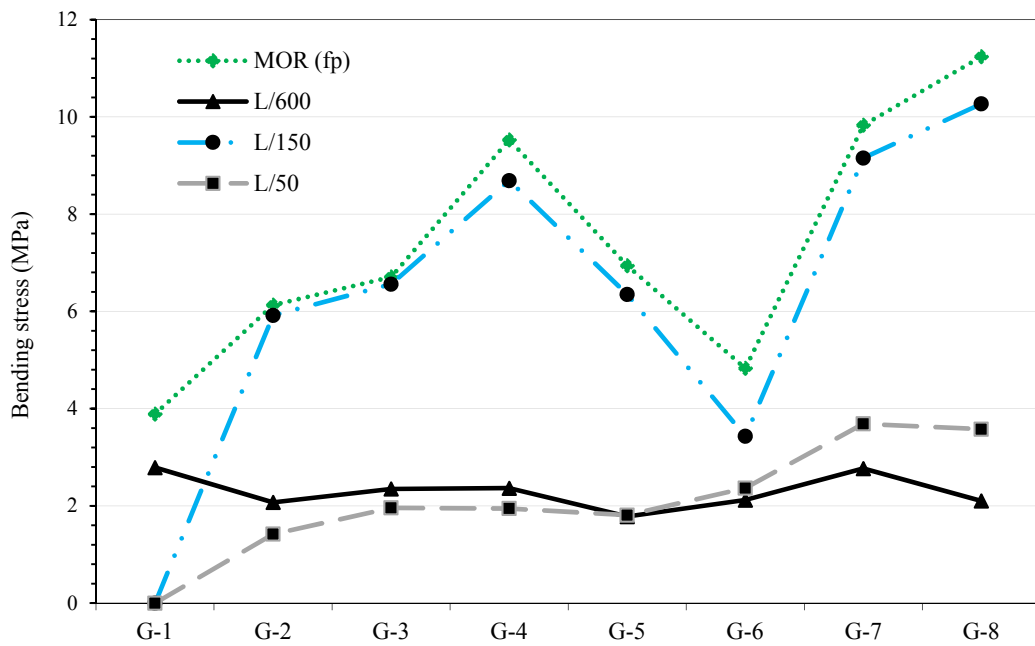
Moreover, by comparing the toughness results, it is apparent that the G-6 combination containing spiral steel fibers with HSPE fibers showed relatively reduced energy absorption capacity in comparison to G-2 or G-5 matrices. Yet, it can also be identified from the load-deflection curves that the geopolymer matrix cracked at a mid-span deflection of about 0.65

mm, which postulates that the tested samples from G-6 series were already cracked and assumed to be beyond their elastic region before reaching their maximum load carrying capacity. It is believed that for the same volume fraction of steel fibers, the rate of crack propagation was much higher in the absence of hooked-end steel fibers and the neutral axis shifted at a much faster rate towards the compression zone. The reduced energy absorption capacity for G-6 series was primarily related to the insufficient number of steel fibers available for the matrix reinforcement. Once the peak load was reduced, the corresponding area under the load-deflection curve that relates to the toughness of the tested samples was also computed to be on the lower side. Nevertheless, the residual strength values calculated for G-6 series at L/50 were much higher in relation to the samples from G-2, G-3, G-4 or G-5 series that highlights the superior efficiency of spiral steel fiber in controlling the propagation of cracks during the post-peak loading regions.

Figure 4-12(b) illustrates a variation between equivalent bending stresses or other characteristic values ascertained from the load-deflection curves at the designated points, i.e. (L/600, L/150, L/50, and MOR) as explained previously. As can be seen, the residual strength ($f_{\frac{L}{600}}$) at L/600 was 2.79 MPa for G-1, 2.07 MPa for G-2, 2.35 MPa for G-3 and 2.10 MPa for G-8. The rest of the values can be seen on the graph. Clearly, the recommended limit for computation of residual strength by the standard at $f_{\frac{L}{600}}$ is not suitable for deflection hardening composites. Similar results were obtained by Kim et al. (2008), where the said point was consistently found on the ascending portion of the load-deflection curves. A more prominent effect of the different fiber combinations used for the matrix reinforcement can be seen in the descending parts of the curves at the net deflection limits of L/150 and L/50. The residual strength capacity ($f_{\frac{L}{150}}$) at L/150 and ($f_{\frac{L}{50}}$) at L/50 for G-1 are both 0, 5.92 MPa and 1.42 MPa for G-2, 6.56 MPa and 1.96 MPa for G-3, 8.69 MPa and 1.95 MPa for G-4, 6.35 MPa and 1.81 MPa for G-5, 3.43 MPa and 2.37 MPa for G-6, 9.15 MPa and 3.69 MPa for G-7 and 10.27 MPa and 3.58 MPa for G-8. Clearly, in terms of post-peak residual strength, the hybrid fiber combinations were more effective than other counterparts. Moreover, as highlighted previously the G-6 reinforcement combination had 67% and 31% more post-peak residual strength capacity at L/50 in comparison to G-2 and G-5 fiber combinations. However, for a balanced consideration of peak and residual strength of the composites, a combination with an equal dosage of the spiral and hooked end steel fibers is more useful for the matrix reinforcement. A summary of average characteristic response values for different geopolymer composites in flexural tensile behaviour is also shown in Table 4-5.



(a)



(b)

Figure 4-12 Effect of different fiber combinations on (a) toughness and (b) equivalent bending stress until designated points in geopolymer composites.

Table 4-5 Average characteristic response values for flexural tensile behaviour of geopolymer composites

Composite No	f_p (MPa)	Std. Dev.	$f \frac{L}{600}$ (MPa)	Std. Dev.	$f \frac{L}{600}$ (MPa)	Std. Dev.	$f \frac{L}{600}$ (MPa)	Std. Dev.	$f \frac{L}{600}$ (N.m.)	$f \frac{L}{600}$ (N.m.)
G-1	3.89	0.08	2.79	0.00	-	-	-	-	6.68	6.68
G-2	6.13	0.29	2.07	0.11	5.92	0.19	1.42	0.05	39.64	92.23
G-3	6.72	0.36	2.35	0.18	6.56	0.29	1.96	0.03	44.94	115.71
G-4	9.56	0.28	2.36	0.21	8.69	0.04	1.95	0.15	54.95	127.13
G-5	6.95	0.19	1.78	0.03	6.35	0.27	1.81	0.04	40.72	97.60
G-6	4.86	0.24	2.12	0.17	3.43	0.23	2.37	0.10	32.78	75.25
G-7	9.83	0.11	2.77	0.31	9.15	0.21	3.69	0.39	51.47	181.98
G-8	11.30	0.35	2.10	0.04	10.27	0.09	3.58	0.28	52.94	189.98

4.5.4.4 Cracking behaviour of geopolymer composites

The cracking behaviour of geopolymer composites is an important parameter to characterize the performance of different fiber combinations used to reinforce the brittle matrix. It is obvious from Figure 4-13 that the addition of fibers did generate multiple cracks in the composites; however, the number of cracks, crack widths and shapes vary distinctively among the considered batches. Generally, failure in strain hardening composites follows the development of a steady state cracking, i.e., instead of the formation of a large macro-crack and its unstable propagation, a series of parallel cracks are developed which lead the samples to fail in a multiple crack mode (Li and Wu, 1992).

As observed, the plain geopolymer matrix containing 2% of steel fibers exhibited more multiple cracks in comparison to matrices having lower fiber contents, such as G-6 that showed only 5-6 major cracks. This is clearly related to the insufficient number of steel fibers present within the matrix. Moreover, unlike many studies in the literature (Li and Wu, 1992; Shaikh, 2013; Nematollahi et al., 2016) which present either very fine hairline distributed cracking or a slightly widely spaced straight parallel cracks in strain hardening composites, the appearance of zig-zag crack patterns on the tension side of the samples is more closely related to the use of spiral steel fibers for the matrix reinforcement. A wide opening in the center of samples and significant spalling of the geopolymer matrix such as in the case of G-4 samples, suggests adequate yielding of the spiral steel fibers and their excellent potential for crack controllability.

The inclusion of hybrid steel and HSPE fiber combination at a higher volume fraction in the geopolymer matrix was found to reduce the crack widths (can be seen with G-8). However,

the formation of cracks was more localized towards the central opening. In specific, lesser spalling of the matrix combined with a tearing fracture in the composites was recognized. Further, Figure 4-13(b) shows a magnified image for one of the samples from G-8 series, where most of the steel fibers can be observed either elongated or pulled-out from the matrix, while at a few places some fibers do experience fiber breakage. The said observation is interesting and implies the existence of an efficient bond between the spiral steel fiber and the matrix. It appears from the test results that in the presence of sufficient embedment length, the spiral steel fibers were able to utilize their full strength capacity.

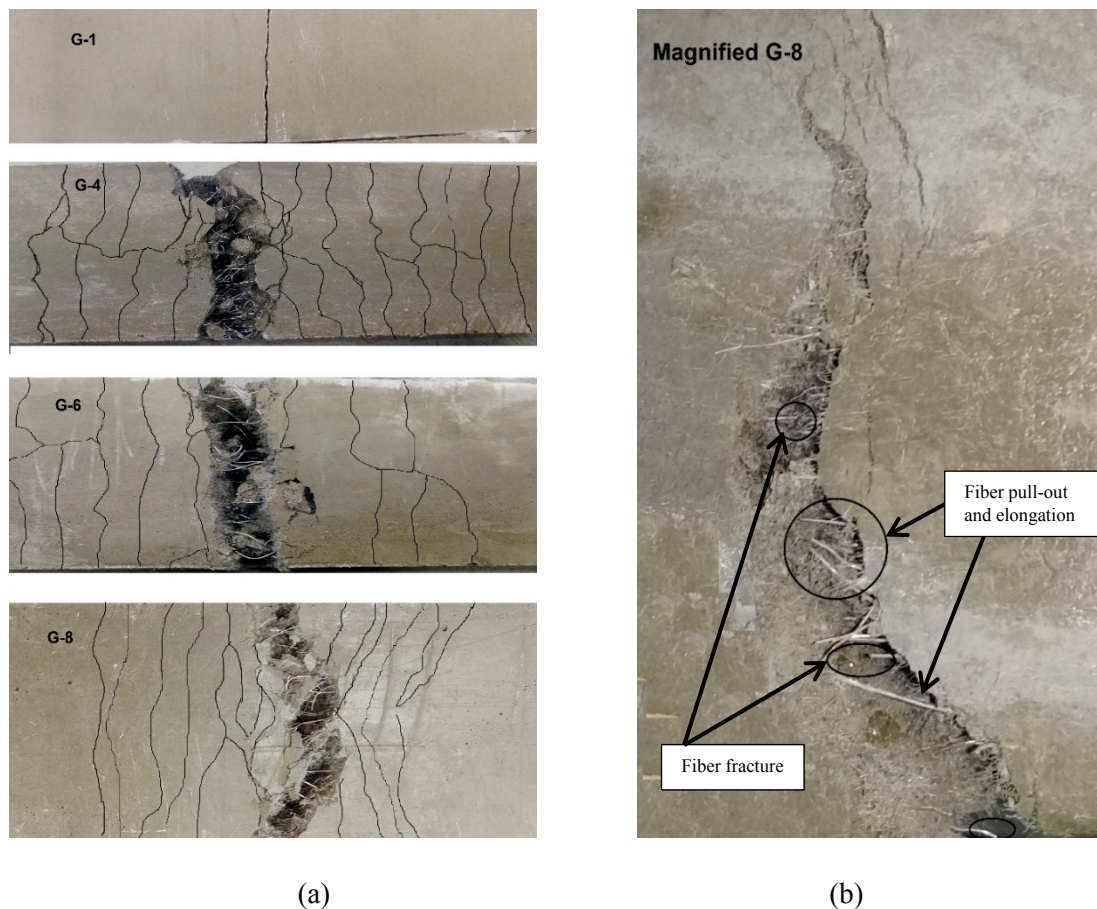
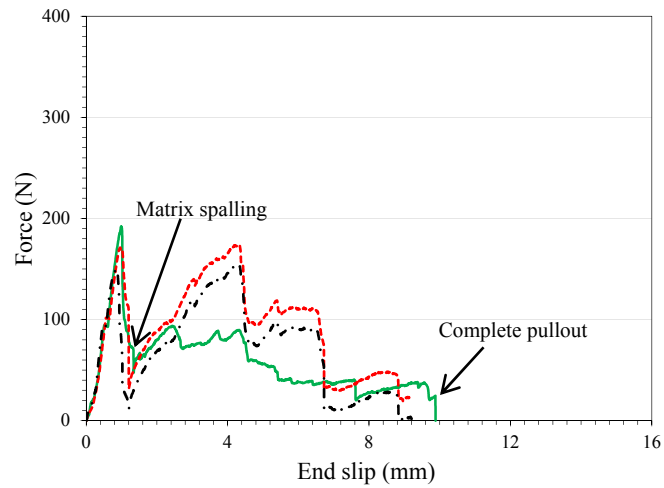


Figure 4-13 Cracking behaviour of geopolymer composites.

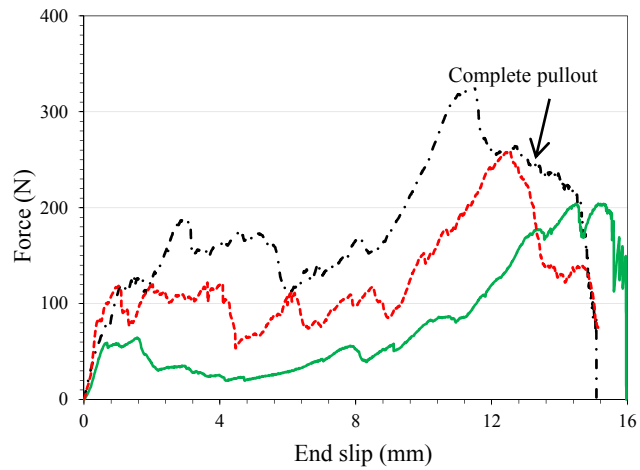
4.5.5 Pull-out behaviour of spiral steel fibers

The pull-out behaviour of commonly used hooked-end steel fibers is usually governed by a single peak, i.e., after reaching a maximum pull-out force and completion of debonding process by the fiber, a significant reduction in the pull-out force is noted (Bhutta et al., 2016). Much of the resistance comes from the hooks present at the end of the fibers or after debonding via the frictional bond present between the fiber-matrix interfaces. On the contrary, the pull-

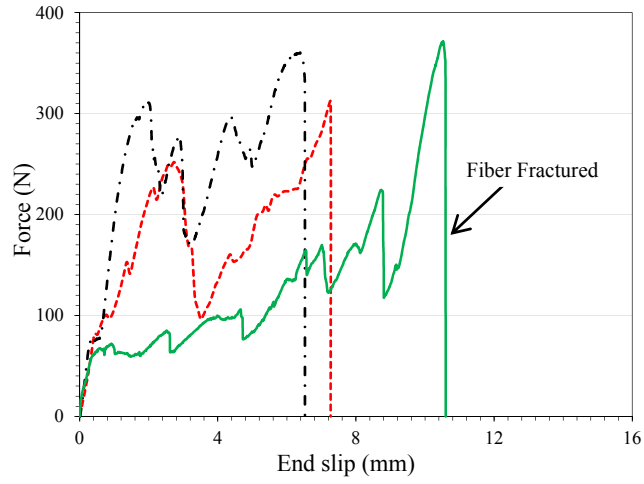
out response of spiral steel fibers from the geopolymer matrix is significantly different from that of hooked-end fibers as shown in Figure 4-14, which evidences a series of peaks before reaching a maximum pull-out load, followed by a complete drop either indicating the complete pull-out of the fiber or fiber breakage due to the bond strength exceeding fiber strength, thus marking the test completion.



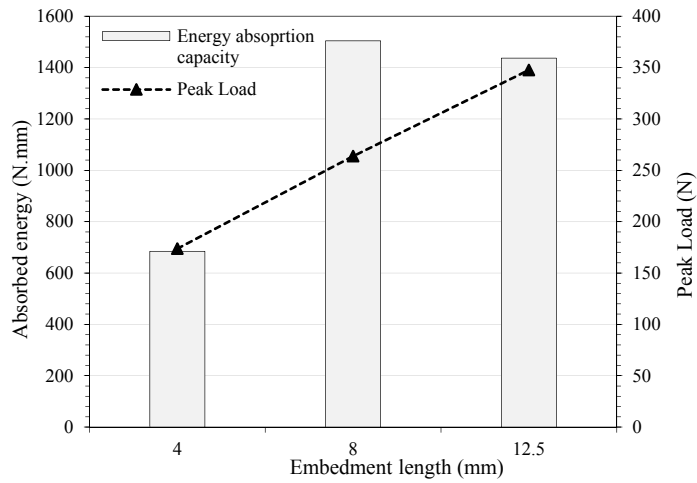
(a)



(b)



(c)



(d)

Figure 4-14 Comparison of force end-slip curves (a-c) for three different embedment lengths and (d) absorbed energy during the pull-out tests.

As shown, an increase in the embedment length of fibers had a clear influence on the maximum pull-out force, such that the average pull-out force for an embedment length of 4 mm is 174 N, for 8 mm is 264 N, and for 12.5 mm is 348 N, respectively. It can be further established that for all samples having an embedment length of 4 and 8mm, a complete fiber-pull out from the matrix was realized while for the third tested case, i.e., for an embedment length of 12.5mm, all the three tests from this batch revealed that the fibers were found to fracture after reaching a certain peak load. Tests conducted for establishing the wire strength found the average fiber break force to be around 352 N corresponding to a tensile strength of 1480 MPa. This clearly agrees to the maximum pull-out forces obtained during the individual fiber pull-out tests for an embedment length of 12.5 mm and rationalizes why some of the spiral steel fiber were found fractured during the bending tests.

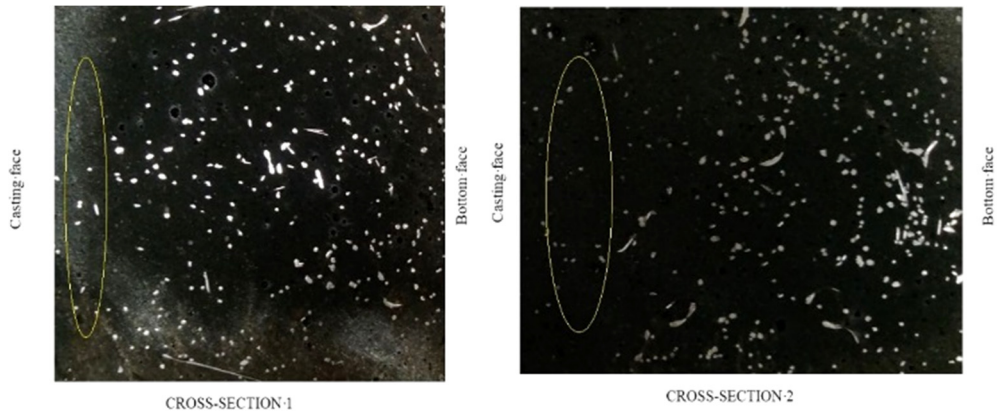
Similar findings were seen in an earlier investigation (Hao and Hao, 2017), where the pull-out behavior of spiral steel fibers was investigated in OPC concrete mixtures at three different embedment lengths, i.e., 10mm, 20mm, and 30mm. It was observed for the tests with smaller embedment lengths that they ended with complete pull-out of fibers, while the samples with increased embedment lengths resulted in fibers rupture. It should be noted that unlike the current investigation, the matrix in the previous study also contained aggregates which potentially may also influence the pull-out behaviour of spiral steel fibers. Furthermore, the test curves shown in Figures 4-14(a-c) suggest that with the progression of the fiber pull-out process, a much larger force was required to overcome an increasingly large volume of geopolymer mortar present on top of the embedded spirals. A major reason for this increase is related to the helical geometry of the spiral steel fibers, where these fibers were believed to be pulled-out from their central axis at a gradually reduced inclination angle instead of the opening of spirals in a circular manner along the coil diameter (Hao and Hao, 2017).

Figure 4-14(d) summarizes the amount of energy absorbed by the spiral steel fibers during the pull-out process. The absorbed energy was computed as the area under each pull-out versus end-slip curve. By comparing the results, it can be seen that the efficiency of spiral steel fiber and total pull-out energy increased with the increase in the embedment length. Theoretically, the embedment length of fiber spanning a crack cannot be more than half of its nominal length and usually debonding occurs along the shorter side. By observing the absorbed energy values, it can be seen that the pull-out work computed for an embedment length of 12.5mm was slightly lower than the case with 8mm embedment length. This can be associated with the lower end-slip deformation observed during the fiber pull-out process and the occurrence of fiber rupture. Generally, fiber fracture is avoided to ensure higher ductility in the composite materials; however, it also depends on the tensile strength of the fibers used for the matrix reinforcement. Similar findings were reported by other researchers (Banthia and Trottier, 1994; Soetens et al., 2013), where the inclusion of steel fibers in high strength matrix was found to cause brittle failures in certain cases. On the other hand, the reported outcome may also be considered as an advantage which underlines the strong affinity of spiral steel fiber with geopolymer mortar that has allowed the plastic deformation to occur.

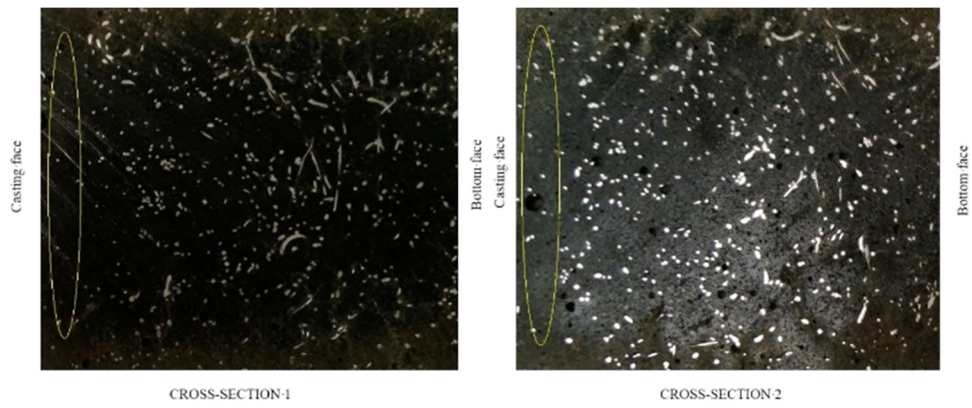
4.5.6 Fiber distribution in geopolymer composites

The proper distribution of steel fibers in any concrete matrix has always been a significant challenge, where the effectiveness of fibers in improving the composite properties depends upon their location and orientation within the cast samples. A non-uniform distribution of fibers may result in underutilization of their ability and can significantly influence the material performance. Therefore apart from investigating the mechanical behaviour of synthesized

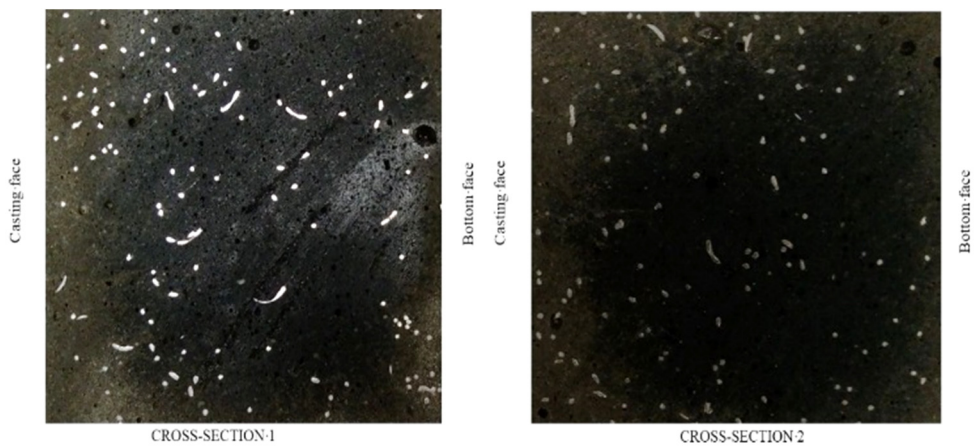
geopolymer composites, fiber distribution in different mixes was also examined. All composites were cast using an identical routine under the influence of an external vibrator. Figure 4-15 shows the cross sections for five of the studied mixtures, such that the bottom face of beams from the sliced up cross-sections are present on the right-hand side of each image.



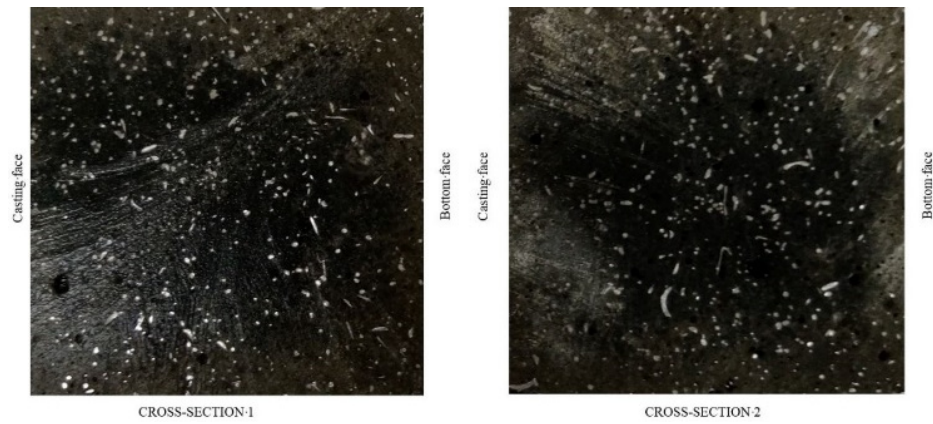
(a)



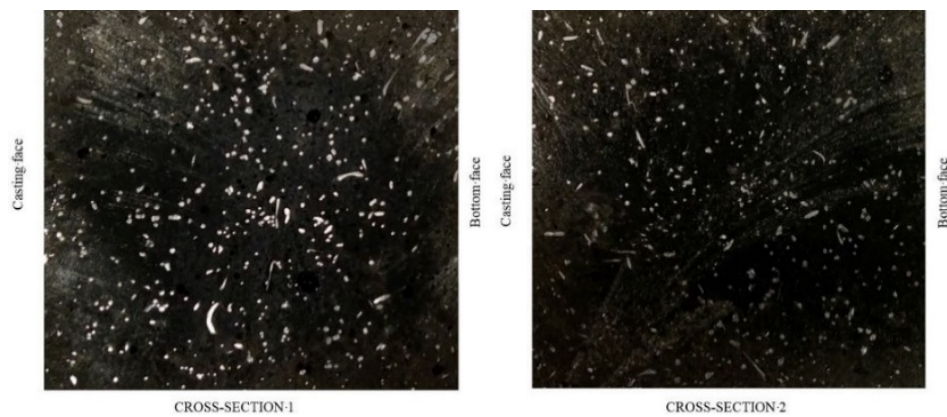
(b)



(c)



(d)



(e)

Figure 4-15 Comparison of fiber distribution along two cross-sections in (a) G-2 (b) G-4 (c) G-6 (d) G-7 (e) G-8.

The visual inspection of all cross-sections provides a qualitative estimate of the observed mechanical behaviour. It can be seen that for higher fiber volume fractions such as in the case of G-4 (Figure 4-15b), G-7 (Figure 4-15d) and G-8 (Figure 4-15e), a relatively large number of fiber counts can be made within the cross-sections, whereas fewer fibers are present in the cross-section for G-2 (Figure 4-15a) and G-6 (Figure 4-15c) combinations. Hence a direct correlation can be recognized in regards to the load carrying ability of each composite. Moreover, based on the evidence, it is reasonable to conclude that although steel fibers were seen well distributed in all composites, however, if observed carefully, the distribution of steel fibers appeared more random in the presence of HSPE fibers, whereas minor empty spaces could be found on top surfaces of the cast samples for G-2 and G-4 series, as indicated. This slightest of fiber gravitation is believed to have contributed to the reduction of peak load carrying capacity for steel fiber reinforced geopolymer composites in comparison to G-5, G-7 or G-8 composites.

4.6 Conclusions

This research investigated the mechanical performance of high strength fiber reinforced geopolymer composites (FRGCs) synthesized by using an equal-part combination of hooked-end+spiral steel and HSPE fibers. The fibers were included in different combinations and varying proportions up to 2% by volume. The investigation provides a valuable insight into the fracture behaviour of FRGCs along with other material properties. The authors believe that the current work encourages the use of geopolymer material at a wider scale. Based on the limited experimental program undertaken in this study, the following conclusions can be drawn.

- 1) The inclusion of steel fibers at higher volume fractions reduced the workability of fresh composite mixtures, though the addition of HSPE was found to generate higher shear resistance against the flow.
- 2) The developed geopolymer composites exhibited high compressive strength at 28 days of ambient curing, i.e., the plain geopolymer matrix realized a strength value of 72 MPa. The inclusion of a paired combination of hooked-end+spiral steel fibers improved the post-crack performance of samples under compression. An increase of 18% in the compressive strength of samples was seen with the addition of 2% steel fibers, while the failure modes transferred from brittle to ductile.
- 3) The evaluated modulus of elasticity (E) and Poisson's ratio (μ) for the unreinforced geopolymer and different FRGCs were compared with the existing models in the literature. No direct correlation was found for the results reported in this work and previous studies on geopolymer materials. The described material parameters are believed to be significantly influenced with the mix constituents and the nature of curing method.
- 4) All FRGCs exhibited stable deflection-hardening response rather than a catastrophic brittle failure observed for geopolymer matrix, hence indicating a high energy absorption capacity.
- 5) Although a varying degree of performance in terms of peak load carrying capacity, toughness, cracking behaviours and post-peak residual strengths in bending for FRGCs was observed, as a function of fiber volume fractions and combination, a hybrid combination between steel and HSPE fibers (i.e., 1.60%+0.40%) created a three-fold increase in the load carrying capacity of geopolymer matrix. Similarly, the inclusion of HSPE in a small percentage increased the deflection capacity of geopolymer composites at peak resistance.

- 6) Post-peak residual strengths at certain net deflections, such as $L/150$ or $L/50$ were also found higher for hybrid combinations between steel and synthetic fibers, for a given fiber volume content.
- 7) The multiple cracking behaviours observed for FRGCs differ from the patterns available for deflection-hardening composites in the past research. A slight zig-zag fracture pattern on the tension side of samples is due to the presence of spiral steel fibers in the geopolymer matrices. FRGCs containing 2% steel fibers showed the highest number of multiple cracks.
- 8) The individual fiber pull-out tests indicated a strong affinity of spiral steel fibers with the geopolymer matrix. The peak pull-out loads increased with increase in the embedment length; however, the failure modes of fibers shifted from pull-out to rupture beyond a certain embedment length.

4.7 References

ASTM. (1997). Standard test method for flexural toughness and first-crack strength of fiber-reinforced concrete (using beam with third-point loading). *ASTM C1018-97*, Philadelphia.

AS. (2009). Concrete Structures, *AS 3600*, Australian Standards.

ASTM. (2012). Standard test method for flexural performance of fiber reinforced concrete (using beam with third-point loading). *ASTM C1609-12*, Philadelphia.

ASTM. (2012a). Standard specification for coal fly ash and raw or calcined natural pozzolan for use in concrete. *ASTM C618-12a*, Philadelphia.

ASTM. (2013a). Standard test method for compressive strength of hydraulic cement mortars, (using 50-mm cube specimens). *ASTM C109-13*, Philadelphia.

ASTM. (2013b). Standard test method for flow of hydraulic cement mortar. *ASTM C1437-13*, Philadelphia.

ASTM. (2014). Standard test method for static modulus of elasticity and Poisson's Ratio of concrete in compression. *ASTM C469-14*, Philadelphia.

ASTM. (2015a). Standard test method for compressive strength of cylindrical concrete specimens. *ASTM C39-15*, Philadelphia.

ASTM. (2015b). Standard test method for relative density (Specific Gravity) and absorption of fine aggregate. *ASTM C128-15*, Philadelphia.

Abbas, Y. M., & Iqbal Khan, M. (2016). Fiber–Matrix Interactions in Fiber-Reinforced Concrete: A Review. *Arabian Journal for Science and Engineering*, 41(4), 1183-1198.

Ahmad, S. H., & Shah, S. P. (1985). Structural properties of high strength concrete and its implications for precast prestressed concrete. *PCI Journal*, 30(6), 92-119.

- Ahmed, S. F. U., Maalej, M., & Paramasivam, P. (2007). Flexural responses of hybrid steel–polyethylene fiber reinforced cement composites containing high volume fly ash. *Construction and Building Materials*, 21(5), 1088-1097.
- Ahmed, S. F. U., & Ronnie, Z. (2017). Ductile behavior of polyethylene fibre reinforced geopolymer composite. *Paper presented at the MATEC Web of Conferences*.
- Alomayri, T., Shaikh, F. U. A., & Low, I. M. (2013). Characterisation of cotton fibre-reinforced geopolymer composites. *Composites Part B: Engineering*, 50(0), 1-6.
- Ambily, P. S., Ravisankar, K., Umarani, C., Dattatreya, J. K., & Iyer, N. R. (2014). Development of ultra-high-performance geopolymer concrete. *Magazine of Concrete Research*, 66, 82-89.
- Assaedi, H., Shaikh, F., & Low, I. M. (2016). Influence of mixing methods of nano silica on the microstructural and mechanical properties of flax fabric reinforced geopolymer composites. *Construction and Building Materials*, 123, 541-552.
- Banthia, N., & Gupta, R. (2004). Hybrid fiber reinforced concrete (HyFRC): fiber synergy in high strength matrices. *Materials and Structures*, 37(10), 707-716.
- Banthia, N., & Trottier, J.-F. (1994). Concrete reinforced with deformed steel fibers, part I: bond-slip mechanisms. *ACI Materials Journal-American Concrete Institute*, 91(5), 435-446.
- Bernal, S., De Gutierrez, R., Delvasto, S., & Rodriguez, E. (2010). Performance of an alkali-activated slag concrete reinforced with steel fibers. *Construction and Building Materials*, 24(2), 208-214.
- Bhutta, A., Farooq, M., Zanotti, C., & Banthia, N. (2016). Pull-out behavior of different fibers in geopolymer mortars: effects of alkaline solution concentration and curing. *Materials and Structures*, 50(1), 80.
- Carraquillo, R., Nilson, A., & Slate, F. (1981). Properties of highstrength concrete subjected to short-term load. *ACI Materials Journal*, 78(3).
- Chandransu, K., & Naaman, A. (2003). Comparison of tensile and bending response of three high performance fiber reinforced cement composites. *Paper presented at the International Workshop High Performance Fiber Reinforced Cement Composites*.
- Chen, Z., Yang, Y., & Yao, Y. (2013). Quasi-static and dynamic compressive mechanical properties of engineered cementitious composite incorporating ground granulated blast furnace slag. *Materials & Design*, 44, 500-508.
- Choi, J.-I., Lee, B. Y., Ranade, R., Li, V. C., & Lee, Y. (2016). Ultra-high-ductile behavior of a polyethylene fiber-reinforced alkali-activated slag-based composite. *Cement and Concrete Composites*, 70, 153-158.
- Davidovits, J. (1988). Soft mineralogy and geopolymers. *Paper presented at the Proceedings 1st International Conference on Geopolymers*, Volume 1.
- Davidovits, J. (1991). Geopolymers. *Journal of thermal analysis*, 37(8), 1633-1656.
- Davidovits, J. (1994). High-alkali cements for 21st century concretes. *ACI Special Publication*, 144, 383-398.

- Dylmar Penteado Dias, C. T. (2005). Fracture toughness of geopolymeric concretes reinforced with basalt fibers. *Cement & Concrete Composites*, 27, 49–54.
- Feng, K. N., Ruan, D., Pan, Z., Collins, F., Bai, Y., Wang, C. M., & Duan, W. H. (2014). Effect of strain rate on splitting tensile strength of geopolymer concrete. *Magazine of Concrete Research*, 66, 825-835.
- Fernandez-Jimenez, A. M., Palomo, A., & Lopez-Hombrados, C. (2006). Engineering properties of alkali-activated fly ash concrete. *ACI Materials Journal*, 103(2), 106-112.
- Ganesan, N., Abraham, R., & Deepa Raj, S. (2015). Durability characteristics of steel fibre reinforced geopolymer concrete. *Construction and Building Materials*, 93, 471-476.
- Gao, X., Yu, Q. L., Yu, R., & Brouwers, H. J. H. (2017). Evaluation of hybrid steel fiber reinforcement in high performance geopolymer composites. *Materials and Structures*, 50(2), 165.
- Hao, Y., & Hao, H. (2016). Mechanical properties and behaviour of concrete reinforced with spiral-shaped steel fibres under dynamic splitting tension. *Magazine of Concrete Research*, 68(21), 1110-1121.
- Hao, Y., & Hao, H. (2017). Pull-out behaviour of spiral-shaped steel fibres from normal-strength concrete matrix. *Construction and Building Materials*, 139, 34-44.
- Hao, Y., Hao, H., & Chen, G. (2016). Experimental investigation of the behaviour of spiral steel fibre reinforced concrete beams subjected to drop-weight impact loads. *Materials and Structures*, 49(1), 353-370.
- Hardjito, D., Wallah, S. E., Sumajouw, D. M., & Rangan, B. V. (2004). On the development of fly ash-based geopolymer concrete. *ACI Materials Journal-American Concrete Institute*, 101(6), 467-472.
- Hardjito, D. (2005). Studies on Fly Ash-Based Geopolymer Concrete, *PhD Thesis, Department of Civil Engineering*, Curtin University, Australia.
- Huntzinger, D. N., & Eatmon, T. D. (2009). A life-cycle assessment of Portland cement manufacturing: comparing the traditional process with alternative technologies. *Journal of Cleaner Production*, 17(7), 668-675.
- Ivan Diaz-Loya, E., Allouche, E. N., & Vaidya, S. (2011). Mechanical Properties of Fly-Ash-Based Geopolymer Concrete. *ACI Materials Journal*, 108(3).
- Khan, M. Z. N., Shaikh, F. U. A., Hao, Y., & Hao, H. (2016). Synthesis of high strength ambient cured geopolymer composite by using low calcium fly ash. *Construction and Building Materials*, 125, 809-820.
- Kim, D. j., Naaman, A. E., & El-Tawil, S. (2008). Comparative flexural behavior of four fiber reinforced cementitious composites. *Cement and Concrete Composites*, 30(10), 917-928.
- Li, V. C., & Wu, H.-C. (1992). Conditions for pseudo strain-hardening in fiber reinforced brittle matrix composites. *Journal of Applied Mechanics Review*, 45(8), 390-398.

- Madloul, N. A., Saidur, R., Hossain, M. S., & Rahim, N. A. (2011). A critical review on energy use and savings in the cement industries. *Renewable and Sustainable Energy Reviews*, 15(4), 2042-2060.
- Marchese, B., & Marchese, G. (1993). Fibre pullout-microstructural relationships for cementitious mortars. *Journal of materials science letters*, 12(20), 1592-1595.
- Natali, A., Manzi, S., & Bignozzi, M. C. (2011). Novel fiber-reinforced composite materials based on sustainable geopolymer matrix. *Procedia Engineering*, 21(0), 1124-1131.
- Nematollahi, B., Sanjayan, J., & Shaikh, F. U. A. (2014). Comparative deflection hardening behavior of short fiber reinforced geopolymer composites. *Construction and Building Materials*, 70, 54-64.
- Nematollahi, B., Sanjayan, J., & Shaikh, F. U. A. (2016). Matrix design of strain hardening fiber reinforced engineered geopolymer composite. *Composites Part B: Engineering*, 89, 253-265.
- Ng, T. S., Amin, A., & Foster, S. J. (2013). The behaviour of steel-fibre-reinforced geopolymer concrete beams in shear. *Magazine of Concrete Research*, 65(5), 308-318.
- Pan, Z., Sanjayan, J. G., & Rangan, B. V. (2011). Fracture properties of geopolymer paste and concrete. *Magazine of Concrete Research*, 63(10), 763-771.
- Ranjbar, N., Mehrali, M., Mehrali, M., Alengaram, U. J., & Jumaat, M. Z. (2016). High tensile strength fly ash based geopolymer composite using copper coated micro steel fiber. *Construction and Building Materials*, 112, 629-638.
- Ranjbar, N., Talebian, S., Mehrali, M., Kuenzel, C., Cornelis Metselaar, H. S., & Jumaat, M. Z. (2016). Mechanisms of interfacial bond in steel and polypropylene fiber reinforced geopolymer composites. *Composites Science and Technology*, 122, 73-81.
- Roviello, G., Menna, C., Tarallo, O., Ricciotti, L., Ferone, C., Colangelo, F., . . . Cioffi, R. (2015). Preparation, structure and properties of hybrid materials based on geopolymers and polysiloxanes. *Materials & Design*, 87, 82-94.
- Shaikh, F. U. A. (2013). Deflection hardening behaviour of short fibre reinforced fly ash based geopolymer composites. *Materials & Design*, 50, 674-682.
- Shaikh, F. U. A. (2013). Review of mechanical properties of short fibre reinforced geopolymer composites. *Construction and Building Materials*, 43(0), 37-49.
- Shaikh, F. U. A., & Supit, S. W. M. (2015). Compressive strength and durability properties of high volume fly ash (HVFA) concretes containing ultrafine fly ash (UFFA). *Construction and Building Materials*, 82, 192-205.
- Shi, C., Jiménez, A. F., & Palomo, A. (2011). New cements for the 21st century: The pursuit of an alternative to Portland cement. *Cement and Concrete Research*, 41(7), 750-763.
- Singh, B., Ishwarya, G., Gupta, M., & Bhattacharyya, S. K. (2015). Geopolymer concrete: A review of some recent developments. *Construction and Building Materials*, 85, 78-90.
- Soetens, T., Van Gysel, A., Matthys, S., & Taerwe, L. (2013). A semi-analytical model to predict the pull-out behaviour of inclined hooked-end steel fibres. *Construction and Building Materials*, 43, 253-265.

- Sofi, M., van Deventer, J. S. J., Mendis, P. A., & Lukey, G. C. (2007). Engineering properties of inorganic polymer concretes (IPCs). *Cement and Concrete Research*, 37(2), 251-257.
- Sumajouw, D. M. J., Hardjito, D., Wallah, S. E., & Rangan, B. V. (2007). Fly ash-based geopolymer concrete: study of slender reinforced columns. *Journal of Materials Science*, 42(9), 3124-3130.
- Xu, H., & Van Deventer, J. S. J. (2000). The geopolymerisation of alumino-silicate minerals. *International Journal of Mineral Processing*, 59(3), 247-266.
- Xu, Z., Hao, H., & Li, H. (2012). Dynamic tensile behaviour of fibre reinforced concrete with spiral fibres. *Materials & Design*, 42, 72-88.
- Xu, Z., Hao, H., & Li, H. N. (2012). Experimental study of dynamic compressive properties of fibre reinforced concrete material with different fibres. *Materials & Design*, 33, 42-55.
- Yunsheng, Z., Wei, S., Zongjin, L., Xiangming, Z., Eddie, & Chungkong, C. (2008). Impact properties of geopolymer based extrudates incorporated with fly ash and PVA short fiber. *Construction and Building Materials*, 22(3), 370-38.

CHAPTER 5 MECHANICAL PROPERTIES AND BEHAVIOUR OF HIGH-STRENGTH PLAIN AND HYBRID- FIBER REINFORCED GEOPOLYMER COMPOSITES UNDER DYNAMIC SPLITTING TENSION

5.1 Abstract

Geopolymer materials have been of particular interest to the construction industry due to their environmental benefits. However, their behaviour has rarely been investigated under dynamic loadings, although it is of fundamental concern to assess their vulnerability against higher loading rates. In this study, the dynamic tensile properties of a newly fabricated high-strength ambient cured geopolymer material and fiber reinforced geopolymer composites (FRGC) are presented. Since geopolymers are intrinsically brittle, novel equal-part blend of hooked-end and spiral-shaped steel fibers at two different fiber volume fractions and hybrid steel-polyethylene combination were used to reinforce the geopolymer matrix. The quasi-static splitting tensile tests were performed using a 300 kN displacement controlled Shimadzu test machine, while a modified Ø100-mm split Hopkinson pressure bar (SHPB) apparatus was used to conduct the dynamic splitting-tensile tests. A high-speed camera was used to capture the fracture development processes and crack-opening of different types of FRGC. The test results show that under quasi-static splitting tension, the unreinforced geopolymer exhibited minimal tensile strain capacity. With the addition of steel fibers and hybrid steel-polyethylene fiber reinforcement, the energy absorption capability of FRGC samples was significantly improved. The dynamic tests reveal the strong strain rate dependency and prominent tensile strength enhancements for all composites, although unreinforced geopolymer samples were more sensitive to the strain rate effect within the considered test range. A comparison between the test data and modified CEB guidelines reflect the non-suitability of code formulae to establish the dynamic increase factor (DIF_f) relation for geopolymers. Based on the test data, empirical DIF_f relationships are proposed for unreinforced and different types of FRGC samples. It is also indicated by image analyses that the excellent bonding of spiral steel fibers with the geopolymer matrix is befittingly complemented by polyethylene fibers to maintain the material integrity.

5.2 Introduction

Geopolymer materials have shown potential as a binder in the concrete industry and received particular attention (Davidovits, 1991). Unlike OPC, the synthesis of these novel binders

involve geopolymerisation reaction and have opened up new applications due to their versatile properties (Rahier et al., 1996). Previous research shows that geopolymer materials can achieve comparable performance to that of OPC with some additional benefits, such as conservation of virgin resources and increased use of industrial by-products (Khale and Chaudhary, 2007), reduced global warming potential (Duxson et al., 2007), high early-age strength (Hardjito et al., 2004; Atiş et al., 2015), increased durability (Thokchom et al., 2009), and better fire endurance (Pan and Sanjayan, 2010; Hosan et al., 2016).

As far as their materials properties are concerned, a majority of the previous experimental studies were carried out in the quasi-static regime. These investigations establish the microstructure development (Fernández-Jiménez et al., 2005), or the influence of many factors on the mechanical properties (i.e., compressive strength, Young's modulus, and tensile strength) of geopolymers (Mustafa et al., 2012; Khan et al., 2016; Khan et al., 2017). Others improved their structural resilience, fracture toughness, and limited tensile strain capacity by including different types of fibers (natural, metallic, synthetic, organic, and glass) (Dylmar Penteadó Dias, 2005; Shaikh, 2013; Ranjbar et al., 2016; Gao et al., 2017; Khan et al., 2018b) or polymeric fillers (Menna et al., 2015) in various geopolymer formulations. It is worth mentioning that structures in their designed lifespan are vulnerable to natural hazards and may well be subjected to unwanted vehicle impacts or accidental explosions, etc. Under these dynamic loading conditions, the materials endure high-rate deformation, and the response characteristics of structures are significantly different from those observed in the quasi-static loading modes.

Although the effect of strain rate has been studied extensively on OPC concrete (Bischoff and Perry, 1991), limited studies have considered the dynamic material properties of geopolymer-based construction materials. For geopolymer based mortars, concretes, and composites, though few in numbers, previous studies have predominantly focused on the dynamic compressive properties and damping behaviour (Pan et al., 2013; Xin et al., 2014; Feng et al., 2015; Gao et al., 2015). It has been found that the geopolymer materials exhibit strong strain rate sensitivity in compression (Khan et al., 2018a). However, their tensile behaviour under high loading rates has rarely been investigated. So far, only three studies report the dynamic tensile properties of geopolymers at high-rate loadings in the literature (Luo and Xu, 2013; Feng et al., 2014; Menna et al., 2015) with fundamental differences include the nature of source materials, curing conditions, sample sizes, and the size of split Hopkinson pressure bar (SHPB) equipment.

For example, Menna et al. (2015) studied the dynamic splitting-tensile properties of metakaolin-based geopolymers and hybrid-organic, inorganic metakaolin composites at

medium and high strain rates (i.e., 5 sec^{-1} and 150 sec^{-1}). It should be noted that metakaolin is expensive and may not be suitable for large-scale applications. Samples ($\text{Ø}20 \text{ mm} \times 20 \text{ mm}$) were cured at 60°C for 48 hours followed by their storage at a relative humidity of $> 95\%$ and in the air for the next 5, and 21 days, respectively. The test results indicated a strong strain rate dependency for the three types of materials and dynamic increase factor (DIF_f) of around 4 was observed under dynamic splitting tension. Furthermore, samples containing organic and inorganic polymer resins exhibited similar values of DIF_f at strain rates of 5 sec^{-1} and 150 sec^{-1} , respectively.

In another investigation, Luo and Xu (2013) reported the dynamic tensile characteristics of highly fluidized geopolymer concrete (GC) using the Brazilian test method. The GC was fabricated by activating a combination of slag and fly ash with sodium hydroxide (NaOH) and sodium carbonate (Na_2CO_3) solutions. Surprisingly, the authors gave the entire description of the materials' chemical composition, mixing, and the curing process; however, no details were provided for the mix proportions that were used for the sample preparation. Nevertheless, the synthesized GC exhibited strong rate sensitivity between strain rates $1 - 10 \text{ sec}^{-1}$, and the sensitivity threshold was found to exist at 5.027 sec^{-1} . The DIF_f values were found to vary from 1 to 3.70, and both the strength and deformation properties increased approximately linearly with the logarithm of the average strain rate.

In addition, Feng et al. (2014) investigated the dynamic splitting-tensile properties of three types of fly ash-based GCs and one geopolymer mortar under the strain rates of 10^{-7} sec^{-1} to 25 sec^{-1} . The geopolymer concrete and mortar samples were cured in a preheated oven at 60°C for 24 hrs. Two differently sized SHPB equipment, i.e., $\text{Ø}14.5\text{-mm}$ and $\text{Ø}50\text{-mm}$ diameter were used for testing mortar and concretes samples, respectively. The results for geopolymer materials were also compared with a conventional grade 40 OPC concrete. It was found that both OPC and geopolymer based concretes showed similar damage mechanisms and inertial resistance was stated to be mainly responsible for the improvement in the tensile strength for strain rates higher than 1 sec^{-1} .

As apparent from the reviewed literature, the research gap is of a complex nature, i.e., previous studies have predominantly employed the heat curing method which may affect the dynamic material properties hence lead to different characteristics from the proposed mixes cured in the ambient environment. Moreover, a thorough understanding of dynamic material properties of geopolymer materials such as the effect of strain rate on their tensile strength, fracture development process, and energy absorption capability under high-rate loadings is also of considerable interest. In regards to the above limitations, a high-strength ambient-cured geopolymer mixture has been recently developed (Khan et al., 2016) which is reinforced with

novel equal-part combinations of hooked-end and spiral-shaped steel fibers and hybrid steel-polyethylene fiber combination. A complete description of fiber reinforcement can be found here (Khan et al., 2018b). The proposed composites showed excellent material characteristics in dynamic compression and under triaxial compression (Khan et al., 2018a; Khan et al., 2018c). However, the tensile properties of the synthesized geopolymer composites at high strain rates are unknown.

Therefore, in this study, the quasi-static and dynamic splitting-tensile properties of the newly fabricated ambient-cured high-strength geopolymer composite materials are presented. A Ø100-mm Split-Hopkinson Pressure bar (SHPB) is used to characterize the dynamic tensile performance of the synthesized materials. The obtained results are related to the respective quasi-static test cases, and the DIF_{ft} curves are generated to describe the material behaviours at higher strain rates. Moreover, the results for plain geopolymer matrix are compared with the latest CEB recommendations and those reported by other researchers on the tensile strength enhancement of geopolymers. The damage processes and crack opening displacements (COD) for different types of geopolymer samples at different loading rates are obtained by the high-speed camera and digital image correlation (DIC) technology. The post-test failure modes of the specimens both after the quasi-static and dynamic tests are also presented.

5.3 Materials and Experimental methods

5.3.1 Description of materials

5.3.1.1 Fly ash and slag

Fly ash with parameters satisfying the guidelines of ASTM C618 (ASTM, 2012a) for type “F” and construction grade slag is used in the sample preparation. Additional details on the particle-size distribution and chemical oxide composition of aluminosilicate materials are available in (Khan et al., 2018c).

5.3.1.2 Alkaline solution, fine aggregates, and water

The alkaline activator used in this study is a mixture of D-grade Na_2SiO_3 (specific gravity = 1.53cc/g) and 12M NaOH solution at a mass ratio ($\text{Na}_2\text{SiO}_3/\text{NaOH}$) of 2.50, while local silica sand with a maximum particle size of 1.18mm is prepared in saturated surface dry (SSD) as recommended by ASTM C128 (ASTM, 2015b). Other information on the suppliers of chemical activators and procedure for preparing NaOH solution with ordinary potable water can be found in earlier studies (Khan et al., 2018c).

5.3.1.3 Fibers

Three types of fibers, i.e., spiral steel (donated as SS), hooked-end steel (HS) and the high-strength polyethylene (briefed as HSPE) fibers are used for geopolymer material reinforcement. The visual appearance, source locations, and the technical specifications of fibers are provided in (Khan et al., 2018c).

5.3.2 Mix proportion and fiber combinations

Four different types of geopolymer composites are considered in this study, i.e., one unreinforced and three fiber-reinforced geopolymer composites. Table 5-1 shows the mix proportions and the fiber combinations used in each batch. As such, two of the steel fiber reinforced geopolymer composites (SFRGC) contain an equal-part composition of HS and SS fibers at two different volume fractions, i.e., 1.0% and 2.0%. While in the third series, a small volume fraction of steel fibers is replaced with high-strength polyethylene (HSPE) fibers maintaining an overall fiber volume fraction of 2% (labeled as HFRGC). The suggested hybrid-fiber reinforcement is found highly useful in the geopolymer matrix. The addition of HSPE fibers in a small percentage as a replacement of steel fibers have been observed to significantly increase the deflection capacity of geopolymer composites at the peak load in flexural tensile tests and generate multiple-cracking failure response.

Table 5-1 Mixture proportions of plain and fiber reinforced geopolymer composites

Mix ID	Mixture Proportions (kg/m ³)					w/s* ratio	Fiber Type	Fiber volume fraction (%)		Flow diameter (mm)
	FA	Slag	Sand	Na ₂ SiO ₃	NaOH			V _f	Total	
Plain Geopolymer	412	275	1100	295	118	0.28	-	-	-	145
SFRGC - 1	412	275	1100	295	118	0.28	HS [#] SS [^]	0.50 0.50	1.00	100
SFRGC - 2	412	275	1100	295	118	0.28	HS SS	1.00 1.00	2.00	85
HFRGC	412	275	1100	295	118	0.28	HS SS HSPE ^{&}	0.80 0.80 0.40	2.00	65

*w/s, water to solids ratio

[#]HS, hooked-end steel fibers

[^]SS, spiral steel fibers

[&]HSPE, high-strength polyethylene fibers

5.3.3 Sample preparation

Figure 5-1 depicts the entire process for the preparation of plain and fiber reinforced geopolymer composites (FRGC). A 70-liters large size pan mixer is used for the sample preparation, and a standard routine regarding the batching process of ingredients, fiber inclusion, mixing time, and curing procedure is followed (Khan et al., 2018b).. The mixtures were poured in $\text{Ø } 100 \text{ mm} \times 200 \text{ mm}$ steel molds. Upon the completion of curing period, the samples were cut into the desired size, i.e., $\text{Ø } 50\text{mm} \times 100 \text{ mm}$ for quasi-static and dynamic tensile tests and were polished and leveled along with $\text{Ø } 100 \text{ mm} \times 200 \text{ mm}$ size samples used for the quasi-static compression tests.

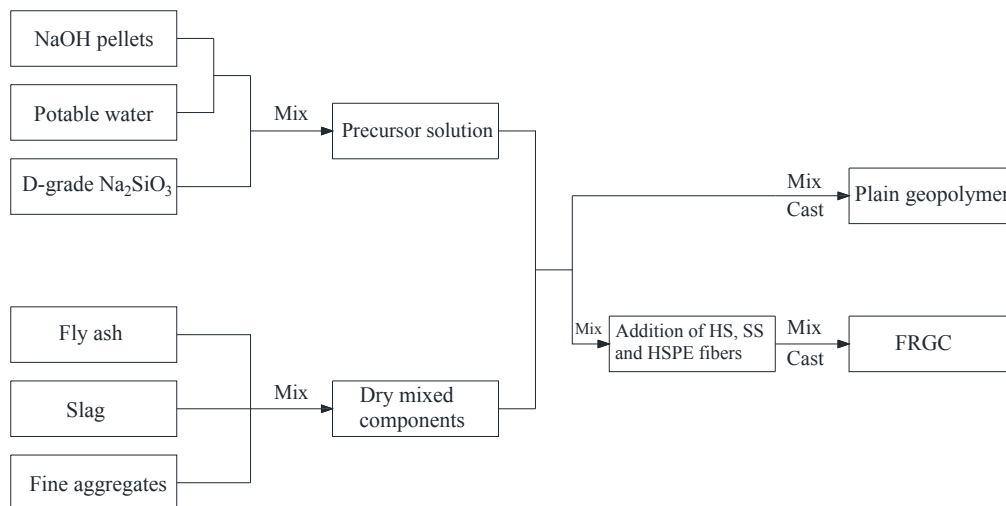


Figure 5-1 Flow chart for the preparation of plain geopolymer and FRGC.

Figures 5-2 (a) and (b) illustrate the final prepared specimens. It is to be noted that before dynamic tests, random stochastic speckle patterns were painted on the surface of samples to achieve good contrast. The process enabled performing the analysis in regards to the evolution of cracks (i.e., fracture development process and commonly crack opening displacements (COD)) in different types of samples during the impact loading. A brief description of the DIC technique follows in section 5.4.4.



Figure 5-2 Samples for (a) quasi-static compression (b) quasi-static and dynamic splitting-tensile tests.

5.4 Test Methods and Equipment details

Three types of apparatuses, i.e., 160-ton hydraulic test machine, displacement controlled 300 kN Shimadzu test machine, and \varnothing 100-mm SHPB equipment were used for the quasi-static and dynamic material tests, respectively. The following paragraphs provide a detailed description of each test method.

5.4.1 Quasi-static compressive strength and modulus of elasticity tests

According to the specifications of ASTM C39 (ASTM, 2015a) and ASTM C469 (ASTM, 2014), a set of three samples with dimension of \varnothing 100 mm \times 200 mm (i.e., length to diameter (L/D) ratio of 2.0) were tested from each series using a 160-ton hydraulic machine (see Figure 5-3). A sufficient amount of multi-purpose grease was smeared on the loading platens to reduce the end friction effects. Pairs of strain gauges were installed at mid-height of the specimens and separated apart by 180° to avoid any superfluous measurements contributed by the compression arm of the test machine. The tests were carried out at a loading rate of 0.25 ± 0.05 MPa, and the samples were firstly loaded to 40% of their ultimate load-carrying capacities, followed by unloading phase. The above procedure was repeated for two times to estimate Young's modulus (E). In the third cycle, the samples were loaded to the complete failure to determine the quasi-static compressive strengths.

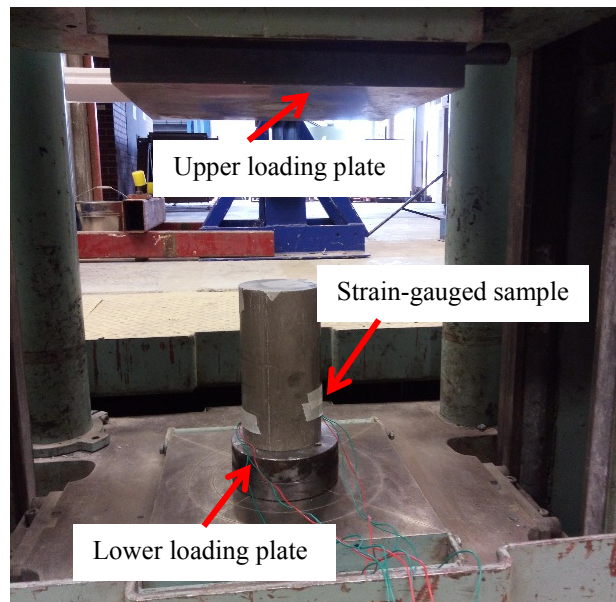


Figure 5-3 Testing set-up for quasi-static compression and strain-gauge installation.

5.4.2 Quasi-static split-tensile tests

The quasi-static split tensile tests were carried out on cylindrical samples with dimensions of $\text{Ø}100 \times 50$ mm. An L/D ratio of 0.5 was used instead of 2.0 as prescribed in ASTM C496 (ASTM, 2011) to maintain a consistent size for the test samples used in the dynamic tests. The approach has been commonly adopted by different researchers in the past to establish more reliable dynamic material properties, such as DIF_{ft} . Moreover, it is relevant to mention that the direct tension test method is an ideal choice to determine the tensile strength of concrete-like materials. However, in these conventional tests, the achievement of uniform stress-state throughout the specimen is extremely challenging, as premature failures are often observed around the grips due to the stress concentration. Besides, the complexities of variation in the loading process and attaching samples to the pressure bars in SHPB tests are eminent. In the same way, the fib model code recommends using notched beam specimens in three-point bend tests to establish the tensile strength of fiber reinforced materials via back calculation analysis (Beverly, 2013). However, the inertial resistance offered by the large samples in high-speed impact tests is significant which cannot be quantified directly. Hence, an accurate estimation of the material strength becomes difficult. An alternative approach which is more convenient for the instrumentation and allows better reliability for the strength results is the “Brazilian” or “Indirect -splitting tensile” tests.

During each splitting-tensile test, the sample under investigation was sandwiched horizontally between the upper and lower compression loading platens of the test machine as shown in Figure 5-4. The vertical load along the length of the cylinder was applied continuously at a

displacement rate of 0.5mm/min. Two pieces of 25 mm × 3 mm plywood as per ASTM C 496 (ASTM, 2011) were inserted between the compression loading plates and the test sample to prevent the compressive stress concentration around the point of load application and achieve more uniform stress distribution. The applied vertical force was recorded at a time interval of 0.1 sec via inbuilt load sensor, while an EPSILON clip-gauge extensometer was attached in the middle of the samples to measure the lateral deformation capacity (LDC) (see Figure 5-4). The extensometer had a measuring range of 10mm ± 10%. The tests were stopped either upon the sample failure (as in the case of plain geopolymer matrix) or until the lateral expansion of the samples reaching the measuring range of the extensometer.

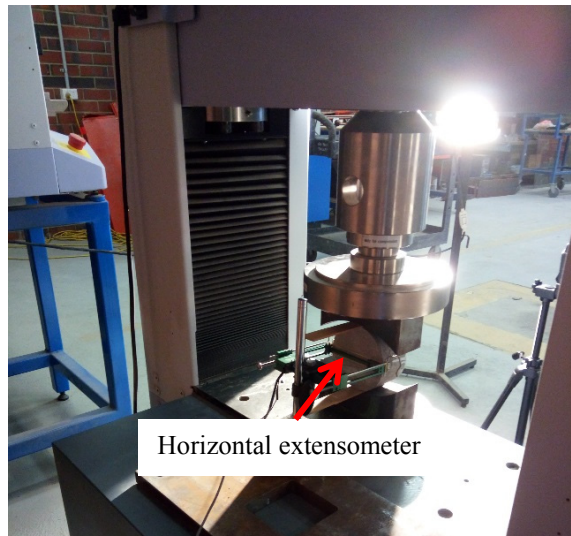


Figure 5-4 Testing set-up for quasi-static splitting tensile and extensometer installation.

5.4.3 Dynamic splitting-tensile tests and SHPB equipment

The dynamic material tests were performed at the Centre for Infrastructure Monitoring and Protection, Curtin University, Australia using the Ø100-mm split Hopkinson Pressure bar (SHPB) apparatus. Figure 5-5 illustrates the full SHPB test setup used in this study.

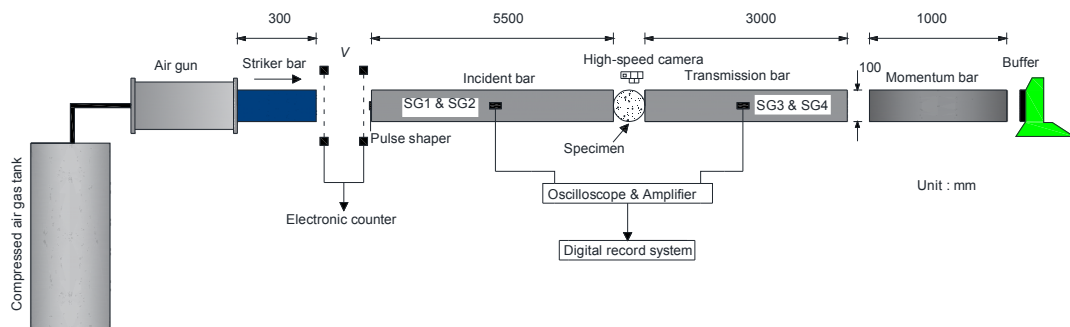


Figure 5-5 Schematic illustration of Split-Hopkinson pressure bar (SHPB) device.

As seen in Figure 5-5, the Ø 100mm SHPB device consists of the incident (I), transmitted (T), and absorption (A) bars having lengths of 5.5m, 3m, and 1m, respectively. All three bars are made of stainless steel with a density (ρ) of 7800 kg/m³, modulus of elasticity (E) of 200 GPa, elastic wave velocity (c_0) of 5100 m/sec, and Poisson's ratio (μ) of 0.30. Other devices included the oscilloscope, time counter, wheat-stone bridge strain-meter, and velocity measurement setups. During each test, the speckled sample was sandwiched between the (I) and (T) bars, and soft tissue was placed beneath the specimen to support it and prevent from sliding down under its weight before the test. The tensile stress within the samples was generated via far-end compression using a striker bar of 300 mm in length. Since the collision of two circular bars produces the square-shaped waveform, wave dispersion and wave oscillation are violent in larger sized pressure bars; a rubber pulse shaper (3 mm × 20 mm) was used to transform the loading waveform into a half-sine-like shape (Khan et al., 2018a). The entire fracture development process was captured with the assistance of an externally triggered high-speed camera. A transparent acrylic plastic box was used to cover the sample to prevent the debris scatter and protect the camera optics from the specimen fragments.

5.4.4 Digital image correlation (DIC) technique, set-up, and analysis

DIC is an optical contact-less method that allows full field measurements, such as displacements, strains, and COD, etc., on the surface of the objects by relating the images obtained during the different stages of the loading process. The technique has become increasingly popular for the material testing after the availability of high-speed cameras with high spatial and temporal resolutions. The whole principle relies on tracking 2-D stochastic patterns in a square reference subset $(2N + 1) \times (2N - 1)$ and counting the number of pixels both in the reference and a series of deformed images. The DIC algorithms compute the displacements in the center of each subset which are combined to establish the deformation over the entire region of interest (ROI). During the tests, the camera was placed at a certain distance away from the sample such that it allowed covering the full ROI for the image acquisition. The camera was positioned perpendicular to the object to avoid any pseudo strains due to the out of the plane movement and focused on getting a sharp image. Several previous studies have effectively used the DIC technique in SHPB tests to establish dynamic material properties of rock specimens [e.g., (Zhang and Zhao, 2013)], such as crack tip formation and fracture toughness, etc.

In this study, the DIC technique is primarily used to record the history of COD versus time for unreinforced and different types of FRGC samples due to the non-reliability of conventional measurement techniques (i.e., mechanical strain gauges) at higher loading rates. The high-speed camera was operated at a frame rate of 36,000 fps and resolution of 768 × 744

pixels to record at least two images before the stress wave arrived the specimen and several frames after the impact. It is to be noted that a critical point in DIC analysis is the proper scaling of the images which in the present study was performed by bringing in a scale in the first image for the calibration purposes. The recorded data are processed with the help of a commercially available open source free software “GOM Correlate.” The software has the capability of analyzing the video format instead of a series of images, the approach followed in this work. For more information, readers are encouraged to refer to the uniform resource locator (GOM, 2018).

5.5 Results and Discussions

5.5.1 Quasi-static compression test results (modulus of elasticity, compressive strength) and density

The quasi-static compressive strengths and other material parameters (i.e., modulus of elasticity and density) of plain and FRGC having different volume fractions and types of fibers are summarized in Table 5-2. Overall, it can be observed that the density of plain geopolymer matrix increased with the addition of steel fibers. Furthermore, the influence of fibers on the strength properties and modulus of elasticity of SFRGC samples is evident. It can be seen that the compressive strength of unreinforced geopolymer samples improved by 13% and 16.46% with the addition of 1.0% and 2.0% steel fibers, respectively. Similarly, the addition of steel fibers also had a positive influence on the elastic modulus of the plain geopolymer material.

However, the inclusion of HSPE fibers in replacement to steel fibers reduced the compressive strength and the stiffness of the matrix. A marginal reduction in the density of HFRGC samples was also due to the low unit weight of the HSPE fibers. The obtained results are consistent with previous work, where the inclusion of synthetic fibers reduced the compressive strength (Khan et al., 2018b). However, other material properties, such as the tensile strength and energy absorption capability (presented in next section) were significantly improved with the addition of synthetic fibers, i.e., a trade-off to enhance one material parameter by preceding the other. Upon the completion of tests, the unreinforced geopolymer samples failed violently and broke into several large pieces, while all types of FRGC samples retained their original shapes after sustaining the failure load.

Table 5-2 Quasi-static compressive strengths and material properties of plain geopolymer and FRGC

Mix ID	Dry density (kg/m ³)	Modulus of Elasticity (GPa)	Compressive Strength (MPa)
Plain geopolymer	2252.32 ± 9.01	25.41 ± 3.17	94.53 ± 0.68
SFRGC - 1	2296.28 ± 5.80	28.45 ± 0.76	106.95 ± 0.22
SFRGC - 2	2377.20 ± 24.3	30.60 ± 0.62	110.09 ± 1.24
HFRGC	2301.69 ± 6.16	23.24 ± 0.73	87.95 ± 3.26

5.5.2 Quasi-static splitting tensile results

The quasi-static splitting tensile strengths, calculated by Equation (5.1) of plain and FRGC samples are listed in Table 5-3.

$$\sigma = \frac{2P_o}{\pi L D^{\wedge}} \quad (5.1)$$

where σ is the quasi-static tensile strength, P_o is the maximum compressive failure load, L and D^{\wedge} are the length and the diameter of the samples, respectively.

Table 5-3 Quasi-static splitting tensile strength of plain geopolymer and FRGC

Mix ID	Tensile strength (MPa)				Avg. Tensile strength (MPa)	Standard deviation	Coefficient of variation (%)	Energy dissipated (N.m.)
Plain geopolymer	5.46	5.05	5.71	5.46	0.29	5.30	1.52	
SFRGC - 1	7.00	7.04	6.03	6.69	0.46	6.80	238.45	
SFRGC - 2	9.05	8.62	9.48	9.05	0.35	3.80	265.01	
HFRGC	9.30	9.00	9.47	9.26	0.19	2.00	394.64	

In Table 5-3, it can be seen that the unreinforced geopolymer matrix exhibited the lowest splitting tensile strength (5.46 MPa). There was a significant increase in the load-carrying capacity of the plain geopolymer with the addition of fiber reinforcement. The splitting tensile strength of SFRGC samples improved to 6.69 MPa and 9.05 MPa with the addition of 1.0% and 2.0% steel fibers, respectively. Moreover, the load carrying capacity of HFRGC samples was the highest among all types of composites, i.e., 9.26 MPa. It can be established that the splitting tensile strengths of the FRGC samples were 22%, 65%, and 70% higher than that of the unreinforced geopolymer material.

Figure 5-6 shows the typical load versus LDC plots for the plain geopolymer matrix and FRGC samples. It can be seen that the plain geopolymer samples were a lot weaker in tension in comparison to their compressive strengths. The unreinforced geopolymer samples showed extremely brittle failure and an insufficient tensile strain capacity. In contrast, the fiber reinforced geopolymer samples experienced large lateral displacements. During the tests, it was observed that SFRGC samples showed a linear elastic behaviour until a first crack was formed at a failure load similar to that of the plain geopolymer matrix. However, due to the presence of fibers, the load stabilized rapidly and started to increase until a second, third, and subsequently, several peaks were reached before the localization of a single crack. It is evident that the applied stress was effectively transferred between the fibers and the matrix. The most considerable deformation for the first crack was observed for the HFRGC containing hybrid-steel polyethylene fiber reinforcement.

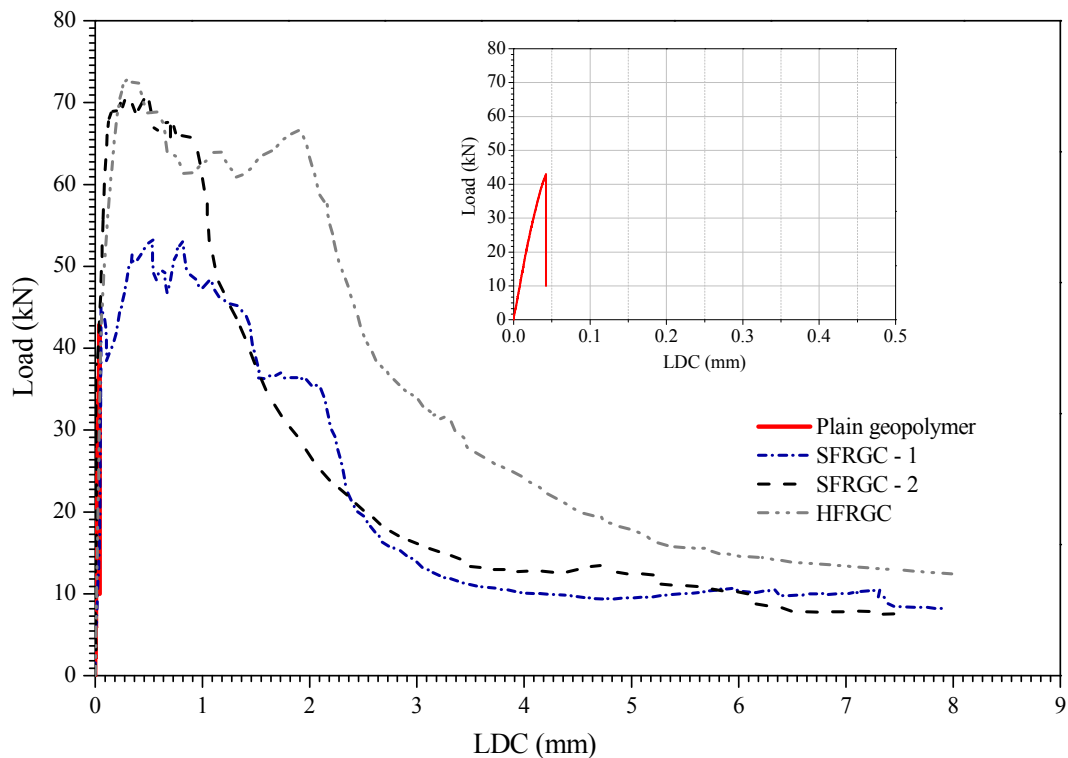


Figure 5-6 Comparison of quasi-static splitting tensile strengths vs. LDC of plain geopolymer and FRGCs.

The typical failure modes of unreinforced geopolymer samples, those reinforced with 1.0% of steel fibers and HFRGC are presented in Figure 5-7. For plain geopolymer samples, it can be seen that a single splitting-tensile crack caused the failure. The specimens were reasonably split into two halves immediately after reaching the maximum load. However, the SFRGC

specimens evidenced the existence of a strong bond between the fibers and the matrix. The spiral and hooked-end steel fibers were found firmly held by the geopolymer matrix spanning across a series of cracks which maintained the integrity of the samples. The cracks developed continuously during the tests as the spiral steel fibers were gradually stretched and hooked-end steel fibers pulled-out from the matrix. However, the extent of spiral steel fiber elongation was found to be more significant in the upper portion of the specimens as compared to the bottom sections. It is believed that the ability of spiral steel fibers to maintain the specimen integrity provided an additional mechanism for the load transfer between the split halves beside the fiber debonding process which allowed the SFRGC samples to carry more load than the plain geopolymer matrix in the post-crack region.

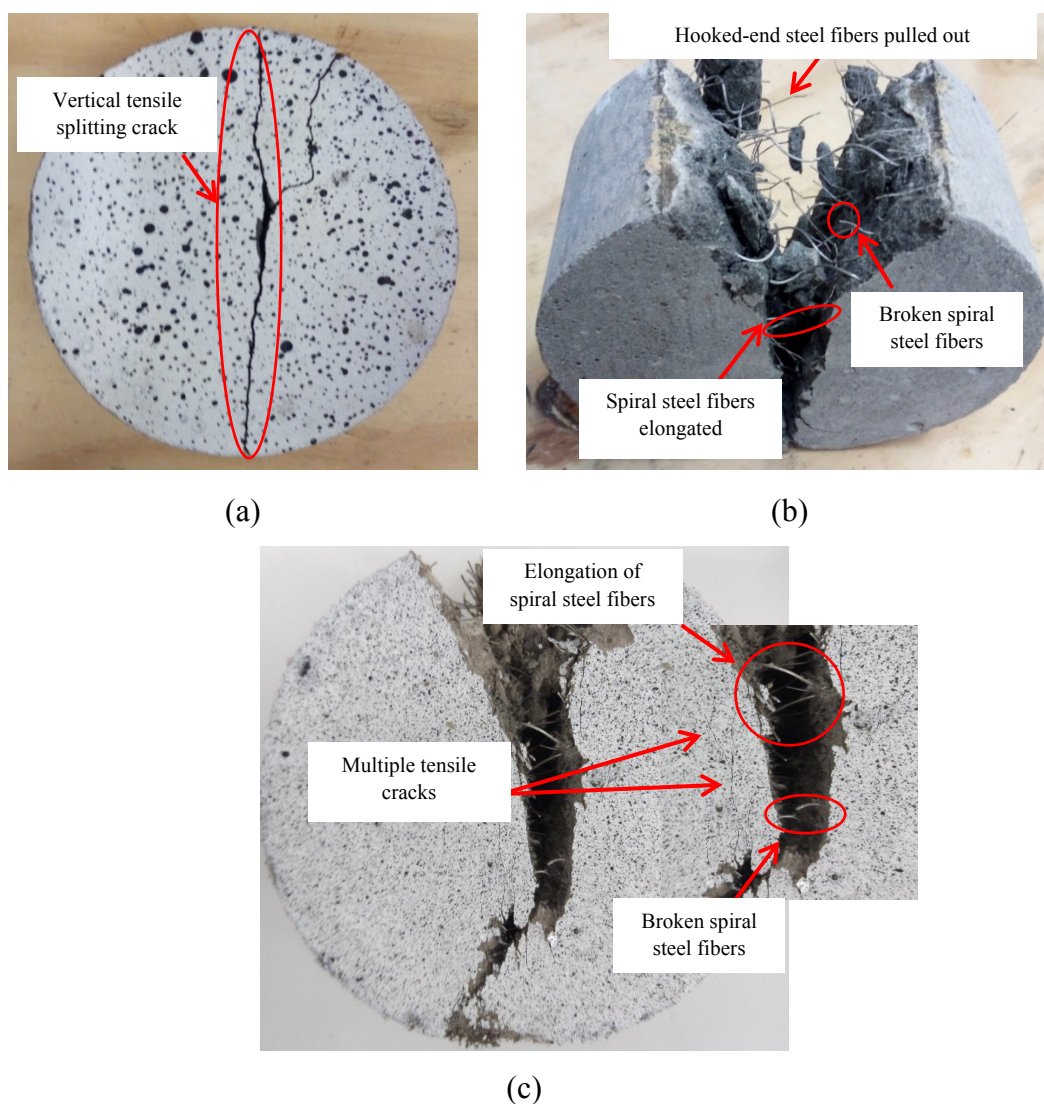


Figure 5-7 Failed samples (a) plain geopolymer (b) SFRGC-1 in quasi-static splitting tensile tests (c) HFRGC.

The inclusion of HSPE fibers in HFRGC series allowed the geopolymer composites to sustain even higher loads at increased lateral deformations. In this case, the hooked-end and spiral

steel fibers not only contributed towards improving the splitting-tensile strength but also the presence of HSPE fibers influenced both the peak load and LDC of the test samples due to their high strength and low stiffness. Published experimental results suggest that both spiral steel and HSPE fibers generate an efficient interfacial bond with the geopolymer matrix (Ahmed and Ronnie, 2017; Khan et al., 2018b). It is believed that due to their high strength, the HSPE fibers effectively bridged the wide splitting-tensile cracks without being fractured and generated multiple failure cracks hence resulting in an increased lateral deformation in addition to the lower rate of strength loss in the post-crack region. From Table 5-3, it can be seen that the HFRGC samples dissipated a significantly higher amount of energy in the tensile splitting mode in comparison to the plain geopolymer matrix. The specimens reinforced with 1.0% and 2.0% of steel fibers required 156 and 174 times more energy for the specimen fracture. Similarly, the energy consumed by the HFRGC samples was approximately 260 times more than that of the plain geopolymer samples. It is evident that the effectiveness of steel-fiber reinforcement was markedly enhanced with the addition of HSPE fibers.

5.5.3 Dynamic splitting-tensile SHPB test results

5.5.3.1 Processing of the SHPB test data

The data during SHPB tests was acquired at 2.5μsec interval using an oscilloscope and by attaching pairs of strain gauges, i.e., SG1 and SG2 on the incident bar and SG3 and SG4 on the transmitted bar (see Figure 5-7), respectively. The processing of the strain data depends on the assumption of 1-D stress wave propagation in the pressure bars. According to 1-D stress wave theory, for a long bar assumed to have a uniform, homogeneous, and isotropic cross-section throughout its length, the stress is in the linear elastic state. Upon the validity of this assumption, the amplitude of the transmitted strain $\varepsilon_t(t)$ is proportional to the peak strength (f_{td}) of the cylindrical samples in dynamic splitting-tensile tests as expressed in Equation (5.2). The stress-rate and the strain-rate in samples can be estimated using the formulations given in Equations (5.2) to (5.4) (Tedesco et al., 1993):

$$f_{td} = \left(\frac{R_b^2 E_b}{R_{so} H_{so}} \right) \varepsilon_t(t) \quad (5.2)$$

$$\dot{\sigma} = \frac{f_{td}}{t} \quad (5.3)$$

$$\dot{\varepsilon} = \frac{\dot{\sigma}}{E} \quad (5.4)$$

where f_{id} is the maximum dynamic tensile strength, R_{so} and H_{so} are the radius and height of the sample. R_B and E_B are the radius and modulus of elasticity of the pressure bars, $\varepsilon_t(t)$ is the transmitted strain, “ t ” is the time lag between the initiation to the peak of the transmitted stress wave, and E is the modulus of elasticity of the sample.

5.5.3.2 Typical voltage data output, stress-balance check in SHPB tests

A typical data set for voltage history is illustrated in Figure 5-8. The stress wave has three components, i.e., the incident, reflected, and transmitted. It can be noticed that the transmitted wave signal is rather weak in comparison to the incident or reflected wave. This is mainly due to the reason that the splitting tensile strength of geopolymer matrix is low in contrast to its compressive strength; hence, a significant portion of the elastic stress wave reflects along the incident bar as a tensile wave after the sample failure. The observation has a significant implication as far as the response of the fiber reinforced geopolymer samples is concerned and is discussed further in section 5.5.3.6. Moreover, it may be seen that the use of rubber pulse shaper has adequately transformed the loading waveform into a half-sine-like shape and increased the rise time considered beneficial to achieve dynamic stress equilibrium.

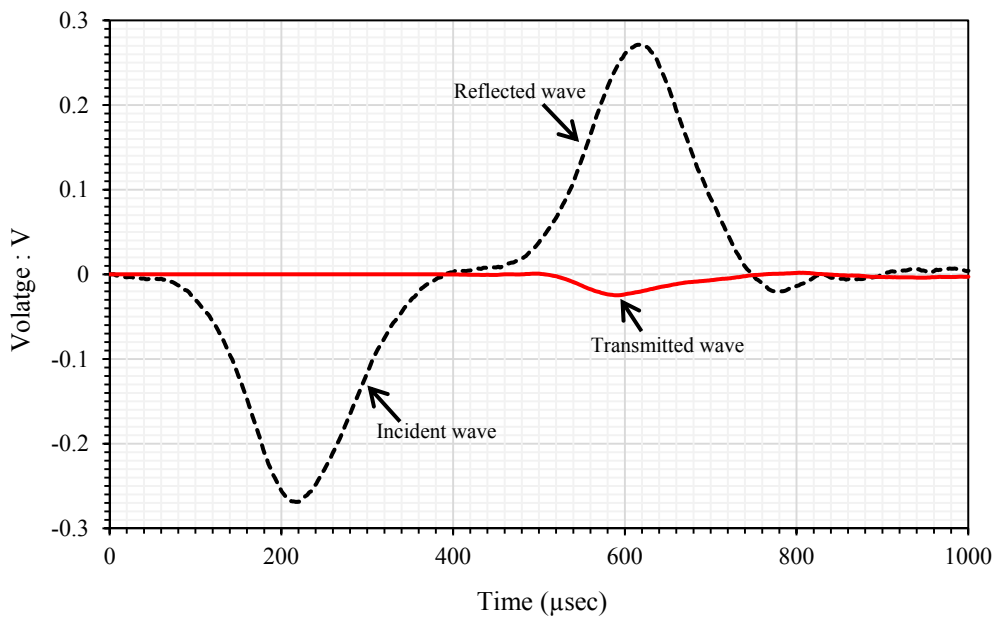


Figure 5-8 Typical waveform from SHPB dynamic splitting tensile tests.

As an example, Figure 5-9 shows the stress equilibrium check for a typical case after removing the time lags between the three types of waves. As observed, the stress at the incident end of the sample is very close to the transmitted stress over the complete data range and show that the stress equilibrium was achieved during the SHPB tests and specifies the reliability of results reported in this study.

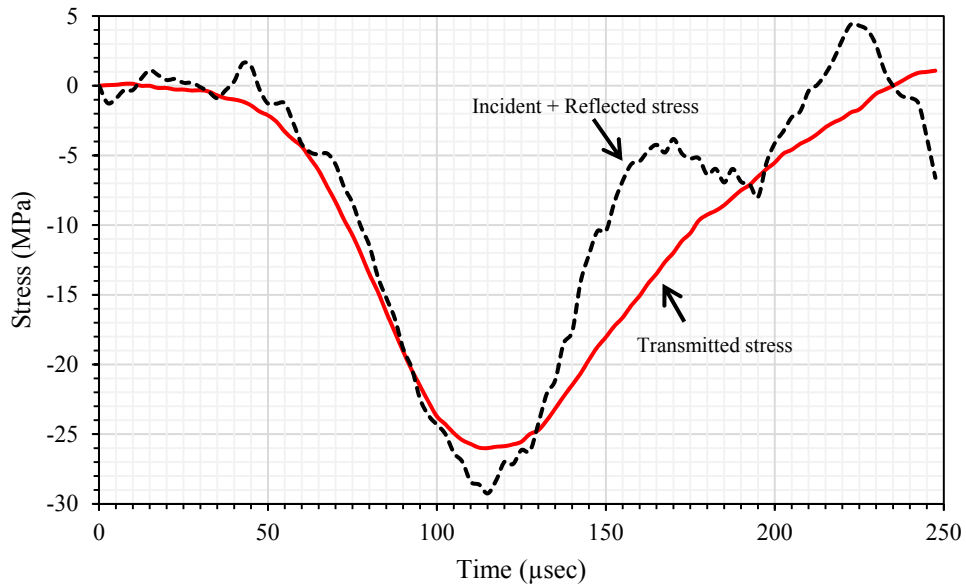


Figure 5-9 Typical dynamic stress equilibrium check.

5.5.3.3 Effect of strain rate on DIF_{ft} and tensile strength characteristics of plain and FRGC mixtures

The increase in the tensile strength of concrete-like materials is usually quantified in terms of the dynamic increase factor (DIF_{ft}) which is the ratio of the quasi-static (f_{ts}) and dynamic (f_{td}) material strength at higher loading rates. The parameter is expressed in Equation (5.5):

$$DIF_{ft} = \frac{f_{td}}{f_{ts}} \quad (5.5)$$

In the past, the DIF_{ft} versus strain-rate relationships for the tensile strength enhancement of concrete have been suggested in different design guidelines, e.g., the CEB concrete model code (CEB, 2013). The formulae allowed defining the concrete material behaviour more accurately for the design of reinforced structures and perform the numerical analysis. However, owing to the novelty of geopolymer binders, such empirical relationships or analytical models do not exist at present and is one of the objectives of this study. It is to be noted that, the DIF_{ft} curves are typically divided into two sections, i.e., an equation for the strain rate below the sensitivity threshold and the other from then on.

Previous studies on OPC concrete conclude that the DIF_{ft} curves tend to vary linearly with the logarithm of strain rate until the transition point beyond which a sharp increase occurs. From this stage onwards, different formulae can be found in the literature (Tedesco and Ross, 1993; Malvar and Ross, 1998; CEB, 2013; Hao et al., 2012; Hao and Hao, 2014). As such, in the experimental investigations carried out by Malvar and Ross (1998) and Tedesco and Ross (1993), the tension DIF_{ft} of concrete varied linearly with the logarithmic strain rate and the

strain rate sensitivity threshold was reported to exist at 1 sec^{-1} . However, other researchers recommend using bi-linear (Hao and Hao, 2014) and higher-degree polynomials (Hao et al., 2012) to describe the increase in the tensile strength of concrete past this threshold.

Figure 5-10 presents the dynamic tensile strength enhancement of plain geopolymer matrix with the DIF_{ft} test data on geopolymer concrete and mortar specimens from preceding studies. Besides, the recommended DIF_{ft} relation by CEB concrete model for concrete material with 94 MPa compressive strength are plotted. A prediction proposed by Feng et al. (2014) is also included for comparison. The graph shows that almost all data fall to the left of CEB DIF_{ft} for high-strength concrete. Furthermore, it is also interesting to note that the experimental results from all investigations suggest similar DIF_{ft} in tension for geopolymer materials irrespective of the strength or curing method used in their synthesis, i.e., either heat or ambient curing.

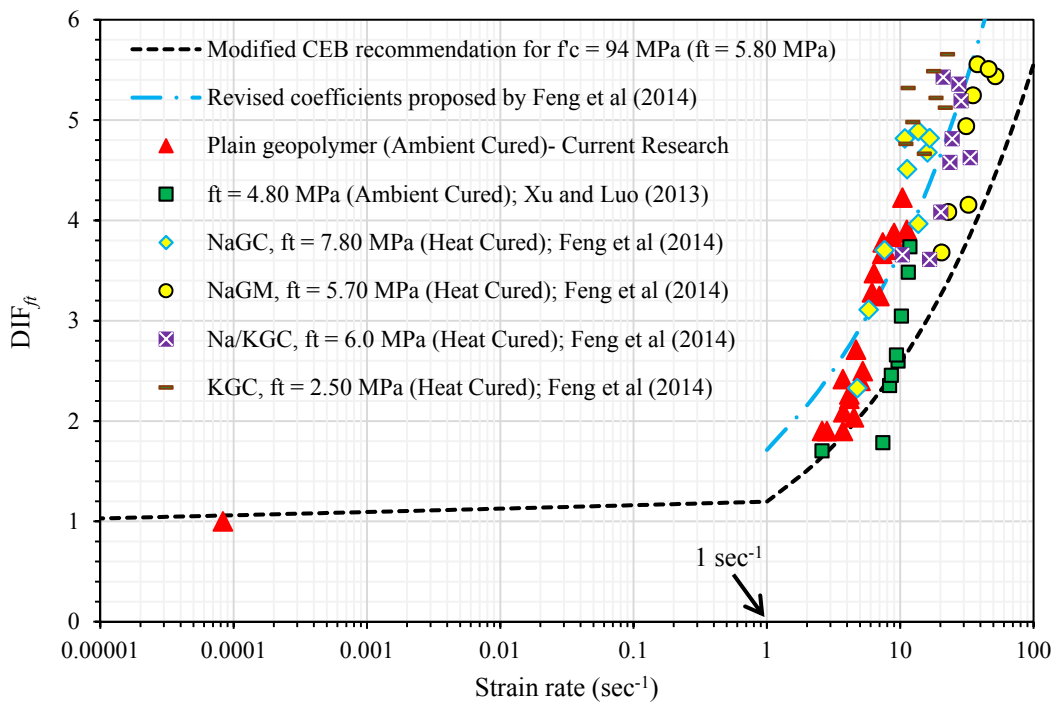


Figure 5-10 Comparison of DIF_{ft} of plain geopolymer with modified CEB recommendations and results from previous studies.

A minor variance in the scatter is probably due to the difference in the synthesis procedures, the mixture proportions, sample sizes, and the presence of coarse aggregates. It is believed that the difference of the binding gels formed during the geopolymerisation process from different types of activators plays a significant role in modifying the three-dimensional amorphous structure and the aggregate gel-interface properties. It is also evident from the graph that the modifications suggested by Feng et al. (2014) are not precise. The test data

points to a transition in slope for the DIF_{ft} scatter at a value higher than 1 sec^{-1} . Similarly, the existing modified CEB guidelines considerably underestimate the tension DIF_{ft} of geopolymers and are not appropriate for the design of geopolymer structures. Therefore, based on the existing results, empirical relations are proposed for the studied materials.

The influence of strain rate on the tensile strength of plain and FRGC samples is illustrated in Figure 5-11. It can be seen that all types of geopolymer mixtures show prominent tensile strength increase at higher loading rates. Based on the extensive test data, the fitting formulae for the constitutive relationships between the tensile strength and the average strain rate for different types of geopolymer composites are obtained.

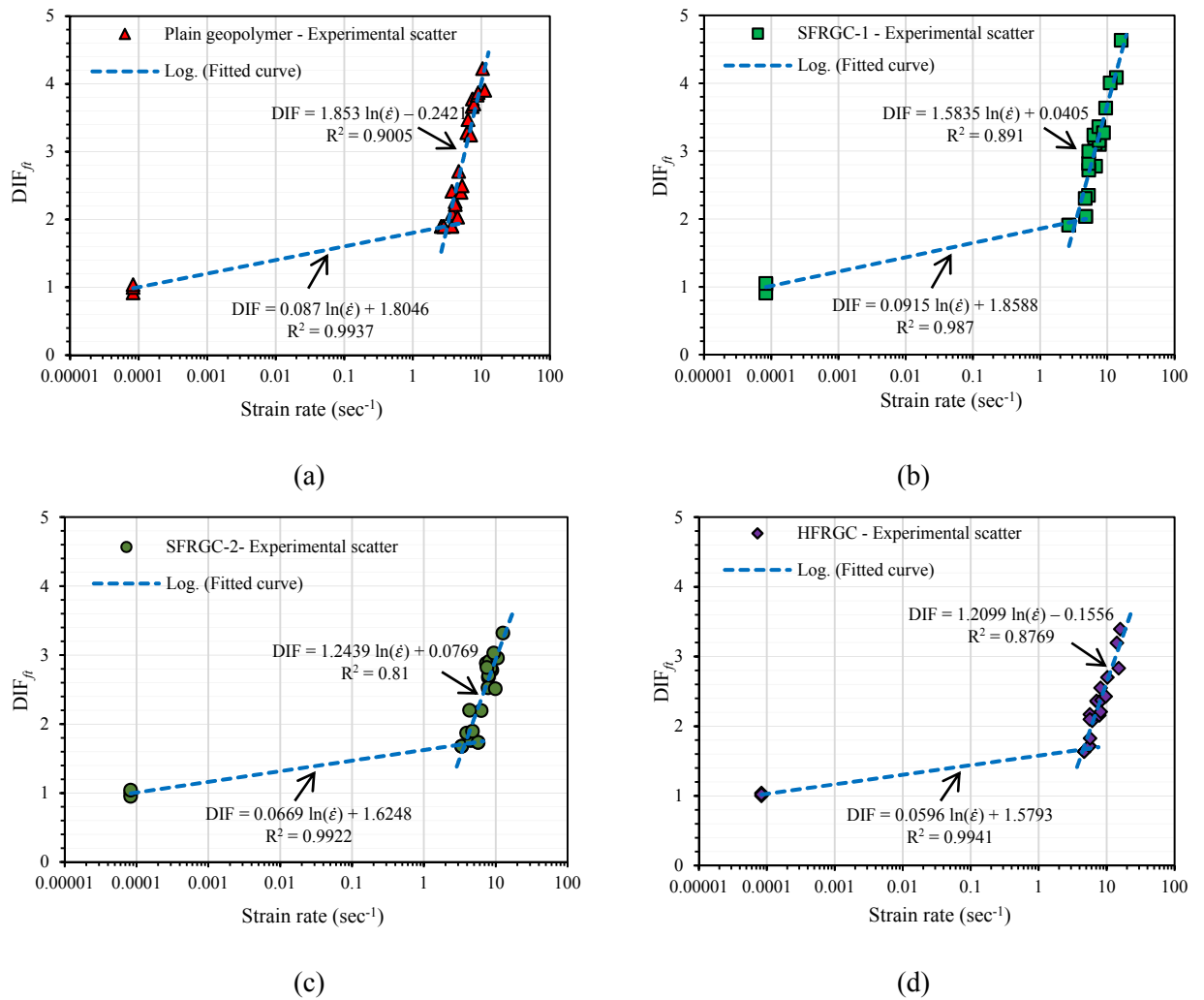


Figure 5-11 DIF_{ft} versus strain rate relationships of (a) plain geopolymer (b) SFRGC-1 (c) SFRGC-2 and (d) HFRGC.

The present study makes use of the linear approach to quantify the increase in the dynamic material strength for the unreinforced and FRGC mixtures due to better fitting, which is presented as follows:

$$DIF_{fi} = x \ln(\dot{\epsilon}) + y \quad 10^{-5} \leq \dot{\epsilon} \leq (\dot{\epsilon}) \quad (5.6)$$

$$DIF_{fi} = x_1 \ln(\dot{\epsilon}) + y_1 \quad (\dot{\epsilon}) \leq \dot{\epsilon} \leq 15.00 \quad (5.7)$$

where $(\dot{\epsilon})$ represents the strain rate sensitivity threshold, and x , y , x_1 , and y_1 are the parameter values for four types of geopolymer composites. The values for these material constants are listed in Table 5-4.

Table 5-4 Parameters values for DIF_{fi} formulae of geopolymer composites

Composite type	x	y	x ₁	y ₁	($\dot{\epsilon}$) sec ⁻¹
Plain geopolymer	0.0870	1.8046	1.853	-0.2421	3.00
SFRGC – 1	0.0915	1.8588	1.5835	0.0405	3.00
SFRGC – 2	0.0699	1.6248	1.2439	0.0769	4.00
HFRGC	0.0596	1.5793	1.2099	-0.1556	4.00

From Figures 5-11 (a-d) it can be established that although the addition of fibers into the plain geopolymer matrix is certainly useful to improve the dynamic material strengths (e.g., at a strain rate of 5 sec⁻¹, the strength for plain geopolymer, SFRGC-1, SFRGC-2, and HFRGC are 13.10 MPa, 15.67 MPa, 20.03 MPa, and 19.87 MPa respectively), the DIF_{fi} of plain geopolymer is higher than that of FRGC mixtures at a given strain rate. This implies that the dynamic tensile strength of plain geopolymer is more strain rate sensitive than FRGC mixtures and can be explained from different perspectives.

In FRGC composites the reinforcing material, i.e., steel and/or HSPE fibers are much less strain rate sensitive in comparison to the matrix (Malvar, 1998). In other words, at a given strain rate, the strength increment ratio of high-strength fibers from quasi-static action is a lot less, or even trivial, than that of the geopolymer matrix, although the fibers do contribute to the overall strength of the specimen. Moreover, according to the calculation of DIF_{fi} (Equation 5.5), the larger the denominator, the smaller the division result. Thus the inclusion of fibers reduces the overall strain rate sensitivity of the FRGC materials and display lower DIF_{fi} at higher strain rates.

Another more plausible justification is related to the existence of inevitable lateral inertial confinement in high-speed impact tests which improves DIF_{ft} (Hao and Hao, 2016). During quasi-static and low strain rate tests, cracks in the material expand to achieve mechanical equilibrium and the dynamic strength (f_{td}) is equal to the quasi-static strength (f_{ts}). When the loading rate approaches the critical strain rate ($\dot{\epsilon}$), and crack-opening velocity reaches its threshold, mainly due to the inertial resistance the deformation is surpassed. Once the deformation reaches a certain extent, macroscopic sample failure occurs due to the formation of new cracks with the expansion of existing ones. This translates into a sharp increase in the DIF_{ft} (see Figure 5-11), as the hysteresis process continues upon further increase in the strain rate. The qualitative trend presented by plain geopolymer material in this study is consistent with the behaviour of OPC concrete (Malvar and Ross, 1998).

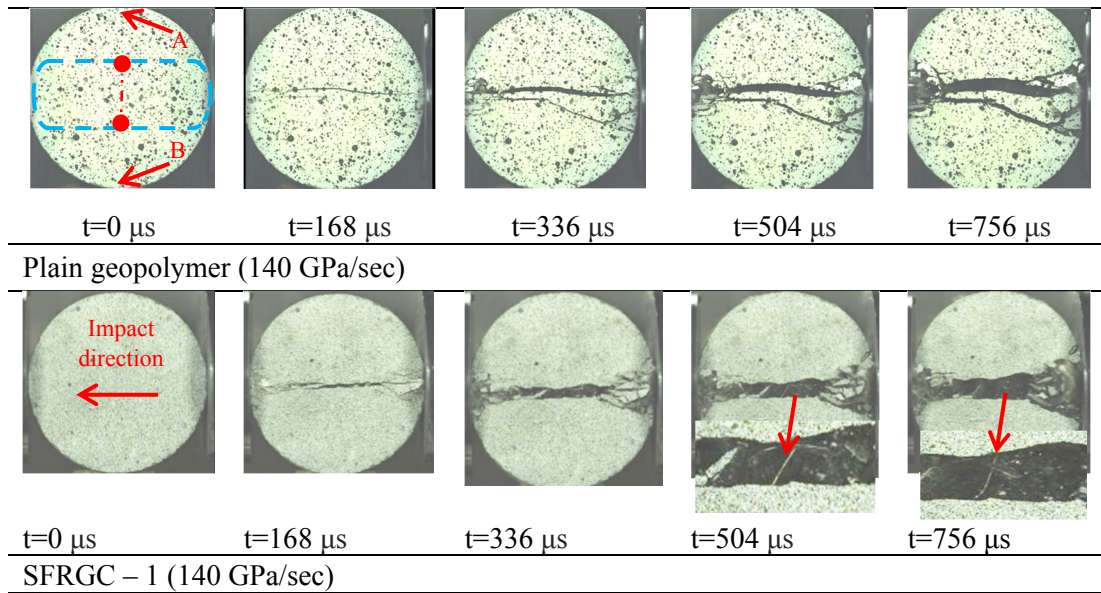
However, in the case of FRGC samples, the inclusion of fibers generate fewer failure surfaces as the fracture process zone is concentrated in a narrow area. This can be observed by comparing the damage patterns of different materials at 756 μ s in Figures 5-12 and 5-13. The fibers consume a part of the energy to slow the crack expansion and reduce the crack-opening velocity which leads to less significant strength enhancement under a similar loading rate. Higher the fiber volume fractions, the more the number of fibers arresting the crack development and lower the rate sensitivity. Since the current work also utilizes hybrid steel-polyethylene combination, the fitted curves for HFRGC series show the least DIF_{ft} increase at a given strain rate. For a small volume fraction, a relatively large quantity of fibers is incorporated into the matrix due to the higher aspect ratio which acts as a micro reinforcement. Under high-speed impact, HSPE fibers along with the spiral steel fibers tend to resist the radial expansion and significantly retard the crack expansion under the splitting-tensile loading. The discussion is further supported by the COD results presented in section 5.5.3.6.

5.5.3.4 Comparison of fracture development processes of plain and FRGC samples

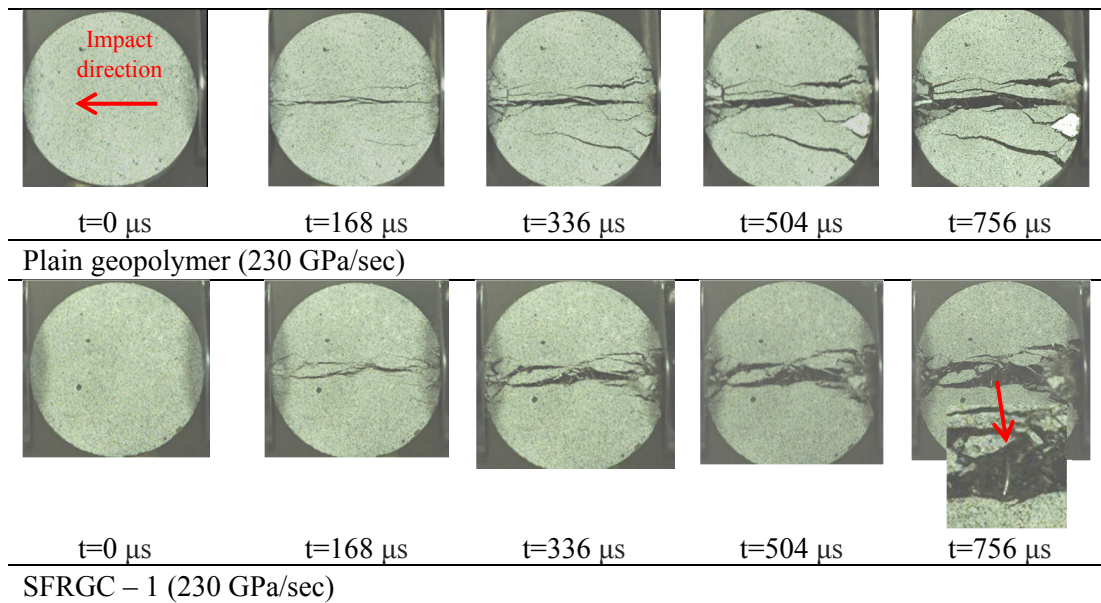
The fracture development processes of plain and fiber reinforced geopolymer samples are investigated from two aspects. At first, it is essential to identify the place of crack initiation in different specimens, i.e., whether the failure process started from the center. Secondly, the path of crack proliferation has to be along the loading diameter of the discs. Hence, to observe these two phenomena and establish a thorough understanding of the behaviour of plain and FRGC samples in dynamic splitting tension, each test was filmed with the assistance of a Photron (FASTCAM SA-Z) high-speed camera. The sample responses were acquired at a time interval of 28 μ s, and camera images are compared at different time instants to evaluate the effectiveness of fibers for crack control.

Generally speaking, in all types of samples, the cracks initiated from the middle where the tensile stress was maximum. However, the extent of crack propagation and crushed areas were dependent upon the type and fiber volume fraction. Figure 5-12 depicts a comparison between the failure processes of plain geopolymer matrix and SFRGC-1 samples under two different stress rates of around 140 GPa/sec and 230 GPa/sec, respectively. As observed in Figure 5-12, the elastic stress waves strike the samples from the right side. The time corresponding to the instant when the samples were stressed initially was set to zero; and, the first photograph in each typical case was used as a reference to compare the damage modes. For image analysis, two points were selected, marked as “A” and “B” on top and bottom of the samples. The pixel counts between these points were used as a reference to represent the original diameter of the specimen, i.e., 100 mm. A narrow bandwidth was then selected in the middle-third (as highlighted with blue lines) to define the ROI as the software automatically computed the facet points. Subsequently, a line was constructed to connect two points identified at the boundaries of ROI which symbolized the unchanged length. Upon impact, the change of distance between these dots established the crack opening displacements (COD) (see Figure 5-12(a)).

In the case of plain geopolymer matrix, it can be seen that at a loading rate of around 140 GPa/sec, the tested sample exhibited a diametrical split with minor compression damage appearing at the ends of the specimen at 504 μ s. When the stress rate was 230 GPa/sec, several major cracks had already developed in the sample at 336 μ s. Through comparison with the quasi-static tests in which plain geopolymer samples fractured into two halves; it is evident that at higher stress rates the formation of additional failure surfaces allowed more energy to be absorbed from the loading source and improved the tensile strength. The geopolymer samples reinforced with 1.0% of steel fibers also presented similar failure patterns, though the cracked areas were confined to crushed straps in the center beside the damage at the ends of the samples. At the time instants of 504 μ s and 756 μ s, an evident extension of spiral steel fibers can also be seen which reduced the crack opening velocity and resulted in smaller COD as given in Figure 5-15.



(a)

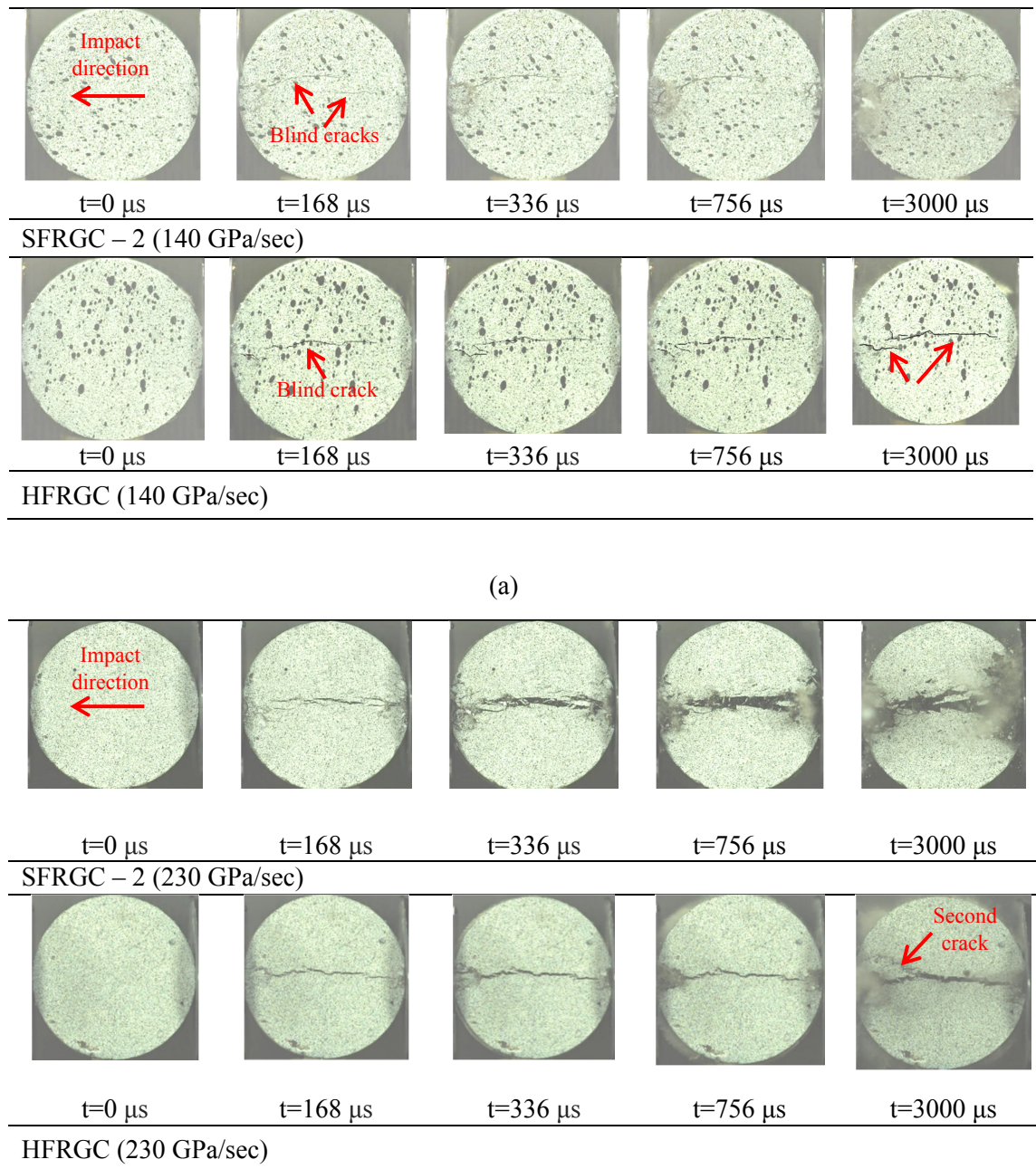


(b)

Figure 5-12 Failure modes and high-speed camera image comparison of plain geopolymer and SFRGC-1 samples under loading rates of (a) 140 GPa/sec (b) 230 GPa/sec.

Figure 5-13 compares the failure modes of samples from SFRGC-2 and HFRGC series containing 2.0% volume fraction of fibers. The fracture development processes of these samples were significantly different from that of plain geopolymer and SFRGC-1 series. It can be seen that under a stress rate of 140 GPa/sec, a first failure crack appeared in the center of the specimens at 168 μs . However, as the time elapsed, the tensile crack in SFRGC-2 sample perforated along the compressed direction and apparent specimen disintegration can be noticed after 756 μs and later at 3 msec at the ends. The test sample containing hybrid steel-

polyethylene fiber combination showed a minor end crushing damage with an apparent tensile crack opening at 3 msec.



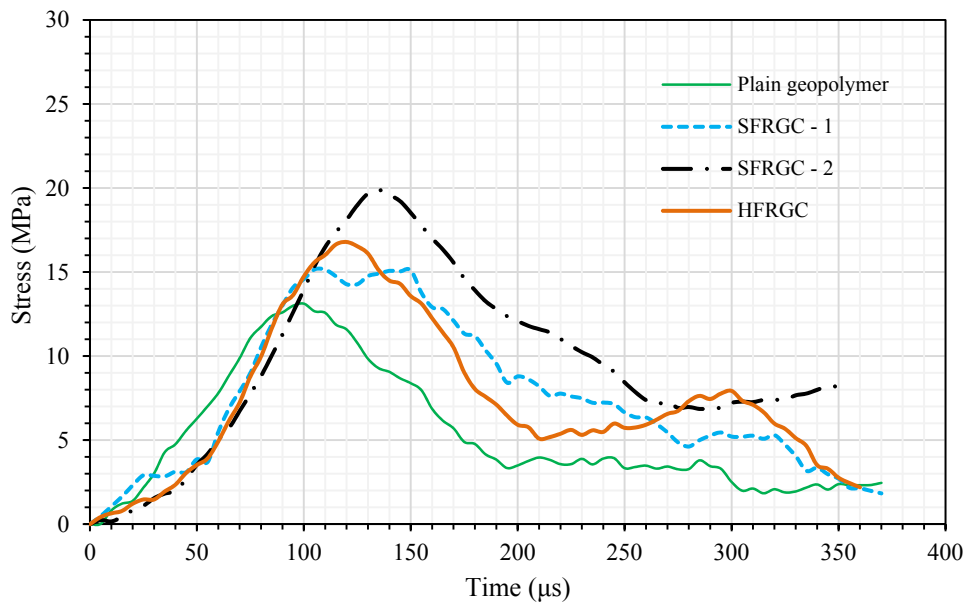
(a)

(b)

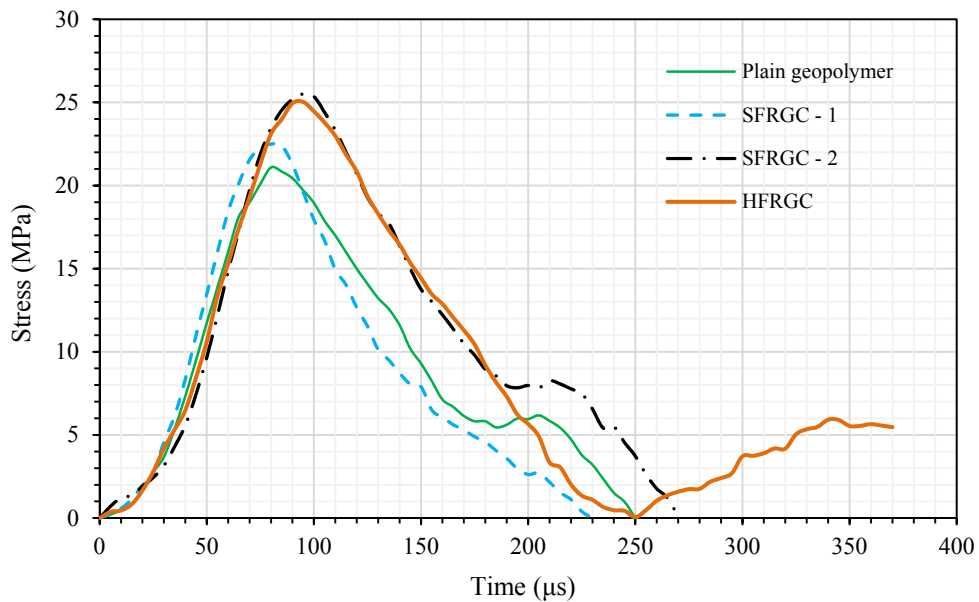
Figure 5-13 Failure modes and high-speed camera image comparison of SFRGC-2 and HFRGC samples under loading rates of (a) 140 GPa/sec (b) 230 GPa/sec.

At the stress rate of 230 GPa/sec, the initiated cracks in both types of samples propagated rapidly towards the ends at 168 μ s. However, the extent of damage in SFRGC-2 and HFRGC samples was less severe in comparison to SFRGC-1 series at this time instant. At around 336 μ s, multiple failure cracks formed in the middle of SFRGC-2 sample as spiral steel fibers were

stretched and damage appeared alongside the split halves. Later, the crack opened further, and crushed zones were produced on the two bar/geopolymer interfaces at 756 μs and 3 msec, respectively for SFRGC-2 and HFRGC. However, the HFRGC sample showed less radial expansion than SFRGC-2 specimen. In addition to end crushing damage, a second crack developed after a series of impacts at 3 msec. Figure 5-14 presents the corresponding tensile stress time histories for all of the samples under these loading rates.



(a)



(b)

Figure 5-14 Comparison of tensile stress time histories of plain geopolymer and FRGC samples under loading rates of (a) 140 GPa/sec (b) 230 GPa/sec.

5.5.3.5 Comparison of crack-opening displacement (COD) of plain and FRGC samples

For the above presented typical cases, the videos recorded by the high-speed camera at a loading rate of 230 GPa/sec were processed with the DIC technique for crack opening displacements. Figure 5-15 presents a comparison between the COD time histories for the unreinforced and fiber reinforced geopolymer samples up to a time duration of 1 msec. It can be seen that the COD in HFRGC sample was only 6.5% of that of plain geopolymer material at 1msec. Similarly, the samples containing equal-part combinations of hooked-end and spiral steel fibers at fiber volume fractions of 1.0% and 2.0% reduced the COD of unreinforced geopolymer samples by 27% and 61%, respectively. It is evident that the addition of hybrid steel-polyethylene fiber combination has unusually slowed the crack development process in the matrix and crack opening velocity under splitting tension.

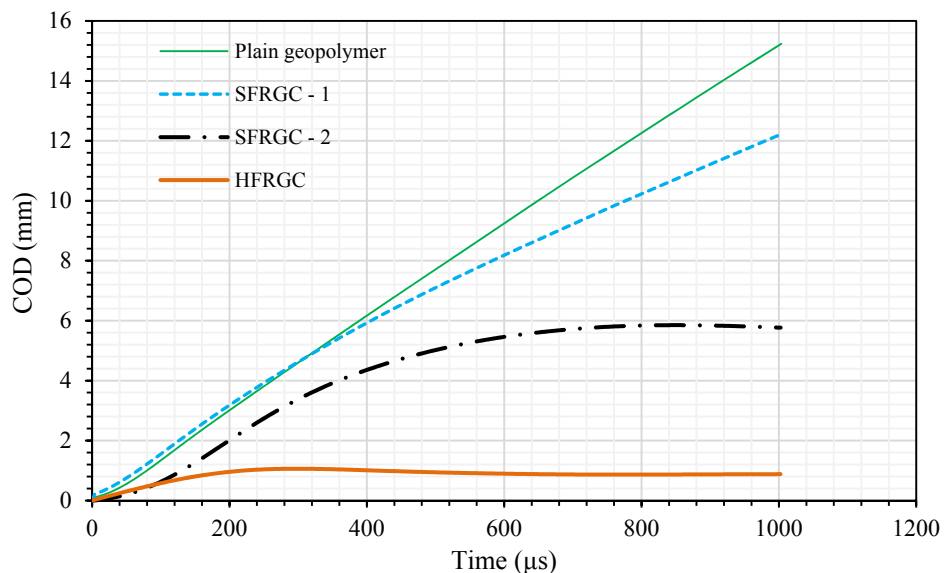


Figure 5-15 Comparison of COD time histories of plain geopolymer and FRGC samples under stress rate of 230 GPa/sec.

As mentioned in section 5.5.3.2, in dynamic splitting tensile tests, when the stress wave strikes the discs, due to the impedance mismatch at the specimen-bar interface, a significant portion of the elastic compressive stress wave rebounds into the incident bar. After reflection, the tensile wave travels through the incident bar and reaches the far end. Once at the free end, the stress wave reverses its direction and gives another strike to the damaged sample. The process mentioned above is repeated except when the specimen fails in the first impact (as in the case plain geopolymer), or it is no longer in contact with the incident and transmitted bars. Usually, for the strength analysis in SHPB technique, the first incident, transmitted, and reflected peak voltage signals are used to check the stress balance and establish the dynamic strength of the material. However, it has been observed that at an increased fiber volume fraction, the fibers

can withstand the initial loading and may resist the subsequent impacts. Although these succeeding impacts have less significance for the dynamic strength analysis, it can provide a qualitative estimate for the effectiveness of a specific fiber type or fiber combination used for reinforcement purposes.

In order to further explain this point, a comparison is shown in Figure 5-16 between the COD time histories of samples from SFRGC-2 and HFRGC series over an extended time duration of 6 msec. It can be seen that even after a series of impacts, at 5 msec the COD in SFRGC-2 and HFRGC samples were significantly lower than that of the unreinforced geopolymer material. Moreover, it can also be established that for both types of materials, a portion of COD was recovered to some extent after the first impact. The initial COD of HFRGC was remarkably small in comparison with that of SFRGC-2, and the hysteresis of crack recovery continued after each impact. This is an interesting observation which signifies the ability of spiral steel fibers to generate an efficient bond with the geopolymer matrix and improve the post-peak ductility by maintaining the integrity of samples. A previous study (Hao and Hao, 2016) also reported similar failure mechanism where spiral steel fibers were included in the ordinary strength OPC concrete to improve the tensile properties. It is evident that the use of HSPE fibers in combination with the hooked-end and spiral steel fibers in this research have significantly transformed the non-ductile behaviour of unreinforced high-strength geopolymer matrix.

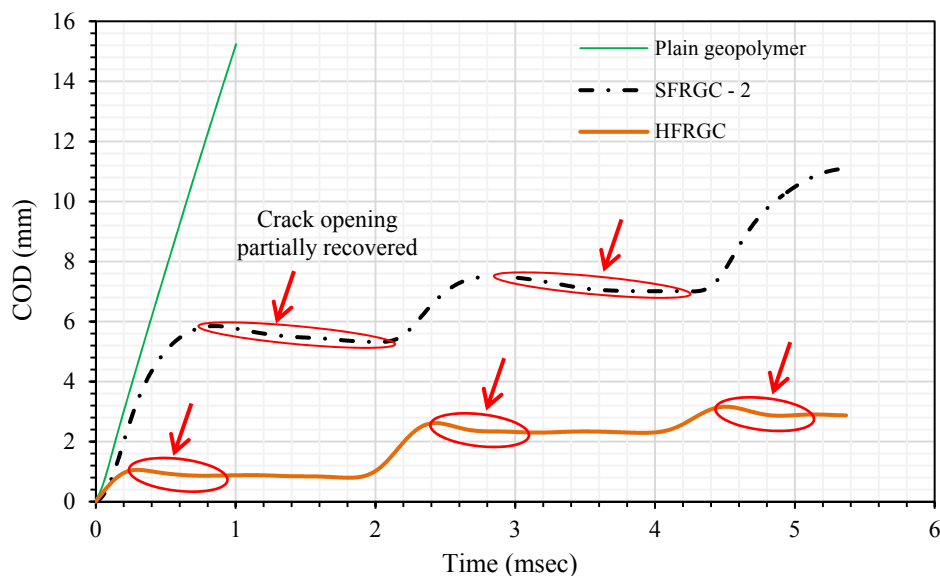


Figure 5-16 Comparison of COD time histories of SFRGC-2 and HFRGC samples over extended time duration.

5.5.3.6 Comparison of post-test failure patterns of plain geopolymer and FRGC samples

Figure 5-17 compares the typical post-test failure patterns of plain geopolymer, SFRGC, and HFRGC samples under two different splitting loading rates of around 150 GPa/sec and 200 GPa/sec, respectively. In general, it can be seen that the post-test failure patterns of both plain geopolymer and FRGC samples are stress rate dependent. For plain geopolymer, it can be seen that the failure modes under different loading rates are very similar, i.e., the tested samples primarily fractured into two halves and most of the disintegration was observed in the middle alongside some partial triangular damage at the ends. This is mainly due to the reason that in splitting tensile tests, the process of crack initiation and proliferation is limited to the loading diameter because of the maximum and uniform stress along this section under splitting load. For SFRGC-1 series, it can be seen that at a loading rate of 150 GPa/sec, the sample retained its structural integrity upon the impact and many spiral steel fibers were found elongated. However, at a higher stress rate (200 GPa/sec), the sample from this batch also split into two halves. It can be seen that almost the entire cluster of spiral steel and hooked-end steel fibers was pulled-out and unbonded from both sides of the matrix to resist the crack propagation.



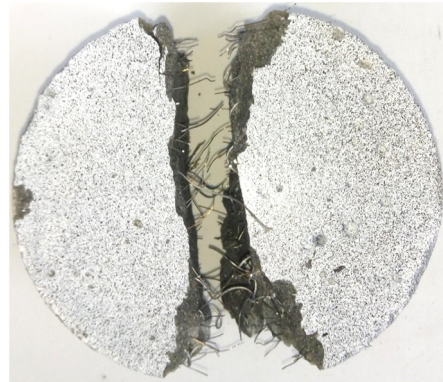
Plain Geopolymer (150 GPa/sec)



Plain Geopolymer (200 GPa/sec)



SFRGC -1 (150 GPa/sec)



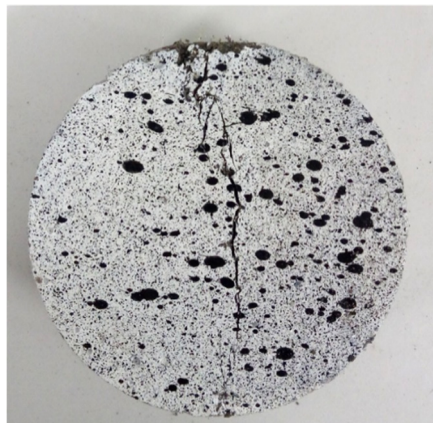
SFRGC-1 (200 GPa/sec)



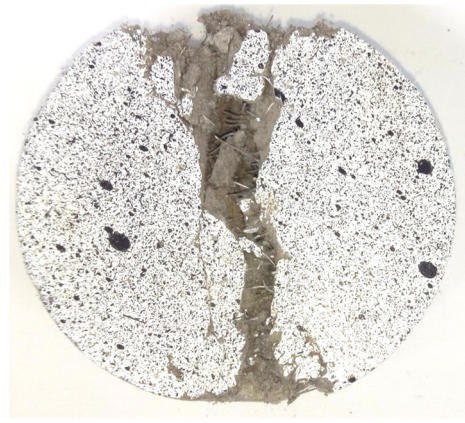
SFRGC -2 (150 GPa/sec)



SFRGC-2 (200 GPa/sec)



HFRGC (150 GPa/sec)



HFRGC (200 GPa/sec)

Figure 5-17 Comparison of post-test failure patterns of plain geopolymer and FRGC specimens in dynamic splitting tension.

With an increase in fiber volume fraction to 2.0%, the samples from both SFRGC-2 and HFRGC matrices did not show extensive damage under 150 GPa/sec loading, and the split halves were firmly held together by the spiral steel and HSPE fibers. Besides, none of the samples showed any fiber pull-out or fracture response at this load level. At a higher stress rate (200 GPa/sec), even though both types of fiber combinations maintained the integrity of high-strength geopolymer samples, the HFRGC containing polyethylene fibers demonstrated an explicit toughness. The damaged areas in these samples were exclusively restricted, and most of the fragments were found attached to the original samples after the tests. For SFRGC-2 samples, the geopolymer material was crushed into fine debris and the spiral steel elongated along the path of cracks. This again specifies the exclusivity of hybrid steel-polyethylene fiber reinforcement and synthesized geopolymer composite for its use in specialized applications.

5.6 Conclusions

This study presents experimental results on the quasi-static and dynamic tensile properties of high-strength ambient cured geopolymer material and fiber reinforced geopolymer composites. The fiber reinforcement used in this study primarily consists of newly proposed equal-part combinations of the hooked end and spiral-shaped steel fibers along with hybrid steel-polyethylene fiber composite. A total fiber volume fraction of 1% and 2% were used for reinforcement purposes. In quasi-static tests, the material responses were examined via displacement controlled 300 kN Shimadzu test machine, while a series of dynamic tests were conducted using a 100-mm SHPB equipment to characterize the material constitutive relationships within the strain rate range of 10^{-5} sec^{-1} to 15 sec^{-1} . Based on the test data, the main findings can be summarized as follows:

- 1) The newly synthesized geopolymer material exhibited high-compressive strength and the addition of steel fibers had a positive influence both on the strength and stiffness properties of neat geopolymer. The inclusion of polyethylene fibers marginally reduced these parameters.
- 2) Under quasi-static splitting tension, the unreinforced geopolymer samples showed extremely brittle failure and limited tensile strain capacity. However, the addition of steel fibers significantly improved the tensile strength in proportion to the fiber volume fraction. Moreover, a hybrid steel-polyethylene fiber combination resulted in approximately 70% increase in the tensile strength of the plain geopolymer.
- 3) A series of multiple cracks were observed before the steel fiber reinforced composites reached the maximum failure load. During the post-peak loading region, the spiral steel fibers showed superior ability to maintain the sample integrity which allowed the FRGC specimens to endure large displacements. The addition of HSPE fibers exclusively improved the toughness and energy absorption capability such that an effective load-transfer mechanism between the fibers and the matrix facilitated the designed composite to resist higher loads at large lateral deformations.
- 4) In dynamic tests, the tensile strength of both unreinforced and FRGC materials increased with an increase in the average strain rate. A strong strain rate dependency was observed for the synthesized materials within the strain rate range of 3 sec^{-1} and 15 sec^{-1} . Unreinforced geopolymer was found more sensitive to the strain rate than FRGC, with the DIF_f of unreinforced geopolymer material higher than that of the FRGC mixtures.
- 5) Comparisons between the existing literature and the results obtained in this study reveal a substantial deviation between the existing CEB recommended formulae for

OPC concrete and the DIF_{f_t} values measured in the tests. The suggested empirical formulae underestimate the increase in tensile strength.

- 6) Based on the test data, empirical DIF_{f_t} formulae are proposed which can be used to simulate the behaviour of geopolymer materials under impact loadings. The DIF_{f_t} curves are a linear function of the logarithmic strain rate, and the sensitivity threshold exists at 3 sec^{-1} and 4 sec^{-1} for plain and FRGC materials, respectively.
- 7) Image analysis reveals a strong bonding of the spiral steel fibers with geopolymer matrix which augments further with the inclusion of HSPE fibers. The comparison of results indicates that at a given time instant, the COD in HFRGC sample was as small as 6.5% of that of plain geopolymer. The inclusion of equal-part spiral steel and hooked-end steel fiber reinforcement also reduced the COD in proportion to the fiber dosage.
- 8) The post-test failure modes of both plain and FRGC are stress rate dependent. The plain geopolymer primarily split into two halves, and the extent of damage along the loading diameter increased proportionately to the loading rate. The FRGC samples were able to maintain their structural integrity to a large scale, and the degree of damage reduced significantly by increasing the fiber volume fraction and including HSPE fibers.

5.7 References

ASTM. (2011). Standard test method for splitting tensile strength of cylindrical concrete specimens. *ASTM C496-11*, Philadelphia.

ASTM. (2012a). Standard specification for coal fly ash and raw or calcined natural pozzolan for use in concrete. *ASTM C618-12a*, Philadelphia.

ASTM. (2014). Standard test method for static modulus of elasticity and Poisson's Ratio of concrete in compression. *ASTM C469-14*, Philadelphia.

ASTM. (2015a). Standard test method for compressive strength of cylindrical concrete specimens. *ASTM C39-15*, Philadelphia.

ASTM. (2015b). Standard test method for relative density (Specific Gravity) and absorption of fine aggregate. *ASTM C128-15*, Philadelphia.

Ahmed, S. F. U., & Ronnie, Z. (2017). Ductile behavior of polyethylene fibre reinforced geopolymer composite. *Paper presented at the MATEC Web of Conferences*.

Atiş, C. D., Görür, E. B., Karahan, O., Bilim, C., İlkentapar, S., & Luga, E. (2015). Very high strength (120 MPa) class F fly ash geopolymer mortar activated at different NaOH amount, heat curing temperature and heat curing duration. *Construction and Building Materials*, 96, 673-678.

Beverly, P. (2013). *fib model code for concrete structures 2010*: Ernst & Sohn.

Bischoff, P. H., & Perry, S. H. (1991). Compressive behaviour of concrete at high strain rates. *Materials and Structures*, 24(6), 425-450.

CEB. (2013). Comite Euro-International Du Beton, CEB-fib model code for Concrete Structures, 2010, Telford.

Davidovits, J. (1991). Geopolymers: inorganic polymeric new materials. *Journal of Thermal Analysis and Calorimetry*, 37(8), 1633-1656.

Duxson, P., Fernández-Jiménez, A., Provis, J. L., Lukey, G. C., Palomo, A., & van Deventer, J. S. J. (2007). Geopolymer technology: the current state of the art. *Journal of Materials Science*, 42(9), 2917-2933.

Dylmar Penteadó Dias, C. T. (2005). Fracture toughness of geopolymeric concretes reinforced with basalt fibers. *Cement & Concrete Composites*, 27, 49–54.

Feng, K. N., Ruan, D., Pan, Z., Collins, F., Bai, Y., Wang, C. M., & Duan, W. H. (2014). Effect of strain rate on splitting tensile strength of geopolymer concrete. *Magazine of Concrete Research*, 66, 825-835.

Feng, K. N., Ruan, D., Pan, Z., Collins, F., Bai, Y., Wang, C. M., & Duan, W. H. (2015). Mechanical behavior of geopolymer concrete subjected to high strain rate compressive loadings. *Materials and Structures*, 48(3), 671-681.

Fernández-Jiménez, A., Palomo, A., & Criado, M. (2005). Microstructure development of alkali-activated fly ash cement: a descriptive model. *Cement and Concrete Research*, 35(6), 1204-1209.

Gao, X., Yu, Q. L., Yu, R., & Brouwers, H. J. H. (2017). Evaluation of hybrid steel fiber reinforcement in high performance geopolymer composites. *Materials and Structures*, 50(2), 165.

Gao, Y., Xu, J., Bai, E., Luo, X., Zhu, J., & Nie, L. (2015). Static and dynamic mechanical properties of high early strength alkali activated slag concrete. *Ceramics International*, 41(10, Part A), 12901-12909.

GOM (2018). <https://www.gom.com/3d-software/gom-correlate/download.html>

Hao, Y., & Hao, H. (2014). Influence of the concrete DIF model on the numerical predictions of RC wall responses to blast loadings. *Engineering Structures*, 73, 24-38.

Hao, Y., & Hao, H. (2016a). Finite element modelling of mesoscale concrete material in dynamic splitting test. *Advances in Structural Engineering*, 19(6), 1027-1039.

Hao, Y., & Hao, H. (2016b). Mechanical properties and behaviour of concrete reinforced with spiral-shaped steel fibres under dynamic splitting tension. *Magazine of Concrete Research*, 68(21), 1110-1121.

Hao, Y., & Hao, H. (2016). Mechanical properties and behaviour of concrete reinforced with spiral-shaped steel fibres under dynamic splitting tension. *Magazine of Concrete Research*, 68(21), 1110-1121.

Hao, Y., Hao, H., & Zhang, X. H. (2012). Numerical analysis of concrete material properties at high strain rate under direct tension. *International Journal of Impact Engineering*, 39(1), 51-62.

- Hardjito, D., Wallah, S. E., Sumajouw, D. M., & Rangan, B. V. (2004). On the development of fly ash-based geopolymer concrete. *ACI Materials Journal-American Concrete Institute*, 101(6), 467-472.
- Hosan, A., Haque, S., & Shaikh, F. (2016). Compressive behaviour of sodium and potassium activators synthesized fly ash geopolymer at elevated temperatures: A comparative study. *Journal of Building Engineering*, 8, 123-130.
- Khale, D., & Chaudhary, R. (2007). Mechanism of geopolymerization and factors influencing its development: a review. *Journal of Materials Science*, 42(3), 729-746.
- Khan, M. Z. N., Hao, Y., Hao, H., & Shaikh, F. U. A. (2018a). Experimental evaluation of quasi-static and dynamic compressive properties of ambient-cured high-strength plain and fiber reinforced geopolymer composites. *Construction and Building Materials*, 166, 482-499.
- Khan, M. Z. N., Hao, Y., Hao, H., & Shaikh, F. U. A. (2018b). Mechanical properties of ambient cured high strength hybrid steel and synthetic fibers reinforced geopolymer composites. *Cement and Concrete Composites*, 85(Supplement C), 133-152.
- Khan, M. Z. N., Hao, Y., Hao, H., Shaikh, F. U. A., & Liu, K. (2018c). Mechanical properties of ambient cured high-strength plain and hybrid fiber reinforced geopolymer composites from triaxial compressive tests. *Construction and Building Materials*, 185, 338-353.
- Khan, M. Z. N., Shaikh, F. U. A., Hao, Y., & Hao, H. (2016). Synthesis of high strength ambient cured geopolymer composite by using low calcium fly ash. *Construction and Building Materials*, 125, 809-820.
- Khan, M. Z. N., Shaikh, F. U. A., Hao, Y., & Hao, H. (2017). Effects of Curing Conditions and Sand-to-Binder Ratios on Compressive Strength Development of Fly Ash Geopolymer. *Journal of Materials in Civil Engineering*, 30(2), 04017267.
- Malvar, L. J. (1998). Review of static and dynamic properties of steel reinforcing bars. *Materials Journal*, 95(5), 609-616.
- Malvar, L. J., & Ross, C. A. (1998). Review of strain rate effects for concrete in tension. *ACI Mater. J.*, 95, 735.
- Menna, C., Asprone, D., Forni, D., Roviello, G., Ricciotti, L., Ferone, C., Cadoni, E. (2015). Tensile behaviour of geopolymer-based materials under medium and high strain rates. *Paper presented at the EPJ Web of Conferences*.
- Mustafa Al Bakri, A., Kamarudin, H., Bnhussain, M., Rafiza, A., & Zarina, Y. (2012). Effect of $\text{Na}_2\text{SiO}_3/\text{NaOH}$ Ratios and NaOH Molarities on Compressive Strength of Fly-Ash-Based Geopolymer. *ACI Materials Journal*, 109(5).
- Pan, Z., Feng, K. N., Gong, K., Zou, B., Korayem, A. H., Sanjayan, J., Collins, F. (2013). Damping and microstructure of fly ash-based geopolymers. *Journal of Materials Science*, 48(8), 3128-3137.
- Pan, Z., & Sanjayan, J. G. (2010). Stress-strain behaviour and abrupt loss of stiffness of geopolymer at elevated temperatures. *Cement and Concrete Composites*, 32(9), 657-664.
- Rahier, H., Van Mele, B., Biesemans, M., Wastiels, J., & Wu, X. (1996). Low-temperature synthesized aluminosilicate glasses. *Journal of Materials Science*, 31(1), 71-79.

- Ranjbar, N., Talebian, S., Mehrali, M., Kuenzel, C., Cornelis Metselaar, H. S., & Jumaat, M. Z. (2016). Mechanisms of interfacial bond in steel and polypropylene fiber reinforced geopolymer composites. *Composites Science and Technology*, 122, 73-81.
- Shaikh, F. U. A. (2013). Review of mechanical properties of short fibre reinforced geopolymer composites. *Construction and Building Materials*, 43(0), 37-49.
- Tedesco, J. W., Ross, C. A., & Kuennen, S. T. (1993). Experimental and numerical analysis of high strain rates splitting tensile tests. *ACI Materials Journal*, 90, 162.
- Thokchom, S., Ghosh, P., & Ghosh, S. (2009). Acid resistance of fly ash based geopolymer mortars. *International Journal of Recent Trends in Engineering*, 1(6), 36.
- Xin, L., Jin-yu, X., Weimin, L., & Erlei, B. (2014). Effect of alkali-activator types on the dynamic compressive deformation behavior of geopolymer concrete. *Materials Letters*, 124(0), 310-312.
- Xin Luo, J.-y. X. (2013). Dynamic splitting-tensile testing of highly fluidised geopolymer concrete. *Magazine of Concrete Research*, 65(14), 7.
- Zhang, Q., & Zhao, J. (2013). Determination of mechanical properties and full-field strain measurements of rock material under dynamic loads. *International Journal of Rock Mechanics and Mining Sciences*, 60, 423-439.

CHAPTER 6 EXPERIMENTAL EVALUATION OF QUASI-STATIC AND DYNAMIC COMPRESSIVE PROPERTIES OF AMBIENT-CURED HIGH-STRENGTH PLAIN AND FIBER REINFORCED GEOPOLYMER COMPOSITES

6.1 Abstract

Heat cured geopolymer binders have been studied extensively to establish their mechanical behaviour under quasi-static loading conditions and it has been found that they are capable of achieving comparable and in some cases better properties than ordinary Portland cement (OPC). However, as a novel binding material, minimal research has been conducted to understand their dynamic material response. This paper presents the dynamic compressive properties of a newly synthesized high-strength ambient cured geopolymer mortar and hybrid steel-polyethylene fiber reinforced geopolymer composite (FRGC). Dynamic compressive tests are carried out using the Ø100-mm split Hopkinson pressure bar (SHPB) apparatus with pulse shaping technique whereas a 160-ton hydraulic test machine is used for quasi-static compressive tests. The dynamic compressive properties of plain and FRGC including stress-strain curves, strength enhancement, impact toughness, and energy absorption capability are obtained and compared with those observed under quasi-static actions. A high-speed camera is used to record the failure processes of samples under impact. The test results show that the dynamic compressive mechanical properties of plain and FRGC exhibit strong strain rate dependency. The DIFs (dynamic increase factors) of samples increase approximately linearly with the average strain rate in a logarithmic manner. Obvious binomial relationships are noticed between the energy absorption capacity and average strain rate of tested samples, such that the strain rate sensitivity threshold exists at 30 sec^{-1} and 66 sec^{-1} for plain and FRGC materials, respectively. Empirical DIF_{f_c} relations are proposed which can be used to model the developed composite materials and structures subjected to static and impact loads.

6.2 Introduction

Concrete is used extensively for construction of buildings, dams, roads, and bridges, where the most primary ingredient used in the composite is ordinary Portland cement (OPC). However, the process of manufacturing OPC is highly energy intensive since it involves the calcination of limestone and sintering of ground materials to form clinker. As a result, carbon dioxide (CO_2) is released both during the calcination and through the burning of the fossil fuels. Due to an overwhelmingly increasing demand to reduce the global anthropogenic CO_2

emissions from cement industry (typically 5-7%) (Benhelal et al., 2013), recent decades have seen a new wave of research on alkali-activated cementitious materials (AACMs) (Garcia-Lodeiro et al., 2015). Unlike OPC, the synthesis of these binders involves activating potential hydraulic waste products (fly ash (FA) and slag) with an alkaline solution. Previous studies have established their improved thermal stability (Pan and Sanjayan, 2010; Atiş et al., 2015), lower water permeability (Nasvi et al., 2016), enhanced resistance to acid or sulfate attack (Baščarević, 2015), and better durability (Fernandez-Jimenez et al., 2007). However, in reality, the use of AACMs which can broadly be classified as alkali-activated slag (Collins and Sanjayan, 2001 or alkali-activated FA (commonly known as “Geopolymer”) (Khale and Chaudhary, 2007) has been limited. The main reason is primarily related to their early age properties, i.e., the geopolymer formulations containing low calcium FA as the only binder do not achieve noticeable strength at room temperature and may not be feasible for cast in-situ concrete applications (Hardjito et al., 2004), while AAS cement may experience shrinkage problems (Chi and Huang, 2013).

Nevertheless, some recent research efforts with the focus on geopolymer material preparation have demonstrated the advantages of combining FA and slag materials together (Khan et al., 2016). The studies conducted at the microstructural level have explained the rationale behind the strength development, indicating the co-formation of sodium aluminosilicate hydrate (N-A-S-H) and calcium silicate hydrate (C-S-H) / calcium aluminium silicate hydrate (C-A-S-H) type gels (Deb et al., 2014; Khan et al., 2017). It has been observed that similar to OPC concrete, a range of mixing parameters can influence the mechanical properties of geopolymer mortar and concrete mixtures (Nath and Sarker, 2014). However, with an array of mixture designs, fiber reinforcements, and preparation techniques (Yunsheng et al., 2008), most of the previous studies on geopolymer binders were limited to investigating the material performance under quasi-static loading conditions, i.e., under uniaxial compression, split-tensile and flexural loads only (Sakulich, 2011; Shaikh, 2013). Little efforts have been made to understand the impact behaviour or dynamic material properties of these novel binders.

Generally, all structures during their design life are likely to be vulnerable to natural hazards such as an earthquake, high-velocity impact or blast. It is well-documented that the response of engineering materials and structures under impulsive loadings could be strikingly different to that observed under quasi-static loading conditions (Li and Meng, 2003; Zhu et al., 2013), where for concrete-like materials, it has been noticed that both the compressive and tensile strengths increase with the strain rate. A numerical fraction of the dynamic strength and the quasi-static strength, also known as the Dynamic increase factor (DIF), is used to quantify the enhancement (Lok et al., 2003). Based on the extensive testing data set available for a wide range and type of mortar and concrete mixes as reviewed in (Bischoff and Perry, 1991), the

Comite Euro-International du Beton CEB (2013) has suggested some guidelines to estimate the DIF_{fc} for critical compressive stress for OPC concrete subjected to high strain-rate loadings, as expressed in Equations (6.1) and (6.2).

$$DIF_{fc} = f_{c, imp, k} / f_{cm} = (\dot{\epsilon}_c / \dot{\epsilon}_{co})^{0.014} \quad \dot{\epsilon}_c \leq 30 \text{ sec}^{-1} \quad (6.1)$$

$$DIF_{fc} = f_{c, imp, k} / f_{cm} = 0.012(\dot{\epsilon}_c / \dot{\epsilon}_{co})^{1/3} \quad \dot{\epsilon}_c > 30 \text{ sec}^{-1} \quad (6.2)$$

where $f_{c, imp, k}$ is the impact compressive strength; f_{cm} is the mean compressive strength; $\dot{\epsilon}_c$ is the strain rate in sec^{-1} , and $\dot{\epsilon}_{co}$ is the reference strain rate of $30 \times 10^{-6} \text{ sec}^{-1}$.

However, very few researchers have investigated the dynamic material properties of geopolymer binders. For those undertaken, the fundamental differences are related to the type of source materials, activating solutions, the presence of aggregates in test samples, sample sizes, and the loading rates achieved during the tests (Khandelwal et al., 2013; Luo et al., 2013; Luo and Xu, 2013; Xin et al., 2014; Feng et al., 2015; Gao et al., 2015; Menna et al., 2015). A majority of the researchers used heat curing method for the synthesis of geopolymer which on its own could be a major limitation.

Nevertheless, the existing literature on the dynamic compressive behaviour of geopolymer binder includes the experimental investigation carried out by Khandelwal et al. (2013) who studied the dynamic compressive properties of geopolymer mortar at four different low strain rates, i.e., $1e^{-5}$, $5e^{-5}$, $1e^{-4}$ and $5e^{-4} \text{ sec}^{-1}$. The samples were prepared under the influence of heat curing. It was concluded that the ultimate compressive strength and elastic properties of geopolymer mortar increased with the strain rate. Similarly, other researchers (Luo et al., 2013; Luo and Xu, 2013; Xin et al., 2014; Feng et al., 2015; Gao et al., 2015) used different types of geopolymer concrete (GC) mixtures to study their impact behaviour at higher loading rates. Interestingly, the reported outcomes in these studies are conflicting. In order to apprehend a succinct comparison, the DIF_{fc} scatters for strength from these investigations are plotted in Figure 6-1 alongside the CEB recommendations. A brief review of the mix ingredients and results are presented thereafter.

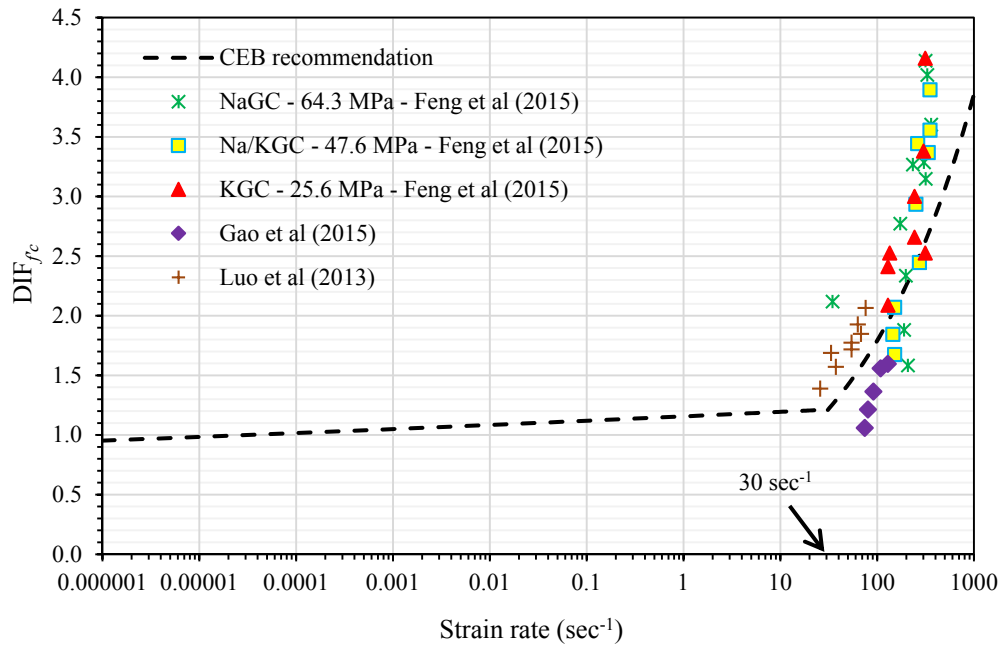


Figure 6-1 DIF_{fc} results for geopolymer concrete mixtures from past investigations (Luo et al., 2013; Feng et al., 2015; Gao et al., 2015).

As seen, three types of GC mixtures and one geopolymer mortar mix (not shown in the graph) was tested by Feng et al. (2015). Groups of three different activator combinations were used to prepare the mixes under the influence of heat curing. It was concluded that the quasi-static compressive strengths of these mixtures were highly dependent on the potency of alkali-activating solutions, i.e., the sodium hydroxide (SH) and sodium silicate (SS) based activators were more effective in comparison to a combination of potassium hydroxide (KOH) and SS solutions. For dynamic tests, it was specified that the prevailing CEB recommendations may be used to establish the DIF_{fc} for different GC mixtures since the strength enhancement trend in GC is similar to that of OPC concrete. However, it can be established from Figure 6-1 that their reported test results do not match the CEB guidelines precisely. Moreover, the CEB formulae were found to underestimate the DIF_{fc} , i.e., the increase in critical axial strain at peak stress with an increase in average strain rate.

On the other hand, Gao et al. (2015) studied the quasi-static and dynamic compressive material properties of AAS concrete samples. The dynamic material tests were conducted up to a strain rate of 130 sec^{-1} . Contradictorily to the conclusions conveyed by Feng et al. (2015), the rate of strength increase in AAS concrete samples was significantly lower than OPC concrete samples at higher loading rates. Similarly, no obvious relationship was observed between the increase in average strain rate and critical axial strain values. Instead, the critical axial strain corresponding to the maximum stress fluctuated within a small range.

Recently, Luo et al. (2013) prepared GC specimens with the combined use of FA and slag (FA/slag = 0.33) at three different water/binder ratios. The source materials were activated with SS and SH solutions. To overcome the inherent brittleness of geopolymer material, the matrix was reinforced with basalt fibers of 15 μ m diameter and 18mm length. However, it should be noted that the geopolymer mixtures used in this study contained a relatively higher volume fraction of slag and SS/SH ratios (6.70, 4.20 and 3.50) which may not be useful in reducing the carbon footprint typically associated with this novel binder. Nonetheless, it may be seen (see Figure 6-1) that the synthesized material exhibited strong strain rate dependency at strain rates 30 to 100 sec⁻¹ and the results suggest higher sensitivity of geopolymer binder in comparison to OPC. Based on the test data, empirical relationships of DIF_{fc} with the strain rate were proposed.

Likewise, in other studies, (Luo and Xu, 2013; Xin et al., 2014) also used a combination of FA and slag to synthesize the GC mixtures with two different types of activators. Despite the fact that no information was presented in their studies in regards to the mix proportions, it was concluded that GC mixtures prepared with SS and SH based activators exhibit increased deformation upon impact as compared to the other activators. The test data showed that the strain rate sensitivity threshold for GC is apparently lower than that of OPC, i.e., 28.89 sec⁻¹ instead of 63.1 sec⁻¹ (Ross et al., 1996). However, different to other researchers, the critical axial strain was found to increase initially up to 66.7 sec⁻¹ with an increase in the average strain rate and decreased later for the other test cases at higher strain rates. Strong strain rate dependency for compressive strength of the material was noticed as the DIF of compressive strength was found to increase linearly with the logarithm of the strain rate.

As reviewed, the dynamic behaviour of geopolymer material is different from that of OPC, which depend largely upon the mix designs and are mostly observed for GC mixtures. It is well known that the properties of concrete vary considerably depending upon those of coarse aggregates. Moreover, the existing results for the prediction of DIF_{fc} for geopolymer mixtures differ significantly and the increase in stress and strain capacities with the average strain rate could be less marked or otherwise. Unfortunately, the current database on dynamic testing of geopolymer materials is fairly limited to corroborate the previous findings. Therefore looking at a wider perspective, in the current study, the quasi-static and dynamic compressive properties of the newly developed high-performance geopolymer mortar material and fiber reinforced geopolymer composite (FRGC) are presented. Furthermore, owing to the brittle nature and keeping in view the reduced effectiveness of conventional fibers under dynamic loading conditions, the matrix is reinforced with a novel hybrid steel-polyethylene mix at a total fiber volume fraction of 2%.

The proposed reinforcement creates synergy between the three types of fibers, such that the spiral steel fibers are capable of providing better 3D anchorage bonding due to their helical shape, while hooked-end steel fibers offer frictional resistance along two dimensions (Xu et al., 2012). In a previous investigation (Hao and Hao, 2017), it was established that the post-crack resistance of hook-end steel fibers is much lower than spiral steel fibers and is rarely available under dynamic loadings. However, an equal-part combination of these two fibers significantly improves the post-failure load carrying capacity of structural elements without compromising their ultimate strength. On the other hand, hybridizing the fibers having higher strength and stiffness along with those possessing ductility surpasses the performance of the mono-fiber reinforced composites (Banthia and Gupta, 2004). The use of high-strength polyethylene (HSPE) fibers with the above reinforcement has been found to increase the toughness of geopolymer material explicitly (Khan et al., 2018). It is pertinent to mention that no studies in the literature have considered the dynamic compressive properties of ambient-cured high-strength geopolymer material or such form of fiber reinforcement yet. The material performance is characterized by analyzing the strengths and stress-strain curves under quasi-static condition and high strain rates. The energy absorption capability of both unreinforced and FRGC samples at higher strain rates is obtained and compared, whereas, the strain-rate effect on compressive strengths of the two types of materials is also discussed. Moreover, the empirical DIF relationships of compressive strength of geopolymer mortar and FRGC are proposed, while the failure patterns of the samples both during and after the tests are also presented.

6.3 Experimental Section

6.3.1 Material classification

Low calcium fly ash, type F (as per ASTM C618 (ASTM, 2012) sourced from Gladstone power station in Queensland Australia and commercially available slag obtained locally from BGC cement, Perth, Australia, were used to prepare the high-performance geopolymer matrix (“plain geopolymer matrix” for short in the following context) and FRGC in this research. The chemical compositions of the source materials as determined via X-ray fluorescence analysis (XRF) are presented in Table 6-1, while the median particle sizes of the pozzolanic wastes, i.e., slag and FA were 11.5 μm and 9.7 μm respectively.

Table 6-1 Constituents of low-calcium FA and slag

Material	Oxide Component: mass (%)												LOI* (%)
	SiO ₂	Al ₂ O ₃	Fe ₂ O ₃	CaO	K ₂ O	MgO	Na ₂ O	MnO	SO ₃	P ₂ O ₅	TiO ₂	Others	
FA	51.11	25.56	12.48	4.30	0.70	1.45	0.77	0.15	0.24	0.88	1.32	0.46	0.57
Slag	32.45	13.56	0.85	41.22	0.35	5.10	0.27	0.25	3.20	0.03	0.49	1.12	1.11

*Loss on ignition

The aluminosilicate source materials were activated with a unified mixture of 12M SH and D-grade SS (specific gravity = 1.53cc/g, component ratio, $M_s = \text{SiO}_2/\text{Na}_2\text{O} = 2.0$; $\text{SiO}_2 = 29.4\%$, $\text{Na}_2\text{O} = 14.7\%$, $\text{H}_2\text{O} = 55.9\%$) solutions. Fine silica sand with the fineness modulus of 2.77, specific gravity of 2.65, and maximum nominal size of 1.18mm was prepared in saturated surface dry (SSD) condition before being used for the preparation of test samples as per ASTM C128 (ASTM, 2015b). The properties of fibers used in the preparation of reinforced samples are summarized in Table 6-2, and their visual appearance is shown in Figure 6-2. The steel fibers were purchased from two different vendors based in China, whereas the HSPE fibers were donated by Dyneema Group, Toyobo Corporation Japan for the research purposes.

Table 6-2 Properties of spiral steel, hooked-end steel and HSPE fibers

Fiber type	Fiber length (mm)	Diameter (μm)	Pitch length (mm)	Aspect ratio L/D	Coil diameter (mm)	Fiber density (kg/m^3)	Young's modulus (GPa)	Tensile Strength (MPa)
Spiral steel	25	550	6	45	10	7800	200	2000
Hooked-end steel	25	300	-	85	-	7800	200	2500
Polyethylene	12	12	-	1000	-	970	123	3500

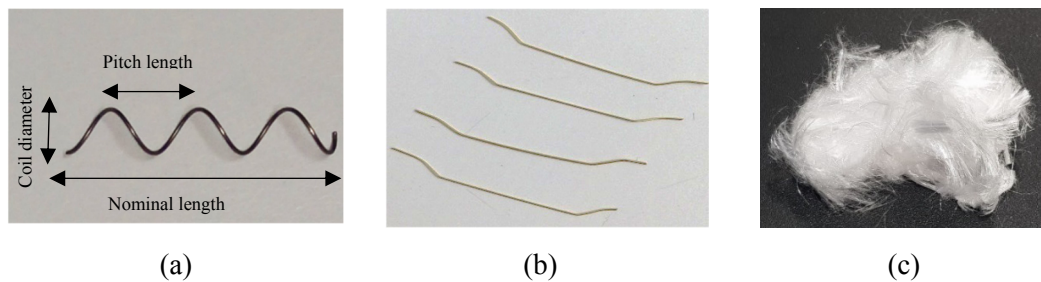


Figure 6-2 Picture of (a) Spiral steel (b) Hooked-end steel (c) HSPE fibers.

6.3.2 Mix proportions, Workability, Sample preparation and Curing

6.3.2.1 Mix Proportions

The mix proportions of both series are given in Table 6-3. The fiber reinforcement is selected based on a previous research by the authors where the said fiber combination and volume fraction displayed improved flexure strength and energy absorption capacity under quasi-static loading conditions (Khan et al., 2018). It should be noted that both the plain and FRGC samples had an equal amount of alkaline activator with a constant water-to-solids (w/s) ratio of 0.28. No extra water or superplasticizer was included in any of the mixtures. Moreover, the fibers were incorporated by volume, such that the geopolymer mixture designated as FRGC contained 0.80% of spiral steel fibers (SS), 0.80% of hooked-end steel fibers (HES) and 0.40% of HSPE fibers, respectively.

Table 6-3 Mix Proportions of geopolymer matrix and fiber reinforced composites

Mix Type	w/s	Fiber Type	Fiber volume (%)	Fly ash (kg/m ³)	Slag (kg/m ³)	Sand (kg/m ³)	Na ₂ SiO ₃ (kg/m ³)	NaOH (kg/m ³)	Fiber (kg/m ³)	Flow (mm)
Plain	0.28	-	-	412	276	1100	294.30	117.72	-	145
		Spiral	0.80						62.4	
FRGC	0.28	Hooked	0.80	412	276	1100	294.30	117.72	62.4	65
		HSPE	0.40						3.88	

6.3.2.2 Synthesis, workability, and curing of plain & fiber geopolymer composite samples

The plain and FRGC mixtures were prepared in a 70L large size pan mixer. However, since the dissolution of caustic soda pellets in water is an exothermal process, and the initial temperature of the alkali-activator can rise more than 80°C; therefore 12M SH solution was prepared at least a day ahead of the casting schedule. Moreover, the SS and SH solutions were also compounded together 30 minutes before the start of the mixing process. The said procedure increases the potency of the activating solution. At first, the solid ingredients, including low calcium FA and sand were dry mixed for approximately 60 seconds. The slag was then added and the dry mixing was continued for another 2 to 3 minutes. Finally, the alkaline activator was gradually included over a 60 sec period and the fresh mixtures were allowed to mix further until a uniform mass was formed. For FRGC mixture, the steel and HSPE fibers were dosed at the end. Due care was taken to prevent fiber agglomeration in the fresh mixture by including both the spiral steel and hooked-end steel fibers through a continuous sieve shaking process, while the HSPE fibers were separated loosely before being

added in portions into the wet mixture. The workability of both mixtures was determined immediately after mixing all the constituents by measuring the flow diameters according to ASTM C1437 (ASTM, 2013). As seen in Table 6-3, the plain and FRGC mixtures had a flow diameter of 145 mm and 65 mm, respectively.

Subsequently, after measuring the workability, the fresh geopolymer mixtures were poured in three layers into a custom-made formwork arrangement (i.e., a set of PVC pipes with an internal diameter of 76 mm and length of 250 mm) as shown in Figures 6-3(a) and (b). During the pour, a continuous external vibration process was used to release the entrapped air bubbles introduced while batching different ingredients in the pan mixer. It is pertinent to mention that due to the sticky nature of geopolymer binder and presence of HSPE fibers, no fiber sinking was noticed in the molding tubes.



Figure 6-3 PVC formwork (a) before and (b) after the pour.

Later, the exposed surfaces of the molds were covered with cling sheet to prevent the moisture loss and moved into an ambient curing room at a temperature of $23\pm 2^{\circ}\text{C}$ and relative humidity (RH) of $50 \pm 5\%$. The cast samples were left to cure within the PVC pipes and after about 21 days, four cylindrical samples with a dimension of $\text{Ø}76 \times 40\text{mm}$ were cut from each pipe. For the determination of the reference quasi-static compressive strength, samples with size of $\text{Ø}76 \times 154\text{mm}$ were sectioned. Afterwards, the cut surfaces of the samples were polished with an end surface grinder to achieve a smooth and perpendicular surface to the axis of rotation. The samples were later pushed out from PVC pipes for the testing purposes. The cross-sectional appearance of the prepared samples is shown in Figures 6-4 (a) and (b).



(a)



(b)

Figure 6-4 Prepared samples for (a) quasi-static and (b) dynamic compression tests on plain and FRGC samples.

6.3.3 Test Methods

The quasi-static and dynamic compressive tests are carried out using hydraulic testing machine and SHPB test system, respectively. For quasi-static compressive tests, the samples are designed with a dimension of $\text{Ø}76 \times 152$ mm, i.e., $L/D = 2.0$, whereas, for dynamic tests, the samples with $\text{Ø}76 \times 38$ mm L/D , i.e., $L/D = 0.50$ are used to avoid the axial inertial effect during impact loading. It should be noted that since under quasi-static loading condition the test samples are loaded very slowly, hence sufficient time is available for samples to reach stress equilibrium with negligible inertial effects, whereas, the influence of end friction in both the loading situations is minimized using grease on sample-apparatus interfaces. Further details on each type of test is provided in the subsequent paragraphs.

6.3.3.1 Density & Quasi-static compressive strength tests

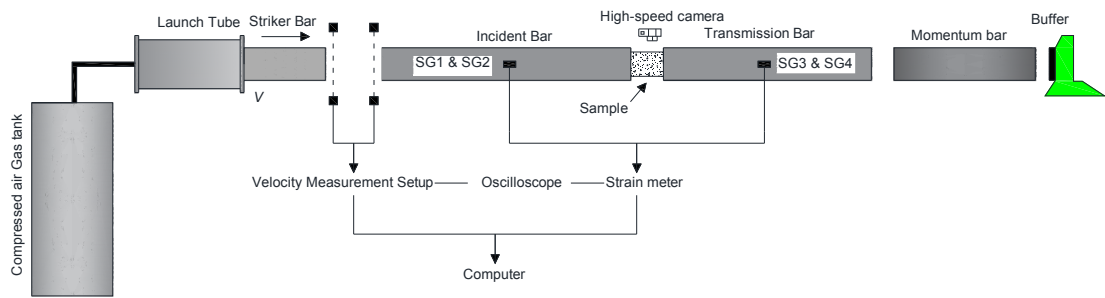
The dry density was calculated using the weight and dimensions of plain and FRGC samples as per ASTM C1688 (ASTM, 2014). A set of three samples was used for measuring the density of each geopolymer mixture, while the quasi-static compression tests were performed using a 160-ton universal testing machine as per ASTM C39 (ASTM, 2015a). The tests were conducted under load-control and by increasing the load at a specific pace, i.e., 80 kN/min, strain rate equivalent to $2.74 \times 10^{-5} \text{ sec}^{-1}$ was realized on the test samples. The actual test set-up is shown in Figure 6-5. However, since the use of cross-head displacement may also include the extraneous deformations from the compression arm of the machine, hence, the strain of geopolymer samples was measured over a gauge length of 5mm by attaching a pair of strain gauges, separated by 180° at mid-height of the test samples (as seen in Figure 6-4(a)). The average strain data obtained from these gauges were later used to establish the quasi-static stress-strain curves for plain and FRGC samples. It should be noted that in order to minimize the influence from end friction effects, an adequate amount of grease was applied to the sample-apparatus interfaces.



Figure 6-5 Quasi-static test set-up in 160-ton universal testing machine.

6.3.2.2 Dynamic impact compression test set-up and equipment details

The dynamic compressive tests were carried out using a 100-mm SHPB apparatus at the Centre for Infrastructure Monitoring and Protection, Curtin University, Australia. The schematic appearance and an actual picture of the equipment are shown in Figures 5-6(a) and (b).



(a)



(b)

Figure 6-6 (a) Schematic and (b) actual picture of the SHPB equipment.

As seen, the SHPB test system consists of an energy source, a launch vessel, three pressure bars, i.e., incident (I), transmitted (T) and absorption bars (A). The other support devices included the laser velocity measurement system, oscilloscope, amplifier, high-speed camera and a wheat-stone bridge strain meter. A laser system was mounted on top of the launch tube to measure the impact velocity of the striker bar. The pressure bars are made of stainless steel with density (ρ), elastic wave velocity (c_0), Poisson's ratio (μ) and Young's modulus (E) of 7800 kg/m^3 , 5064 m/sec , 0.30 and 240 GPa , respectively. The lengths of I, T and A bars are 5500 mm , 3000 mm and 1000 mm respectively. A striker bar having a length of 300 mm and made of the same material as that of the other bars was used. For each test, a thoroughly prepared sample with a surface roughness of less than 0.02 mm was sandwiched between the incident and transmitted bars, such that its centroid was aligned to the centre of bars as shown in Figure 6-7.

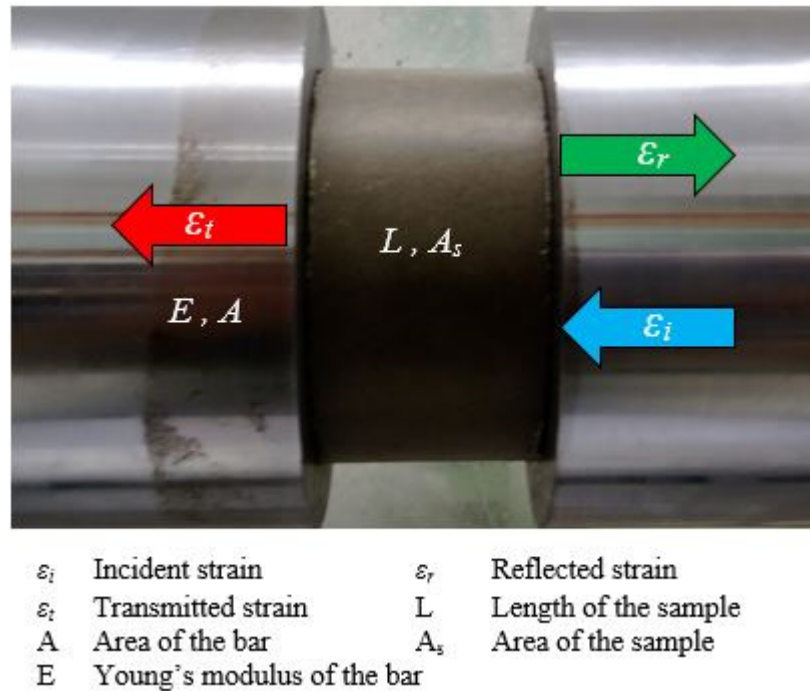


Figure 6-7 Compressive wave initiated strains and interfaces between pressure bars-sample.

A set of strain gauges was installed on both the incident and transmitted bars to record the time-dependent strain readings. It should be noted that by controlling the compressed air pressure in the launch vessel and launch distance, the amplitude of the stress wave and the resulting strain rates were justified. A high-speed camera was used to record the deformation and failure process of plain geopolymer matrix and FRGC test samples. The camera was triggered externally, while a transparent plexiglass box was used to cover the samples to prevent the debris scatter. Moreover, to minimize the influence of end friction effect, grease was used on both sample-bar interfaces.

In general, at a given time (t), the striker bar was accelerated towards the incident bar such that upon impact between the two, an elastic compressive stress wave of a particular amplitude was generated and traveled towards the sample. This wave impinged upon the sample and due to an impedance mismatch at the specimen-input bar interface, a part of it transmitted through the sample and the rest reflected back along the incident bar. The incident, reflected, and transmitted strains ($\varepsilon(i)$, $\varepsilon(r)$, $\varepsilon(t)$) were recorded by the strain gauges placed in the middle of the incident and transmitted bars. It should be noted that to overcome the inherent disadvantage in SHPB technique of strong wave oscillation and wave dispersion, rubber pulse shapers having a diameter of 20 mm and 3 mm thickness (as shown in Figure 6-8) were used. The material and size of the shaper were chosen based upon a number of trial tests.

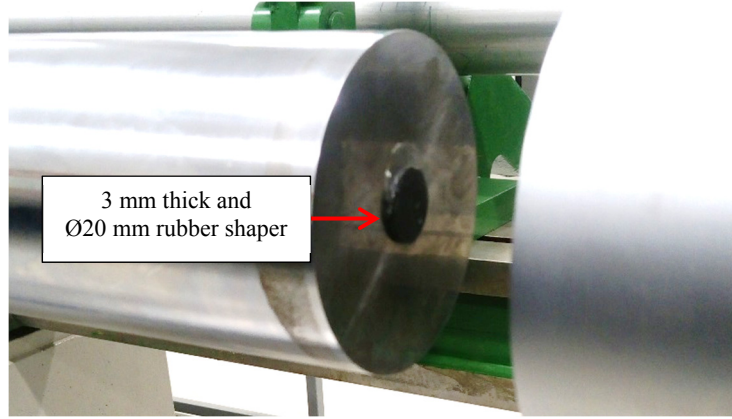


Figure 6-8 Rubber pulse shaper placed on the incident bar.

Once the strain data was recorded, based on the one-dimensional stress wave propagation theory, the amplitudes of the transmitted and the reflected stress wave are the measure of the stress level and the strain rate in the specimen, respectively. In the present study, the strain rate ($\dot{\varepsilon}(t)$) is determined by averaging the strain rate values over a specific period of time, i.e., the time from achieving stress equilibrium to the point of failure [41]. The integral of the time-dependent strain rate yields the strain in the specimen. The following three Equations (6.3) to (6.5) are used to determine stress ($\sigma(t)$), strain ($\varepsilon(t)$) and strain rate ($\dot{\varepsilon}(t)$) of the test samples.

$$\sigma(t) = \frac{AE}{A_s} \varepsilon_t(t) \quad (6.3)$$

$$\dot{\varepsilon}(t) = \frac{2c_o}{L_o} \varepsilon_r(t) \quad (6.4)$$

$$\varepsilon(t) = \int_0^T \dot{\varepsilon}(t) dt \quad (6.5)$$

where A, E, ε_t and ε_r are the cross-sectional area, the elastic modulus, the transmitted and the reflected strains of the elastic bars respectively, c_o , t, L_o and A_s and are longitudinal wave velocity of the bars, time, thickness and cross-sectional area of the specimen.

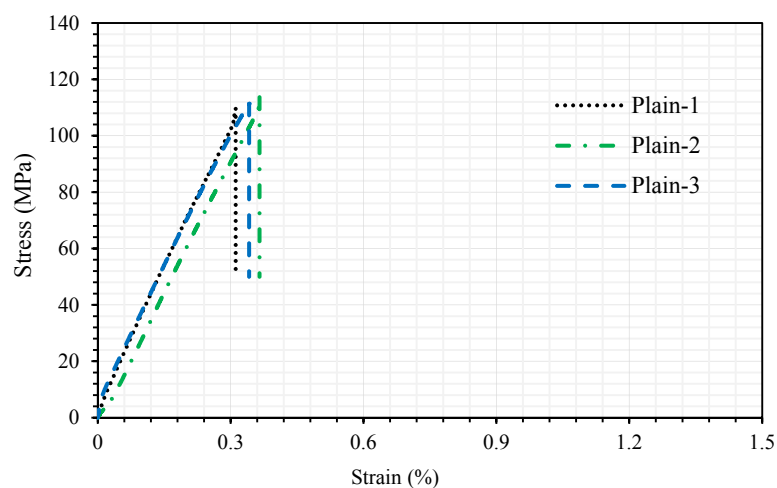
6.4 Results and Discussions

6.4.1 Density & Quasi-static compressive strength test results

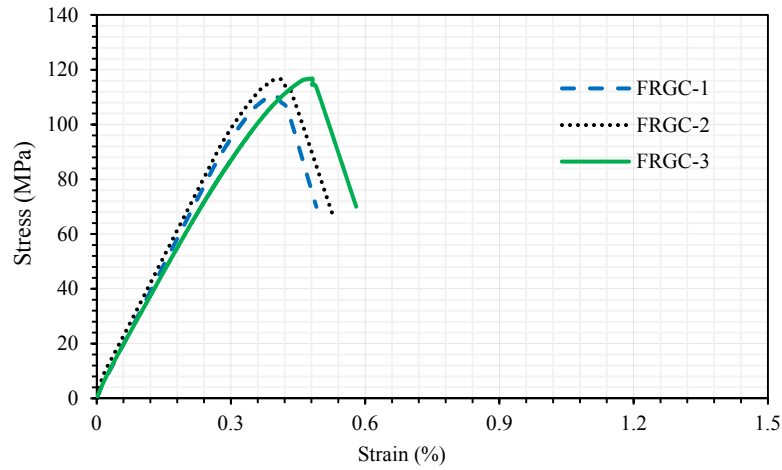
The dry densities of plain and fiber reinforced geopolymer mixtures were $2219.94 \pm 18 \text{ kg/m}^3$ and $2313.25 \pm 21 \text{ kg/m}^3$ respectively. Since the unit weight of mortar or concrete mixtures is dependent upon their constituents, therefore, the density of FRGC mixtures was slightly higher

in comparison with the plain geopolymer matrix mainly due to the inclusion of steel fibers. The quasi-static and dynamic tests were carried out at the age of about 60 days, where the average 60-day compressive strength of plain geopolymer matrix and FRGC mixtures were 112 ± 1.86 MPa and 114 ± 2.95 MPa, respectively. The 28-day reference compressive strengths of these mixtures were 95 and 88 MPa, apiece. As reflected from the results, the strength increased continuously with age, similar to OPC concrete. A more detailed description of the static strength development pattern can be found in a former research by the authors (Khan et al., 2016). Moreover, it should be noted that the compressive strengths at the age of 60 days are used to calculate the respective DIF.

The typical stress-strain curves obtained from the quasi-static testing of plain and FRGC samples are presented in Figure 6-9. It can be seen in Figure 6-9(a) that the high strength geopolymer matrix presented a linear elastic stress-strain behaviour under quasi-static compression. The three tested samples failed under a consistent ultimate load with an average failure strain of about $0.34\% \pm 0.02\%$. The abrupt fall in the stress-strain curve is primarily related to the brittle failure of the material. Many previous studies such as (Pan and Sanjayan, 2010) and (Khandelwal et al., 2013) had noticed a similar trend, i.e., the stress-strain curves of geopolymer mortars after reaching the peak load plunged vertically without evidencing any post-peak failure region. It should be noted that in the present work, the plain geopolymer matrix samples failed in an explosive manner and broke into several pieces. The failure mode of plain geopolymer matrix samples in quasi-static loading condition is presented in Figure 6-10(a).



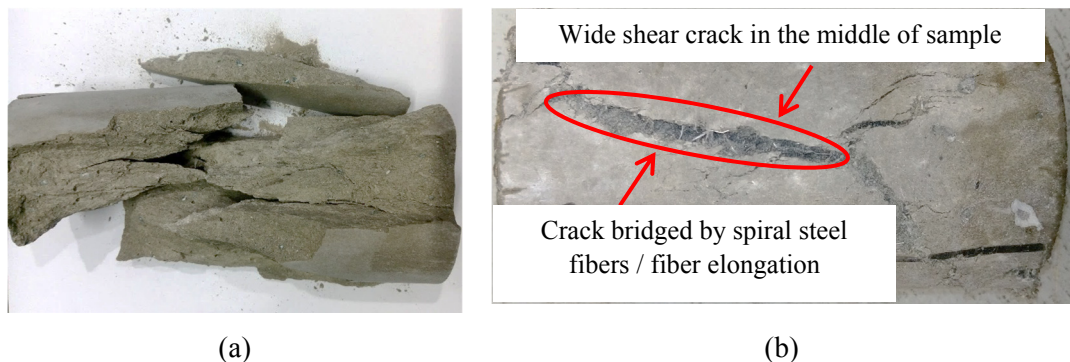
(a)



(b)

Figure 6-9 Comparison of quasi-static stress-strain relation of (a) plain geopolymer matrix
(b) FRGC.

The stress-strain curves of FRGC samples are presented in Figure 6-9(b). It can be seen that the FRGC samples failed under a similar load value as that of plain geopolymer matrix. However, with the addition of fibers, the average critical strain corresponding to the maximum stress increased up to $0.44\% \pm 0.03\%$, which is approximately 30% higher than the unreinforced counterparts, thus indicating an improved deformation capability of high-strength geopolymer matrix under uniaxial compression. It can also be observed that FRGC samples displayed a gradual reduction in stiffness upon reaching the ultimate load carrying capacity. This is primarily related to the formation of numerous micro-cracks and their coalescence due to the presence of fibers in the pre-peak loading stage. However, the non-availability of the tail part of the curves in the post-peak loading region is unfortunately related to the inability of equipment in capturing that portion of the tests.



(a)

(b)

Figure 6-10 Failure modes of (a) plain geopolymer matrix (b) FRGC under quasi-static loading.

Unlike the plain geopolymer matrix, the FRGC samples retained their original shape and a single wide shear crack ran through the middle of all tested samples such that numerous spiral steel fibers were found elongated along the path of these cracks. It is hypothesized that these fibers may have elongated upon the continuity of loading to contribute further towards the post-crack load-bearing capacity of the samples as shown in Figure 6-10(b), which was obviously not possible for unreinforced geopolymer mortar samples.

6.4.2 Dynamic SHPB test results

6.4.2.1 Typical stress-wave output signal in SHPB tests

The impact tests on plain and FRGC samples were carried out using 100-mm SHPB test apparatus. Typical I, R and T stress histories are shown in Figure 6-11 where the shape of the incident wave has been modified with the use of rubber pulse shaper described earlier. The half-sine shaped incident stress wave allows for the elimination of high-frequency wave oscillation and the increase in rising time, which are beneficial for the achievement of dynamic stress equilibrium in the tested samples.

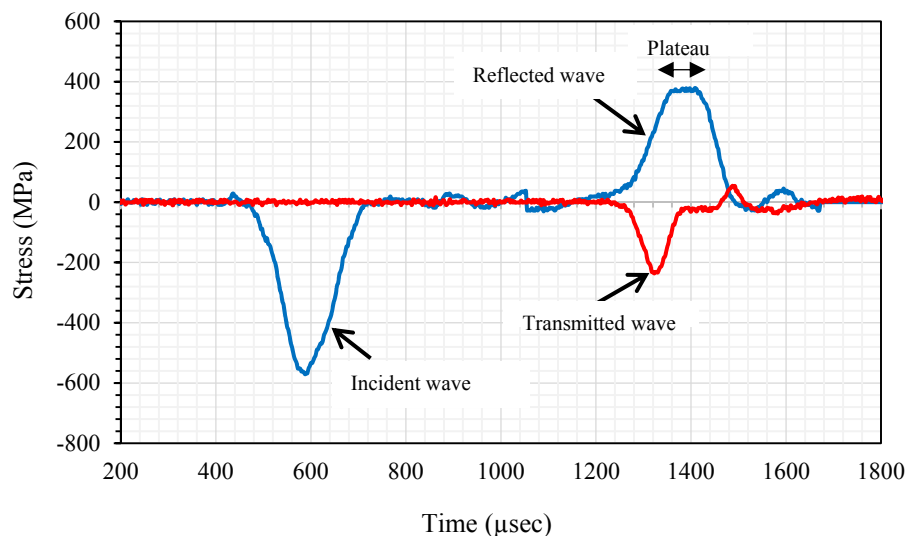


Figure 6-11 Typical stress wave histories in SHPB tests.

6.4.2.2 Data processing, test validity assumptions and stress equilibrium check

Further to the above recorded data, the processing of the stress wave signals is dependent upon the following three assumptions:

- (a) The pressure bars remained elastic during the impact tests and one-dimensional (1D) wave propagation theory is applicable.
- (b) All samples achieved dynamic stress equilibrium and deformed homogeneously without any premature failure during the tests.

(c) End friction effects were minimized.

The formulae for calculating stress, strain and strain rate histories have been given in equations 3-5. However, it should be noted that the applicability of these equations is subjected to satisfying the uniformity of longitudinal stress, strain and equilibrium condition in the sample during the test. This can be checked by comparing the summation of the incident and reflected stress wave at the incident surface of the sample, against the transmitted wave signal to ascertain the dynamic stress equilibrium (Hao and Hao, 2013). A typical stress-balance check after the removal of time lags is shown in Figure 6-12. As observed the “incident + reflected” stress curve is in good agreement with the transmitted stress wave which indicates that stress equilibrium is achieved.

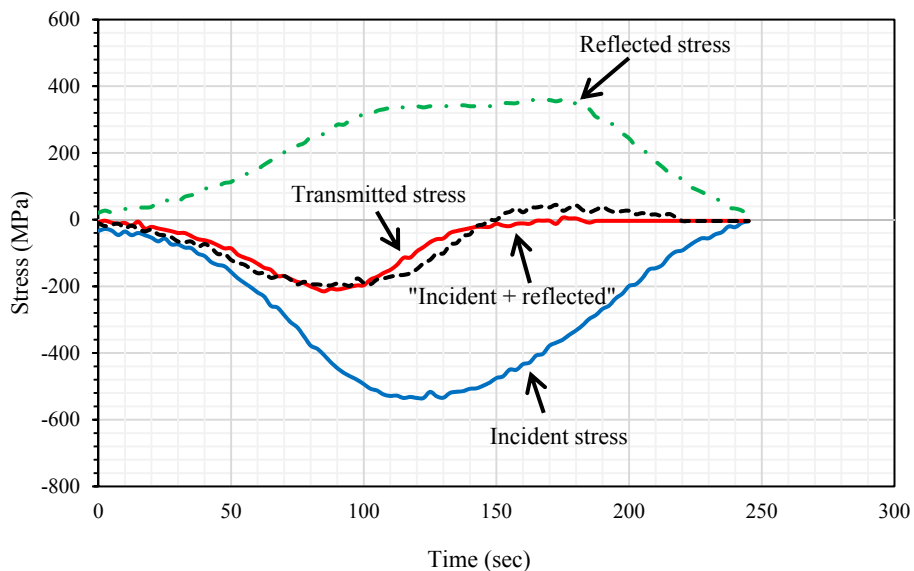
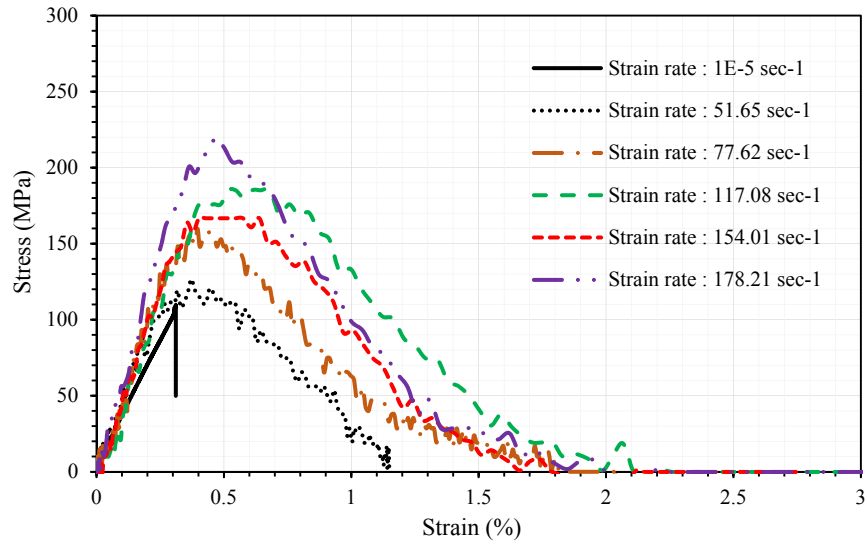


Figure 6-12 Typical dynamic stress equilibrium relationship between stress and time.

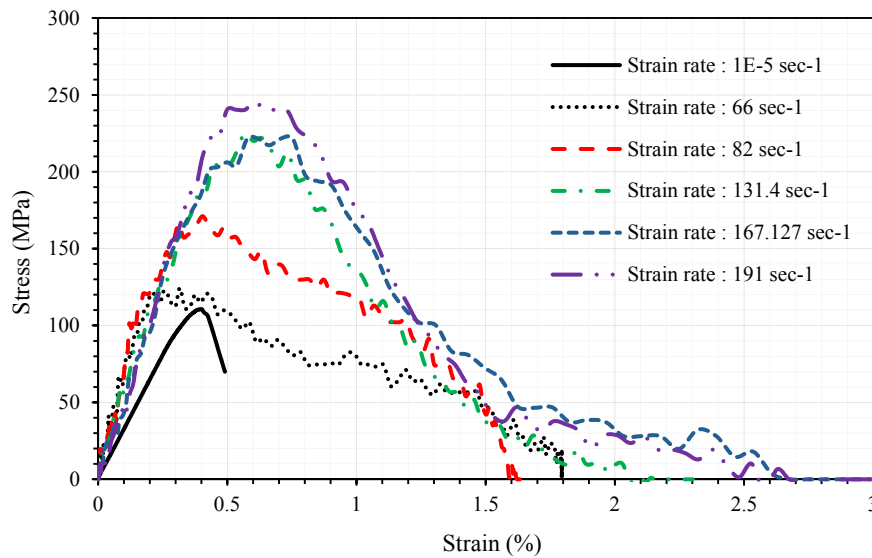
6.4.2.3 Comparison of dynamic stress-strain curves

The typical dynamic stress-strain curves of the plain geopolymer matrix and FRGC samples in a range of strain rates are shown in Figure 6-13. These curves are obtained using the formulae listed in Equations (6.3) to (6.5) and compared with an average quasi-static curve for the respective mix. An obvious strain rate effect is observed, which is apparently higher in FRGC samples in relation to the plain geopolymer matrix samples. It can be seen that the stress increases up to a peak value and then decreases at a given strain rate. Moreover, it can also be observed that the initial slope at different strain rates for both types of test samples is higher than that in the quasi-static loading condition, which reduced slightly upon reaching the ultimate load carrying capacity. This is mainly related to a sharp increase in strength at

higher loading rates in comparison to deformation (Su and Xu, 2013). A high level of geometric similarity in the stress-strain curves at different strain rates for plain geopolymer matrix is noticeable in Figure 6-13a, where a sharp increase in strength is followed by its loss during the unloading process. This is in good agreement to the impact tests carried out on cement mortars, where no ductility was present in the test samples (Chen et al., 2013).



(a)



(b)

Figure 6-13 Comparison of dynamic stress-strain curves of (a) plain geopolymer matrix (b) FRGC.

It can be established in Figure 6-13(b) that at a similar strain rate, a combined increase in compressive strength and deformation was realized due to the addition of fibers in

unreinforced geopolymer mortar. For example, at a strain rate of approximately 82 sec^{-1} , 131 sec^{-1} and 167 sec^{-1} the compressive strength increment in FRGC samples was 8%, 20%, and 18% more than plain geopolymer matrix. Furthermore, it has been reported that the critical strain corresponding to the peak stress increases at higher stress rates in comparison to quasi-static loading conditions (Hand Hao, 2013). The observation is also valid for both types of test samples in the current experimental investigation. However, in comparison to plain geopolymer matrix samples, the increase of critical strain in FRGC samples was more prominent. It can be seen that the critical strain under dynamic load increases up to 0.68% and 0.80% for plain geopolymer matrix and FRGC samples, respectively. The improved strength and deformation characteristics of FRGC samples specify the effective utilization of fibers towards the improvement in the impact resistance and ductility of mortar material at higher loading rates. On the other hand, the slightly less deformation increase in geopolymer matrix in comparison to fiber reinforced samples is typically associated with its brittle nature, where a rapid increase in strength is also accompanied by its lack of flexibility or deformability. A previous investigation on geopolymer concrete samples had a similar outcome (Gao et al., 2015), where a diminutive increase in critical strain was seen in regards to the increase in average strain rate or the maximum stress.

6.4.2.4 Comparison of rate effects on strength characteristics

Figure 6-14 illustrates the influence of strain rate effect on compressive strength characteristics of plain and FRGC samples. In general, the peak stress corresponding to a higher stress rate is known as the dynamic compressive strength, whereas, the dynamic increase factor (DIF_{fc}) is quantified by normalizing the strength value under impact load with respect to quasi-static compressive strength. The parameter has been proposed in different design codes such as CEB (2013) and UFC (2008) for the quantification of material behaviour at high-stress rates and its easy application towards the analysis and prediction of structural response against impact loadings.

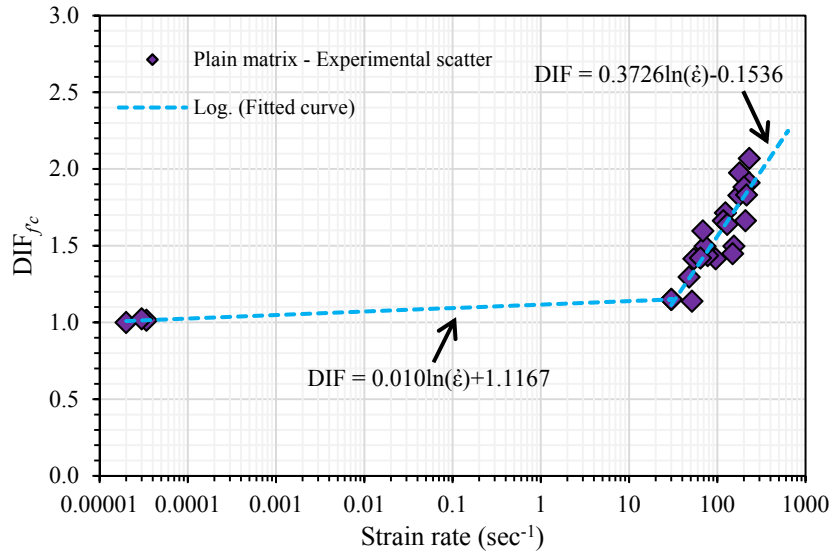
Based on a vast amount of test data, the DIFs of geopolymer mortar and FRGC within considered strain rate range, i.e., 10^{-5} to 230.38 sec^{-1} and 10^{-5} to 340 sec^{-1} , respectively are given as:

For geopolymer mortar:

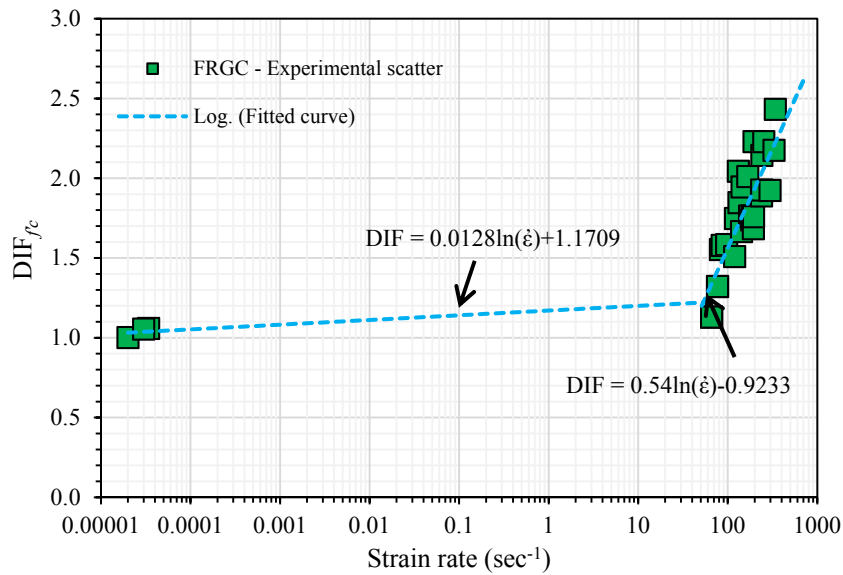
$$\begin{aligned} DIF_{fc} &= 0.010 \ln \dot{\epsilon} + 1.1167 & 10^{-5} \leq \dot{\epsilon} \leq 30.00 \text{ sec}^{-1} \\ DIF_{fc} &= 0.3726 \ln \dot{\epsilon} - 0.1536 & 30.00 \leq \dot{\epsilon} \leq 230.38 \text{ sec}^{-1} \end{aligned} \quad (6.6)$$

For FRGC:

$$\begin{aligned}
 DIF_{fc} &= 0.0128 \ln \dot{\epsilon} + 1.1709 & 10^{-5} \leq \dot{\epsilon} \leq 66.00 \text{ sec}^{-1} \\
 DIF_{fc} &= 0.540 \ln \dot{\epsilon} - 0.9233 & 66.00 \leq \dot{\epsilon} \leq 340 \text{ sec}^{-1}
 \end{aligned}
 \tag{6.7}$$



(a)



(b)

Figure 6-14 Relationship between the compressive DIF and strain rate of (a) plain and (b) FRGC.

It should be noted that in SHPB testing technique, the loading rates cannot always be controlled precisely. Due to the brittle nature of geopolymer material associated with its high compressive strength and the complicated nature of the SHPB technique especially for concrete-like materials, the maximum strain rates achieved were 230 and 340 sec^{-1} for geopolymer mortar and FRGC samples, respectively. Moreover, as with the majority of the previous studies on dynamic testing of concrete-like materials, the DIF between 10^{-5} and 30 sec^{-1} or 66 sec^{-1} are assumed to be proportional to the strain rates in a logarithmic manner mainly because of the non-availability of data in this range (Ross et al., 1996). It can be seen that the transition strain rates for plain and FRGC samples are located at 30.00 sec^{-1} and 66.00 sec^{-1} beyond which a high rate sensitivity occurs. Moreover, even though the transitional strain rate sensitivity of geopolymer mortar samples exists at a lower strain rate, it can be noticed that the FRGC samples displayed a higher increase in strength since the slopes of the fitted curves are steeper. At strain rate 30 sec^{-1} , the DIF of geopolymer mortar increases by 15% which is amplified by 106% at 230 sec^{-1} . On the other hand, at strain rate of 66 sec^{-1} , the DIF of fiber reinforced samples is improved by 13% which increases by 146% at a strain rate of 340 sec^{-1} .

According to Hao et al. (2016), generally for concrete-like materials, the increase in dynamic compressive strength at higher strain rates can be associated with the following reasons, i.e., (1) material strain-rate effect, (2) lateral inertial confinement, and (3) the end friction effects generated by the contact surface restrictions. Since in the current work, grease was applied at bar-sample interfaces, it is logical to assume that minimal contribution is made by boundary conditions to DIF. However, the inevitable presence of lateral inertia in high-speed impact tests and its involvement in the strength increment in proportion to the sample diameter has been reported in numerous investigations previously (Hao and Hao, 2011). Yet, it has also been observed that a significant effect from lateral inertial confinement exists only when the strain rates exceed 200 sec^{-1} . For that reason, it is believed that the test results presented herein are a material property rather than a structural effect for the geopolymer mortar samples since the samples are tested only up to a strain rate of 230 sec^{-1} . For FRGC samples, the influence of lateral inertial confinement is an additional factor that may have influenced the measured uniaxial compressive stress at higher strain rates. However, further research is required based on the practices reported by Hao and Hao (2010) to ascertain the precise nature of this phenomenon on the dynamic compressive strength of fiber reinforced geopolymer material.

Figure 6-15 compares the data from previous studies on the dynamic compressive strength of geopolymer mortar and concrete samples with the current test data. Also in Figure 6-15 the DIF from the constitutive CEB concrete model code for a compressive strength of 112 MPa is plotted. It can be seen that the test results reported herein are the closest to the trend line.

Furthermore, it is interesting to note that the test results reported by Feng et al. (2015) displayed relatively lower strain rate sensitivity, whereas, a higher strength increase was observed in (Luo et al., 2013).

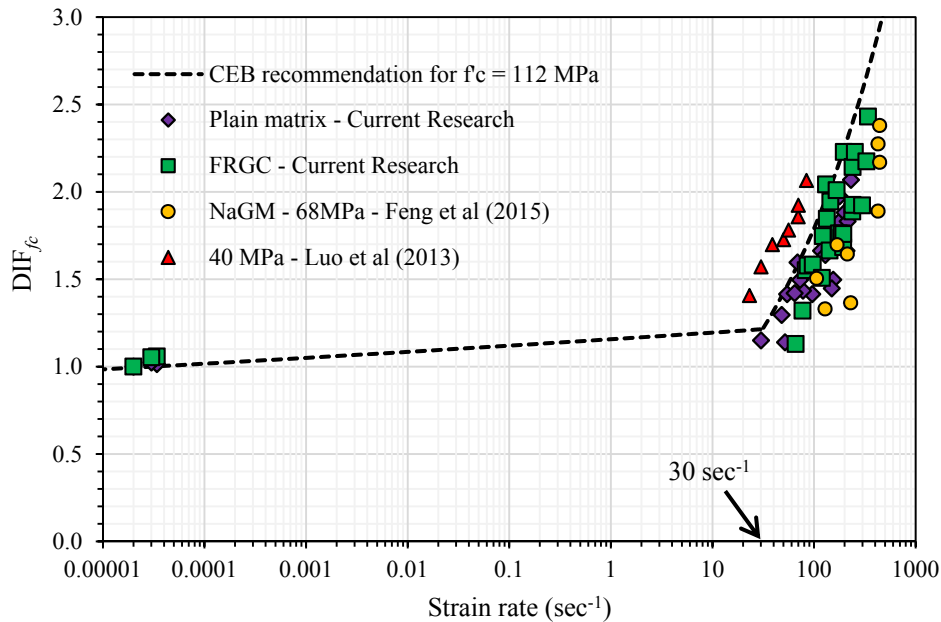


Figure 6-15 Comparison of DIF and average strain rate from current research and previous studies.

A major reason for this variance is considered to be related with the differences in the mixture proportions, curing conditions and the synthesis environment among these studies, i.e. the geopolymer mortar samples tested in (Feng et al., 2015) were prepared under the influence of heat curing, while, coarse aggregates were present in the samples used by Luo et al. (2013). For geopolymer binder, it is well-known that the variation of curing environment and temperature may influence the microstructure or moisture conditions within the test samples (Xie and Kayali, 2014) that could significantly change the material behaviour at higher stress rates. The fact that concrete-like materials are hydrostatic stress dependent (Rutland and Wang, 1997) and crack-inertia plays a major role in contributing to macroscopic strain-rate dependent strength enhancement at higher strain rates is another potential reason for the amplified sensitivity of test samples containing coarse aggregates.

Moreover, it is pertinent to highlight that the geopolymer mortar material investigated in the current research has a high compressive strength (112 MPa). In general, for high-strength concrete mixes (Xu and Li, 2009) the internal structure of the material is more compact and the stress transfers efficiently from the loading position towards the interior structure of the material, as a result, the strength properties of geopolymer mortar reported herein display

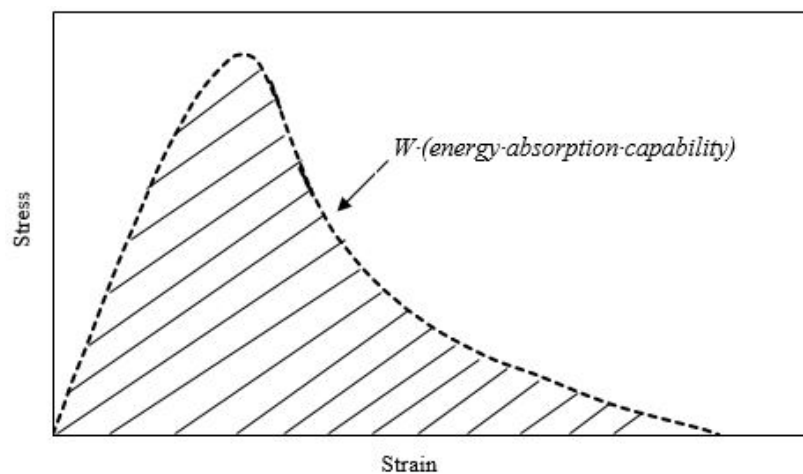
relatively lower sensitivity than in ref (Luo et al., 2013). While the increased sensitivity of FRGC samples in comparison with plain geopolymer matrix samples is primarily related to the additional resistance provided by the fibers to undergo high-speed lateral deformation. It should be noted that the quasi-static compressive strength of GC samples tested in (Luo et al., 2013) was 40 MPa only. Nevertheless, since the majority of data from the present study is concentrated just below the CEB guidelines which reflect the non-suitability of existing standards to some extent, and a slight overestimation of strength increase for the proposed geopolymer mixtures. The empirical DIF_{fc} strength relations proposed earlier in Equations (6.6) and (6.7) for the strength increase may be used for the prediction of material behaviour at higher stress states.

6.4.2.5 Comparison of Impact Toughness

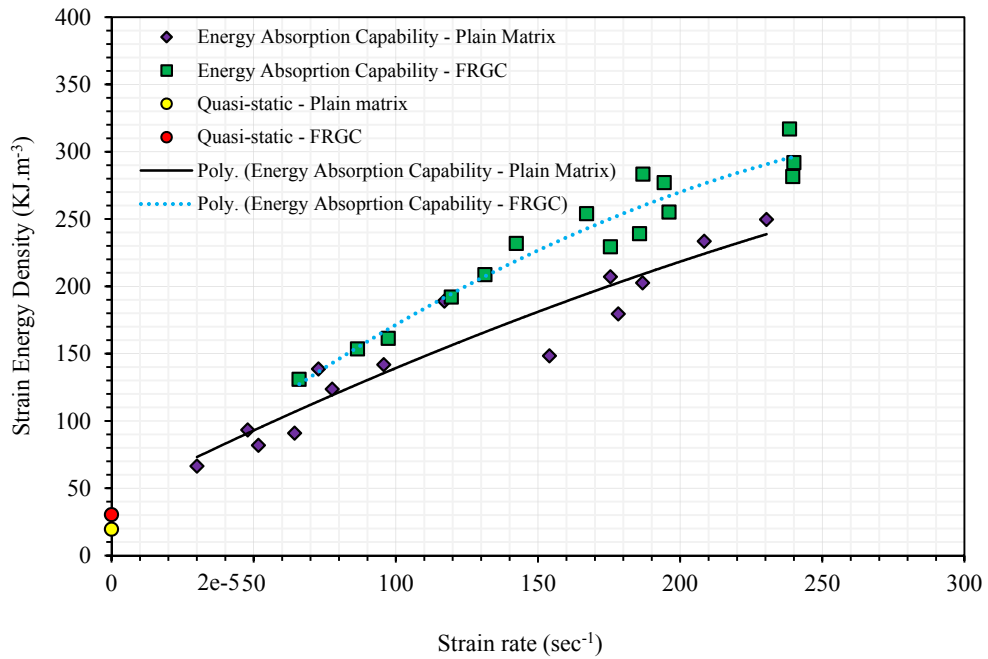
In order to demonstrate the influence of strain-rate effect on the response of plain geopolymer matrix and FRGC more clearly and estimate their energy-absorption capability at higher loading rates, the present section utilizes the expression in Equation (6.8). In general, in SHPB tests the toughness of material can be determined by estimating the area under the stress-strain curves as shown in Figure 6-16(a), also known as “strain energy density (SED)” of the material (Hao and Hao, 2011). The calculated results for a range of strain rates are plotted in Figure 6-16(b) and are compared with quasi-static results for both types of test samples.

$$W = \int \sigma_{(t)} d\varepsilon_{(t)} \quad (6.8)$$

Where “W” represents the energy absorption capability of the material and $\sigma(t)$ and $\varepsilon(t)$ are the time-dependent stress and strains, respectively.



(a)



(b)

Figure 6-16 Comparison of energy absorption capability of plain and FRGC at different strain rates.

As shown in Figure 6-16(b), under quasi-static compression, the SED of FRGC and plain geopolymer matrix samples were 19.50KJ.m^{-3} and 30.35KJ.m^{-3} , respectively. It can be seen that the energy consumed by the fiber reinforced specimens during the fracture process was 56% higher than the samples made of plain geopolymer matrix. However, since the FRGC samples were still intact when the tests were stopped, therefore, it is believed that the reported SED value is a slight underestimation of the material's capacity in comparison to geopolymer matrix.

Moreover, it can also be observed that at higher strain rates “W” ranges from 66.40KJ.m^{-3} to 249.77KJ.m^{-3} for unreinforced samples within the strain rate range of 30 sec^{-1} to 230 sec^{-1} , whereas, for fiber reinforced counterparts at a similar strain rate range, i.e., 66 sec^{-1} to 240 sec^{-1} , “W” ranges from 130KJ.m^{-3} to 316 KJ.m^{-3} . On the one hand, this indicates that the plain geopolymer mortar matrix samples achieved good impact toughness with an increase in the strain rate, however, it can also be appreciated that at an identical strain rate, e.g., 65 sec^{-1} , 150 sec^{-1} , and 230 sec^{-1} , the SED during the fracture and failure process of FRGC samples was 44%, 56% and 27% more than the unreinforced counterparts. The test results indicate that the presence of fibers effectively improved the overall toughness of the plain geopolymer matrix under impact. The relationship between the SED (W) and average strain rate within the considered range can be expressed as:

$$\begin{aligned}
 \text{Plain matrix} : W &= -0.0009\varepsilon^2 + 1.0623\varepsilon + 42.053 \\
 \text{FRGC} : W &= -0.0024\varepsilon^2 + 1.6907\varepsilon + 25.983
 \end{aligned}
 \tag{6.9}$$

6.4.2.6 Comparison of failure processes

For a better understanding of the impact behaviour of plain and FRGC samples, the failure processes were recorded using a high-speed camera with forty thousand fps and resolution of 1024×512 pixels. Figures 6-17 and 6-18 draw a comparison between the failure processes of plain geopolymer matrix and FRGC samples under the same impact, i.e., the striker bar was launched with 0.1 MPa pressure in the vessel.

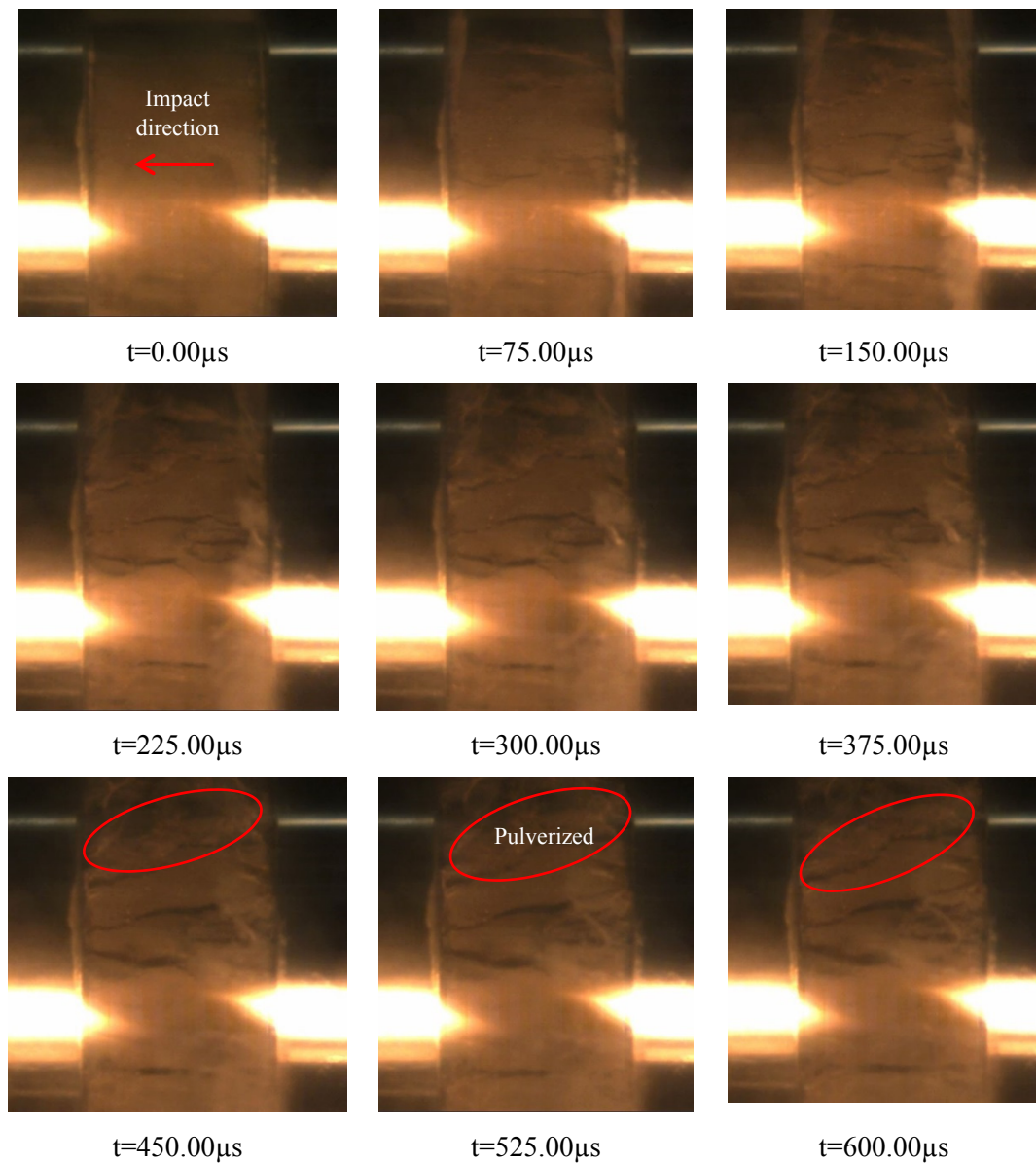


Figure 6-17 Fracture images and failure process of plain geopolymer matrix at different time instants.

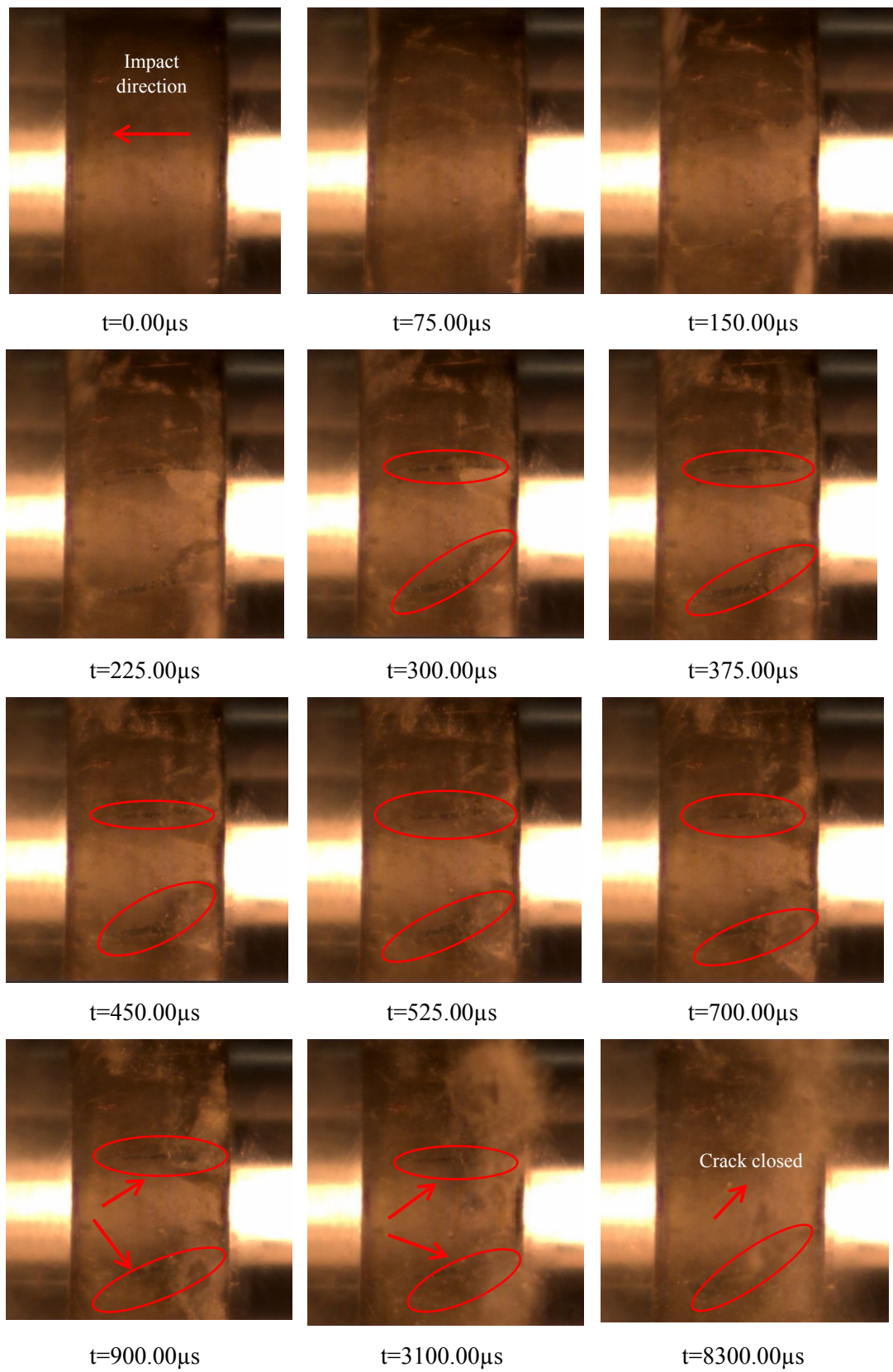


Figure 6-18 Fracture images and failure process of FRGC at different time instants.

The first image corresponds to the time instant when the samples were stressed initially and are used as a reference. As evident from the screenshots, the samples were impacted on the right side. By focusing on the failure process of plain geopolymer matrix in Figure 6-17, it can be established that after several wave reflections and the superposition of the incident and reflected wave, the cracks initiated from both edges of the sample at $75\mu\text{s}$ which began to extend further along with the formation of more columnar cracks at $150\mu\text{s}$. Later, these cracks became wider at $225\mu\text{s}/300\mu\text{s}$ and several major cracks may be seen throughout the test sample within the time period of $375\mu\text{s}$ and $600\mu\text{s}$, which resulted in the complete pulverization of test specimen and formation of a significant amount of debris.

On the other hand, the failure process of FRGC sample under the same impact presented a slightly different damage mechanism as shown in Figure 6-18. From the comparison, it can be observed that unlike the plain geopolymer matrix where a significant number of cracks developed during the initial $150\mu\text{s}$ of the loading process, the FRGC sample remained undamaged with minor hairline cracking noticed appearing on the surface of the test specimens from the right edge. However, as the time elapsed, at least three to four major cracks were formed at $225\mu\text{s}$ which became wider with the progression of loading process until $525\mu\text{s}$. Compared to unreinforced geopolymer mortar samples with microscale cracks developed continuously and extended rapidly throughout the test samples, the addition of fibers played a significant role in sustaining the integrity of FRGC samples. It can be seen that the use of hybrid-fiber reinforcement not only prevented the formation of vast amounts of cracks but also effectively improved the ability of crack recovering. As evident, some of the cracks which are clearly visible in the images taken at $450\mu\text{s}$, $525\mu\text{s}$, and $700\mu\text{s}$ are found to disappear at $900\mu\text{s}$ and 3.1ms . It can be observed that at 8.3ms after the initial impact there was no crack present.

This is an interesting observation and is primarily related to the use of spiral steel fibers for the matrix reinforcement, which enabled the partial recovery of crack openings. A similar response was reported in a previous study, where the use of spiral steel fibers in OPC concrete samples that were tested in dynamic split tension showed the improved ability of fiber in controlling the crack propagation at higher loading rates (Hao and Hao, 2016).

6.4.2.7 Comparison of post-test failure patterns

The post-test damage patterns of plain geopolymer matrix and FRGC samples under high-rate impact tests are shown in Figures 6-19 and 6-20. Generally, the failure pattern of both unreinforced and reinforced geopolymer composite samples changed with the increase in the strain rate. It can be seen in Figure 6-19 for test samples containing no fibers that at strain rate

51.65 sec⁻¹, the samples broke into several pieces and were partially crushed. However, as the loading rate was increased, the test samples disintegrated into numerous fragments of irregular sizes, i.e., 178.21 sec⁻¹ and 230.38 sec⁻¹ the tested samples pulverized into small pieces, such that, the average size of fragments decreased proportionately to the strain rate.

It should be noted that based on the fracture theory (Lee et al., 2006), ideally, upon impact, the damage should accumulate from the edges towards the centre of the sample. Although the present study is carried out on geopolymer mortars and no coarse aggregates are present in the test samples, the test samples may not be completely regarded as isotropic or homogenous in nature since random flaws and hydration cracks always exist (Gao et al., 2015). Therefore, the failure patterns of plain geopolymer matrix observed here were not strict edge type failures.



Figure 6-19 Damage pattern of plain geopolymer matrix samples in a range of strain rates.

Moreover, the material strain effect, i.e., the increase in peak stress with the increase in average strain rate typically known as “strain-rate hardening effect”, can be explained by relating the damage patterns of plain and FRGC samples. It is believed that upon pouring of the mixtures and curing process, tiny cracks or damage compartments were produced mainly because of geopolymer cement slurry shrinkage or local compression, etc. (Luo et al., 2013). As observed, under quasi-static compression tests the geopolymer mortar samples split into four or five large pieces. In this situation, the loading procedure was more of a crack expansion process.

However, when the strain rate was increased and the crack propagation velocity reached the sensitivity threshold, mainly due to the inertial resistance, the failure occurred because of the initiation of both the newer cracks and the expansion of existing ones. In this case, significantly more amount of energy was required for the production of new cracks alongside with that required for crack expansion process. Higher the impact velocity or strain rate, more the number of cracks and the amount of energy required for this procedure. The hysteresis behaviour continued upon further increase in the pressure, however, since the impact duration was short, therefore according to the principle of impulse-momentum or work-energy, the increase in external energy and impulse can only be offset by an increase in stress.

A similar explanation applicable for FRGC samples. However, due to the presence of fibers, the test samples did not show an extensive amount of fragmentation; instead, the extent of micro-crack damage within the composite samples increased at high strain rates. As can be seen in Figure 6-20, the FRGC samples kept their structural integrity to a large extent. The post-test damage patterns are in complete synergy to the aforementioned failure process. It can be observed that at low strain rates, i.e., 66 sec^{-1} , and 82 sec^{-1} , the FRGC samples remained unscathed and only minor damage was seen at the edges of the samples. However, at higher strain rates, these cracks became wider and extensive micro-cracking was noticed throughout the test samples. Numerous spiral steel fibers were found elongated or broken with the maximum damage occurring at the edges of the samples.

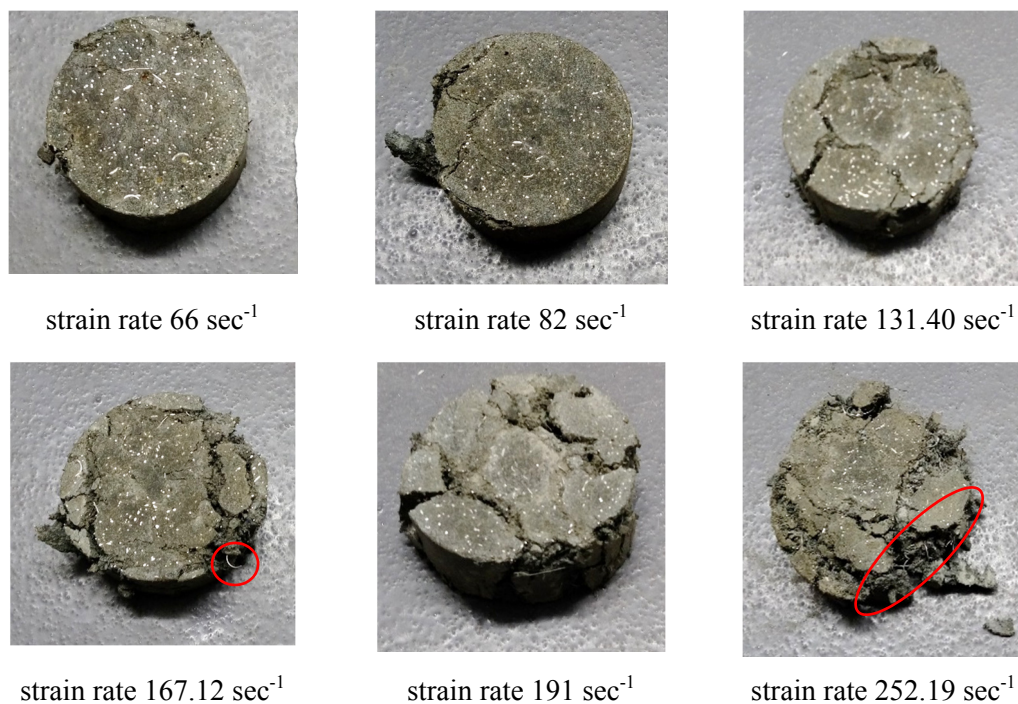


Figure 6-20 Damage pattern of FRGC samples in a range of strain rates.

A previous study (Nazarimofrad et al., 2017) on steel fiber reinforced concrete observed similar damage behaviour where fibrous concrete mixtures exhibited higher impact resistance and a majority of the cracks were intercepted by steel fibers to retain bulk of the samples intact. It is obvious that the inclusion of HSPE fibers in conjunction with spiral steel and hooked-end steel fibers has significantly increased the toughness of the geopolymer material explicitly. Besides, it can also be concluded that the used fiber combination had clung onto the fragments without the formation of any major amount of debris, thus, signifying higher prospect for the synthesized geopolymer composites for use in structures with strategic importance but much improved green credentials.

6.5 Conclusions

The present study investigated the impact response of high-strength plain and fiber reinforced geopolymer composites using Ø100-mm SHPB apparatus. The source materials used here are primarily the industrial waste products and the FRGC mixtures contained an equal-part combination of hooked-end steel and spiral steel fibers at a fiber volume fraction of 1.60% which is combined with 0.40% of HSPE fibers to improve the toughness of the material. The geopolymer mixtures are prepared by conventional methods which signify a great potential for their use in the actual construction. Based on the test results, the major conclusions are:

- 1) The synthesized geopolymer mixtures exhibited high compressive strength at 28 days of ambient curing, i.e., 95 MPa and 88 MPa for plain and FRGC samples, respectively. Under quasi-static loading, the high-strength geopolymer matrix samples failed in an explosive manner whereas the FRGC samples retained their original shape after the tests.
- 2) The dynamic compressive mechanical properties were measured at the age of 60 days and the reference quasi-static compressive strengths were 112 MPa and 114 MPa for plain and FRGC samples, respectively. A strong strain rate dependency was observed for both types of materials within the strain rate range of 30 sec^{-1} to 340 sec^{-1} .
- 3) The dynamic strength enhancement is found to be higher for fiber reinforced geopolymer samples in comparison with unreinforced counterparts such that DIFs increase linearly in a logarithmic manner with the average strain rate and the sensitivity threshold exists at 30 sec^{-1} and 66.01 sec^{-1} for plain and FRGC samples, respectively.
- 4) The existing CEB code guidelines do not reflect the true increase in the dynamic compressive strength of geopolymer mixtures. Based on the test results, empirical DIF relations are proposed which may be used to simulate the behaviour of the studied plain and fiber reinforced geopolymer materials at higher loading rates.

- 5) A relatively good impact toughness is observed for both types of samples where obvious relationships between the average strain rate and energy absorption capability are noted in the form of binomial curves. Within the considered strain rate range, i.e., 30 sec^{-1} to 230 sec^{-1} and 66 sec^{-1} and 340 sec^{-1} , the energy laws confirm the strain rate dependency of plain and fiber reinforced samples such that the compression resistibility of high-strength mortar matrix increases with the addition of fibers.
- 6) The post-test damage patterns are strain rate dependent. Under quasi-static loading, geopolymer mortar samples broke into several large pieces, whereas for FRGC samples, a wide shear crack is noticed in the test samples. At high strain-rate loadings, the geopolymer mortar samples ground into numerous small fragments, while the FRGC samples kept their structural integrity to a large extent with extensive micro-cracking throughout the tested samples.

6.6 References

ASTM. (2012a). Standard specification for coal fly ash and raw or calcined natural pozzolan for use in concrete. *ASTM C618-12a*, Philadelphia.

ASTM. (2013). Standard test method for flow of hydraulic cement mortar. *ASTM C1437-13*, Philadelphia.

ASTM. (2014). Standard test method for Density and Void Content of freshly mixed pervious concrete. *ASTM C1688-14*, Philadelphia.

ASTM. (2015a). Standard test method for compressive strength of cylindrical concrete specimens.. *ASTM C39-15*, Philadelphia.

ASTM. (2015b). Standard test method for relative density (Specific Gravity) and absorption of fine aggregate. *ASTM C128-15*, Philadelphia.

Atiř, C. D., Görür, E. B., Karahan, O., Bilim, C., İlkentapar, S., & Luga, E. (2015). Very high strength (120 MPa) class F fly ash geopolymer mortar activated at different NaOH amount, heat curing temperature and heat curing duration. *Construction and Building Materials*, *96*, 673-678.

Banthia, N., & Gupta, R. (2004). Hybrid fiber reinforced concrete (HyFRC): fiber synergy in high strength matrices. *Materials and Structures*, *37*(10), 707-716.

Bařčarevć, Z. (2015). 14 - The resistance of alkali-activated cement-based binders to chemical attack *Handbook of Alkali-Activated Cements, Mortars and Concretes* (pp. 373-396). Oxford: Woodhead Publishing.

Benhelal, E., Zahedi, G., Shamsaei, E., & Bahadori, A. (2013). Global strategies and potentials to curb CO₂ emissions in cement industry. *Journal of Cleaner Production*, *51*, 142-161.

Bischoff, P. H., & Perry, S. H. (1991). Compressive behaviour of concrete at high strain rates. *Materials and Structures*, *24*(6), 425-450.

- CEB. (2013). Comite Euro-International Du Beton (CEB)-fib model code for Concrete Structures 2010. Telford.
- Chen, X., Wu, S., & Zhou, J. (2013). Experimental and modeling study of dynamic mechanical properties of cement paste, mortar and concrete. *Construction and Building Materials*, 47, 419-430.
- Chi, M., & Huang, R. (2013). Binding mechanism and properties of alkali-activated fly ash/slag mortars. *Construction and Building Materials*, 40, 291-298.
- Collins, F., & Sanjayan, J. G. (2001). Microcracking and strength development of alkali activated slag concrete. *Cement and Concrete Composites*, 23(4-5), 345-352.
- Deb, P. S., Nath, P., & Sarker, P. K. (2014). The effects of ground granulated blast-furnace slag blending with fly ash and activator content on the workability and strength properties of geopolymer concrete cured at ambient temperature. *Materials & Design*, 62, 32-39.
- Feng, K. N., Ruan, D., Pan, Z., Collins, F., Bai, Y., Wang, C. M., & Duan, W. H. (2015). Mechanical behavior of geopolymer concrete subjected to high strain rate compressive loadings. *Materials and Structures*, 48(3), 671-681.
- Fernandez-Jimenez, A., García-Lodeiro, I., & Palomo, A. (2007). Durability of alkali-activated fly ash cementitious materials. *Journal of Materials Science*, 42(9), 3055-3065.
- Gao, Y., Xu, J., Bai, E., Luo, X., Zhu, J., & Nie, L. (2015). Static and dynamic mechanical properties of high early strength alkali activated slag concrete. *Ceramics International*, 41(10, Part A), 12901-12909.
- Garcia-Lodeiro, I., Palomo, A., & Fernández-Jiménez, A. (2015). 2 - An overview of the chemistry of alkali-activated cement-based binders *Handbook of Alkali-Activated Cements, Mortars and Concretes* (pp. 19-47). Oxford: Woodhead Publishing.
- Hao, H., Hao, Y., Li, J., & Chen, W. (2016). Review of the current practices in blast-resistant analysis and design of concrete structures. *Advances in Structural Engineering*, 19(8), 1193-1223.
- Hao, Y., Hao, H., & Li, Z.-X. (2010). Numerical Analysis of Lateral Inertial Confinement Effects on Impact Test of Concrete Compressive Material Properties. *International Journal of Protective Structures*, 1(1), 145-167.
- Hao, Y., & Hao, H. (2011). Numerical Evaluation of the Influence of Aggregates on Concrete Compressive Strength at High Strain Rate. *International Journal of Protective Structures*, 2(2), 177-206.
- Hao, Y., & Hao, H. (2013). Dynamic compressive behaviour of spiral steel fibre reinforced concrete in split Hopkinson pressure bar tests. *Construction and Building Materials*, 48, 521-532.
- Hao, Y., & Hao, H. (2016). Mechanical properties and behaviour of concrete reinforced with spiral-shaped steel fibres under dynamic splitting tension. *Magazine of Concrete Research*, 68(21), 1110-1121.
- Hao, Y., & Hao, H. (2017). Pull-out behaviour of spiral-shaped steel fibres from normal-strength concrete matrix. *Construction and Building Materials*, 139, 34-44.

- Hardjito, D., Wallah, S. E., Sumajouw, D. M., & Rangan, B. V. (2004). On the development of fly ash-based geopolymer concrete. *ACI Materials Journal-American Concrete Institute*, 101(6), 467-472.
- Khale, D., & Chaudhary, R. (2007). Mechanism of geopolymerization and factors influencing its development: a review. *Journal of Materials Science*, 42(3), 729-746.
- Khan, M. Z. N., Hao, Y., Hao, H., & Shaikh, F. U. A. (2018). Mechanical properties of ambient cured high strength hybrid steel and synthetic fibers reinforced geopolymer composites. *Cement and Concrete Composites*, 85(Supplement C), 133-152.
- Khan, M. Z. N., Shaikh, F. U. A., Hao, Y., & Hao, H. (2016). Synthesis of high strength ambient cured geopolymer composite by using low calcium fly ash. *Construction and Building Materials*, 125, 809-820.
- Khan, M. Z. N., Shaikh, F. U. A., Hao, Y., & Hao, H. (2017). Effects of Curing Conditions and Sand-to-Binder Ratios on Compressive Strength Development of Fly Ash Geopolymer. *Journal of Materials in Civil Engineering*, 30(2), 04017267.
- Khandelwal, M., Ranjith, P. G., Pan, Z., & Sanjayan, J. G. (2013). Effect of strain rate on strength properties of low-calcium fly-ash-based geopolymer mortar under dry condition. *Arabian Journal of Geosciences*, 6(7), 2383-2389.
- Lee, O. S., Kim, S. H., & Lee, J. W. (2006). Thickness effect of pulse shaper on dynamic stress equilibrium in the NBR rubber specimen. *Key Engineering Materials, Volumes (306-308)*, 1007-1012.
- Li, Q. M., & Meng, H. (2003). About the dynamic strength enhancement of concrete-like materials in a split Hopkinson pressure bar test. *Int. J. Solids Struct.*, 40, 343.
- Li, W., & Xu, J. (2009). Impact characterization of basalt fiber reinforced geopolymeric concrete using a 100-mm-diameter split Hopkinson pressure bar. *Materials Science and Engineering: A*, 513–514(0), 145-153.
- Lok, T. S., Zhao, P. J., & Lu, G. (2003). Using the split Hopkinson pressure bar to investigate the dynamic behaviour of SFRC. *Magazine of Concrete Research*, 55(2), 183-191.
- Luo, X., Xu, J.-y., Bai, E.-l., & Li, W. (2013). Research on the dynamic compressive test of highly fluidized geopolymer concrete. *Construction and Building Materials*, 48, 166-172.
- Menna, C., Asprone, D., Forni, D., Roviello, G., Ricciotti, L., Ferone, C., Cadoni, E. (2015). Tensile behaviour of geopolymer-based materials under medium and high strain rates. *Paper presented at the EPJ Web of Conferences*.
- Nasvi, M. C. M., Rathnaweera, T. D., & Padmanabhan, E. (2016). Geopolymer as well cement and its mechanical integrity under deep down-hole stress conditions: application for carbon capture and storage wells. *Geomechanics and Geophysics for Geo-Energy and Geo-Resources*, 2(4), 245-256.
- Nath, P., & Sarker, P. K. (2014). Effect of GGBFS on setting, workability and early strength properties of fly ash geopolymer concrete cured in ambient condition. *Construction and Building Materials*, 66(0), 163-171.

- Nazarimofrad, E., Shaikh, F. U. A., & Nili, M. (2017). Effects of steel fibre and silica fume on impact behaviour of recycled aggregate concrete. *Journal of Sustainable Cement-Based Materials*, 6(1), 54-68.
- Pan, Z., & Sanjayan, J. G. (2010). Stress–strain behaviour and abrupt loss of stiffness of geopolymer at elevated temperatures. *Cement and Concrete Composites*, 32(9), 657-664.
- Ross, C. A., Jerome, D. M., Tedesco, J. W., & Hughes, M. L. (1996). Moisture and strain rate effects on concrete strength. *ACI Mater. J.*, 93, 293.
- Rutland, C. A., & Wang, M. L. (1997). The effects of confinement on the failure orientation in cementitious materials experimental observations. *Cement and Concrete Composites*, 19(2), 149-160.
- Sakulich, A. R. (2011). Reinforced geopolymer composites for enhanced material greenness and durability. *Sustainable Cities and Society*, 1(4), 195-210.
- Shaikh, F. U. A. (2013). Review of mechanical properties of short fibre reinforced geopolymer composites. *Construction and Building Materials*, 43(0), 37-49.
- Su, H., & Xu, J. (2013). Dynamic compressive behavior of ceramic fiber reinforced concrete under impact load. *Construction and Building Materials*, 45(Supplement C), 306-313.
- UFC 3-340-02 (2008). Structures to resist the effects of accidental explosions. Department of Defense, USA.
- Xie, J., & Kayali, O. (2014). Effect of initial water content and curing moisture conditions on the development of fly ash-based geopolymers in heat and ambient temperature. *Construction and Building Materials*, 67, Part A(0), 20-28.
- Xin, L., Jin-yu, X., Weimin, L., & Erlei, B. (2014). Effect of alkali-activator types on the dynamic compressive deformation behavior of geopolymer concrete. *Materials Letters*, 124(0), 310-312.
- Xin Luo, J.-Y. X. (2013). Dynamic splitting-tensile testing of highly fluidised geopolymer concrete. *Magazine of Concrete Research*, 65(14), 7.
- Xu, Z., Hao, H., & Li, H. N. (2012). Experimental study of dynamic compressive properties of fibre reinforced concrete material with different fibres. *Materials & Design*, 33, 42-55.
- Yunsheng, Z., Wei, S., Zongjin, L., Xiangming, Z., Eddie, & Chungkong, C. (2008). Impact properties of geopolymer based extrudates incorporated with fly ash and PVA short fiber. *Construction and Building Materials*, 22(3), 370-383.
- Zhu, D., Mobasher, B., & Peled, A. (2013). Experimental study of dynamic behavior of cement-based composites. *Journal of Sustainable Cement-Based Materials*, 2(1), 1-12.

CHAPTER 7 MECHANICAL PROPERTIES OF AMBIENT CURED HIGH-STRENGTH PLAIN AND HYBRID FIBER REINFORCED GEOPOLYMER COMPOSITES FROM TRIAXIAL COMPRESSIVE TESTS

7.1 Abstract

Geopolymer binders have evolved as a promising alternative to ordinary Portland cement (OPC) in concrete over the last few decades. However, many aspects of their mechanical behaviour such as their performance under multiaxial stress conditions are still unknown, which are of primary importance for their structural application. In this paper, the triaxial compressive behaviour of newly developed ambient-cured high-strength geopolymer (HSG) mortar, and fiber reinforced geopolymer composites (FRGC) is studied. A series of $\text{Ø}50 \times 100$ mm cylindrical samples were prepared using low-calcium fly ash and ground granulated blast furnace slag, while hybrid steel-polyethylene fiber reinforcement with fiber volume fraction of 2% was used to reinforce the brittle geopolymer matrix. Standard triaxial tests with fifteen different levels of confining pressures [(σ_3) ; ranging between 0 and 100 MPa] were employed to comprehensively investigate the triaxial stress-strain characteristics of synthesized materials from low to high range of confining pressures. According to test results, the unreinforced HSG samples exhibited linear elastic stress-strain behaviour under uniaxial stress condition and showed catastrophic brittle failure. Instead, the samples tested under confinement showed pseudo-ductile behaviour. On the other hand, the inclusion of hybrid-fiber reinforcement has meaningfully helped to improve the ductility of HSG matrix. The peak axial stress and the corresponding axial strain was found to increase with the increase of confining pressure, although the influence of active lateral confinement was more pronounced on the triaxial strength of HSG samples. The two most commonly used failure criteria for OPC concrete, i.e., Power-law and Willam-Warnke failure criterion were used to develop the empirical relations to predict the peak axial stress as a function of confining pressure for the studied materials. The proposed relationships can be used for the calibration of existing concrete material models. The obtained test results were also compared with the existing triaxial compression test data on high strength cement based concretes and composites in the literature to highlight the differences between geopolymers and OPC concrete.

7.2 Introduction

With an ever growing demand for using sustainable alternatives to ordinary Portland cement (OPC), the modern construction materials have seen a new cementless binder in the form of “Geopolymer” (Davidovits, 1994). The specific advantages of using by-product source materials (Sakulich, 2011), high early-age strength (Atiş et al., 2015), improved fire resistance (Hosan et al., 2016) and reduced carbon dioxide (CO₂) emissions (Benhelal et al., 2013) have driven an increased research interest in these new alkali-activated cementitious materials (AACMs). Previous studies on geopolymer materials have identified numerous factors, such as, the nature of silico-aluminous materials (Khan et al., 2016), types of alkali-activators (Rashad, 2014), mixing sequences (Part et al., 2015), and curing conditions (Khan et al., 2017) that could significantly influence their mechanical properties. Some other investigators focused on improving their structural resistance, toughness, and flexure tensile strength by introducing epoxy-resins (Roviello et al., 2015) and a range of fiber types in different geopolymer formulations (Shaikh, 2013).

However, for practical use of geopolymers in civil engineering applications, the availability of constitutive relationships which can empirically predict their behaviour under combined stress states is still a grey area for these novel binders. Generally, the compressive strength of concrete is the fundamental property commonly used in the design of reinforced concrete structures. However, in the majority of the cases, the failure of concrete in a structure occurs under complex stress states (He and Song, 2010). Besides, it is well established that owing to an inherent microstructural variation, almost all engineering materials deform distinctively. Thus it is the information on failure mechanism under complex loading conditions that form the basis of developing constitutive models or failure criteria for them (Chen, 1993). A thorough understanding of the behaviour of geopolymer binders under multiaxial stress states is necessary. In this regard, the stress-strain behaviour of the materials is usually investigated under a series of lateral confinements or more commonly referred to as “triaxial stress” conditions.

In the past, starting from as early as 1929, Richart et al. (1929) made the pioneer investigation to understand the triaxial behaviour of concrete. Many researchers have studied the behaviour of ordinary and cement affluent, high and ultra-high strength fiber reinforced concretes (NSC, HSC or UHSFRC) under multiaxial compression. Various stress-strain models have been proposed, which can adequately regenerate the load-deformation behaviour of concrete under confinement, e.g., for the concrete material used in infilled steel tubular columns or concrete columns confined with high tensile strength fiber-reinforced polymer fabric and steel reinforcements, etc. (Cusson and Paultre, 1995). Other researchers, e.g. (Ottosen, 1979;

Menetrey and Willam, 1995; Xie et al., 1995; Imran and Pantazopoulou, 1996; Ansari and Li, 1998; Candappa et al., 2001; Samani and Attard, 2012), used the triaxial compression test results to predict the generalized strength enhancement, material deformation, residual strength capacity, and volumetric expansion for OPC concrete. However, some apparent differences in these studies are related to the type of concrete materials, including NSC or HSC, the presence of fibers, sample sizes, and the range of low or high confining pressures used during the tests.

On the other hand, the existing database on the triaxial compressive behaviour of geopolymer mortar, concrete, and composite materials is trivial. The existing studies only provide preliminary information on the triaxial stress-strain behaviour of geopolymer pastes. For example, amongst the very few, Giasuddin et al. (2014) investigated the stress-strain characteristics of two differently graded geopolymer pastes, (i.e. high (85 MPa) and low (28 MPa) under a range of low confining pressures, i.e. $\sigma_3/f'_c \leq 0.40$, where σ_3 is the confining pressure, and f'_c denotes the compressive strength. Based on their test data, linear strength constitutive model as per Mohr coulomb's failure criteria and modified parabolic relation of Xiao et al. (2010) with slightly different material constants was proposed. They concluded that the trend of strength enhancement of geopolymer paste is similar to OPC concrete under confinement. However, previous studies show that the constitutive relationships proposed for low levels of confinement ratios (σ_3/f'_c) may lead to an erroneous prediction of the material behaviour at higher levels of confinement (Franam et al. 2010). Similarly, for critical axial strain corresponding to peak axial stress, they also modified Xiao et al. (2010) parabolic equation proposed for axial deformation. The constant in the constitutive relation for geopolymer paste was found to be significantly lower than that of NSC or HSC. The fitted curves suggested increased stiffness in geopolymer material as compared to OPC concrete. Given that the conclusion may be valid for geopolymer binders due to their ceramics-like nature, however, it is believed that the finding may also stem from the difference in the employed load paths. In Xiao et al.'s tests (2010), the longitudinal axial stress was only applied after the confining pressure reached a specified target value (i.e., proportional load path) instead of a standard loading path used by Giasuddin et al. (2014). The slopes of ascending portions of the stress-strain curves tend to be lower than that of the samples tested in uniaxial compression in the latter case and could be otherwise as reported in other investigations (Ansari and Li, 1998; Lu and Hsu, 2006).

In another investigation (Lyu et al., 2013), metakaolin based geopolymer mixtures containing varying silicon dioxide to sodium oxide ($\text{SiO}_2/\text{Na}_2\text{O}$) molar ratios were tested under uniaxial and triaxial compressive stress states. The primary goal of this research was to identify the influence of various $\text{SiO}_2/\text{Na}_2\text{O}$ molar oxide ratios on the microstructure development of

geopolymers and their modification under a set of low confining pressures. The microstructure of geopolymer intrinsically relied on the level of polymerization and the formation of $Q^4(nAl)$ network within the binding gels which control their failure modes under confinement. The research concludes that a well-formed geopolymer material fails in a brittle manner in uniaxial compression, while with an increase in the confining stress the failure mode changes from brittle to ductile.

Very recently, with an objective of using geopolymer cement in carbon storage sequestration wells, Nasvi et al. (2015) carried out a numerical study to investigate the influence of various confining pressures (from 5 MPa to 25 MPa) on geopolymer materials prepared under different curing temperatures (i.e., from 23°C to 80°C). According to test results, at a given confining pressure, the deviatoric strength increased for geopolymer binders synthesized up to a temperature of 60°C beyond which the increase in deviatoric strength reduced by 15% for all levels of curing temperatures. However, the geopolymer paste synthesized at 80°C had lower uniaxial compressive strength in comparison to the samples cured at 60°C or more moderate temperatures. As such, the stress-strain curve used for the calibration of the numerical model had lower peak axial stress value. Hence, a noticeable reduction in the deviatoric strength increase was not a surprise. Besides, for a given curing temperature, the increase in deviatoric strength at lower confinement levels (5 MPa to 15 MPa) was more as compared to higher lateral confinements (20 MPa and 25 MPa). Although, as reasonable as this finding may be, the exact reason for the observed mechanical behaviour is unknown.

As apparent from the technical review, for the broader use of geopolymer composites in the construction of structures that could be potentially at risk of experiencing moderate to high levels of confinement, no research data are available in the literature. In the same way, no literature exists for the case where fibers are present in geopolymer mixtures to improve their ductility, and the cracking is restrained from other sources such as confinement apart from the fiber reinforcement. Also, as highlighted above, two out of three investigations utilized heat curing method for the synthesis of geopolymer which could be a significant limitation for the proposed mixtures in a more generalized cast-in-situ situation. To the best knowledge of the authors, no study has been carried out in the past which comprehensively investigates the triaxial compressive behaviour of high-strength ambient cured geopolymer mortar and fiber-reinforced composite materials under a high level of confining stress.

Therefore, the current research attempts to bridge these gaps in the literature and acquires test data concerning the behaviour of ambient cured high-performance geopolymer mortar and fiber reinforced geopolymer composites under uniaxial and triaxial compressive stress states. The experimental program comprises of testing two types of geopolymer mixtures, i.e., high-

strength geopolymer mortar and fiber reinforced geopolymer composite under uniaxial and triaxial compression stress states over a range of confinement ratios ranging from 0.02 to 1.00. Based on the results presented in this paper, empirical relationships are proposed to predict the peak axial strength and critical axial strain at peak stress as a function of the confining pressure for the studied materials. Similarly, the uniaxial and triaxial stress-strain curves of the two types of materials are compared and discussed alongside their failure patterns. Finally, the two most common failure criteria (i.e., Power-law and Willam-Warnke) are calibrated with the results of HSG and FRGC for failure envelopes and compared to those of high strength concrete and fiber reinforced cement composites (FRCCs) available in the literature.

7.3 Experimental Approach

7.3.1 Mixture proportions

This research utilizes two types of geopolymer mixtures, i.e., high strength geopolymer mortar and fiber reinforced geopolymer composite (from now on referred as “HSG” and “FRGC” respectively). Table 7-1 presents the mixture proportions for HSG and FRGC samples. As such, these proportions are adopted from preceding studies, where they were found to have desirable workability, strength properties, and showed uniform fiber distribution (Khan et al., 2016; Khan et al., 2018b).

Table 7-1 Mix proportions of HSG and FRGC

Mix type / Mix ingredient		Material details	Quantity (kg/m ³)
HSG	FRGC		
Fly ash	Fly ash	ASTM - Class F	412
Slag	Slag	Construction grade	276
Fine aggregates	Fine aggregates	Silica sand (0-1.18 mm)	1100
Na ₂ SiO ₃ ^a	Na ₂ SiO ₃	D-grade	294
12M NaOH ^b	12M NaOH	99% pure NaOH beads	118
	Steel fibers	Hooked-end	0.80 ^c
-		Spiral steel	0.80 ^c
	Synthetic fibers	HSPE	0.40 ^c
Water-binder ratio	-	0.28 ^d	0.28 ^d
	Na ₂ O/SiO ₂	0.21	0.21
	Na ₂ O/Al ₂ O ₃	0.95	0.95
Critical oxide molar ratios	Si/Al	2.30	2.30
	H ₂ O/Na ₂ O	10.49	10.49

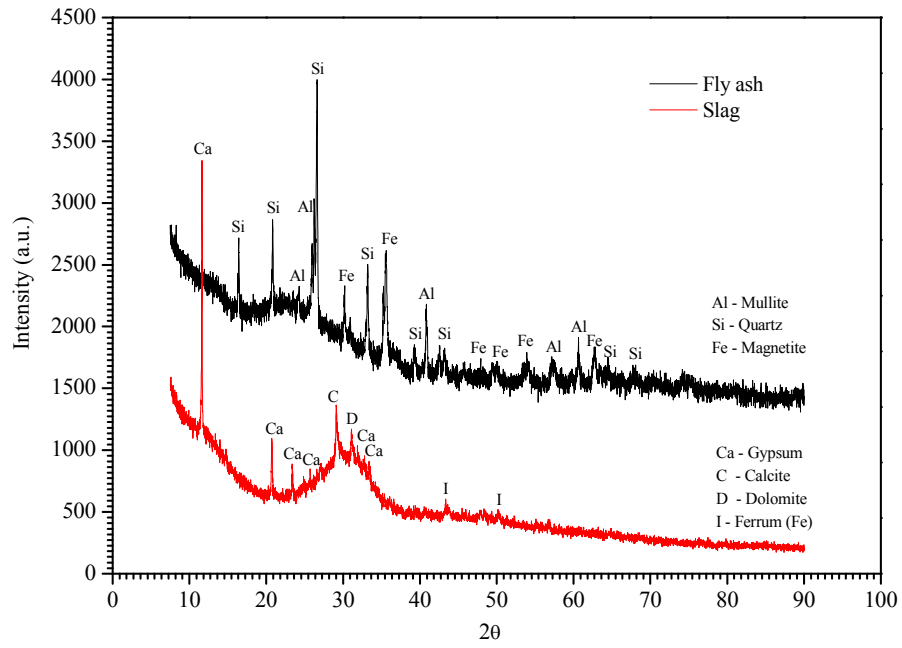
^aD-grade Sodium silicate; ^b99% pure Sodium hydroxide pellets; ^cFibers are included by volume percentage ($V_f\%$); ^dNumerical fraction

The FRGC mixture contained a hybrid-fiber blend of steel and high-strength polyethylene (HSPE) fibers at a predetermined ratio. No expensive raw materials including the high content of fine quartz sand or silica fume were used in these mixtures, while, the rationality of using a hybrid-fiber mix has been explained elsewhere (Khan et al., 2018a). Moreover, for the use of FRGC as a structural material, it is necessary to include sufficient volume fraction of fibers such that they can play a significant role in improving the mechanical properties of HSG. Therefore, we chose a total fiber volume fraction of 2% for the active involvement of fibers in enhancing the ductility of HSG matrix.

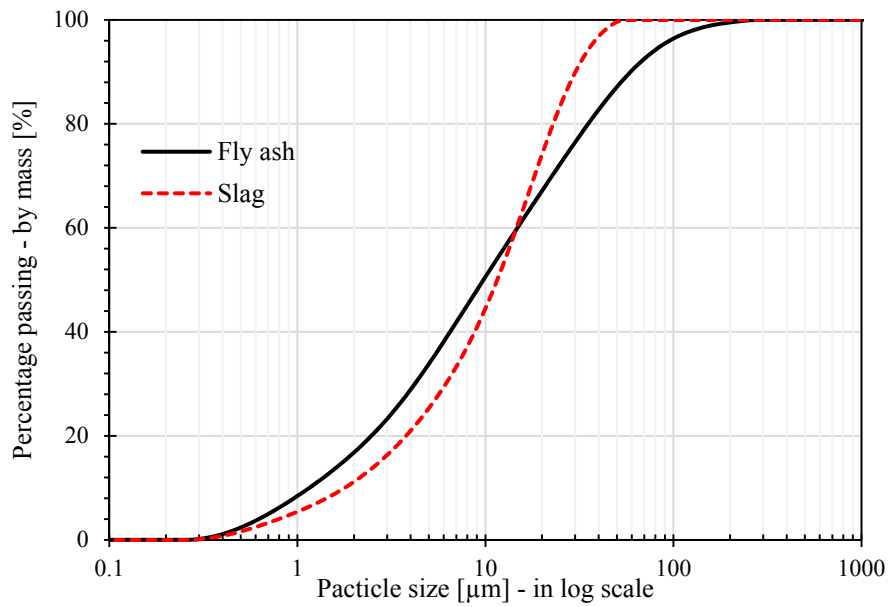
7.3.2 Material composition and fiber properties

The low-calcium fly ash (fly ash), equivalent to ASTM Class-F, C618 (ASTM, 2012) with a specific surface area of 3400 cm²/g and median particle size of 9.7μm was sourced from Gladstone Power Station in Queensland, Australia. Ground-granulated blast furnace slag (slag) having a specific surface area of 3700 cm²/g and median particle size of 11.5μm was used as an additive to the fly ash. Figure 7-1 shows the X-ray diffraction (XRD) patterns and particle size distributions of the solid precursors, while their chemical properties and loss on ignition (LOI) established via X-ray fluorescence (XRF) analysis are included in Table 7-2.

The unprocessed pozzolanic waste contains both the amorphous and crystalline components (see Figure 7-1), however, during activation only the amorphous contents react while the crystalline components act as a filler. It has been used as an advantage in this study by incorporating local silica sand having a fineness modulus of 2.77 and specific gravity of 2.65 in the geopolymer mixes. However, the fine aggregates were prepared in saturated surface dry (SSD) condition before being used for the preparation of mixtures as per ASTM C128 (ASTM, 2015). The alkaline-activator was a blended mixture of 12M sodium hydroxide (NaOH) and D-grade sodium silicate (Na₂SiO₃) solution, supplied by Chem Supply Pty Ltd and PQ-Australia Pty Ltd (Khan et al., 2016). The 99% pure NaOH beads were diluted in tap water to achieve a mass ratio of 2.50 between Na₂SiO₃/NaOH and, Table 7-2 reflects their final chemical compositions.



(a)



(b)

Figure 7-1 (a) XRD 2θ ($^\circ$) Cu, K- α patterns and (b) particle size distributions of fly ash and slag.

Table 7-2 Chemical composition of low-calcium fly ash, slag and alkali-activators

Chemical analyses (%)	Slag	Fly ash	NaOH	Na ₂ SiO ₃
Calcium oxide (CaO)	41.22	4.30	-	-
Silicon dioxide (SiO ₂)	32.45	51.11	-	29.40
Aluminum oxide (Al ₂ O ₃)	13.56	25.56	-	-
Magnesium oxide (MgO)	5.10	1.45	-	-
Sulfur trioxide (SO ₃)	3.20	0.24	-	-
Ferric oxide (Fe ₂ O ₃)	0.85	12.48	-	-
Potassium oxide (K ₂ O)	0.35	0.70	-	-
Sodium oxide (Na ₂ O)	0.27	0.77	28.05	14.70
Manganese oxide (MnO)	0.25	0.15	-	-
Phosphorus pentoxide (P ₂ O ₅)	0.03	0.89	-	-
Others	1.61	1.78	-	-
Loss on ignition (LOI)	1.11	0.57	-	-
Water (H ₂ O)	-	-	71.95	55.90

The physical appearance and the properties of fibers used in the investigation are presented in Figure 7-2 and Table 7-3, respectively. The hooked-end and spiral steel fibers were purchased from two different suppliers based in China, while Dyneema Group, Toyobo Corporation Ltd Japan supplied the HSPE fibers.

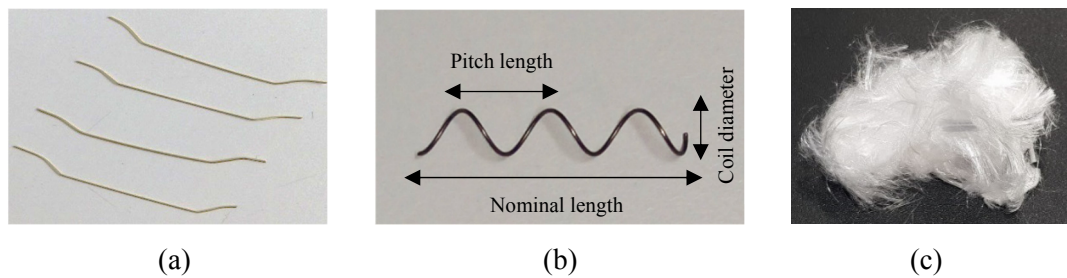


Figure 7-2 Physical appearances of (a) Hooked-end steel (b) Spiral steel (c) HSPE fibers.

Table 7-3 Physical and mechanical properties of fibers

Fiber type / Property	Hooked-end steel (GSF-025)	Spiral steel	High strength polyethylene (HSPE-SK71)
Wire diameter (mm)	0.30	0.55	0.012
Nominal length (mm)	25	25	12
Coil diameter (mm)	-	6	-
Pitch length (mm)	-	10	-
Aspect ratio (l/d)	85	45	1000
Nominal tensile strength (MPa)	2500	2000	3500
Elongation capacity (%)	<1.00	<1.00	3.30
Modulus of elasticity (GPa)	200	200	123
Density (gm/cm ³)	7.80	7.80	0.97

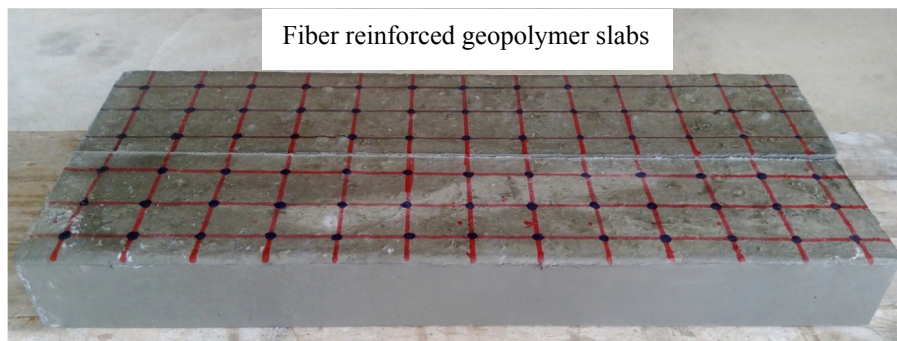
7.3.3 Mixing process, casting, curing, and sample design

After preparing the ingredients mentioned in Table 7-1, the mixing process was carried out in a 70L large size pan mixer. The mixing speed was controlled rigorously at 50 revolutions per minute (RPM) to ensure the uniform distribution of ingredients. Following steps were then taken to prepare the mixtures:

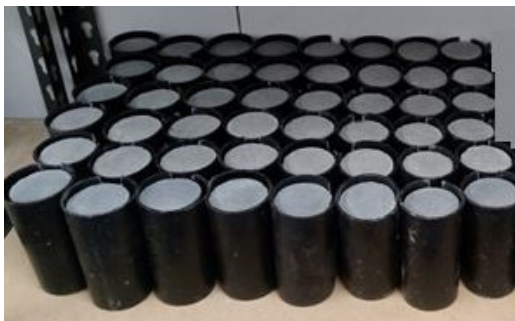
1. At first, all the dry constituents including fly ash, fine aggregates, and slag were mixed for 4 minutes. The dry-mixed ingredients were checked for lumps formation as small particles tend to agglomerate and can be broken easily when dry.
2. Subsequently, the pre-compounded mixture of Na₂SiO₃ and NaOH solutions was included over a 60 sec period, and the mixing process was continued for another 4 to 5 minutes. Once all the components were mixed thoroughly in a consistent fresh flowable state, the workability of HSG mortar was measured to make sure that it is within a desirable range for the next process.
3. At this stage, the freshly prepared HSG mixture was poured into Ø50 mm × 110 mm cylindrical PVC plastic molds. The molds were filled in three layers, while a continuous external vibration process was used to remove the entrapped air bubbles.
4. For FRGC, the measurement of workability was followed by the addition of hooked-end and spiral steel fibers through a constant sieve shaking process while continuously mixing the ingredients during the process. Finally, to provide the uniform dispersion of HSPE fibers, they were separated loosely and included in small portions via hand into the wet mixture. The total mixing time of FRGC mixture was around 20-25 mins.

According to ASTM C1437 (ASTM, 2013), the measured flow diameters of geopolymer mortar and FRGC mixes were 145 mm and 65 mm, respectively.

Unlike HSG mix, the freshly prepared FRGC mixture was poured into rectangular slab timber molds having a dimension of 110 mm × 200 mm × 1000 mm and compacted via an external vibrating table. It was mainly done to assure the random distribution and orientation of fibers as well as to represent the typical volumetric element size as compared to the Ø50 mm × 110 mm cylindrical molds. The inner surfaces were lined with oil to minimize the friction between the poured material and the timber material. The cast samples and slabs were cured at a temperature of $23 \pm 2^\circ\text{C}$ for the next 24 hrs. Later, the hardened specimens were demolded and stored in a standard environment ($23 \pm 2^\circ\text{C}$ and relative humidity of $50 \pm 5\%$) for the next three weeks. After about 21 days, a grid layout (see Figure 7-3) was marked on the slabs to core cylindrical FRGC samples having a dimension of Ø50 mm × 110 mm from each square cross-section. An end surface grinder was used to ground these cored samples to a final size of Ø50 mm × 100 ± 1 mm along with unreinforced counterparts to provide smooth bearing ends for loading during the tests. Figures 7-3(b) and 7-3(c) show the final prepared samples.



(a)



(b)



(c)

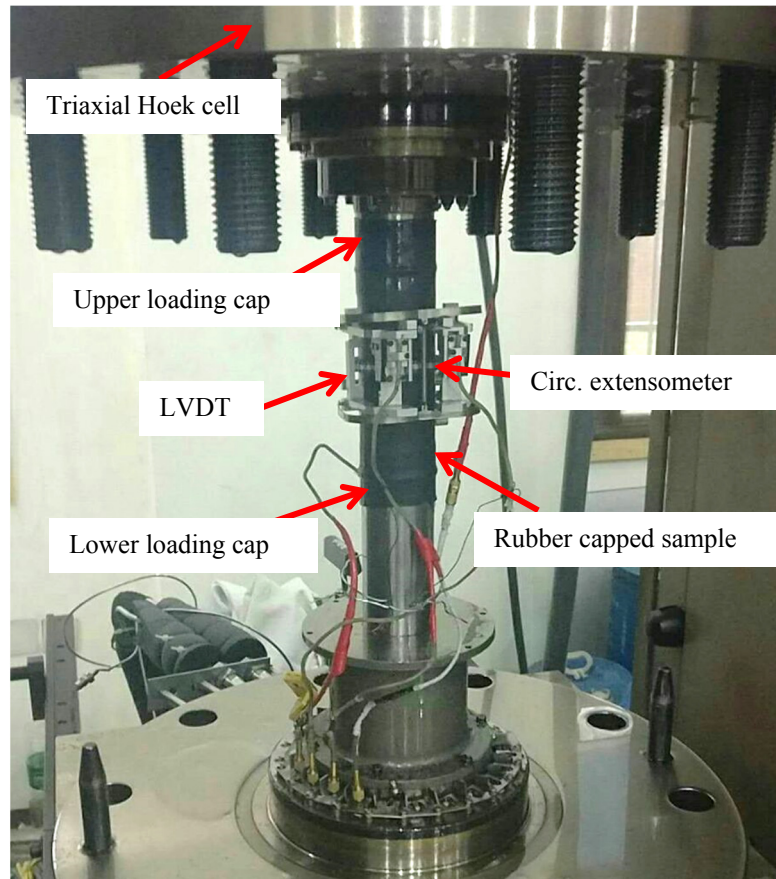
Figure 7-3 (a) Cast slab and prepared samples (b) HSG and (c) FRGC for uniaxial and triaxial tests.

7.3.4 Test Procedures - Uniaxial and Triaxial compression test setup

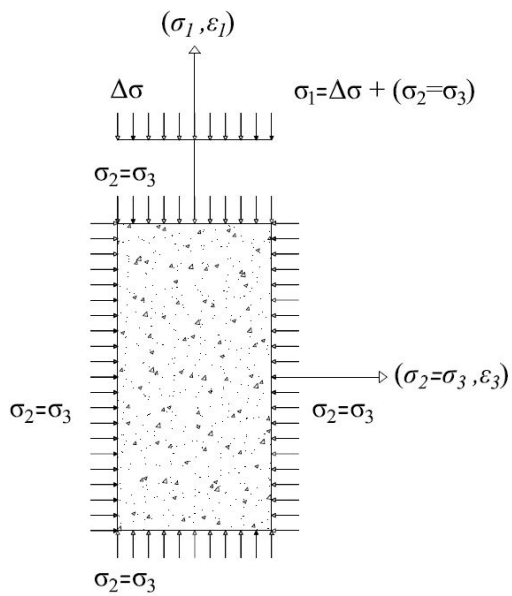
All the uniaxial and triaxial compression tests were performed between the ages of 90 and 120 days after casting using the MTS 815 servo-hydraulic closed-loop equipment. The machine has a very stiff rigid frame rated at 11.0×10^9 N/m and the maximum load capacity of 4.60×10^6 N, whereas the triaxial Hoek cell is capable of applying a confining pressure of up to 140 MPa on 50 mm \times 100 mm sample. During each test, the triaxial Hoek cell was pressurized with the confining fluid using a confining pressure intensifier, while the confining pressure (σ_3) was measured directly with an inbuilt pressure transducer inside the intensifier. However, to prevent the penetration of confining fluid inside the samples during pressurization, the specimens were covered with 2 mm thick rubber bladder before each triaxial test. Two linear variable differential transducers (LVDTs) attached to either side, and a circumferential extensometer at mid-height of the sample recorded the axial and lateral displacements of the samples. It is relevant to mention that for the measurement of strain, generally the clip gauges are considered more advantageous in comparison to the electrical strain gauges attached to the surfaces of the test samples since they are capable of capturing the deformation of a much more significant portion of the sample.

7.3.4.1 Loading schemes

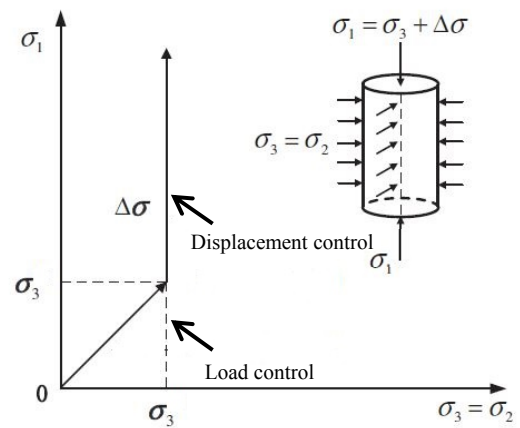
The samples enclosed in rubber membrane were placed between the upper and lower loading caps of the triaxial Hoek cell to perform each test [see Figure 7-4(a)]. An actuator applied the axial load in the vertical direction, and appropriate computer commands were programmed to control the servo-hydraulic valve which in turn regulated the confining pressure intensifier via in-vessel pressure transducers. The experiments were controlled digitally, and minicomputers were employed for the data acquisition. For uniaxial compression tests, the loading procedure was controlled in displacement mode from the start at a loading rate of 0.002 mm/sec, while all samples in triaxial tests were gradually loaded according to the load path shown in Figure 7-4(c).



(a)



(b)



(c)

Figure 7-4 (a) Triaxial test setup (b) Axis direction and (c) Load path for triaxial tests.

The samples in triaxial compressive tests were subjected to hydrostatic stress initially such that the axial and lateral stresses were applied simultaneously at a loading rate of 0.80 MPa/sec until the confining pressure (σ_3) reached the predetermined target value. At this point, the confining pressure (σ_3) was held constant, and the additional axial deviatoric stress ($\Delta\sigma = \sigma_1 - \sigma_3$) was increased in the displacement mode at a loading rate of 0.002 mm/sec up to the sample failure or strain within the samples reaching the measuring range of the extensometers. It is pertinent to mention that at times during the triaxial tests, the increasing application of deviatoric stress ($\Delta\sigma$) may cause the samples to dilate or contract, hence, resulting in loss or increase of the confining pressure. As a result, to keep the confining pressure constant, some confining fluid must be injected into or drained from the triaxial Hoek cell. For this, hydraulic valves were used to relax or compress the confining fluid to accommodate a specific volume of oil in or out of the cell. The said approach allowed keeping the confining pressure constant within $\pm 0.5\%$ accuracy.

From the view of plasticity, application of varying lateral confining pressures leads to different lodge angles, thus allowing the trace of failure curve in the deviatoric plane. Table 7-4 shows the details of the complete test program with a total of 15 different confinement ratios (σ_3/f'_c) that were considered. Moreover, at each confinement level, on average at least three replicate were tested. The peak axial stress (σ_1) was obtained with the summation of confining stress (σ_3) and the deviatoric stress ($\Delta\sigma; F_o/A_s$), where F_o is the deviatoric load and A_s is the cross-sectional area of the sample.

Table 7-4 Experimental program for uniaxial and triaxial compression tests

Serial No	Confining Pressure (MPa)	High strength geopolymer mix (HSG)		Fiber reinforced geopolymer composite (FRGC)	
		Sample designation	Confinement ratio (σ_3/f'_c)	Sample designation	Confinement ratio (σ_3/f'_c)
		1	0 (Uniaxial)	HSG - 0	0.0
2	2	HSG - 2	0.021	FRGC - 2	0.022
3	4	HSG - 4	0.042	FRGC - 4	0.044
4	8	HSG - 8	0.084	FRGC - 8	0.089
5	10	HSG - 10	0.104	FRGC - 10	0.112
6	12	HSG - 12	0.125	FRGC - 12	0.134
7	16	HSG - 16	0.170	FRGC - 16	0.178
8	20	HSG - 20	0.208	FRGC - 20	0.223
9	25	HSG - 25	0.260	FRGC - 25	0.278
10	30	HSG - 30	0.312	FRGC - 30	0.334
11	40	HSG - 40	0.416	FRGC - 40	0.445
12	50	HSG - 50	0.520	FRGC - 50	0.556
13	60	HSG - 60	0.625	FRGC - 60	0.667
14	80	HSG - 80	0.834	FRGC - 80	0.889
15	100	HSG - 100	1.041	FRGC - 100	1.120

7.4 Results and Discussions

7.4.1 Effect of confining pressure on stress-strain response of HSG

The typical stress-strain behaviour of HSG samples under unconfined uniaxial loading condition and confined condition with different confining pressures of 4 MPa, 12 MPa, 25 MPa, 50 MPa, 80 MPa, and 100 MPa are plotted in Figure 7-5. It is to be noted that the presented curves show the deviatoric portion ($\Delta\sigma = \sigma_1 - \sigma_3$) of the tests. Moreover, the axial strain is taken as positive (in compression), while the lateral expansion is designated as negative (tension) in the graphs. As observed, the unreinforced geopolymer mortar samples exhibited high-compressive strength (96 MPa, $\sigma_3 = 0$ MPa) and showed a linear elastic, perfectly brittle response in uniaxial compression. The three tested samples failed abruptly once their lateral deformation exceeded the tensile capacity of the material, hence displaying an average peak axial strain (ϵ_{cu}) of $0.29 \pm 0.02\%$ at the ultimate load.

For tests with confinement, all HSG samples experienced softening behaviour after the peak stress. The peak axial stress (obtained from the summation of deviatoric stress and the confining pressure, $(\sigma_1 = \Delta\sigma + \sigma_3)$) and axial strain increased from the beginning to ultimate load, and an apparent non-linearity is observed both in the pre- and post-peak loading regions of the stress-strain curves. By comparing the stress-strain curves, it can be seen that the peak axial stress improved from 96 MPa in the uniaxial compression ($\sigma_3 = 0$ MPa) to deviatoric strengths ($\Delta\sigma$) of 148 MPa, 235 MPa, and 244 MPa under the lateral confinements of 4 MPa, 50 MPa, and 100 MPa, respectively; hence, signifying an overall increase of 58%, 216%, and 258% in the triaxial strength of HSG. The results for the other test cases are summarized in Table 7-5.

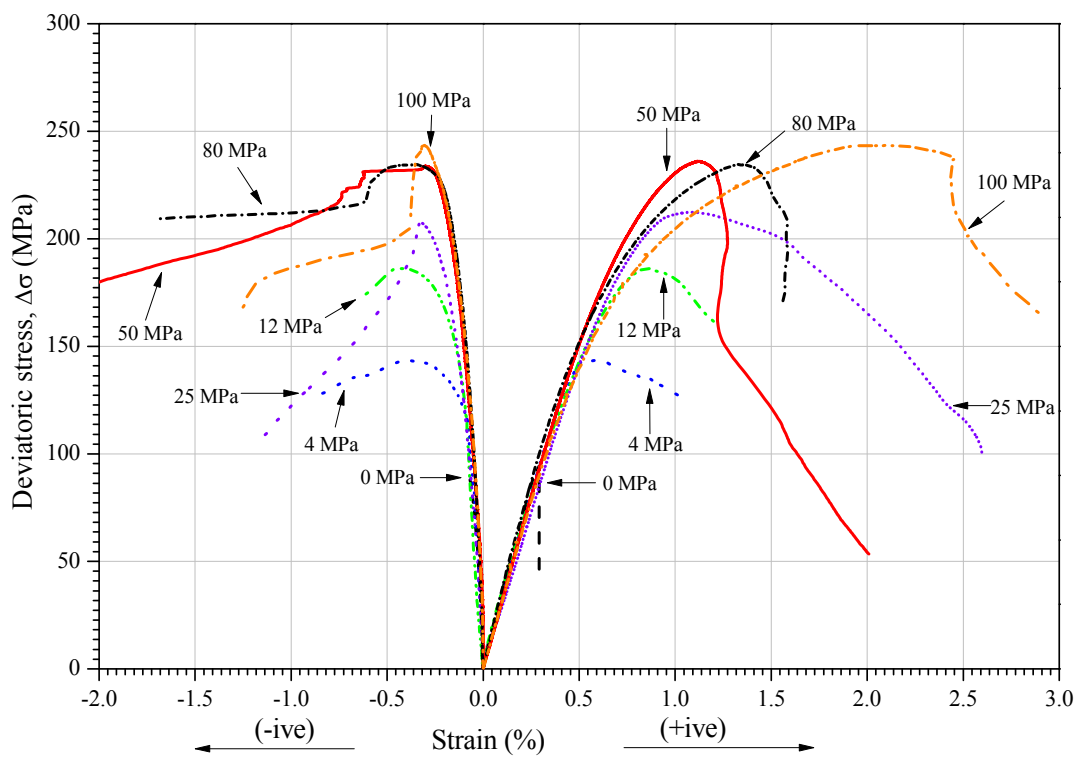


Figure 7-5 Uniaxial and triaxial stress-strain behaviour of HSG under various confining pressures.

As such, it is evident that the increase in lateral confinement from 0 to 100 MPa has a remarkable effect on the triaxial strength of HSG samples. The peak axial strength and ductility of HSG samples increased with an increase in the confining pressure, and pseudo-ductile responses were observed under the triaxial compressive stress conditions. Moreover, it can also be concluded that the increment in peak axial stress and critical axial strain of HSG samples is associated with the confining pressure, i.e., the higher the confinement, the more significant the increase in peak axial stress and the samples behaved more ductile. Similarly,

the initial elastic modulus of HSG samples was noticed to vary slightly once the confining pressure was increased from 0 to 100 MPa, while a minor reduction in stiffness was also observed as the specimens reached their maximum load carrying capacity.

Generally, the main reason for an increase in the deviatoric strength of confined HSG is partially related to the inter-particle friction between the fractured surfaces along with the contribution made by shear resistance of the geopolymer matrix. It is believed that random cracks and pores always exist in concrete-like materials primarily due to the shrinkage of the cement slurry pastes or local compression from drying of the wet mixtures etc. Upon the application of axial stress, these “flaws” tend to propagate until one or numerous large cracks are formed. At a load level of around 40% of the peak load, not only the cracks become wider but also the ruptured surfaces tend to lose the contact between themselves. However, with lateral confinement holding these surfaces together; the inter-particle frictional forces may continue to support the additional axial load which is generally higher than the unconfined loading case (Vu et al., 2009). Some other researchers believe that the early application of hydrostatic pressure during the triaxial tests delays the formation of microcrack damage due to shear; hence increasing the load carrying capacity of concrete-like materials upon confinement (Bazant and Tsubaki, 1981; Attard and Setunge, 1996).

In general, HSC mixtures are characterized to have lower porosity in comparison to the conventional concrete mixes and are found less sensitive to the influence of confinement. For the present case, HSG samples have a cumulative porosity of 7.93% (Khan et al., 2017). In this study as well, the increase in peak axial stress of HSG samples is more pronounced at lower levels than at higher confining pressures. This, on one hand, is in complete agreement to the experimental results reported by Ansari and Li (1998) and Mander et al. (1988) in the past, where a similar rate of increase in deviatoric strength was observed for high strength concrete (HSC, 100 MPa) mixtures at these confinement ratios [i.e. (σ_3/f'_c) of 0.40 and beyond]. On the other hand, it is assumed that the difference in binding gels formed during the geopolymerization process may have also contributed to the observed mechanical behaviour. It is well established that in geopolymerization reaction, the mechanical strength develops from the formation of sodium aluminosilicate hydrate (N-A-S-H) gel network or combination of calcium aluminum silicate hydrates (C-A-S-H) in the presence of slag.

Although the exact mechanism for the geopolymerization process has not been understood completely, according to Davidovits (1991), it can be schematized as an imaginary polycondensation of orthosilicate ions. Unlike the OPC's chemical reaction, where water is continuously required for the completion of hydration process; in case of the geopolymerization, it is one of the end products produced during the polycondensation and

hardening process of oligomers (Duxson et al., 2005). The excluded water remains either free or bound within final reaction products and has no role to play in the geopolymerization process, leaving behind a discontinuous nano-porous structure regarded beneficial for the performance of geopolymers (Hardjito and Rangan, 2005). It is presumed that owing to the low porosity of HSG samples and the possible presence of water in the test samples that could have remained in the microstructure during the curing and further drying periods, a slight increase in the pore pressure upon the application of higher lateral confinements may have occurred. This is understood to have resulted in the lower increment in deviatoric/shear strength of HSG samples at higher confining pressures. However, additional tests along with pore pressure measurements are suggested to be carried out in future studies to validate this assumption.

7.4.2 Effect of confining pressure on stress-strain response of FRGC

Figure 7-6 shows the typical stress-strain relations of FRGC samples under uniaxial and triaxial compressive stress states. It can be seen that the FRGC samples exhibited higher ductility without evidencing the sudden breakage of cylinders in uniaxial compression tests. The critical axial strain (ϵ_{cu}) of HSG samples increased from $0.29 \pm 0.02\%$ to $0.54 \pm 0.05\%$, resulting in an overall increase of 86% in the strain capacity of geopolymer. It is believed that the percentage increase in ductility is due to the improvement in the tensile capacity of HSG samples with the addition of hybrid-fiber reinforcement. However, the maximum load carrying capacity of FRGC samples was slightly lower than the unreinforced counterparts, i.e., 90 MPa. It can also be observed that the FRGC samples had a lower stiffness which is mainly due to the higher elongation capacity of HSPE (3.30%) fibers.

The main reason for the reduction in compressive strength of FRGC samples is primarily associated with the inclusion of synthetic fibers. It has been noticed that polyethylene fibers tend to reduce the shear strength of concrete mainly because of the formation of air voids around the fiber-matrix interface which have also been reported by other researchers (Pantazopoulou and Zanganeh, 2001; Ahmed and Ronnie, 2017). However, a three-fold increase in flexural tensile strength and toughness of HSG material is possible using the proposed hybrid-fiber reinforcement due to an improvement in the slip-forming characteristics and increased cohesiveness of fiber reinforced geopolymer mixture. Further details on this aspect may be found in (Khan et al., 2018b).

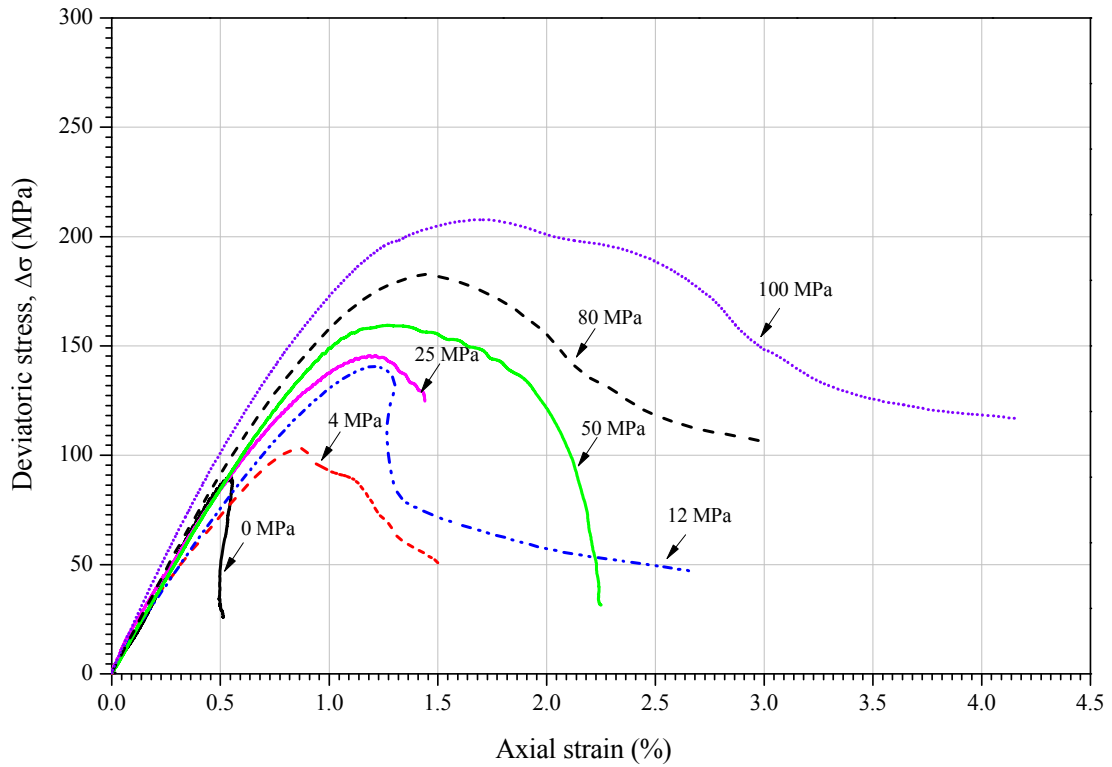


Figure 7-6 Uniaxial and triaxial stress-strain behaviour of FRGC under various confining pressures.

In the context of the present research, from Figure 7-6, it is evident that the peak axial strength of FRGC samples has increased from 90 MPa to deviatoric strengths ($\Delta\sigma$) of 103.11 MPa, 164.35 MPa, and 207.82 MPa under the confining pressures of 4 MPa, 50 MPa, and 100 MPa, respectively. Hence, showing an increase of 19%, 138%, and 242% in the axial strength of fiber reinforced geopolymer samples with lateral confinement. Moreover, it can also be seen that in comparison to unreinforced geopolymer samples, the rate of increase in deviatoric strength for FRGC samples is lower at any given level of medium confining pressure. On the other hand, a distinct rise in peak axial stress was noticed for FRGC samples at higher confining pressures (i.e., 80 MPa or 100 MPa) which are different from the unreinforced counterparts. The strength characteristics of FRGC under triaxial compression apart from those reflected in Figure 7-6 such as peak axial stress (σ_l), failure strength ratio (σ_l/f'_c), critical axial strains ($\epsilon_{l,c}$) are summarized in Table 7-6.

Unfortunately, the circumferential extensometer malfunctioned when the tests were conducted on FRGC samples, and the test readings about the lateral expansion of FRGC samples could not be recorded. Nevertheless, since the primary objective of this research is to study the influence of confinement on the peak axial strength and deformation characteristics of high

strength geopolymer composites, the test results pertaining to the increase in axial strength and axial strain for FRGC samples at different confining pressures are presented and compared with those of unreinforced HSG samples. The influence of fiber addition on enhancing the deformability of high-strength geopolymer matrix at varying levels of confining pressures is apparent (see Figure 7-7). As such in Figure 7-7, the ductility increase for both types of materials under the influence of confinement is normalized against the critical axial strain of HSG under uniaxial compression.

It may be seen that at any given level of confining pressure, the critical axial strain in FRGC samples is higher than that of unreinforced geopolymer matrix. On the one hand, this specifies that the addition of hybrid-fiber reinforcement has implicitly improved the ductility of HSG matrix. On the other hand, it can also be observed that the increasing application of confining pressure appears to have a limiting effect on the ductility of FRGC samples, meaning the presence of fibers in test samples is more beneficial in improving the critical axial strain of HSG samples at low levels of lateral confinement. Some previous investigations conducted by Lu and Hsu (2006) and Noori et al. (2015) have reported similar outcomes, where the addition of steel fiber reinforcement in different volume fractions (1% and 2%) did not show any improvement in the ductility of high-performance concrete mixtures. Instead, the relationship between the critical axial strains at peak stress for steel fiber reinforced high strength concrete had lower coefficients than the unreinforced counterparts.

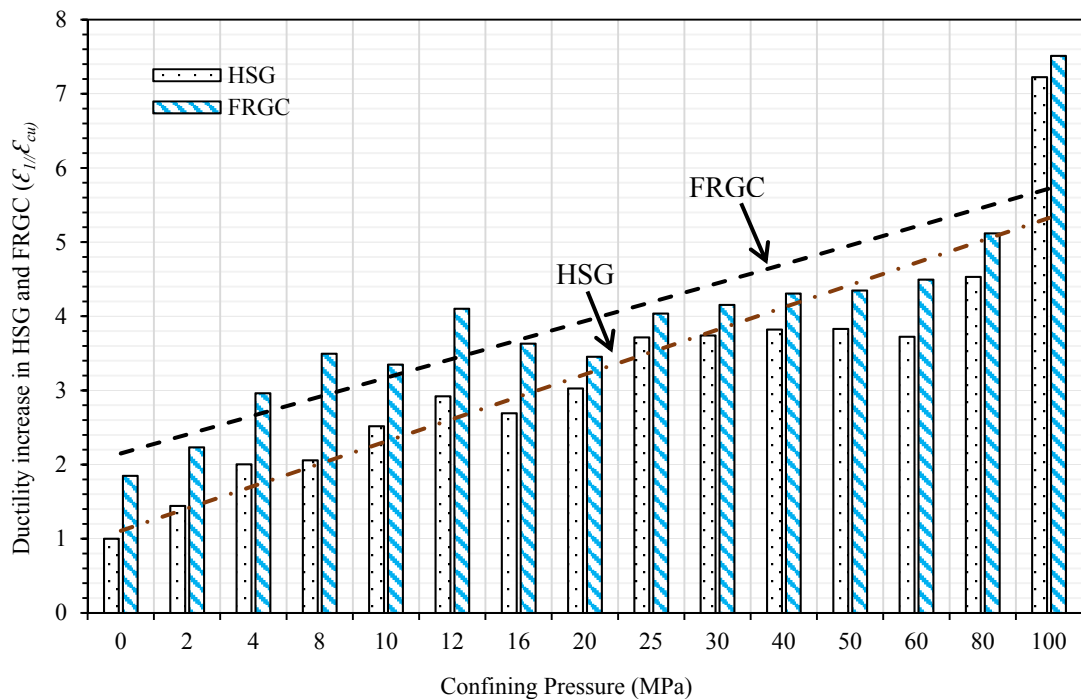


Figure 7-7 Comparison of increase in ductility of HSG and FRGC at different confining pressures.

Table 7-5 Uniaxial and Triaxial compression test results of HSG samples

Sample Designation	f'_c (MPa)	Confinement pressure (MPa)	Confinement ratio (σ_3/f'_c)	Confined Peak axial stress, σ_l (MPa)	Failure strength ratio (σ_l/f'_c)	Percentile increase in strength (%)	Confined Peak axial strain, ϵ_l (%)	Confined Peak lateral strain, ϵ_3 (%)	Modulus of Elasticity, E (GPa)
HSG - 0	96	0	0.0	96.00 ± 0.68	1.00	-	0.293 ± 0.020	-0.079 ± 0.0030	34.51 ± 0.34
HSG - 2	96	2	0.021	132.66 ± 5.11	1.38	38	0.423 ± 0.036	-0.386 ± 0.0017	35.75 ± 2.79
HGS - 4	96	4	0.042	151.58 ± 4.55	1.57	57	0.587 ± 0.014	-0.391 ± 0.0223	32.09 ± 0.56
HSG - 8	96	8	0.084	172.71 ± 1.18	1.79	79	0.603 ± 0.039	-0.405 ± 0.0308	35.44 ± 1.81
HSG - 10	96	10	0.104	187.22 ± 5.07	1.95	95	0.738 ± 0.010	-0.380 ± 0.0368	33.02 ± 2.19
HSG - 12	96	12	0.125	198.91 ± 3.98	2.07	107	0.856 ± 0.024	-0.423 ± 0.0141	31.54 ± 1.03
HSG - 16	96	16	0.170	213.14 ± 3.76	2.22	122	0.789 ± 0.025	-0.257 ± 0.0186	32.72 ± 0.68
HSG - 20	96	20	0.208	225.75 ± 1.68	2.35	135	0.887 ± 0.013	-0.453 ± 0.0344	32.55 ± 1.96
HSG - 25	96	25	0.260	237.45 ± 3.49	2.47	147	1.089 ± 0.074	-0.321 ± 0.0239	32.88 ± 3.65
HSG - 30	96	30	0.312	252.04 ± 9.84	2.63	163	1.096 ± 0.107	-0.277 ± 0.0748	33.80 ± 0.19
HSG - 40	96	40	0.416	267.49 ± 6.70	2.78	178	1.120 ± 0.083	-0.326 ± 0.0750	33.66 ± 0.94
HSG - 50	96	50	0.520	284.76 ± 5.05	2.96	196	1.122 ± 0.048	-0.302 ± 0.0120	34.93 ± 2.19
HSG - 60	96	60	0.625	291.13 ± 3.13	3.03	203	1.091 ± 0.065	-0.285 ± 0.0146	32.21 ± 1.06
HSG - 80	96	80	0.834	315.01 ± 1.08	3.28	228	1.328 ± 0.018	-0.345 ± 0.0051	34.14 ± 1.94
HSG - 100	96	100	1.104	344.98 ± 6.30	3.59	259	2.117 ± 0.073	-0.307 ± 0.0218	30.99 ± 1.74

Table 7-6 Uniaxial and Triaxial compression test results of FRGC samples

Sample Designation	f'_c (MPa)	Confinement pressure (MPa)	Confinement ratio (σ_3/f'_c)	Confined Peak axial stress, σ_1 (MPa)	Failure strength ratio (σ_1/f'_c)	Percentile increase in strength (%)	Confined Peak axial strain, ϵ_1 (%)	Confined Peak lateral strain, ϵ_3 (%)	Modulus of Elasticity, E (GPa)
FRGC - 0	90	0	0.0	90.00 ± 2.95	1.00	-	0.542 ± 0.051	-	17.56 ± 0.25
FRGC - 2	90	2	0.022	95.25 ± 5.79	1.06	6	0.654 ± 0.020	-	16.84 ± 2.50
FRGC - 4	90	4	0.044	107.11 ± 4.37	1.19	19	0.868 ± 0.024	-	16.47 ± 0.12
FRGC - 8	90	8	0.089	130.76 ± 4.69	1.45	45	1.024 ± 0.076	-	18.23 ± 0.73
FRGC - 10	90	10	0.112	136.15 ± 2.08	1.52	52	0.981 ± 0.027	-	15.92 ± 0.36
FRGC - 12	90	12	0.134	151.02 ± 0.80	1.68	68	1.202 ± 0.043	-	15.67 ± 0.29
FRGC - 16	90	16	0.178	143.99 ± 7.84	1.59	59	1.064 ± 0.031	-	17.98 ± 0.39
FRGC - 20	90	20	0.223	146.94 ± 1.95	1.64	64	1.012 ± 0.016	-	16.94 ± 0.14
FRGC - 25	90	25	0.278	170.45 ± 0.36	1.89	89	1.183 ± 0.110	-	17.70 ± 0.91
FRGC - 30	90	30	0.334	176.04 ± 1.75	1.96	96	1.217 ± 0.105	-	17.46 ± 0.43
FRGC - 40	90	40	0.445	188.61 ± 0.45	2.09	109	1.262 ± 0.031	-	17.48 ± 1.31
FRGC - 50	90	50	0.556	214.35 ± 2.66	2.38	138	1.274 ± 0.058	-	17.78 ± 0.81
FRGC - 60	90	60	0.667	231.12 ± 2.01	2.57	157	1.317 ± 0.060	-	19.39 ± 0.92
FRGC - 80	90	80	0.889	262.70 ± 9.54	2.92	192	1.500 ± 0.036	-	19.21 ± 0.71
FRGC - 100	90	100	1.120	307.82 ± 2.84	3.42	242	2.201 ± 0.064	-	20.82 ± 0.68

7.4.3 Effect of confining pressure on triaxial strength of HSG and FRGC

The current section presents the analyses in regards to the increase in peak axial strength as a function of confining pressure for both types of materials. However, before discussing the results, brief information on the shape of concrete failure envelope and failure criteria used in the past is provided. It should be noted that some of these failure criteria were developed initially for soils and rocks and then later extended for OPC concrete. Moreover, among the different types of failure criteria, Mohr-coulomb's linear failure criterion often remains the first choice in describing the strength behaviour of concrete-like materials upon confinement due to its simplicity and relatively good accuracy.

However, one of the main disadvantages of this failure criterion is primarily related to the shape of the described compressive and tensile meridians on the strength envelope, which are all straight lines. It has been observed that the proposed compressive and tensile meridians become far deviant from the actual strength surface when the mean principal stress is high. Similarly, the failure surface in the deviatoric plane is not smooth and inconsistent to the consensus reported by many researchers, e.g. (Ansari and Li, 1998; Lu and Hsu, 2006). Some other triaxial failure criteria include the two-parameter Drucker-Prager's failure criterion, four-parameter Ottosen's failure criterion, and four-parameter Hsieh-Ting-Chen's criterion (Chen, 2007), etc.

In general, as elucidated by Chen (2007), the concrete failure surface is typically an open-ended convex polar figure which has a threefold symmetry along the hydrostatic axis. It has a nearly triangular shape for low compressive and tensile stresses in the deviatoric plane. While with an increase in the hydrostatic pressure or mean principal stress; it becomes more circular in the three-dimensional stress space. Furthermore, it has been concluded that the influence of confining pressure on the failure strength is different for ordinary and high strength concrete (HSC) and usually the effect is more pronounced for low strength concrete mixtures (Ansari and Li, 1988).

An initial examination of the results obtained in this study also suggested that non-linear analyses would establish better correlations for peak axial strength as a function of confining pressure for the studied materials. Therefore, for the present work, Mohr-coulomb's linear failure criterion has not been used due to the above-stated reasons and limited correlation for the test data. Instead, two other failure criteria, i.e., Power-law failure criterion (an extended non-linear form of Mohr-coulomb failure criterion) and Willam-Warnke failure criterion are used to calibrate the models with the triaxial compression results of HSG and FRGC. Of note, these models define the compressive meridian on the failure surface as parabolas regarding

the average normal and mean shear stress to fit the curved meridians obtained during the triaxial tests. Further information on these failure criteria is given in the subsequent analyses of the results and discussions.

7.4.3.1 Power-law failure criterion

The pressure-dependent power-law failure criterion is given as:

$$\frac{\sigma_1}{f'_c} = 1 + a(\sigma_3 / f'_c)^b \quad (7.1)$$

where σ_1 denotes the peak axial stress; σ_3 denotes the confining pressure; f'_c represents the uniaxial compressive strength; and “a” and “b” are the material constants.

The variation of peak axial stress (σ_1) as a function of the confining pressure (σ_3) for HSG and FRGC is illustrated in Figures 7-8 and 7-9, respectively which are normalized against their respective uniaxial compressive strengths (f'_c) and compared with previous investigations on cement based counterparts. The non-linear regression analysis of the data in the form of best-fit curves is also shown in these graphs and mathematically described by Equations (7.2) and (7.3) for HSG and FRGC, respectively.

$$\text{For HSG : } \quad \frac{\sigma_1}{f'_c} = 1 + 2.58(\sigma_3 / f'_c)^{0.430} \quad (7.2)$$

$$\text{For FRGC : } \quad \frac{\sigma_1}{f'_c} = 1 + 2.15(\sigma_3 / f'_c)^{0.653} \quad (7.3)$$

In Figure 7-8, it can be seen that at low levels of confinement, a sharp increase in peak axial strength is observed for HSG which tends to reduce as the slope of the failure curve decreases sharply with an increase in the confining pressure. A higher degree of non-linearity exists in the initial portion of the failure curve and is believed to be associated with the unique three-dimensional (N-A-S-H or C-(A)-S-H) polycondensed binding gel network of geopolymers binders which makes the internal structure of material more compact than the crystalline C-S-H structure formed upon the hydration of OPC.

Numerous relations have been proposed in the past to predict the failure strength of confined HSCs. The triaxial compressive strength results of HSCs (having a comparable compressive strength to that of HSG) from the previous studies undertaken by Xie et al. (1995) ($f'_c = 103$ MPa), Ansari and Li (1998) ($f'_c = 107$ MPa), and Attard and Setunge (1996) ($f'_c = 107$ MPa) are compared with the data obtained for HSG. As such, it can be observed that the rate of increase in failure strength for HSG at low to medium levels of confinement is higher than that of HSCs. A large scatter exists between the triaxial strength results of HSCs from the

previous studies which has also been reported by Ansari and Li (1998). However, the exact reason for this discrepancy is not apparent and may require further explanation in future studies. It is believed that the differences in the aspect ratio of the test samples and influence of confining pressures on different material compositions are a few possible reasons for disagreement between these studies.

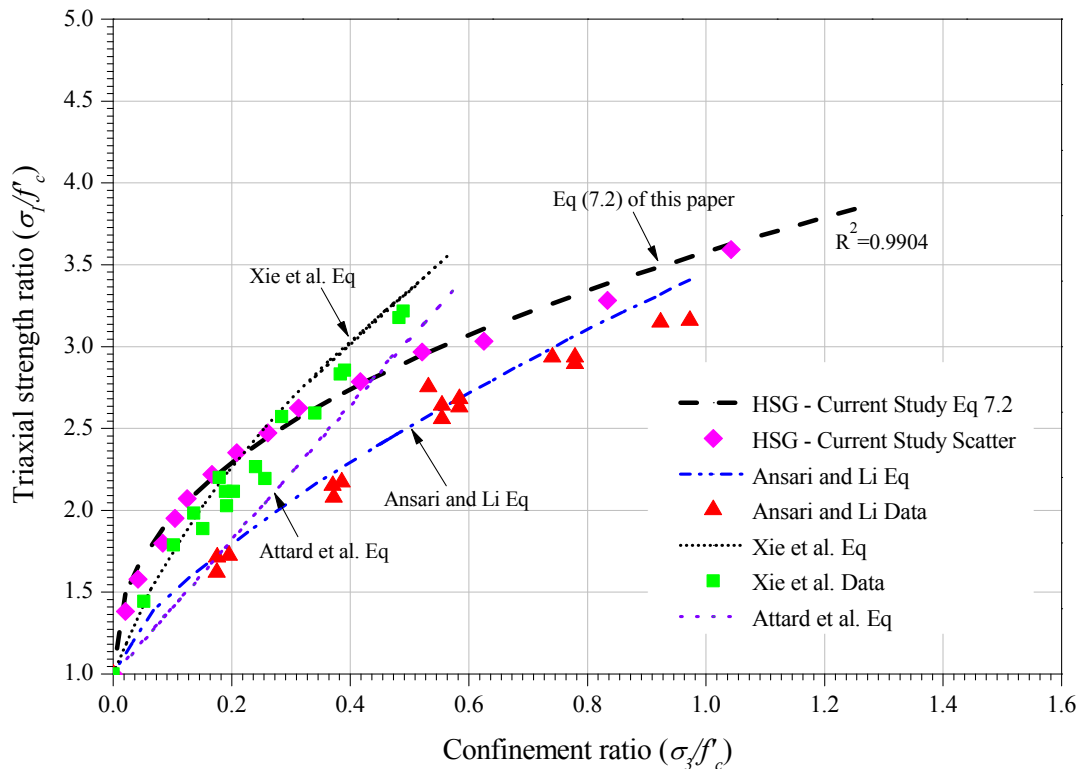


Figure 7-8 Triaxial strength of HSG and comparison with previous experimental studies on HSCs.

Nevertheless based on the available data, it can be concluded that the test data of Ansari and Li (1998) and their suggested failure strength curve for HSC falls well below the defined failure curve of HSG in Equation (7.2). On the other hand, the data of Xie et al. (1995) lies in the proximity of the current experimental results up to $0.40f'_c$. However, the empirical equation suggested by Xie et al. (1995) does not correlate well with their test data. Besides, it may be seen that their experimental research only involved low levels of confinement. Therefore, it is not possible to predict the trend for the whole range of confining pressures used in this study. On the other hand, Attard and Setunge (1996) proposed a linear relationship between the peak axial strength and the confining pressure for HSC at similar confinement ratios, which is different from the non-linear relationship obtained in the current research and two other previous investigations.

Unlike HSCs, limited researchers have investigated the triaxial strength behaviour of fiber reinforced cement composites (FRCCs). In Figure 7-9, the data from the present research on FRGC is compared to that of Farnam et al.'s (2010) high-performance fiber reinforced concrete (HPFRC), Ren et al.'s (2016) ultra-high performance fiber reinforced cement composites (UHPCC), and Noori et al.'s (2015) steel fiber reinforced cementitious mortar (SFRCM). It should be noted that the cement-based composites and concretes in these investigations also contained 2% volumetric ratio of steel fibers, similar to FRGC. From Figure 7-9, it can be seen that the failure curves of cement based composites under low confining pressures from Farnam et al. (2010), Ren et al. (2016), and Noori et al.'s (2015) experiments display a close similarity to the failure strength of FRGC from the current research. In fact, the results reported by Noori et al. (2015) follow an identical strength increase behaviour at the relatively low level of confining pressure as reflected by the initial portion of the fitted curve for FRGC.

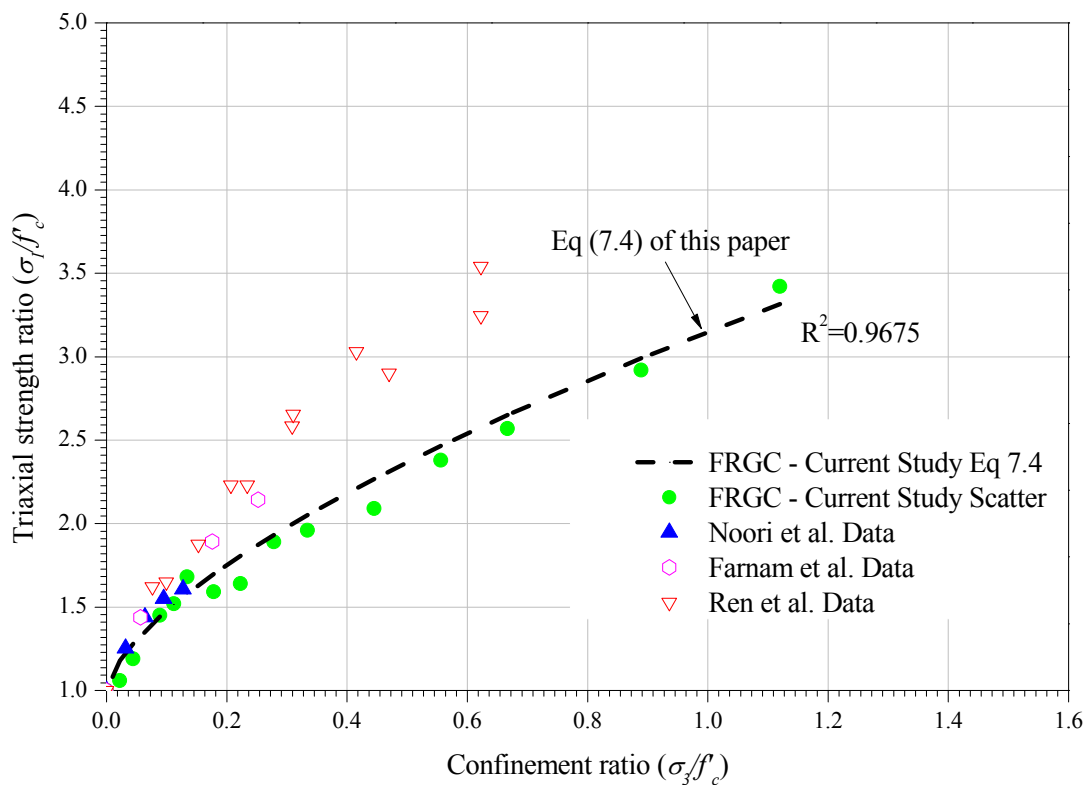


Figure 7-9 Triaxial strength of FRGC and comparison with previous experimental studies of FRCCs.

However, with an increase in the confining pressure, the rate of strength increase in FRGC tends to be lower than that of previously studied FRCCs. Moreover, unlike the HSG samples, where a higher degree of non-linearity was observed in the failure strength curve at low

confinement ratios, the influence of confining pressure on the strength increase of FRGC is gradual, and the compressive meridian of FRGC tends to be more linear at higher confinement ratios. A similar tendency was reported in earlier research where fiber reinforced cement composites showed a lower increase in triaxial strength under lower confinement in comparison to plain concrete mixtures (Noori et al. 2015).

7.4.3.2 Willam-Warnke failure criterion

In addition to the Power-law failure criterion, Willam-Warnke five-parameter model is the most commonly used failure criterion to describe the strength envelope of concrete-like materials and has been adopted to establish material models in hydrocodes. In this section, Willam-Warnke five-parameter model is calibrated using the triaxial compression test results of HSG and FRGC samples. This model describes the ultimate strength surface of concrete in terms of the tensile (at $\theta = 0^\circ$) and compressive meridians (at $\theta = 60^\circ$), such that the compressive meridian of the strength surface takes the form of a quadratic parabola and requires only three parameters for its calibration, as expressed in Equation (7.4):

$$\frac{\tau_m}{f'_c} = b_o + b_1\left(\frac{\sigma_m}{f'_c}\right) + b_2\left(\frac{\sigma_m}{f'_c}\right)^2 \quad (7.4)$$

where in Equation (7.4), $\sigma_m = I_1 / 3 = (\sigma_1 + \sigma_2 + \sigma_3) / 3$;

$\tau_m = \frac{1}{\sqrt{15}} \sqrt{(\sigma_1 - \sigma_2)^2 + (\sigma_2 - \sigma_3)^2 + (\sigma_3 - \sigma_1)^2}$, σ_m and τ_m are the average normal and mean shear stress. I_1 is the first invariant of the stress tensor; f'_c denotes the uniaxial compressive strength; σ_1, σ_2 , and σ_3 denote the stresses in three principal directions, and b_o, b_1 , and b_2 are the three Willam-Warnke material model coefficients, respectively.

For high-strength geopolymer (HSG) and fiber reinforced geopolymer composites (FRGC) tested in the experiments, the compressive meridians as per Willam-Warnke criterion are expressed as follows:

$$\text{For HSG : } \frac{\tau_m}{f'_c} = 0.0684 + 1.05\left(\frac{\sigma_m}{f'_c}\right) - 0.308\left(\frac{\sigma_m}{f'_c}\right)^2 \quad (7.5)$$

$$\text{For FRGC : } \frac{\tau_m}{f'_c} = 0.240 + 0.501\left(\frac{\sigma_m}{f'_c}\right) - 0.105\left(\frac{\sigma_m}{f'_c}\right)^2 \quad (7.6)$$

Figures 7-10 and 7-11 depict the data scatter and the compressive meridians on failure surface for HSG and FRGC, respectively. In these graphs, a comparison has also been made between the failure envelopes of HSG and FRGC from this study with those proposed by other researchers for high strength concrete and cement based fiber reinforced composites.

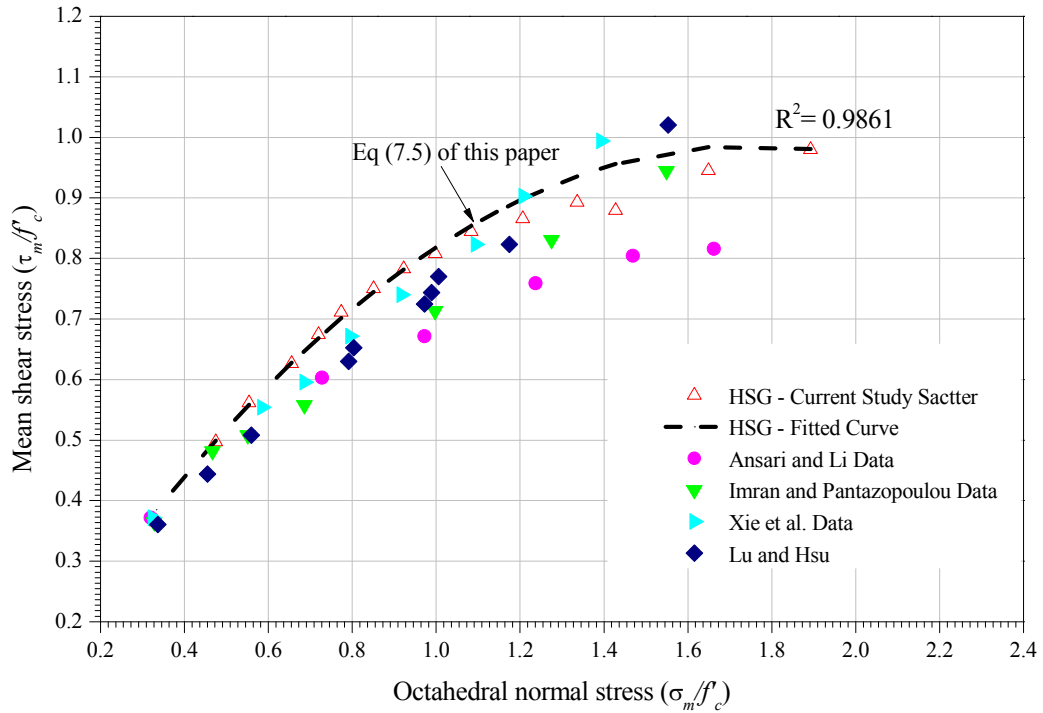


Figure 7-10 Comparison of compressive meridian of HSG and HSCs from previous studies.

As can be seen, the Willam-Warnke failure criterion provides a proper failure envelope for both types of geopolymer materials. Furthermore, in Figure 7-10, it can be seen that the geometric shape of compressive meridian proposed by Ansari and Li (1998) is similar to the failure envelope suggested for HSG in this study, where after a certain level of octahedral normal stress, the compressive meridian of HSG tends to reach a plateau. On the other hand, it is evident that among different investigations, Ansari and Li's model produces a lower strength boundary for all lateral confinement ratios, while the test results from other studies are scattered below the defined compressive meridian of HSG defined by Equation (7.5) within the considered confining pressure range.

Figure 7-11 shows the comparison of the compressive meridian of the FRGC from Equation (7.6) of this research and studies of Lu and Hsu (2006), Ren et al. (2016), and Babanajad et al. (2012). Although the strengths of FRGC samples and cement based fiber reinforced concretes/composites are quite similar, the compressive meridian for FRGC, however, does not fall within the same failure envelope apart from a few data points from this research. Therefore, separate compressive meridians are proposed for the studied materials.

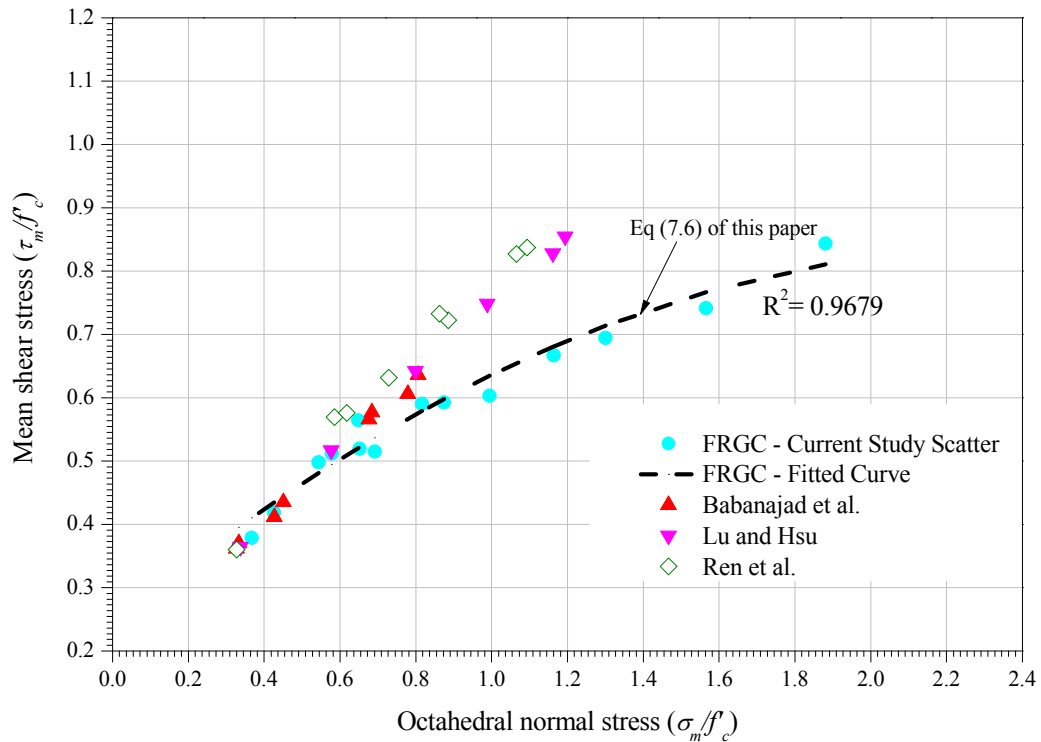


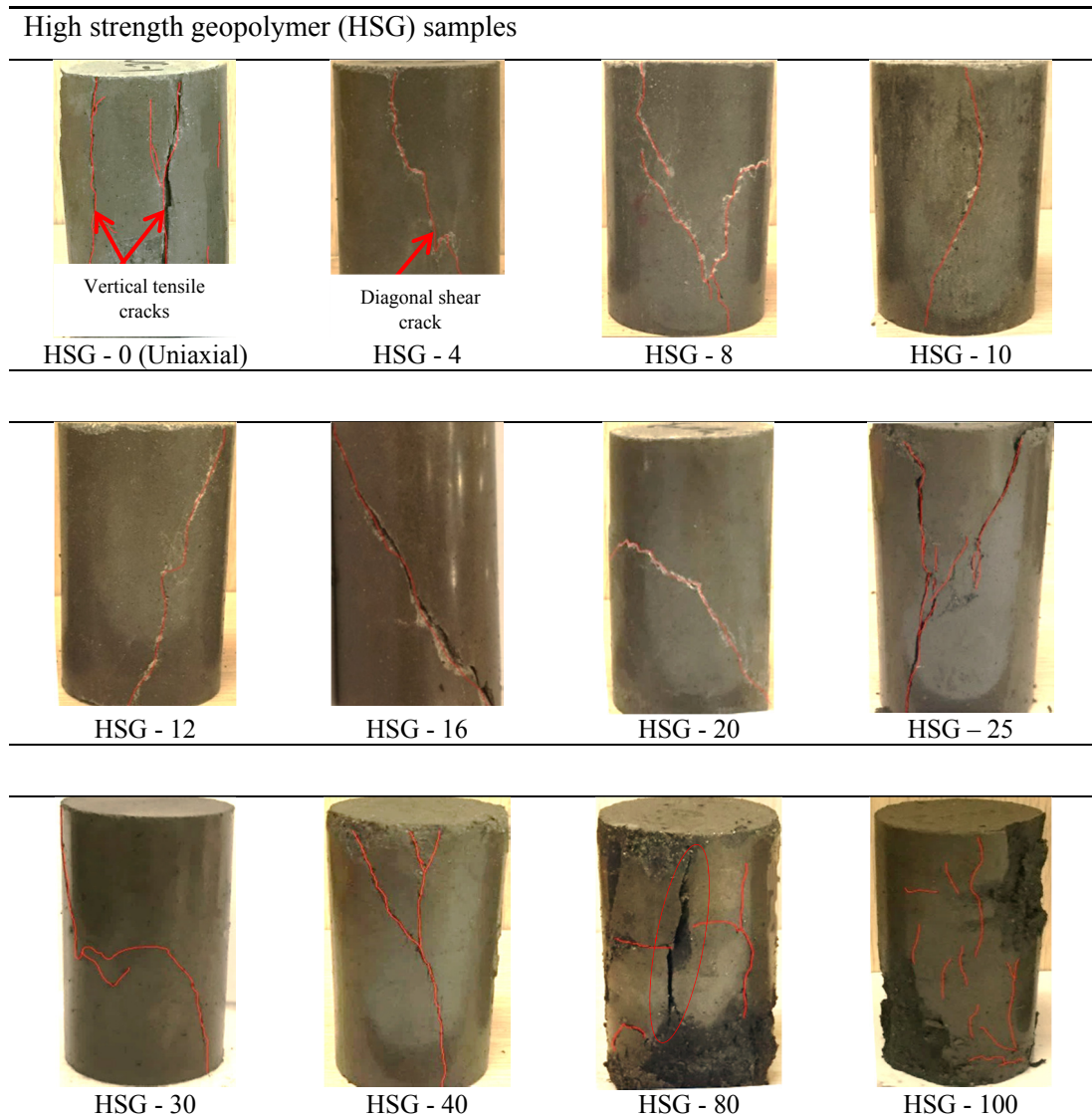
Figure 7-11 Comparison of compressive meridian of FRGC and FRCCs from previous studies.

7.4.4 Damage mechanism of HSG and FRGC samples in uniaxial and triaxial compression

Figure 7-12 depicts the failure patterns of the recovered HSG and FRGC samples after the triaxial tests. It should be noted that at some of the confining pressures, the fracture planes in tested samples were identical. Therefore, failure patterns at discerning lateral confinement ratios are presented only. Generally, the unreinforced HSG samples behaved differently under triaxial compression as compared to what was observed in uniaxial stress condition. It can be seen that in the absence of confinement, several major macroscopic tensile cracks were produced parallel to the axial loading direction which triggered the sample failure. In triaxial compression, the failure planes tilted diagonally to reach an inclination of 45° approximately to the axial direction. These failure planes are typical of shear failure and have frequently been observed for cement-based materials under triaxial compression (Ansari and Li, 1998; Noori et al. 2015).

Moreover, it can also be observed that at relatively low or medium confining pressures, the failure in HSG samples was induced either by a single or a set of multiple inclined shear cracks. While at higher confining pressures such as at 80 MPa or 100 MPa, not only several

major shear cracks were formed but also an extensive amount of abrasion was noticed on top and bottom edges of the tested samples alongside these cracks. A few of the HSG samples subjected to higher levels of confinement (i.e., 80 MPa and 100 MPa) also broke into several pieces once the protective sleeves were removed after the test completion.



(a)

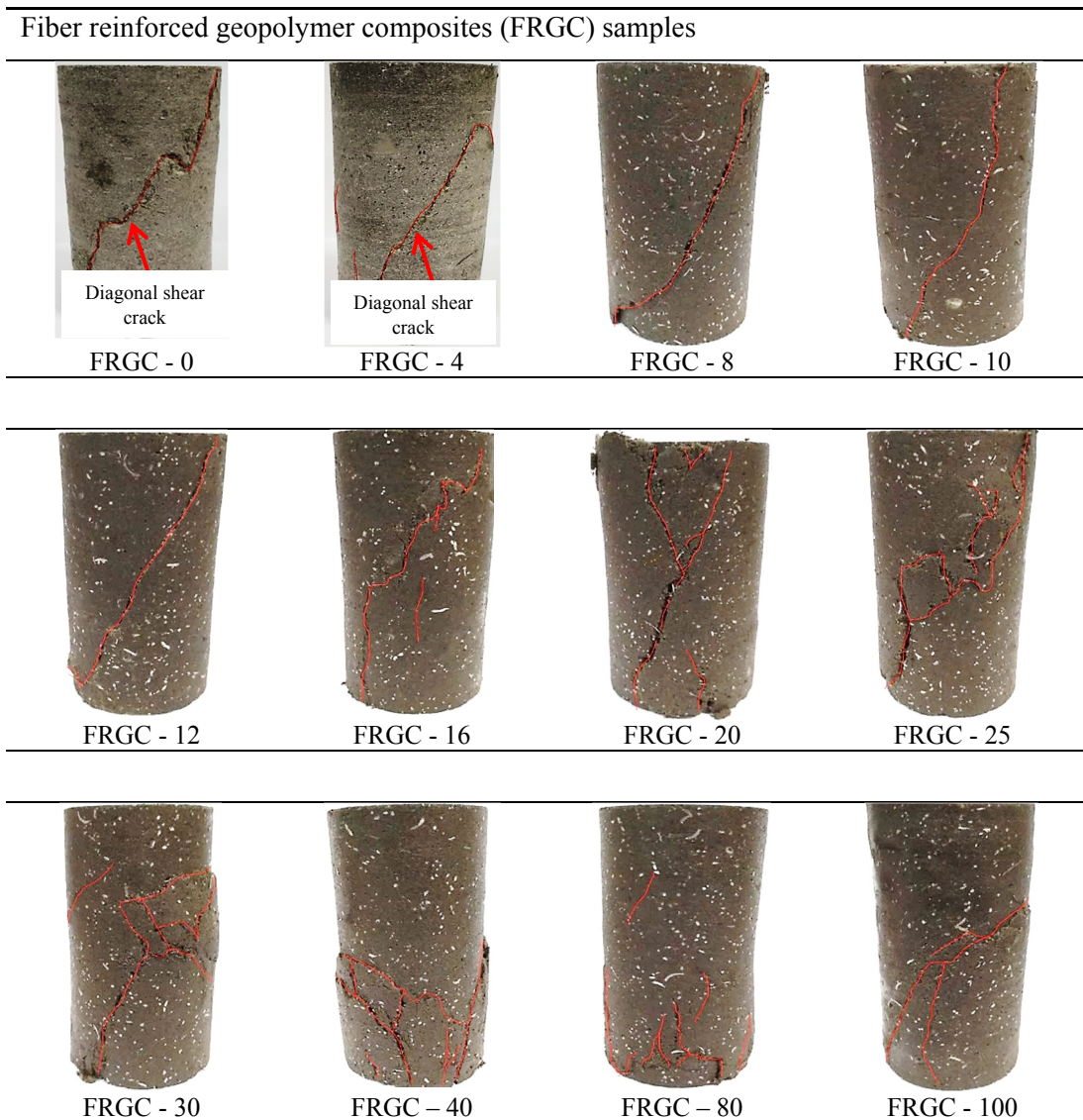


Figure 7-12 Failure modes of (a) HSG and (b) FRGC in uniaxial and triaxial compressive loading conditions.

On the other hand, from Figure 7-12, it can be seen that the FRGC samples maintained their structural integrity to a large extent after enduring the triaxial compression. It can be observed that unlike the unreinforced geopolymer mortar samples, the failure in FRGC samples was induced due to the formation of the inclined shear cracks in uniaxial loading condition. Upon confinement, visible shear cracks developed which caused the sample failure. However, with an increase in the confining stresses, an apparent swelling of samples was noticed around the circumference mainly due to the axial contractions, and minor hair-line cracks appeared on surfaces of the tested samples. It is different to HSG samples and indicates that the addition

of fibers not only improved the failure mode of HSG in uniaxial compression but also allowed the fiber reinforced specimens to retain their integrity at high levels of confining stress states.

7.5 Conclusions

This paper investigated the influence of lateral confinement on ambient cured high-strength geopolymer mortar and fiber-reinforced geopolymer composites through a comprehensive experimental test program. The material behaviours are studied over a range of confining pressures between 0 and 100 MPa. Based on the findings of this experimental study, the following conclusions can be drawn:

- 1) Under uniaxial compression, the unreinforced HSG samples showed a linear elastic response and experienced a catastrophic brittle failure. But a noticeable improvement in ductility and increased resistance to post-peak deformation was observed with the inclusion of hybrid steel-polyethylene fiber reinforcement.
- 2) Under triaxial compression, the axial strength and ductility of HSG and FRGC samples exceeded the corresponding values observed in uniaxial stress states. A concomitant increase in the failure strength and axial strain was seen with an increase in the confining pressures for both types of studied materials.
- 3) Obvious nonlinear relationships existed between the peak axial stress and the confining pressure for both HSG and FRGC materials similar to high strength OPC concretes. However, the influence of confining pressure was more pronounced on the failure strength of HSG material in comparison with fiber reinforced geopolymer composite specimens.
- 4) A distinct effect was noticed on to the compressive meridian of failure surface for HSG at low to medium levels of confinement. At higher confining pressures, the failure curve of HSG tends to reach a plateau. On the other hand, the proposed compressive meridian for FRGC is more linear at higher confinements.
- 5) The calibrated Power-law and Willam-Warnke failure criteria provide an excellent fit to the test data. However, the proposed compressive meridian envelope suggest an upper strength boundary for HSG in comparison to the conventional high strength OPC concrete within the considered test range.
- 6) The proposed empirical relations can be used to calibrate the strength parameters of existing concrete models and to simulate the behaviour of HSG under active lateral confinements.
- 7) The HSG samples failed predominantly due to the formation of vertical tensile cracks in uniaxial compression, while the failure modes transformed to shear under triaxial

compressive stress condition. On the other hand, shear failure patterns were observed for FRGC samples both in the uniaxial and triaxial compressive tests.

7.6 References

ASTM. (2012a). Standard specification for coal fly ash and raw or calcined natural pozzolan for use in concrete. *ASTM C618-12a*, Philadelphia.

ASTM. (2013). Standard test method for flow of hydraulic cement mortar. *ASTM C1437-13*, Philadelphia.

ASTM. (2015). Standard test method for relative density (Specific Gravity) and absorption of fine aggregate. *ASTM C128-15*, Philadelphia.

Ahmed, S. F. U., & Ronnie, Z. (2017). Ductile behavior of polyethylene fibre reinforced geopolymer composite. *Paper presented at the MATEC Web of Conferences*.

Ansari, F., & Li, Q. (1998). High-strength concrete subjected to triaxial compression. *Materials Journal*, 95(6), 747-755.

Atiř, C. D., Görür, E. B., Karahan, O., Bilim, C., İlkentapar, S., & Luga, E. (2015). Very high strength (120 MPa) class F fly ash geopolymer mortar activated at different NaOH amount, heat curing temperature and heat curing duration. *Construction and Building Materials*, 96, 673-678.

Attard, M., & Setunge, S. (1996). Stress-strain relationship of confined and unconfined concrete. *Materials Journal*, 93(5), 432-442.

Babanajad, S. K., Farnam, Y., & Shekarchi, M. (2012). Failure criteria and triaxial behaviour of HPFRC containing high reactivity metakaolin and silica fume. *Construction and Building Materials*, 29, 215-229.

Bazant, Z.P., & Tsubaki, T. (1980). Total strain theory and path-dependence of concrete. *Journal of the Engineering Mechanics Division*, ASCE, Volume 106, no. EM6, pp. 1151-1172.

Benhelal, E., Zahedi, G., Shamsaei, E., & Bahadori, A. (2013). Global strategies and potentials to curb CO₂ emissions in cement industry. *Journal of Cleaner Production*, 51, 142-161.

Candappa, D., Sanjayan, J., & Setunge, S. (2001). Complete triaxial stress-strain curves of high-strength concrete. *Journal of Materials in Civil Engineering*, 13(3), 209-215.

Chen, W.-F. (2007). *Plasticity in reinforced concrete*: J. Ross Publishing.

Chen, W. F. (1993). Concrete plasticity: Macro- and microapproaches. *International Journal of Mechanical Sciences*, 35(12), 1097-1109.

Cusson, D., & Paultre, P. (1995). Stress-strain model for confined high-strength concrete. *Journal of Structural Engineering*, 121(3), 468-477.

Davidovits, J. (1991). Geopolymers. *Journal of thermal analysis*, 37(8), 1633-1656.

- Davidovits, J. (1994). High-alkali cements for 21st century concretes. *ACI Special Publication, 144*, 383-398.
- Duxson, P., Provis, J. L., Lukey, G. C., Mallicoat, S. W., Kriven, W. M., & van Deventer, J. S. J. (2005). Understanding the relationship between geopolymer composition, microstructure and mechanical properties. *Colloids and Surfaces A: Physicochemical and Engineering Aspects, 269*(1-3), 47-58.
- Farnam, Y., Moosavi, M., Shekarchi, M., Babanajad, S. K., & Bagherzadeh, A. (2010). Behaviour of Slurry Infiltrated Fibre Concrete (SIFCON) under triaxial compression. *Cement and Concrete Research, 40*(11), 1571-1581.
- Haider, G. M., Sanjayan, J. G., & Ranjith, P. G. (2014). Complete triaxial stress-strain curves for geopolymer. *Construction and Building Materials, 69*(0), 196-202.
- Hardjito, D., & Rangan, B. V. (2005) Development and Properties of low calcium fly ash based geopolymer concrete. *Research Report GC 1, Curtin University of Technology, Perth, Australia*, 93 pp.
- He, Z.-j., & Song, Y.-p. (2010). Triaxial strength and failure criterion of plain high-strength and high-performance concrete before and after high temperatures. *Cement and Concrete Research, 40*(1), 171-178.
- Hosan, A., Haque, S., & Shaikh, F. (2016). Compressive behaviour of sodium and potassium activators synthesized fly ash geopolymer at elevated temperatures: A comparative study. *Journal of Building Engineering, 8*, 123-130.
- Imran, I., & Pantazopoulou, S. (1996). Experimental study of plain concrete under triaxial stress. *ACI Materials Journal-American Concrete Institute, 93*(6), 589-601.
- Khan, M. Z. N., Hao, Y., Hao, H., & Shaikh, F. U. A. (2018a). Experimental evaluation of quasi-static and dynamic compressive properties of ambient-cured high-strength plain and fiber reinforced geopolymer composites. *Construction and Building Materials, 166*, 482-499.
- Khan, M. Z. N., Hao, Y., Hao, H., & Shaikh, F. U. A. (2018b). Mechanical properties of ambient cured high strength hybrid steel and synthetic fibers reinforced geopolymer composites. *Cement and Concrete Composites, 85*(Supplement C), 133-152.
- Khan, M. Z. N., Shaikh, F. U. A., Hao, Y., & Hao, H. (2016). Synthesis of high strength ambient cured geopolymer composite by using low calcium fly ash. *Construction and Building Materials, 125*, 809-820.
- Khan, M. Z. N., Shaikh, F. U. A., Hao, Y., & Hao, H. (2017). Effects of Curing Conditions and Sand-to-Binder Ratios on Compressive Strength Development of Fly Ash Geopolymer. *Journal of Materials in Civil Engineering, 30*(2), 04017267.
- Lu, X., & Hsu, C.-T. T. (2006). Behavior of high strength concrete with and without steel fiber reinforcement in triaxial compression. *Cement and Concrete Research, 36*(9), 1679-1685.
- Lyu, S.-J., Hsiao, Y.-H., Wang, T.-T., Cheng, T.-W., & Ueng, T.-H. (2013). Microstructure of geopolymer accounting for associated mechanical characteristics under various stress states. *Cement and Concrete Research, 54*(0), 199-207.
- Mander, J., Priestley, M., & Park, R. (1988). Observed stress-strain behavior of confined concrete. *Journal of Structural Engineering, 114*(8), 1827-1849.

- Menetrey, P., & Willam, K. (1995). Triaxial failure criterion for concrete and its generalization. *Structural Journal*, 92(3), 311-318.
- Nasvi, M. C. M., Ranjith, P. G., & Sanjayan, J. (2015). A numerical study of triaxial mechanical behaviour of geopolymer at different curing temperatures: An application for geological sequestration wells. *Journal of Natural Gas Science and Engineering*, 26, 1148-1160.
- Noori, A., Shekarchi, M., Moradian, M., & Moosavi, M. (2015). Behavior of Steel Fiber-Reinforced Cementitious Mortar and High-Performance Concrete in Triaxial Loading. *ACI Materials Journal*, 112(1).
- Ottosen, N. S. (1979). Constitutive model for short-time loading of concrete. *Journal of the Engineering Mechanics Division ASCE*, 105, 127-141.
- Pantazopoulou, S., & Zanganeh, M. (2001). Triaxial tests of fiber-reinforced concrete. *Journal of Materials in Civil Engineering*, 13(5), 340-348.
- Part, W. K., Ramli, M., & Cheah, C. B. (2015). An overview on the influence of various factors on the properties of geopolymer concrete derived from industrial by-products. *Construction and Building Materials*, 77, 370-395.
- Rashad, A. M. (2014). A comprehensive overview about the influence of different admixtures and additives on the properties of alkali-activated fly ash. *Materials & Design*, 53(0), 1005-1025.
- Ren, G. M., Wu, H., Fang, Q., Liu, J. Z., & Gong, Z. M. (2016). Triaxial compressive behavior of UHPCC and applications in the projectile impact analyses. *Construction and Building Materials*, 113(Supplement C), 1-14.
- Richart, F.E, Brantzaeg, A., and Brown, R. L. (1929). The failure of plain and spirally reinforced columns in compression. *University of Illinois Engineering Experimental Station, Bulletin No. 190*.
- Roviello, G., Menna, C., Tarallo, O., Ricciotti, L., Ferone, C., Colangelo, F., Cioffi, R. (2015). Preparation, structure and properties of hybrid materials based on geopolymers and polysiloxanes. *Materials & Design*, 87, 82-94.
- Sakulich, A. R. (2011). Reinforced geopolymer composites for enhanced material greenness and durability. *Sustainable Cities and Society*, 1(4), 195-210.
- Samani, A. K., & Attard, M. M. (2012). A stress-strain model for uniaxial and confined concrete under compression. *Engineering Structures*, 41(Supplement C), 335-349.
- Shaikh, F. U. A. (2013). Review of mechanical properties of short fibre reinforced geopolymer composites. *Construction and Building Materials*, 43(0), 37-49.
- Vu, X. H., Malecot, Y., Daudeville, L., & Buzaud, E. (2009). Experimental analysis of concrete behavior under high confinement: Effect of the saturation ratio. *International Journal of Solids and Structures*, 46(5), 1105-1120.
- Xiao, Q., Teng, J., & Yu, T. (2010). Behavior and modeling of confined high-strength concrete. *Journal of Composites for Construction*, 14(3), 249-259.

Xie, J., Elwi, A., & MacGregor, J. (1995). Mechanical properties of three high-strength concretes containing silica fume. *Materials Journal*, 92(2), 135-145.

CHAPTER 8 CONCLUSIONS AND RECOMMENDATIONS

8.1 Main Findings

This thesis focused on the development of high-strength fiber reinforced geopolymer composites (FRGC) from low-calcium fly ash at the ambient temperature and utilized an innovative spiral-shaped steel fiber in combination with hooked-end steel and high-strength polyethylene fibers (HSPE) for the material reinforcement. The research also investigated the dynamic tensile, dynamic compressive, and multiaxial stress-strain behaviour of high-strength geopolymer materials in general, and newly proposed fiber reinforced composites under a broad range of high strain rates and lateral confinements. The fracture development processes in high-speed impact tests and the post-test damage modes of samples in quasi-static, dynamic tensile/compression, and multiaxial compression are presented. Moreover, the implications of using the existing standards and the latest CEB guidelines recommended for OPC concrete to estimate the dynamic tensile and compressive strength enhancements of geopolymer materials have also been evaluated. Based on the parameters considered in the experimental investigations and detailed analysis of results, the significant contributions/findings of this research and recommendations for future studies are summarized below:

Synthesis of high-strength geopolymer materials at ambient temperature

Geopolymers are sustainable binders; this study demonstrated that high-strength composite materials (i.e., more than 100 MPa) could be produced at the ambient temperature and alleviates the requirement of heat curing. The compressive strength of fly ash-slag geopolymer mixtures continually increased with age. An equal-part combination of fly ash-slag waste products displayed the optimum results with a marginal difference in the strength properties (106 MPa) of the matrix containing 60% fly ash and 40% slag. The improvement was dependent on the formation of calcium aluminate silicate hydrate (C-S-H/C-A-S-H) gel which acted as a secondary binding phase in conjunction with the amorphous geopolymer precursors.

However, the use of calcium hydroxide ($\text{Ca}(\text{OH})_2$) resulted in the incomplete dissolution of fly ash particles and the reduced formation of three-dimensional (3-D) amorphous geopolymer framework. Besides, the integration of ultrafine fly ash (UFFA) in ternary binder combinations showed opposing contributions. For geopolymer mixtures containing $\text{Ca}(\text{OH})_2$, the inclusion of UFFA was beneficial. On the other hand, the addition of UFFA at higher portions (i.e., more than 20%) reached the critical Si/Al ratio threshold which hindered the continuous dissolution of fly ash particles. These acted as defect sites within the microstructure and reduced the compressive strength properties.

Microstructural and physical characteristics of ambient cured geopolymer materials

The findings from different material characterization techniques including the XRD, TGA-DTA, SEM, and MIP conformed well to the measured compressive strengths. As such, broad amorphous humps were established between 25° and 31°, 2-theta angles in X-ray diffractograms whose intensities varied depending upon the additives quantity, included in low-calcium fly ash and the extent of geopolymerisation reaction. Similarly, the TGA-DTA results displayed variable endothermic peaks around 110°C signifying the evaporation of reaction water from the amorphous geopolymer framework. While the pore structure and SEM analyses showed reduced porosity and increasingly refined microstructure of the matrices with the inclusion of slag. In contrast, the SEM observations of specimens containing UFFA in higher proportions and Ca(OH)₂ revealed a substantially large number of unreacted fly ash grains and cracks throughout the microstructure.

Effect of curing conditions and aggregates content on the strength properties of high-strength geopolymers

Unlike previously published research articles which have used variable curing environments for the hybrid binder systems (i.e., fly ash-slag, fly ash-hydrated lime), the experimental results confirmed the crucial importance of this parameter that could significantly influence the mechanical properties of geopolymers. Generally, the use of water curing method resulted in the abridged dissolution of fly ash particles, increased porosity, and change in micro-crack density at the aggregate-gel interface boundaries. Moreover, although the inclusion of slag and UFFA reduced the pore size of fly ash-only geopolymers, the SEM observations revealed spherically shaped fly ash particles, voids, and microcracks in all water cured geopolymer specimens. A concomitant reduction in the compressive strength occurred by increasing the aggregates content in the geopolymer mixture designs irrespective of their curing regimes.

Development of high-performance FRGC materials using spiral-shaped steel, hooked-end steel, and HSPE fibers

From this phase of research, it was accomplished that the non-ductile behaviour of unreinforced geopolymer matrix significantly transformed to stable deflection-hardening in bending with the inclusion of fibers. All FRGCs showed multiple cracking failure responses and demonstrated high energy absorption capability. The most effective fiber reinforcement was found to be a hybrid mix of steel and HSPE fibers that not only generated a three times increase in flexural tensile strength (11.30 MPa) but also improved the deflection capacity of the composites at peak load. The post-test fracture pattern analysis revealed zig-zag cracks on the tension sides of the specimens which differed from those reported typically for the deflection-hardening composites.

The inclusion of steel fibers showed an equal reinforcing efficiency in uniaxial compression tests with an estimated improvement of 20% by including 2.0% steel fibers. However, a minor reduction in strength was noticed in the composites containing HSPE fibers. The individual fiber pull-out tests established a superior 3-D anchorage bond of the spiral steel fiber with the inorganic polymer phase. This allowed spiral steel fibers to yield as the maximum pull-out force increased with increasing embedment lengths and the failure modes shifted from pull-out to rupture. Comparisons for the elastic material parameters including the Poisson's ratio and Young's modulus showed no correlation for the results obtained in this study with those reported in the past. Furthermore, it was also established that the use of Australian Standards and existing concrete models might not be appropriate to predict the stiffness of geopolymer materials.

Influence of strain rate on the dynamic tensile properties of high-strength geopolymer and FRGC materials

The performances of high-strength geopolymer and two types of steel and one hybrid steel-polyethylene FRGC materials were assessed under dynamic splitting-tension. The results revealed an inadequate tensile strain capacity of the geopolymer matrix in quasi-static splitting tension tests. However, composite reinforced with hybrid steel-polyethylene fiber combination showed approximately 70% increase in the tensile strength and required 260 times more energy for the material fracture.

A prominent increase in tensile strengths was observed for all types of geopolymer composite materials with higher strain rates. As such, at a strain rate of 5 sec^{-1} , the tensile strength of unreinforced and FRGC materials reinforced with two different volume fractions and combinations were improved by 140%, 134%, 121%, and 115%, respectively. Comparing between the tension DIF_{ft} (dynamic increase factor) of high-strength geopolymer material obtained in this research, results from previous studies, and the recommended CEB formulae indicated a drastic underestimation of the increase in tensile strength of geopolymers at higher loading rates. This implies that the latest CEB guidelines are not suitable for the design of geopolymer structures. Therefore, the DIF_{ft} versus strain rate curves were plotted to derive the empirical constitutive models. Besides, the exclusivity of the proposed hybrid steel-polyethylene fiber reinforcement in controlling the crack-propagation upon impact was evident. At a given loading rate and time instant, the COD in hybrid FRGC was only 6.5% to that of plain geopolymer matrix.

Dynamic compressive material properties of high-strength geopolymer and FRGC materials

This study also investigated the effect of high strain rates on the dynamic compressive behaviour of newly fabricated geopolymer materials. The results showed that the compressive strengths of plain geopolymer and FRGC materials were approximately enhanced by 100% and 120% at a strain rate of 180 sec^{-1} , respectively. Moreover, the impact toughness analysis demonstrated obvious binomial relationships between the average strain rate and the energy absorption capacity of the studied materials with a distinct contribution from fibers.

Similar to the dynamic tensile tests, comparisons between the DIF_{f_c} data from this study, those reported by others, and CEB recommendations also demonstrated the inadequacy of code formulae to estimate the increase in strength of geopolymer materials in dynamic compression. As a result, the DIF_{f_c} versus strain rate curves were plotted which showed a linear, logarithmic relationship with the average strain rate. The strain rate sensitivity thresholds were found to exist at 30 sec^{-1} , and 66 sec^{-1} for the unreinforced and fiber reinforced samples, respectively. Post-impact fracture patterns were strain rate dependent such that the plain geopolymer specimens gradually shattered into smaller size fragments with an increase in the loading rate. On the other hand, despite the extensive micro-crack damage, the fiber reinforced samples did not show any material disintegration even at higher stress rates.

Influence of lateral confinement on the triaxial stress-strain characteristics of high strength geopolymer and FRGC materials

This research comprehensively studied the influence of high levels of confinement (0 to 100 MPa) on the triaxial stress-strain characteristics of geopolymer materials. The experimental results show that the high-strength geopolymer samples exhibited linear elastic behaviour in uniaxial compression; however, the inclusion of fibers improved their post-crack resistibility.

An associated increase in the axial strength and critical axial strain (ϵ_l) was observed in triaxial compression with the rise of confining pressures, similar to OPC concrete. Although, the failure curves for both types of materials displayed an apparent non-linearity with the increasing confinement ratios, the effect of lateral confining pressure was more pronounced on the triaxial strength of neat geopolymer. A sharp increase on the compressive strength meridian boundary was noticed for high-strength geopolymer material from low to moderate levels of confinement. On the other hand, the failure curve reached a plateau at higher confining pressures, while that of FRGC material was more linear.

Moreover, the commonly used “Willam-Warnke” failure criterion in commercial hydrocodes demonstrated an excellent fit for the obtained test results. However, the fitted curves suggested an upper strength boundary for the geopolymer materials in comparison to previous studies on OPC based HSCs. Empirical constitutive relationships were proposed that could be used to calibrate the strength parameters of existing concrete material models. Besides, the post-

test damage analyses revealed a noteworthy contribution by the fibers in triaxial compressive tests. The inclusion of fiber reinforcement not only had a positive influence in improving the critical axial strain of unreinforced geopolymer material but also enabled the FRGC samples to endure high levels of confining pressures without extensive damage.

8.2 Recommendations and Outlook for future studies

This thesis has dealt with an investigation of fabricating high-strength geopolymer composites at the ambient temperature. Considerable information regarding the microstructural characteristics and mechanical properties of high-performance geopolymer composites under quasi-static, high strain rate loading conditions, and multiaxial compression stress states has been elucidated from this research. At large, the outcomes demonstrate the excellent behaviour of the newly proposed geopolymer composites and encourage their use on a broad scale. However, there are few issues which could not be addressed due to the time constraints/equipment limitations in addition to some new knowledge gaps that can be considered in future to help improve the outlook of this research:

- 1) This research has mainly used the low calcium fly ash obtained from Gladstone, Australia for the synthesis of geopolymer materials. Other types of abundantly available fly ash source materials can be considered in the future studies.
- 2) In this research, the 12M NaOH solution was used to activate various source material combinations. Further studies can be undertaken by using different concentrations of NaOH to optimize the strength properties of geopolymer composites.
- 3) The present study demonstrated that the use of water curing method is not suitable for ambient cured geopolymer concrete, however further research can be undertaken to study the long term performance of geopolymer materials for alternate wet and dry cycles.
- 4) The geopolymer composites developed in this study primarily contained spiral-shaped steel fiber, hooked-end steel, and HSPE fibers. Other types of steel fibers such as Torex and undulated can also be combined with spiral steel fibers to reinforce the geopolymer matrix. Besides, the use of PVA instead of the HSPE fibers may also be considered.
- 5) The individual fiber pull-out tests were only performed for the spiral steel fibers. Additional studies can be carried out to establish the interfacial bond strength between the synthetic fibers and the geopolymer matrix in general and HSPE fibers.
- 6) As deliberated in the thesis, the latest CEB guidelines for OPC concrete are not suitable to estimate the dynamic increase factors for geopolymer based construction

materials both in dynamic tension (DIF_{ft}) and compression (DIF_{fc}). In particular, the empirical formulae significantly underestimate the tensile DIF_{ft} . The available information indicates that the critical strain rate threshold for geopolymer materials exists at a value higher than 1 sec^{-1} . In this regard, continued research is required to enrich the test database on dynamic material properties of geopolymers which will assist in establishing standard guidelines for the design of geopolymer structures, similar to CEB.

- 7) Moreover, differently sized SHPB equipment and cylindrical samples were used by different researchers to establish the dynamic material properties of geopolymers. Lateral inertia confinement is an inevitable factor that exists in high-speed impact tests and depends both on the strain rate and sample size. More experimental studies can be performed from this aspect using samples of variable sizes.
- 8) During the triaxial compression tests, the failure curve of high-strength geopolymer material reached a plateau at higher confining pressures. Although the exhibited behaviour is consistent with the findings reported by some of the researchers on the triaxial strength of OPC concrete, due to the nature of geopolymerization reaction in which water included in the mixtures is hypothesized to be expelled during the hardening and coagulation progress; it is suggested that further triaxial studies can be performed along with pore pressure measurements to validate the assumption.
- 9) Mathematical modeling of geopolymer materials requires due attention in future studies as it will allow simulating their real behaviour in the targeted engineering applications.
- 10) While the present study showed superior performance of the newly proposed geopolymer composites and fiber reinforcement technique at the material level, the concept can also be extended to the structural components.

BIBLIOGRAPHY DISCLAIMER

Every reasonable effort has been made to acknowledge the owners of copyright material. I would be pleased to hear from any copyright owner who has been omitted or incorrectly acknowledged.

APPENDIX - I

COPYRIGHT CLEARANCE AGREEMENTS BETWEEN THE AUTHOR

AND THE JOURNALS

The appendix contains the permissions from the relevant journals to reuse the candidate's published research work presented in this thesis.

*Chapter 2, Article: "Synthesis of high strength ambient cured geopolymer composite by using low calcium fly ash, in the **Journal of Construction and Building Materials.**"*

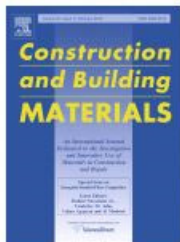


RightsLink®

Home

Account Info

Help



Title: Synthesis of high strength ambient cured geopolymer composite by using low calcium fly ash
Author: Musaad Zaheer Nazir Khan, Faiz uddin Ahmed Shaikh, Yifei Hao, Hong Hao
Publication: Construction and Building Materials
Publisher: Elsevier
Date: 30 October 2016
© 2016 Elsevier Ltd. All rights reserved.

Logged in as:
Musaad Zaheer Khan

LOGOUT

Please note that, as the author of this Elsevier article, you retain the right to include it in a thesis or dissertation, provided it is not published commercially. Permission is not required, but please ensure that you reference the journal as the original source. For more information on this and on your other retained rights, please visit: <https://www.elsevier.com/about/our-business/policies/copyright#Author-rights>

BACK

CLOSE WINDOW

Copyright © 2018 Copyright Clearance Center, Inc. All Rights Reserved. [Privacy statement](#). [Terms and Conditions](#).
Comments? We would like to hear from you. E-mail us at customercare@copyright.com

*Chapter 3, Article: “Effects of curing conditions and sand-to-binder ratio on compressive strength development of fly ash geopolymer, in the **Journal of Materials in Civil Engineering.**”*

8/22/2018

Information for ASCE Authors: Reusing Your Own Material

ASCE



- [Guidelines for Permission Request](#)
- [ASCE Terms and Conditions for Permissions Requests](#)
- [Request Permission Online \(Copyright Clearance Center\)](#)
- [STM Permission Guidelines](#)
- [Reuse Author's Own Material](#)
- [Open Access Options and Rights](#)

REUSE AUTHOR'S OWN MATERIAL

As the original author of an ASCE journal article or proceedings paper, you are permitted to reuse your own content for another ASCE or non-ASCE publication.

The following restrictions apply:

- Permission is denied if you request to republish an entire article in an ASCE or a non-ASCE publication.
- Permission is denied if the requested content constitutes more than 25% of your work in a new publication.
- **Internet posting of the *published version* of your article is strictly prohibited.**
- If the request is for an online coursepack, the site must be password-protected.
- If you wish to photocopy your content, the total number of copies cannot exceed 100. If you need more than 100 copies, please contact [ASCE Permissions](#) directly.

If the content has been prepared by an employee within the scope of employment, the employer shall enjoy the same rights as the authors.

If the content was prepared under a U.S. government contract, the federal government shall have the rights under the copyright law to the extent required by the contract.

POSTING YOUR ARTICLE OR PAPER ONLINE

Published Article

Authors may post a PDF of the ASCE-published version of their work on their employers' *Intranet* with password protection.

Draft Manuscript

Authors may post the final draft of their work on open, unrestricted Internet sites or deposit it in an institutional repository when the draft contains a link to the bibliographic record of the published version in the [ASCE Library](#) or [Civil Engineering Database](#). "Final draft" means the version submitted to ASCE after peer review and prior to copyediting or other ASCE production activities; it does not include the copyedited version, the page proof, or a PDF of the published version. Proceedings papers, with no final draft, may post the abstract.

When posting online, please add the statement: "This material may be downloaded for personal use only. Any other use requires prior permission of the American Society of Civil Engineers. This material may be found at [URL/link of abstract in the ASCE Library or Civil Engineering Database]."

Chapter 4, Article: “Mechanical properties of ambient cured high strength hybrid steel and synthetic fibers reinforced geopolymer composites, in the *Journal of Cement and Concrete Composites.*”



RightsLink®

Home

Account Info

Help



Title: Mechanical properties of ambient cured high strength hybrid steel and synthetic fibers reinforced geopolymer composites

Author: MUSAAD ZAHEER NAZIR KHAN, YIFEI HAO, HONG HAO, FAIZ UDDIN AHMED SHAIKH

Publication: Cement and Concrete Composites

Publisher: Elsevier

Date: January 2018

© 2017 Elsevier Ltd. All rights reserved.

Logged in as:
Musaad Zaheer Khan

LOGOUT

Please note that, as the author of this Elsevier article, you retain the right to include it in a thesis or dissertation, provided it is not published commercially. Permission is not required, but please ensure that you reference the journal as the original source. For more information on this and on your other retained rights, please visit: <https://www.elsevier.com/about/our-business/policies/copyright#Author-rights>

BACK

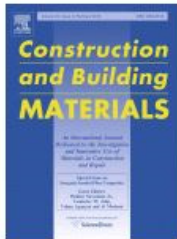
CLOSE WINDOW

Copyright © 2018 Copyright Clearance Center, Inc. All Rights Reserved. [Privacy statement](#). [Terms and Conditions](#). Comments? We would like to hear from you. E-mail us at customercare@copyright.com

Chapter 6, Article: “Experimental evaluation of quasi-static and dynamic compressive properties of ambient-cured high-strength plain and fiber reinforced geopolymer composites, in the *Journal of Construction and Building Materials*.”



RightsLink®



Title: Experimental evaluation of quasi-static and dynamic compressive properties of ambient-cured high-strength plain and fiber reinforced geopolymer composites

Author: Musaad Zaheer Nazir Khan, Yifei Hao, Hong Hao, Faiz Uddin Ahmed Shaikh

Publication: Construction and Building Materials

Publisher: Elsevier

Date: 30 March 2018

© 2018 Elsevier Ltd. All rights reserved.

Logged in as:
Musaad Zaheer Khan
[LOGOUT](#)

Please note that, as the author of this Elsevier article, you retain the right to include it in a thesis or dissertation, provided it is not published commercially. Permission is not required, but please ensure that you reference the journal as the original source. For more information on this and on your other retained rights, please visit: <https://www.elsevier.com/about/our-business/policies/copyright#Author-rights>

[BACK](#) [CLOSE WINDOW](#)

Copyright © 2018 [Copyright Clearance Center, Inc.](#) All Rights Reserved. [Privacy statement](#). [Terms and Conditions](#).
Comments? We would like to hear from you. E-mail us at customercare@copyright.com

Chapter 7, Article: “Experimental evaluation of quasi-static and dynamic compressive properties of ambient-cured high-strength plain and fiber reinforced geopolymer composites, in the *Journal of Construction and Building Materials*.”

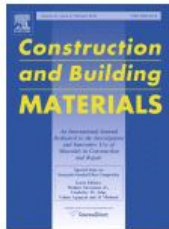


RightsLink®

Home

Account Info

Help



Title: Mechanical properties of ambient cured high-strength plain and hybrid fiber reinforced geopolymer composites from triaxial compressive tests

Author: Musaad Zaheer Nazir Khan, Yifei Hao, Hong Hao, Faiz Uddin Ahmed Shaikh, Kewei Liu

Publication: Construction and Building Materials

Publisher: Elsevier

Date: 10 October 2018

© 2018 Elsevier Ltd. All rights reserved.

Logged in as:
Musaad Zaheer Khan

LOGOUT

Please note that, as the author of this Elsevier article, you retain the right to include it in a thesis or dissertation, provided it is not published commercially. Permission is not required, but please ensure that you reference the journal as the original source. For more information on this and on your other retained rights, please visit: <https://www.elsevier.com/about/our-business/policies/copyright#Author-rights>

BACK

CLOSE WINDOW

Copyright © 2018 [Copyright Clearance Center, Inc.](#) All Rights Reserved. [Privacy statement.](#) [Terms and Conditions.](#) Comments? We would like to hear from you. E-mail us at customercare@copyright.com

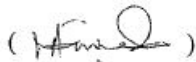
APPENDIX - II

STATEMENTS OF CONTRIBUTION OF OTHERS

To whom it may concern

I, Musaad Zaheer Nazir Khan, carried out the literature review, experimental investigations, analysis of results, and written the manuscripts for the papers titled below. The second co-author assisted in performing the mercury intrusion porosity tests at AIT, Thailand. The third co-author and the fourth co-author revised and edited the manuscript and also helped in the analysis of test results.

- 1) **Synthesis of high strength ambient cured geopolymer composite by using low calcium fly ash**
- 2) **Effects of curing conditions and sand-to-binder ratios on compressive strength development of fly ash geopolymer**

()

I, as a Co-author, endorse that this level of contribution by the candidate indicated above is appropriate.

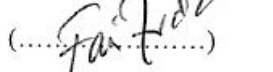
(Prof. Hong Hao)

()

(Prof. Yifei Hao)

()

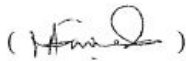
(Assoc. Prof. Faiz Shaikh)

()

To whom it may concern

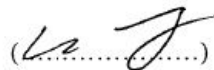
I, Musaad Zaheer Nazir Khan, carried out the literature review, experimental investigations, analysis of results, and written the manuscripts for the papers titled below which were revised and edited by the second co-author and the third co-author. The second and third co-authors also provided significant intellectual support and suggesting the research methodologies. The fourth co-author helped during the tests at Curtin University and in sourcing the synthetic fibers from Japan and proof-read the manuscripts.

- 1) **Mechanical properties of ambient cured high strength hybrid steel and synthetic fibers reinforced geopolymer composites**
- 2) **Mechanical properties and behaviour of high-strength plain and hybrid-fiber reinforced geopolymer composites under dynamic splitting tension**
- 3) **Experimental evaluation of quasi-static and dynamic compressive properties of ambient-cured high-strength plain and fiber reinforced geopolymer composites**

()

I, as a Co-author, endorse that this level of contribution by the candidate indicated above is appropriate.

(Prof. Hong Hao)

()

(Prof. Yifei Hao)

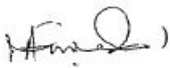
()

(Assoc. Prof. Faiz Shaikh)

()

To whom it may concern

I, Musaad Zaheer Nazir Khan, carried out the literature review, experimental investigation, analyzed the results, and written the manuscript of the paper titled, "**Mechanical properties of ambient cured high-strength plain and hybrid fiber reinforced geopolymer composites from triaxial compressive tests.**" which was revised and edited by the second co-author and the third co-author. The second and third co-author also helped in the conduct of experimental investigations. The fourth co-author assisted with the laboratory procedures at Curtin University. The fifth author provided help during the triaxial compression tests at Central South University, China.

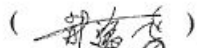
()

I, as a Co-author, endorse that this level of contribution by the candidate indicated above is appropriate.

(Prof. Hong Hao)

()

(Prof. Yifei Hao)

()

(Assoc. Prof. Faiz Shaikh)

()

(Mr. Kewei Liu)

()